Interactions of Multi-Rotors with Surfaces
Aerodynamic Characterization and Performance Modelling

Dekker, H.N.J.

Citation (APA)
Dekker, H. N. J. (2025). *Interactions of Multi-Rotors with Surfaces: Aerodynamic Characterization and Performance Modelling*. [Dissertation (TU Delft), Delft University of Technology]. https://doi.org/10.4233/uuid:947d4bf9-053d-419f-9a2f-cdd76ef0e4a1

Important note
To cite this publication, please use the final published version (if applicable).
Please check the document version above.

Interactions of Multi-Rotors with Surfaces

Aerodynamic Characterization and Performance Modelling
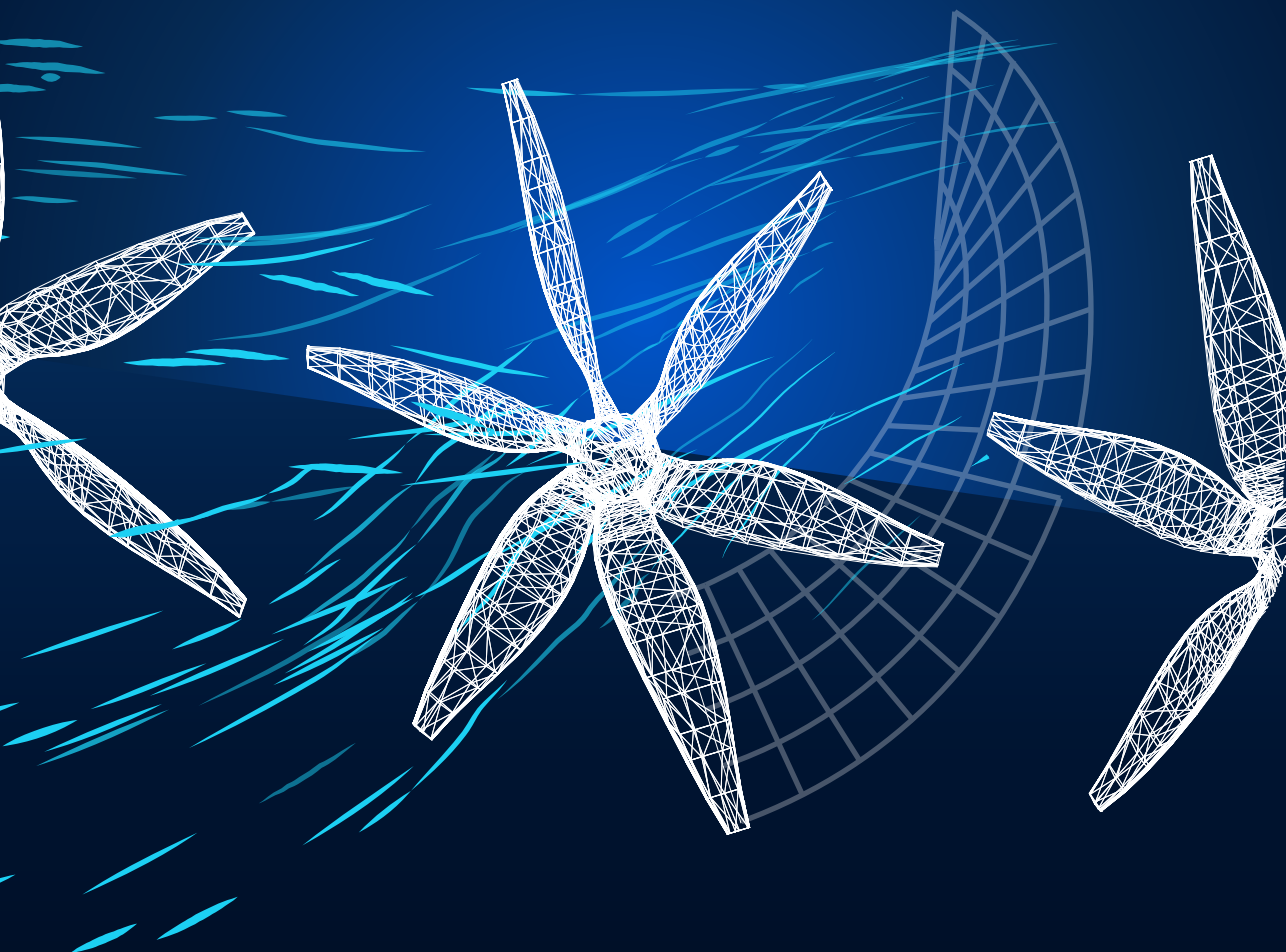
Hasse Dekker

Interactions of Multi-Rotors with Surfaces

Aerodynamic Characterization and Performance Modelling

Interactions of Multi-Rotors with Surfaces

Aerodynamic Characterization and Performance Modelling

Dissertation

by

Hasse Nicolaas Jan DEKKER

Master of Science in Mechanical Engineering, University of Twente, the Netherlands
born in Zutphen, the Netherlands.

This dissertation has been approved by:

promotor: Dr. D. Ragni
copromotor: Dr. ir. W. J. Baars
supervisor: Dr. ir. M. Tuinstra

Composition of the doctoral committee:

Rector Magnificus,	chairperson
Dr. D. Ragni	Delft University of Technology, promotor
Dr. ir. W. J. Baars	Delft University of Technology, copromotor
Dr. ir. M. Tuinstra	Royal Netherlands Aerospace Centre, supervisor

Independent members:

Prof. dr. R. Camussi	University Roma Tre, IT
Prof. dr. ir. C. Schram	Von Karman Institute, BE
Prof. dr. ir. C. H. Venner	University of Twente
Prof. dr. ir. L. L. M. Veldhuis	Delft University of Technology
Prof. dr. D. A. von Terzi	Delft University of Technology, reserve member

An electronic version of this dissertation is available at
http://repository.tudelft.nl/.

Contents

Summary

Recent advancements in electric propulsion technology have paved the way for alternative transportation systems aimed at revolutionizing travel times in congested metropolitan areas. The proposed electric Vertical and Take-Off and Landing (eVTOL) aircraft configurations exist in great diversity, but can be classified depending on their overall propulsion and wing layout. An example is the tilt-wing eVTOL, which combines the maneuverability of a helicopter with the cruise efficiency of an aircraft and therefore provides a promising vehicle architecture for this market. Nonetheless, future eVTOL vehicles face challenges regarding public acceptance and safe operation in urban environments, and successful implementation therefore relies on performance enhancement strategies.

The high power-to-weight ratio and efficiency of electric motors provide an excellent platform to explore disruptive propulsion system configurations. An observable design trend here is the tight integration of distributed, fixed-pitched rotors with aerodynamic surfaces, aimed at generating beneficial aerodynamic coupling effects to increase the aircraft's efficiency and reduce acoustic emissions.

An auspicious integrated tilt-wing propulsion system layout is known as Over-The-Wing propulsion, which promises favorable aerodynamic effects by the rotor-induced flow and reduced noise signature during fly-over by shielding. However, during the operation of Over-The-Wing propulsion in eVTOL flight conditions, several multi-rotor-surface interactions are encountered, resulting in unexplored aerodynamic and aeroacoustic effects. As a consequence, design guidelines to maximize aerodynamic performance and minimize noise signature for Over-The-Wing propulsion for eVTOL flight conditions are missing in the public domain. This thesis focuses on enabling Over-The-Wing propulsion for vertical flight through experimentation and low-order modeling of the fundamental aerodynamic interactions between distributed rotors and surfaces.

The first rotor-surface interaction concerns the initial stages of take-off where the wake of the distributed rotors interacts with the ground surface. The three-dimensional flow topology of side-by-side rotors in these conditions is studied using Lagrangian Particle Tracking. The radial deflection of subsequent rotor slipstreams generates opposing wall jets that interact and separate with the flow emerging from the wall in a fountain-like pattern. From a parametric study on rotor spacing and ground standoff height, a generic classification of flow regimes is proposed. Re-ingestion of the fountain flow occurs when the rotors are sufficiently far apart. During this condition, the flow exhibits a tendency towards asymmetric states, where the fountain flow column and the domain of re-ingestion shift closer to one of the rotors. Moreover, temporal dynamic features are involved in the wake re-ingestion state, resulting in lateral shifting of the fountain flow, which determines a location switch of re-ingestion from one rotor disk to the other. These unsteady phenomena are observed at a frequency that is approximately two orders of magnitude lower than the blade passing frequency. The dominant characteristic time scale is linked

to the flow re-circulation path, relating this to system parameters of thrust and ground stand-off height. Results from a modal analysis by proper orthogonal decomposition are used to formulate a simple dynamic flow model of the re-ingestion switching cycle.

In the second part of the thesis, interactions between distributed rotors and the lifting surface in an Over-The-Wing orientation are investigated, and the performance is predicted using a first-order model approach. A formulation for the aero-propulsive performance incorporates aerodynamic interactions between the rotor-and-wing-induced flow fields. Subsequently, the tonal noise of the rotor is modelled through an analytical description of the inviscid potential effects of the wing's circulation. The related steady inflow distortion serves as input to an aeroacoustic noise prediction chain that computes the unsteady loading on the blades and the resulting tonal noise emission by Helicoidal Surface Theory. Hypotheses about the flow behavior, as well as the final predictions, are validated through experiments performed with an array of five rotors (for the aero-propulsive performance) and a single rotor (for the aeroacoustics) above an airfoil. At moderate angles of attack, the propulsive thrust is reduced by the wing's circulation, in particular for the rotor positioned close to the wing's leading edge. Around the stall angle of the isolated wing, the rotors delay leading edge separation when operated in low-thrust conditions. By increasing the thrust, a pronounced region of reverse flow between the rotors and wing is induced, which cancels any effects of leading-edge separation delay. Under these conditions, the system exhibits increased thrust due to ingestion of low-momentum flow. The rotor-induced flow over the wing augments suction, while the pressure side sees a pressure increase, ascribed to flow entrainment from the rotors' streamtubes. The aero-propulsive model predictions accurately describe the experimental observations for thrust and lift. However, discrepancies in the lift force are present when the rotors are operated in low-thrust conditions. Aeroacoustic measurements below the wing show a reduction of the first BPF with 10 dB compared to an isolated rotor. The high-frequency broadband noise for these emission directions is also reduced. On the suction side of the wing, the predictions and experimental data show a comparable increase in the tonal components relative to the isolated rotor. Around the rotor disk plane, this increase is primarily the result of the reflections due to the presence of the wing. Both experiments and model predictions show a minimization of the tonal noise for a mid-chord rotor position, for these emission directions. The noise increase by unsteady loading is shown to be sensitive to the angle of attack and is primarily radiated downstream, showing an increase of 3-7 dB. Consequently, variations in tonal noise with rotor positioning are enhanced in this direction with a predicted maximization for a 40% chord rotor position.

The final study of the thesis concerns the unsteady three-dimensional aerodynamic interactions during a reference take-off mission of the Over-The-Wing mounted rotor array. The wing's geometric angle of attack and wind tunnel velocity change dynamically during acquisition, corresponding to a steep ascent take-off trajectory. Simultaneously, the flow is characterized using large-scale Lagrangian Particle Tracking employing helium-filled soap bubbles as tracer particles. An analysis of the time-averaged velocity field shows that the most pronounced variations in span direction are found downstream of the rotor disks. The combined swirl of the wakes produced by the counter-rotating rotor array

generates alternating regions of downwash and low vertical velocity between the rotors. Instantaneous results obtained under dynamic operating conditions show a similar flow topology to those where a fixed angle of attack has been prescribed. However, variations in the position of the separated flow regions suggest a change in the effective angle of attack for the dynamic measurements. The behavior is linked to the classical theory of the unsteady angle of attack for thin airfoils; however, a more detailed analysis is required to conclude this.

The studies show that confined rotors under high thrust conditions or large angles of attack generate re-circulating flow patterns that are unsteady and lead to an enhancement in broadband noise and the haystacking phenomenon. Moreover, such flow phenomena reduce the separation delay capabilities of Over-The-Wing propulsion, and therefore careful design of the propulsion system is required to mitigate this.

Based on the thrust, lift and rotor noise sources of Over-The-Wing propulsion at incidence, a rotor position towards the wing trailing edge seems most favorable. On the other hand, the shielding potential is higher for a mid-chord positioned rotor, and a rotor towards the trailing edge increases the likelihood of acoustic scattering of the blade harmonics and gives the largest drag penalty of the wing. Hence, the optimal rotor position is a trade-off between the aforementioned effects and therefore depends on the specific requirements of the system. The proposed low-fidelity tools allow for efficient optimization by varying the geometric and performance parameters of the propulsion system and are therefore particularly useful in the early design phase. Nonetheless, the methods fail to account for complex viscous effects and vortex-induced velocities, thus complementary experiments or high-fidelity simulations are still required.

Samenvatting

Innovaties in elektrische voortstuwing hebben een nieuw conceptueel vervoersysteem mogelijk gemaakt, gericht op het verkorten van reistijden in drukke stedelijke gebieden. Hierbij wordt gebruik gemaakt van vliegtuig configuraties die verticaal opstijgen en landen, en elektrisch worden aangedreven (eVTOLs). Concepten voor eVTOLs bestaan in grote verscheidenheid maar kunnen geclassificeerd worden op basis van hun algehele voortstuwings- en vleugelindeling. Een veelbelovend concept is de 'tilt-wing' eVTOL, wat gebruik maakt van een kantelbare vleugel-rotor combinatie met als doel om de flexibiliteit van een helikopter te combineren met de cruise-efficiëntie van een conventioneel vliegtuig. De succesvolle implementatie van eVTOLs in het publieke domein is echter afhankelijk van het oplossen van maatschappelijke vraagstukken op het gebied van geluidshinder en veiligheid. Om dit mogelijk te maken, zullen de prestaties van dit soort vliegtuigen aanzienlijk verbeterd moeten worden. Het lage gewicht en de hoge efficiëntie van elektromotoren zorgt voor toegenomen flexibiliteit in de inrichting van het voortstuwingsysteem. Een markt trend die hierdoor waarneembaar is, is het verdelen van de voortstuwing over kleinere rotoren die zich dichtbij de romp of vleugels bevinden. Dit wordt gedaan om positieve synergie tussen de stroming van het voortstuwingsysteem en aerodynamische oppervlakken te genereren, met als doel de efficiëntie te verhogen. Daarnaast kunnen de oppervlakken gebruikt worden om de afstraling van het rotor geluid te veranderen en daardoor akoestische emissies te verminderen. Een veelbelovend ontwerp wat van dit soort effecten gebruik maakt is 'Over-The-Wing' voortstuwing waarbij een rij rotoren zich boven een vleugel oppervlak bevindt. Hierdoor wordt, enerzijds, een rotor-geïnduceerde stroming over het vleugel gegenereerd, wat de draagkracht verhoogd, terwijl het vleugeloppervlak voor afscherming van het rotor geluid zorgt. Tijdens een eVTOL vlucht zijn er echter verschillende interacties tussen de rotoren en oppervlakken te verwachten, die resulteren in onbekende aerodynamische en aero-akoestische neveneffecten. Dit betekent dat richtlijnen voor het maximaliseren van de efficiëntie en minimaliseren van het geluid momenteel ontbreken in het publieke domein. Dit proefschrift richt zich daarom op het instaat stellen van 'Over-The-Wing' voortstuwing voor eVTOLs, door middel van het uitvoeren van experimenteren op, en het lage-orde modelleren van, fundamentele aerodynamische interacties tussen rotoren en oppervlakken.

De eerste rotor-oppervlak interactie richt zich op de beginfase van het verticaal opstijgen, waarin de rotoren zich haaks boven een grondoppervlak bevinden. Het driedimensionale stromingsveld rond twee-rotoren in deze condities wordt gemeten door middel van de 'Lagrangian Particle Tracking'-techniek, gebruikmakend van helium-gevulde zeepbellen als stromingsdeeltjes. De resultaten laten de expansie van de twee rotor zoggen zien, wat leidt tot radiale stromingen die parallel aan, en vlak boven, het grondoppervlak voortbewegen. Wanneer deze tegengestelde stromingen op elkaar inwerken, zorgt dit voor loslating vanaf de grond, wat resulteert in een fontein-achtige stromingsorganisatie. Op

basis van een parametrisch onderzoek naar de relatieve afstand tussen de rotoren en de
hoogte ten opzichte van de grond, wordt een indeling van verschillende stromingsregimes
voorgesteld. Als de rotoren voldoende ver van elkaar verwijderd zijn, wordt de fontein-
stroming vanaf de grond opnieuw ingezogen. In deze situatie is er duidelijke asymmetrie
aanwezig in het stromingsveld, waarbij de fontein naar een van de rotoren verschuift en
daar wordt ingezogen. Bovendien zijn er dynamische zijwaartse verschuivingen van de
fonteinstroming aanwezig, waardoor de aanzuiging van de ene naar de andere rotor wis-
selt. Dit verschijnsel wordt waargenomen met een frequentie die ongeveer twee orde van
grootte lager is dan de bladpasseer-frequentie. Deze dominante karakteristieke tijdschaal
is gerelateerd aan het stromings-recirculatie pad, dat weer gekoppeld is aan de rotor stuw-
kracht en de afstand tot de grond.

Het tweede deel van dit proefschrift richt zich op het modelleren van verschillende ae-
rodynamische interacties tussen rotoren en een vleugelprofiel die zich bij 'Over-The-Wing'
voortstuwing voordoen. Een formulering voor de stuw- en draagkracht wordt gevormd
op basis van het rotor- en vleugel-geïnduceerde stromingsveld. Vervolgens wordt het to-
nale geluid van de rotor gemodelleerd door middel van een analytische beschrijving op
basis van de niet-viskeuze potentiaalstroming over de vleugel. De bijbehorende constante
instroomverstoring wordt als input gebruikt voor een geluid voorspellingsketen die de
wisselbelasting en de daaruit voortvloeiende aerodynamische geluidsbronnen berekent
met 'Helicoidal Surface Theory'. Hypothesen over de aerodynamische interacties, evenals
de uiteindelijke voorspellingen, worden gevalideerd door middel van experimenten uitge-
voerd met een array van vijf rotoren (voor de aero-propulsive prestaties) en een enkele
rotor (voor de aero-akoestiek) boven een profiel. Bij gematigde invalshoeken wordt de
stuwkracht verminderd door de ge-induceerde stroming van de vleugel. Dit met name re-
levant wanneer de rotor zich dicht bij de voorkant van de vleugel zij geplaatst. Bij grotere
invalshoeken, en wanneer de rotoren relatief weinig stuwkracht leveren, wordt loslatings-
hoek van het vleugelprofiel verhoogd. Echter, wanneer de stuwkracht toeneemt, wordt er
een recirculatie stroom tussen het vleugeloppervlak en de rotoren gevormd, wat resulteert
in globale loslating van de stroming over het vleugelprofiel. Onder deze omstandigheden
neemt de stuwkracht verder toe als gevolg van de aanzuiging van langzame, turbulente
stroming. De door de rotor geïnduceerde stroming verlaagt de druk aan de zuigkant van de
vleugel, terwijl de druk aan de andere kant toeneemt door een vergroting van de effectieve
invalshoek. De voorspellingen van het aerodynamische model komen overeen met expe-
rimentele waardes voor stuwkracht en lift. Er zijn echter afwijkingen in de draagkracht
van de vleugel wanneer de rotoren weinig stuwkracht leveren. Aero-akoestische metin-
gen onder de vleugel tonen een vermindering van het niveau van de eerste bladpasseer-
frequentie met 10 dB, in vergelijking met een geïsoleerde rotor. Het hoogfrequente breed-
bandgeluid voor deze uitstralingsrichting wordt eveneens verminderd. Aan de zuigkant
van de vleugel laten de voorspellingen en de experimenten een vergelijkbare toename van
het tonale geluid ten opzichte van de geïsoleerde rotor zien. In het rotorvlak is deze toe-
name voornamelijk het gevolg van de akoestische reflecties door de aanwezigheid van de
vleugel. Zowel experimenten als voorspellingen tonen een minimalisatie van het tonale
geluid voor een rotorpositie in het midden van de vleugelkoorde, voor deze uitstraalrich-
ting. De geluidsverhoging door de wisselbelasting is afhankelijk van de invalshoek en

wordt voornamelijk stroomafwaarts uitgestraald, resulterend in een geluidstoename van 3-7 dB. Het tonale geluid in deze afstralingrichting is gevoeliger voor de rotorpositie; een maximalisatie voor een rotor op 40% van de koorde wordt voorspeld.

De afsluitende studie van dit proefschrift betreft de dynamische, driedimensionale aerodynamische interacties tijdens het opstijgen van een 'Over-The-Wing' voortstuwingssysteem. De invalshoek van de vleugel en de snelheid van de windtunnel veranderen dynamisch, wat overeenkomt met een steile klim in de begin fase van een referentie vlucht pad. Tijdens de test wordt de stroming gemeten met behulp van 'Lagrangian Particle Tracking' en helium-gevulde zeepbellen als stromingsdeeltjes. Een analyse van het tijdgemiddelde snelheidsveld toont aan dat de meest uitgesproken variaties in de span-richting zich stroomafwaarts van de rotoren bevinden. Hier worden afwisselende gebieden van op- en neerwaartse stroming tussen de rotoren gevormd, als gevolg van de gecombineerde swirl in het zog van de rotor array. Instantane resultaten onder dynamische condities laten een soortgelijke stromingstopologie zien als die waarbij een vaste, maar overeenkomende, invalshoek is voorgeschreven. Variaties in de positie van de loslatingsgebieden wijzen echter op een verandering in de effectieve invalshoek voor de dynamische metingen. Een link met dit gedrag en bestaande theorie voor de voorspelling van invalshoeken in dynamische condities voor dunne vleugelprofielen is gevonden. Echter, is een grondigere analyse nodig om hier conclusies over te trekken.

Uit de studies is gebleken dat geïntegreerde rotoren, met een hoge stuwkracht of grote invalshoek, recirculerende en onstabiele stromingspatronen kunnen veroorzaken. Wanneer deze worden aangezogen door de rotor, zorgt dit door een toename van het breedband geluid door spectrale verbreding. Bovendien verminderen dergelijke stromingsverschijnselen het potentieel van 'Over-The-Wing' voortstuwing om de loslatingshoek van de vleugel te verhogen en daarom is zorgvuldig ontwerp van het voortstuwingssysteem vereist om recirculatie te beperken.

Op basis van de stuwkracht, draagkracht en de rotor geluidsbronnen van 'Over-The-Wing' voortstuwing blijkt een rotorpositie rond de achterrand van de vleugel het gunstigst. Echter, verhoogt deze positie de waarschijnlijkheid van akoestische verstrooiing via de achterrand en geeft het de grootste luchtweerstand van de vleugel, terwijl het schild potentieel van de vleugel verhoogd wordt voor een rotor in het midden van de koorde. De optimale rotorpositie is dus een afweging tussen bovengenoemde effecten en is daarom afhankelijk van de specifieke eisen van het voortstuwingssysteem. De voorgestelde voorspellings-tools maken optimalisatie mogelijk door de geometrische en prestatieparameters van het voortstuwingssysteem efficiënt te variëren en zijn daarom nuttig in de vroege ontwerpfase van dit soort vliegtuigen. De methoden omvatten echter geen complexe viskeuze effecten of door vortex-geïnduceerde snelheden, dus aanvullende experimenten of numerieke simulaties zijn nog steeds vereist.

NOMENCLATURE

Symbols

a	axial induced velocity factor [-]
a_i	POD temporal coefficients [-]
A_n	auto-power average [-]
b	tangential induced velocity factor [-]
B	number of blades [-]
BPF	blade passing frequency [Hz]
c	chord length [m]
c_0	speed of sound [m·s^{-1}]
c_l	two-dimensional lift coefficient ($c_l = L/(qcS)$) [-]
c_d	two-dimensional drag coefficient ($c_d = D/(qcS)$) [-]
C	generic coefficient [-], seeding concentration [mm^{-3}]
$\boldsymbol{C}$	cross-spectral matrix [-]
C_n	complex average [-]
C_p	pressure coefficient ($C_p = (p - p_\infty)/q$) [-]
C_{SL}	shear layer correction term [-]
C_T	thrust coefficient ($C_T = T/(\rho n^2 D^4)$) [-]
C_T'	sectional thrust coefficient ($C_T' = T'/(\rho n^2 D^3)$) [-]
C_Q	torque coefficient ($C_Q = Q/(\rho n^2 D^5)$) [-]
C_Q'	sectional torque coefficient ($C_Q' = Q'/(\rho n^2 D^4)$) [-]
d	diameter [m]
$\boldsymbol{d_i}, d_{ix}, d_{iy}, d_{iz}$	disparity vector and disparity vector components [px]
dy	offset from surface [m]
D	rotor diameter [m], drag force [N]
D_I	interrogation window size [px^2]
DSR	dynamic spatial range ($DSR = L/D_I$) [-]
DVR	dynamic velocity range ($DVR = V/\sigma_V$) [-]
E	total resolved kinetic energy [m^2·s^{-2}]
f	objective focal length [mm], frequency [Hz]
$f_\#$	numerical aperture
f^*	normalized frequency [-]
g	steering function [-]
G	Green's function in free space [-]
G_{xx}, G_{xy}	power spectrum and cross-power spectrum [Hz^{-1}]
GF	Gauge Factor [-]
h	grid spacing [m]
H	ground stand-off distance [m], vertical displacement [m]

He	Helmholtz number ($He = 2\pi L/\lambda$) [-]
$\hat{H}$	complex normalized thickness of the displaced fluid [-]
I	intensity [-], intensity map [-]
J	rotor advance ratio ($J = V_\infty/(nD)$) [-], Light pulse energy [J]
$\hat{J}_n, \hat{K}_n$	n-th order Bessel function of the first and second kind [-]
J_{T0}	zero thrust rotor advance ratio [-]
k	wavenumber [m^{-1}]
L	lift force [N], characteristic length of measurement domain [m], sensor size length [m]
M	Mach number ($M = V/c_0$) [-], Optical magnification [-], mapping function [-]
M_x	flight Mach number [-]
n	shaft frequency [Hz], loading harmonic number [-]
$\mathbf{n}$	unit normal vector [-]
N	number of uncorrelated recordings [-]
N_r	number of rotors [-]
$OASPL$	Overall Sound Pressure Level [dB]
p	acoustic pressure [Pa]
p_{ref}	acoustic reference pressure (20μPa) [Pa]
p_s	static pressure [Pa]
ppp	particles per pixel [px^{-1}]
P	complex acoustic pressure, [Pa]
q	dynamic pressure [Pa]
Q	rotor torque [N·m]
Q'	sectional rotor torque [N]
r	radial coordinate [m]
$r_0, r_{0,hub}$	normalized radial coordinate (r/R) and normalized hub radius [-]
r_c	wing nose radius [m]
R	rotor radius [m], source-observer distance [m], electrical resistance [Ohm]
$\mathbf{R}$	covariance matrix [-], correlation map [-]
Re_b, Re_c	(3/4)R rotor blade chord and wing chord Reynolds number ($Re = Vc/\nu$) [-]
R_s	local radius of streamtube [m]
$\mathbf{s}$	Cartesian coordinates of vortex line
$\mathbf{s}$	line coordinates in reference frame [m], spatial shift [-]
S	tip-to-tip rotor separation distance [m], wingspan [m], horizontal displacement [m], surface area [m^2]
$\hat{S}$	Sears function [-]
SPL	sound-pressure level [dB]
St	Stokes number ($St = \tau u/L$) [-]
t	time [s]
T	rotor thrust [N], total time [s], timescale [s]
T'	sectional rotor thrust [N·m^{-1}]
T_{ij}	Lighthill stress tensor [Pa]

TKE	Turbulent Kinetic Energy [m^2·s^{-2}]
$\hat{t}_b$	complex blade thickness [m]
t_{SL}	shear layer thickness [m]
u, v, w	Cartesian velocity components [m·s^{-1}]
$\hat{\mathbf{u}}$	reconstructed velocity field [m·s^{-1}]
u_k	windowing function [-]
U_{tip}	rotor tip speed [m·s^{-1}]
V	velocity magnitude [m·s^{-1}], voltage [V]
w_{ind}	induced velocity in hover [m·s^{-1}]
x, y, z	Cartesian coordinates in reference frame [m]
x_i, y_i	image coordinates [px]
$\mathbf{x}$	observer position vector [m]
x'	x-position from the rotor ($x' = x - x_r$) [m]
x_r	x-position of the rotor tip from wing's leading edge [m]
X	normalized blade chord coordinates ($X = x/c$-1/2) [-], distance [m]
$\mathbf{y}$	source position coordinates [m]
y_o	y-position of far-field observer [m]
y_r	y-position of the rotor shaft from wing's surface [m]
y_{SL}	shear layer height [m]
y_t	rotor tip gap from wing's surface ($y_t = y_r - R$) [m]
z_r	axis-to-axis rotor separation [m]
z	ground stand-off distance [m]
Z	distance [m]
α	geometric angle of attack [rad], weighing coefficient [-]
α_0, α_1	blade's trailing edge and leading edge separation angle [rad]
α_c	stall angle [rad]
β	blade pitch angle [rad]
γ	blade lean [m]
γ^2	linear coherence [-]
Γ	circulation [m^2·s^{-1}]
δ_{99}	boundary layer thickness [m]
δz	laser sheet thickness [m]
$\Delta\alpha$	difference in effective angle of attack from isolated wing ($\Delta\alpha = \alpha_{eff} - \alpha_w$) [rad]
Δt	pulse separation [s], sample interval [s]
$\Delta x, \Delta y, \Delta z$	measurement domain [m]
ϵ	streamtube deflection angle [rad], measurement uncertainty [-] mechanical strain [-]
ζ	Prandtl-Glauert compressibility factor [-]
θ	azimuthal coordinate [rad]
θ_o	far-field observer direction [rad]
λ	wavelength [m], Eigenvalue [-], blade sweep [m]
$\tilde{\lambda}$	relative energy fraction [-]
λ_2	λ_2-criterion [s^2]
μ	dynamic viscocity [Pa·s]

ν	kinematic viscocity [m^2·s^{-1}]
ξ	gridpoint coordinates [m]
ρ	density of air [kg·m^{-3}]
σ	reduced frequency [-], standard deviation [-]
σ_{SL}	shear layer spreading coefficient [-]
τ	emission time [s], time delay [s], relaxation time [s]
τ^*	retarded time [s]
ϕ	inflow angle [rad], POD spatial mode [-]
ϕ_0, ϕ_s	phase-lag due to blade lean and blade sweep [rad]
ψ	phase offset [rad], Wagner function [-]
$\psi_{V,n}$, $\psi_{L,n}$, $\psi_{D,n}$	normalized thickness, lift and drag source transforms [-]
ω	angular frequency [rad·s^{-1}], vorticity, [s^{-1}]
Ω	shaft frequency ($\Omega = 2\pi n$) [rad·s^{-1}]
$A\!R$	wing aspect ratio [-]

Acronyms

2D2C	two-dimensional two-component
AWT	Aeroacoustic Wind Tunnel
BEMT	Blade Element Momentum Theory
BFS	Bubble Flow Solution
CCD	Charge-Coupled Device
CMOS	Complementary Metal–Oxide–Semiconductor
CNC	Computer Numerical Control
DEHS	Di-Ethyl-Hexyl-Sebacat
DEP	Distributed Electric Propulsion
eVTOL	electric Vertical Take-off and Landing
HFSB	Helium-Filled Soap Bubbles
IPR	Iterative Particle Reconstruction
LE-DEP	Leading-Edge Distributed Electric Propulsion
LPT	Lagrangian Particle Tracking
OJF	Open-Jet Facility
OTF	Optical Transfer Function
OTW	Over-The-Wing
OTW-DEP	Over-The-Wing Distributed Electric Propulsion
PIV	Particle Image Velocimetry
POD	Proper Orthogonal Decomposition
PTU	Programmable Timing Unit
PTV	Particle Tracking Velocimetry
RO	Rated-Output
sCMOS	scientific Complementary Metal–Oxide–Semiconductor
sPIV	stereoscopic-Particle Image Velocimetry
UAM	Urban Air Mobility
VDC	Volts of Direct Current
VIC+	Vortex-In-Cell

Sub- and Superscripts

ax	axial direction
b	blade
BPF	Blade Passing Frequency
$conv$	convective flow
d	rotor disk
e	streamtube outlet
eff	effective
f	fluid
h	grid value
iso	isolated rotor
I	illumination
IGE	in-ground effect
max	maximum value
O	objective
OGE	out-of-ground effect
p	particle
QS	quasi-steady condition
r	radial position
rms	root-mean-square
SL	shear layer
t	blade-tip condition
U	unsteady condition
V	velocity
w	isolated wing value
x	x-direction
y	y-direction
Γ	circulation
θ	azimuthal direction
∞	free-stream condition
$'$	perturbation
$\hat{}$	complex value
$\bar{}$	averaged value

I

Background

1

INTRODUCTION

THE potential of electric flight [1] has paved the way for a novel transportation system, known as Urban Air Mobility (UAM) [2–5]. This upcoming market aims at revolutionizing travel times in congested metropolitan areas, by enabling air-linked destinations in closer proximity to one another than regular airports. UAM is intended to utilize a vast number of small-scale (capacities of up to ten passengers) piloted or autonomous electric aircraft as transportation devices for personnel or cargo. The proposed vehicles apply an electric Vertical Take-Off and Landing (eVTOL) approach to optimize versatility and manoeuvrability in confined environments.

Through reduced urban traffic congestion, societal benefits in terms of a reduced environmental footprint and enhanced local air quality are expected. Additionally, such technologies can serve the community by more efficient medical and emergency transport [6] or improved connectivity with remote and rural areas. However, considering that the eVTOL vehicles are intended to be operated in populous areas, a larger number of communities will be impacted by their implementation. This leads to revived societal challenges in terms of safety, noise and impact on wildlife [7, 8]. The aircraft design can play a pivotal role in minimizing such adverse environmental effects.

1.1 eVTOL AIRCRAFT DESIGN

An electric motor has, besides no gaseous emissions, another key advantage compared to an internal combustion engine: its small size, high power-to-weight ratio and efficiency, and minimal mechanical parts provide excellent scalability characteristics. This offers greater flexibility in the placement, size and operation of the propulsors. Such enhanced design freedom leverages the development of disruptive configurations of the propulsion system [9] to elevate the performance with respect to traditional aircraft layouts or helicopter. As a consequence, conceptual eVTOL designs exist in great diversity, although the majority of them can be placed into four categories:

1. **Multi-copter**: Wingless vehicles that makes use of rotors for both vertical and forward flight. These vehicles generally have a high hover efficiency but provide limited cruise speed and are therefore intended for short ranges up to 50 km.

2. **Lift+cruise**: Similar to the multi-rotor configuration but include a horizontal mounted propeller and wings to increase the forward flight efficiency.

3. **Tilt-rotor**: Applies vectored thrust to use the same rotors for vertical and forward flight.

4. **Tilt-wing**: The rotors are connected to tilt-able, large aspect ratio, wings. The tilt-wing vehicles promise to give the longest range ($\approx$ 200 km), since these combine take-off and landing flexibility with an efficient forward flight.

1

(a) multi-copter: Volocopter VoloCity Volocopter [10] (b) lift+cruise: Aurora Flight Sciences Pegasus PAV Sciences [11]

(c) tilt-rotor: Joby S4 Aviation [12]   (d) tilt-wing: Airbus A^3 Vahana Airbus [13]

Figure 1.1: Electric Vertical Take-off and Landing (eVTOL) systems

Examples of the different eVTOL vehicle classes are shown in figure 1.1. A general trend can be observed here: the thrust is distributed over multiple but smaller sized (ducted or open), fixed-pitch, rotors. This brings advantages in terms of safety and controllability,

as well as reduced noise emissions through lower tip speeds. The disruptive designs of the eVTOL vehicles lead to formidable complexity in the aerodynamic and acoustic interactions between rotors, airframe and lifting surfaces. This is most apparent for the tilt-wing configuration using open rotors, which is focused on exclusively in this thesis.

TILT-WING CONFIGURATION

Conceptual tilt-wing vehicles employ an array of span-wise distributed propulsors arranged along the wing, which is known to bring beneficial aero-propulsive coupling effects [9]. The widely used example of such a layout is the Leading-Edge Distributed Electric Propulsion (LE-DEP), where open rotors are installed on pylons aligned with the chord and connected to the wing's leading edge, see figure 1.2a. By the induced flow downstream of the disks, LE-DEP is known to increase the wing's lift curve slope, the maximum lift coefficient and stall angle [14, 15].

(a) Leading Edge Distributed Propulsion   (b) Over-The-Wing Distributed Propulsion
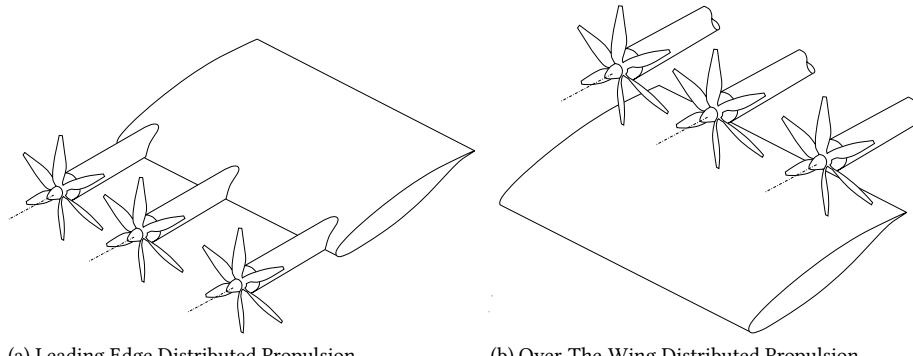
Figure 1.2: Tilt-wing propulsion system architectures

An alternative to LE-DEP is to mount the rotors over the suction side of the wing, with their axes aligned with the wing's chord line, as illustrated in figure 1.2b. This is labeled as Over-The-Wing Distributed Electric Propulsion (OTW-DEP). While OTW-DEP is more complex from a structural viewpoint, it is considered superior in aeroacoustic terms (compared to LE-DEP) due to the potential to use the wing to shield the ground from the rotor noise, effectively reducing fly-over noise [16]. This characteristic can be vital to tackle the societal challenges concerning future eVTOL vehicles. The premise of OTW-DEP also consists of aero-propulsive gains through the rotor-induced flow, leading to greater aerodynamic efficiency of the wing and reduced span-wise lift and drag variations compared to leading-edge propulsion [17]. On the other hand, adverse effects on the rotor performance are to be expected. The wing's aerodynamics generate a non-uniform inflow for the rotor resulting in variation in blade loading during a rotation. Such unsteady loads on the blades can reduce the propulsive efficiency and increase the emitted noise of the rotors. To maximize the potential of OTW-DEP, a proper balance between the adverse and favorable rotor-wing interactions is therefore required.

Flight operation

The aforementioned installation effects of OTW-DEP are well understood for cruise conditions. However, during the vertical take-off of a tilt-wing configuration, the operating conditions radically change. A notional reference flight mission [18] is presented in figure 1.3 and shows a trajectory that consists of multiple stages [19].
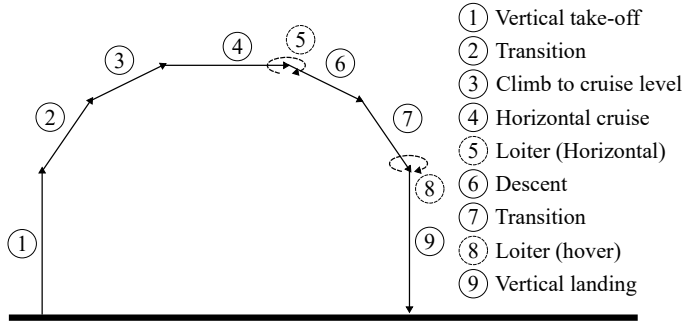
Figure 1.3: Flight path of typical tilt-wing eVTOL vehicle. Figure adapted from [18].

1. **Vertical take-off**: In the initial stages of flight, the rotors are in vertical orientation and are operated at a high thrust level, in close proximity to the ground and nearby infrastructure. As the vehicle gains vertical speed, the effects of these obstructions diminishes, resulting in free-hover conditions. Vertical flight is the most energy-intensive path of the flight envelope; the required power is typically 3 to 6 times higher [20] (dependent on the disk loading [21]) than during cruise.

2. **Transition**: In the transition phase, the vehicle gains horizontal speed by thrust vectoring, during which the dominant lift force gradually changes from propulsive thrust to the wing's circulation. The transition phase typically is completed within a couple of seconds but is challenging due to the shifting angle of attack, close to stall conditions, as the aircraft accelerates [22, 23].

3. **Climb**: After the transition to forward flight, the vehicle ascends towards cruise altitude, which ranges from 300 to 3000 meters [22, 24].

4. **Horziontal cruise**: In cruise flight, the airspeed is high while the thrust of the rotors is minimized. The time spent in cruise generally accounts for the majority of the flight, though it varies depending on the mission length. It can range from 40% of the total flight time for missions of 7 km to as much as 95% for long-range missions (approximately 100 km) [20, 25, 26].

During landing, the flight phases prior to cruise are performed in reversed order and opposite vertical direction. This can include two loitering procedures, indicated by the circular arrows in figure 1.3, if landing space is not immediately available; one at cruise altitude and another when hovering close to the intended landing area [18].

The conditions in the initial and latter stages of the flight envelope are characterized by null-to-low velocity, high thrust and large angles of attack. This could lead to radical changes in the known installation effects of Over-The-Wing propulsion for cruise conditions. Furthermore, additional rotor-surface interactions are expected to contribute, particularly the interaction with the ground surface during near-ground hovering. Such aerodynamic interactions need to be understood extensively to ensure the safe and quiet operation of the Over-The-Wing propulsion system, and to inspire design guidelines to mitigate the adverse and enhance the favorable installation effects.

1.2 Objectives

To enable Over-The-Wing propulsion for vertical flight, the fundamental aerodynamic interactions between the distributed rotors and surfaces need to be understood. The main objective for this thesis is therefore as follows:

> *Understand the key aerodynamic rotor-surface interactions, and their performance impact, of Over-The-Wing propulsion for vertical flight*

The goal is achieved through experimental investigations of the fundamental aerodynamic interactions between distributed rotors and surfaces that occur in the initial stages of flight for a tilt-wing eVTOL vehicle employing Over-The-Wing propulsion. The experimental data are used to formulate and validate a low-fidelity model of the aero-propulsive performance and the rotor noise sources, allowing efficient parameter variations and the decoupling of separate aerodynamic effects. Consequently, the main aim can be split into a number of sub-goals:

1. Identify the fundamental aerodynamic interactions between distributed rotors and surfaces that occur along the tilt-wing flight trajectory, making use of novel flow measurement techniques.

2. Understand the beneficial and detrimental effects that result from the multi-rotor–surface interactions.

3. Develop a low-order model for the aero-propulsive and aeroacoustic performance of Over-The-Wing propulsion at incidence, to inspire design guidelines.

1.3 Thesis outline

The thesis is split into 4 parts, as presented in figure 1.4.

Part 1 introduces background theory required to understand the problems and results in the thesis in detail. In chapter 2 the fundamentals of rotors are introduced. This concerns the isolated rotor's aero-propulsive and aeroacoustic properties, modeling strategies and critical multi-rotor–surface interactions. Chapter 2 is concluded by the definition of challenges and fundamental research questions related to the main aim of the thesis.

Since an experimental approach is considered, the research methodologies are explained in **Part 2**. Theoretical background on the measurements techniques is introduced

in chapter 3 while the research facilities are presented in chapter 4.

Part 3 is the main part of the thesis and deals with the experimental and modeled results. Each chapter in this part is dedicated to answering one of the research questions that are defined in chapter 2, and therefore concerns a different part of the flight envelope as schematically illustrated in figure 1.4. This starts with an experimental investigation of the three-dimensional flow topology of multi-rotors in ground proximity in chapter 5, where the effect of the wing is disregarded. Chapter 6 builds on this but focuses on the unsteady flow behavior around the multi-rotor configuration. In chapter 7, the aero-propulsive performance of the OTW-DEP is investigated and modeled for operating conditions that are typically observed between vertical take-off and forward flight. Chapter 8 deals with similar operating conditions, but instead focuses on the aeroacoustic installation effects and, in particular, the tonal noise sources of the installed rotor. Finally, in chapter 9, a reference take-off trajectory is experimentally simulated, to study the three-dimensional flow interactions and to identify transient aerodynamic effects.

In **Part 4**, the thesis is completed by the conclusions and recommendations for future work in chapter 10.

Part I: Background

Chapter 1	Chapter 2
Introduction	Fundamentals of rotors and installation effects

Part II: Research Methodology

Chapter 3	Chapter 4
Experimental measurement techniques	Experimental arrangements

Part III: Results & Discussion

Multi-rotor ground proximity

Chapter 5	Chapter 6
Aerodynamic wake interaction in ground proximity	Unsteady flow behaviour in ground proximity

Performance of Over-The-Wing propulsion at incidence

Chapter 7	Chapter 8
Aeropropulsive performance of Over-The-Wing propulsion	Aeroacoustics of Over-The-Wing propulsion

Experimental simulation of take-off trajectory

Chapter 9
Experimental simulation of take-off trajectory

Part IV: Final remarks

Chapter 10
Conclusions & Recommendations

Figure 1.4: Visual outline of the thesis.

2

Fundamentals of rotors and installation effects

Rotors are the preferred option for the propulsion system of eVTOL vehicles due to their high propulsive efficiency and excellent compatibility with electric motors. In this chapter, the fundamental aerodynamic and aeroacoustic properties of rotors are introduced. This starts with the rotor's aero-propulsive performance and wake aerodynamics in section 2.1 and rotor noise source in section 2.2. After this, the installation effects of multi-rotor configurations, based on recent literature, are elucidated in section 2.3. Special attention here is given to the aerodynamic interactions of such configurations when operated in ground proximity. In section 2.4, the aerodynamic and aeroacoustic installation effects specific to the Over-The-Wing mounted rotor system are introduced. The chapter is completed by the identification of scientific challenges based on multi-rotor–surface interactions in section 2.5, and the definition of associated research questions in section 2.6.

2.1 Rotor aerodynamics

A rotor's geometry is defined by an azimuthal distribution of a number of B blades that stretch from the hub to the edge of the rotor disk with radius R, see figure 2.1. The geometry of the blades can be described using a similar planform as for wings, by the radial distributions of the chord length $c(r)$, pitch $\beta(r)$, sweep $\Lambda(r)$ and lean $\gamma(r)$, and the airfoil geometry.

2.1.1 Aero-propulsive performance

Each rotor blade can be represented by a radial discretization of two-dimensional blade sections with span dr. When the rotor is operated, an axial V_{ax} and tangential V_θ velocity is generated at the inflow of each blade section, as shown on the right-hand side of figure 2.1, that prescribes a local dynamic pressure q and angle of attack α that is defined by equation 2.1:
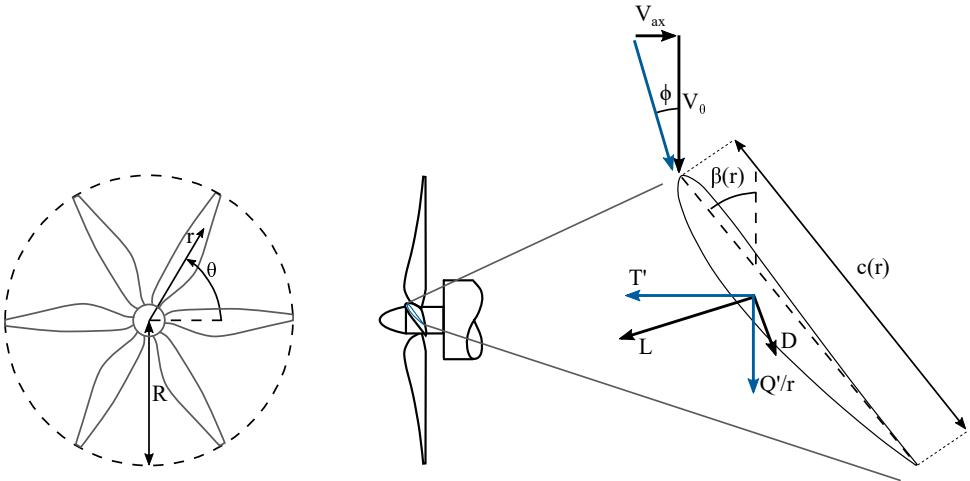
Figure 2.1: Rotor geometry and definition of aero-propulsive forces.

$$q = \frac{\rho \sqrt{V_{ax}^2 + V_\theta^2}}{2} \qquad\qquad \alpha = \beta - \phi = \beta - \tan^{-1}\left(\frac{V_{ax}}{V_\theta}\right) \qquad (2.1)$$

in which ρ is the density of the fluid and ϕ the local inflow angle of the blade section. The resulting lift and drag forces define the sectional thrust T' and torque Q' for a blade section located at a radial station r as:

$$T' = qc\left(c_l\cos(\phi) - c_d\sin(\phi)\right)B\mathrm{d}r \qquad (2.2)$$

$$Q' = qc\left(c_l\sin(\phi) + c_d\cos(\phi)\right)Br\mathrm{d}r \qquad (2.3)$$

where c_l and c_d are the lift and drag coefficient of the given blade section for the local angle of attack α.

The axial V_{ax} and tangential velocity V_θ at the blade section are determined by the combination of the free-stream and rotational velocity of the rotor. Moreover, the rotor itself also induces a flow in the axial and tangential direction that should be considered:

$$V_{ax} = V_\infty(1+a) \qquad\qquad V_\theta = \Omega r(1-b) \qquad (2.4)$$

in which Ω is the rotational velocity of the rotor, and a and b are the axial and tangential induced velocity factors, respectively. These rotor-induced velocities depend again on the aero-propulsive forces of the blade sections through the conservation of axial and angular momentum:

$$T' = 4\pi r\rho V_\infty^2(1+a)a\mathrm{d}r \qquad\qquad Q' = 4\pi r^3 V_\infty(1+a)b\Omega\mathrm{d}r \qquad (2.5)$$

The thrust and torque for each blade section can therefore be predicted from equations 2.2, 2.3 and 2.5 using an iterative scheme. This approach is known as Blade Element Momentum Theory (BEMT) [27, 28], which is an engineering tool for rotor and propeller load prediction. Typically, corrections for compressibility, rotational flow [29] and tip loss effects [30, 31] are also applied to the sectional aero-propulsive forces.

Radial variations in blade sectional chord, pitch, and rotational velocity lead to a distribution of propulsive forces along the radial coordinate of the rotor blades. These variations in blade loading influence both the emitted noise and slipstream characteristics, thereby affecting the installation effects. Generally, thrust and torque forces are maximized around 80% of the rotor radius as is shown by the typical loading distributions presented in figure 2.2.
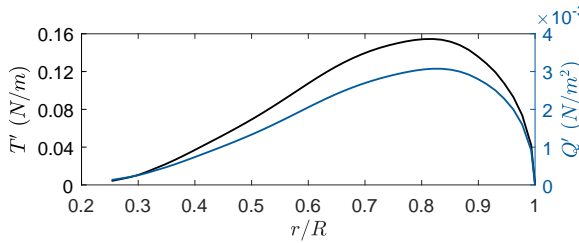
Figure 2.2: Sectional thrust and torque distribution over the blade radius for J = 0.6.

The total thrust and torque of the rotor are returned from integration of the sectional values:

$$T = \int_R T' \mathrm{d}r \qquad\qquad Q = \int_R Q' \mathrm{d}r, \qquad (2.6)$$

To make the performance characteristics of rotors scalable, the integral thrust and torque are typically normalized using a combination of the rotational velocity n, rotor diameter D, and fluid density ρ:

$$C_T = \frac{T}{\rho n^2 D^4} \qquad\qquad C_Q = \frac{Q}{\rho n^2 D^5} \qquad (2.7)$$

Considering that the performance of fixed-pitch rotors is primarily defined by the inflow characteristics through the axial and tangential velocity, a key parameter that describes the operating condition, is the rotor's advance ratio J. This is defined by the ratio between the distance traveled during a rotation and the rotor diameter:

$$J = \frac{V_\infty}{nD} \qquad (2.8)$$

The thrust coefficient C_T and advance ratio J have a convenient linear relationship for fixed pitch rotors when neglecting stall over the blades.

2.1.2 Streamtube properties

As shown in the previous section, a flow is induced by the rotor through the conservation of axial and angular momentum. The extent of the rotor-induced velocity is greater than just the rotor disk, and affects the flow properties in streamwise direction in a domain called the streamtube. To illustrate this, the rotor can be approached in a simplified way, by a uniform pressure jump Δp over a disk with the same radius R as the rotor, and assuming an inviscid and incompressible flow. The pressure jump is determined by the rotor thrust T and the disk area S_d:

$$\Delta p = \frac{T}{S_d} = \frac{T}{\pi R^2} \tag{2.9}$$

The variations in static pressure $p_s(x)$ in streamwise direction then follow from the potential solution of the Laplace equation in cylindrical coordinates, through the uniform distribution of pressure doublets Δp over the rotor disk, positioned at $x = 0$ [32]:

$$p_s(x) = \frac{\Delta p}{2} \left(\frac{x}{\sqrt{x^2}} - \frac{x}{\sqrt{R^2 + x^2}} \right) \tag{2.10}$$

The position of the pressure doublets Δp and the resulting distribution of the static pressure are presented in figure 2.3a and b, respectively.
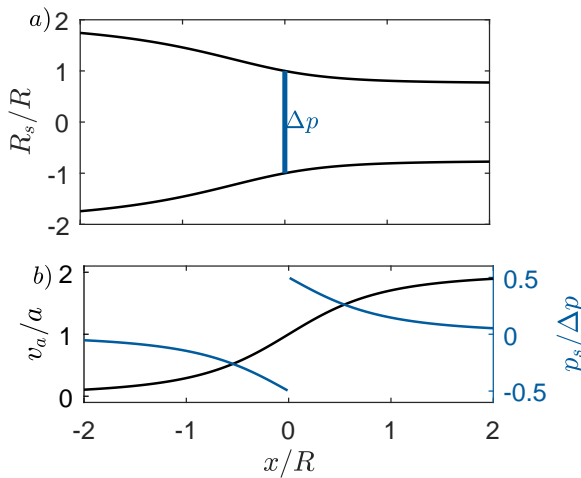
Figure 2.3: a) Rotor streamtube contraction for an induced velocity factor $a = 1$. b) Variations in axial direction of the normalized induced velocity v_a/a and static pressure $p_s/\Delta p$.

As is shown in figure 2.3b, the rotor generates a pressure field in the streamtube that varies from free-stream conditions. Upstream of the disk, the pressure is reduced, while downstream there is an increase in pressure. On both sides of the rotor disk, the pressure recovers gradually to ambient conditions. The resulting pressure gradient in the streamtube accelerates the flow. From the inviscid incompressible momentum equation and equation 2.10, and by considering that the velocity is continuous through the disk, the normalized axial-induced velocity of the rotor yields:

$$\frac{v_a(x)}{V_\infty} = a\left(1 + \frac{x}{\sqrt{R^2 + x^2}}\right), \quad a = \frac{v_a(0)}{V_\infty} = \frac{\Delta p}{2\rho V_\infty^2} \tag{2.11}$$

in which a is the induced velocity factor at the position of the disk (similar to equation 2.5). The distribution of the induced velocity is also presented in figure 2.3b and shows the gradual acceleration of the flow both upstream and downstream of the disk. A consequence of the acceleration of the flow in axial direction is that the streamtube contracts. The streamtube radius R_s can be derived from the induced velocity v_a by the law of continuity:

$$\frac{R_s(x)}{R} = \sqrt{\frac{1 + a}{1 + a\left(1 + \frac{x}{\sqrt{R^2 + x^2}}\right)}} \tag{2.12}$$

The streamtube radius, normalized by the rotor radius, is presented in figure 2.3a for $a = 1$. Note that an increase in a, due to a higher thrust or reduced free-stream velocity, results in a stronger contraction of the streamtube. Furthermore, it must be noted that in equations 2.11 and 2.12, a is normalized by the free-stream velocity, hence these relations are not applicable to rotors in hover.

The results of figure 2.3 show a simplified presentation of the rotor streamtube properties, in which a uniform loading over the disk has been assumed. As already shown in figure 2.2, radial variations in loading are present. Aside from this, unsteady, viscous and rotational effects have been disregarded. In reality, such effects play a role in the wake characteristics of rotors. This is illustrated in figure 2.4 by experimental flow measurements around a rotor in hover condition.
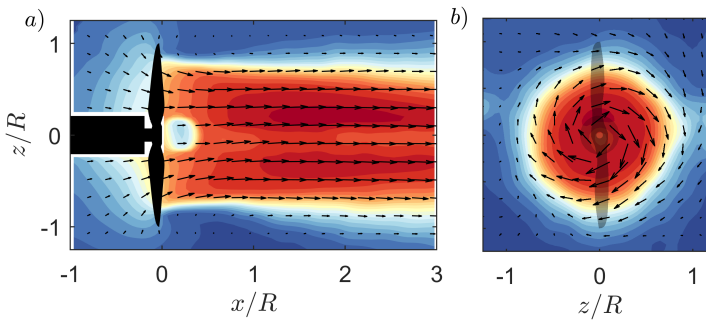
Figure 2.4: a) Experimental time-averaged velocity magnitude slice and 3D vectors through the rotor axis and b) slice extracted one diameter downstream, obtained from [33].

Figure 2.4a depicts a slice through the axis of a two-bladed rotor, showing the time-averaged flow field, where all presented velocities are self-induced by the rotor, as there is no external free-stream. The data indicate that the velocity varies with radial position within the streamtube, generally increasing from the center of the wake outward, which correlates with the thrust distribution along the blade, as illustrated in figure 2.2. Besides

the axial velocity of the rotor, the rotor also induces a flow in tangential direction, as is shown by the velocity field extracted one diameter downstream of the rotor disk in figure 2.4b. The tangential induced velocity, or swirl, is the result of the rotor torque causing the wake to rotate in the same direction as the rotor blades. This angular momentum in the flow does not contribute to the thrust and is therefore a loss in propulsive efficiency.

The circulation of the rotor blades generates coherent structures in the flow that are convected downstream, which are not captured in time-averaged flow results. To illustrate this, a sketch of the rotor wake vortex system [32, 34] is presented in figure 2.5a. The bound vorticity of the airfoil creates trailing vorticity that follows a helicoidal path downstream. Radial variations in the blade circulation (recall figure 2.2) result in the rapid roll-up of the trailing vorticity and cause the formation of a tip vortex at the edge and root vortex at the center of the slipstream. Additionally, the blade's boundary layer generates a shear layer that is convected along a similar helical path.
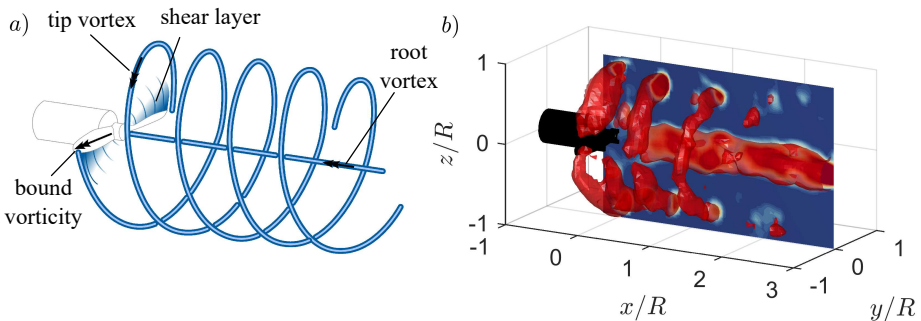
Figure 2.5: a) Schematic of the rotor slipstream characteristics and vortex system, and b) phased-averaged λ_2 contour and iso-surfaces highlighting the coherent structures, obtained from [33].

This creates a time-dependent, three-dimensional wake which is visualized by phase-averaging of the instantaneous, experimental velocity field in figure 2.4b. The contours and iso-surfaces in figure 2.4b show the λ_2-criterion which is used to visualize vortex cores. The iso-surfaces show the helicoidal path of the tip vortices and the root vortex. The tip vortices are gradually reduced in strength while convected downstream through viscous dissipation. Note that the low advance ratio reduces the spacing between the tip vortices, and, combined with the random transverse motion of the vortex about its average path known as wandering or meandering [35, 36], increases the likelihood of vortex merging. Consequently, the vortices are broken after roughly one diameter.

2.1.3 Unsteady blade loading

The analysis has thus far considered isolated rotors, either in hover condition or with the rotor axis parallel to the free-stream. In contrast, during an eVTOL take-off trajectory, the rotors are often inclined relative to the flight direction, resulting in non-axial flow conditions. Additionally, installed propulsion systems employing distributed electric propulsion can experience non-uniform inflow due to aerodynamic interactions with surrounding components, such as fuselages, pylons, lifting surfaces, or the wake generated by other rotors, which create steady and unsteady inflow distortions. The axial and

non-uniform flow leads to periodic variations in dynamic pressure and blade inflow angle during a blade's rotation, causing fluctuating forces along the azimuth, a phenomenon referred to as unsteady blade loading. The response of an airfoil's aero-propulsive forces to varying inflow conditions is often not immediate and can result in a phase delay and amplitude reduction relative to the inflow variations. An important scalability parameter for such unsteady effects is the reduced frequency σ, which is defined as the ratio of the angular frequency ω of the oscillation to the amount of half-chord lengths traveled per unit of time $\left(\frac{2V_\infty}{c}\right)$:

$$\sigma = \frac{\omega c}{2V_\infty} = \frac{\pi f c}{V_\infty} \tag{2.13}$$

in which f is the frequency of the oscillation. A value of $\sigma = 0$ defines the steady aerodynamic case, while positive values indicate unsteady effects. To determine the response of the lift-force of an airfoil, different approaches in time- and frequency-domain are available.

Time-domain

From the classical theory of Wagner [37], the lift response of a thin airfoil can be approximated through the definition of an effective angle of attack $\alpha_U(t)$:

$$c_l(t) = 2\pi\alpha_U(t) \tag{2.14}$$

The effective angle of attack $\alpha_U(t)$ depends on the initial angle of attack α_0 at $t = 0$, and the product of the rate of change of the geometric angle of attack $\frac{d\alpha}{dt}$ and the Wagner function $\psi(t)$, integrated in time:

$$\alpha_U(t) = \alpha_0 + \int_0^t \frac{d\alpha}{dt}\psi(t)dt \tag{2.15}$$

The Wagner function $\psi(t)$ can be approximated [38] as a function of the half-chord lengths travelled:

$$\psi(t) = 1 - 0.165\exp\left(-0.0455\frac{2V_\infty t}{c}\right) - 0.335\exp\left(-0.3\frac{2V_\infty t}{c}\right) \tag{2.16}$$

The distribution of the Wagner function is presented in figure 2.6a and shows an asymptotic relation that starts at values of $\left(\frac{1}{2}\right)$ and limits to unity.

To demonstrate the predicted unsteady response of an airfoil, a synthetic case is generated by an oscillation angle of attack with an amplitude of 5° and angular frequency of $\omega = 4\pi$ rad/s. The geometric angle of attack is shown by the black line in figure 2.6b. The colored lines in figure 2.6b show the unsteady angle of attack, computed through equation 2.15 for two values of the reduced frequency. The corrected angles of attack have the same starting position as the geometric angle of attack, but deviate after initializing through a phase delay and reduced amplitude. As expected, phase and amplitude modulations are greater for higher values of the reduced frequency.
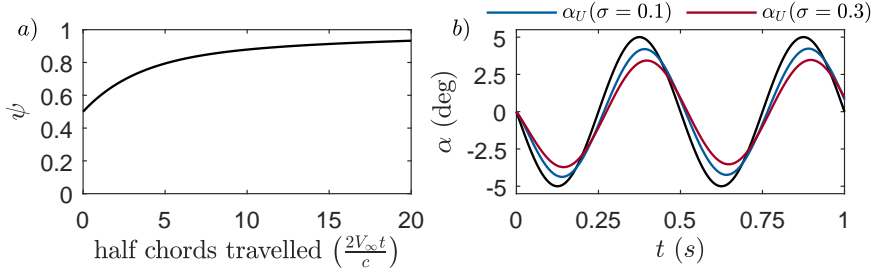
Figure 2.6: a) Wagner function $\psi(t)$ as a function of the half-chord lengths travelled and b) geometric (black line) and unsteady angle of attack according to equation 2.15, for $\sigma = 0.1$ and $\sigma = 0.3$.

Frequency-domain

Correction methods for the unsteady lift response in the frequency domain are particularly useful for rotor applications. For the reduced frequency of a rotor blade section, the induced and rotational velocity of the rotor should also be included. In this case, the reduced frequency σ for a wavenumber k for a local blade section at radius r yields [39]:

$$\sigma(k,r) = \frac{k\Omega c_b(r)}{2V_b(r)} \tag{2.17}$$

where Ω is the shaft-frequency of the rotor in rad/s, V_b the velocity of the local rotor blade section, and c_b the local blade chord length. Note that the velocity V_b, is a combination of the rotational, free-stream and induced velocity of the rotor in steady-state conditions.

To correct the unsteady loads of the rotor in the frequency domain, the sectional lift coefficients during a rotation through the non-uniform inflow field are Fourier decomposed, resulting in the quasi-steady complex lift coefficient $\hat{c}_{l,QS}$ [39]. Such information can effectively be obtained through analytical methods such as Blade Element Momentum Theory. Then, by multiplication with the Sears function [40], the lift is corrected for the unsteady effects:

$$\hat{c}_l(r,\sigma) = \hat{c}_{l,QS}(r,\sigma)\hat{S}(r,\sigma) \tag{2.18}$$

The Sears function for an incompressible flow is presented in equation 2.19, and depends on the reduced frequency:

$$\hat{S}_{M=0}(\sigma) = \frac{\hat{J}_0(\sigma)\hat{K}_1(i\sigma) + i\hat{J}_1(\sigma)\hat{K}_0(i\sigma)}{\hat{K}_1(i\sigma) + \hat{K}_0(i\sigma)} \tag{2.19}$$

in which $\hat{J}_0$ and $\hat{J}_1$ are Bessel functions of the first kind and of the zeroth- and first-order, respectively. Similarly, $\hat{K}_0$ and $\hat{K}_1$ are the zeroth and first-order Bessel functions of the second kind. The incompressible Sears function has real and imaginary components that are presented in figure 2.7a for different values of the reduced frequency. Note that the magnitude of the Sears function is enhanced for decreasing reduced frequency to a limit of one for $\sigma = 0$, indicating steady-state conditions.

A compressibility correction [41] can be applied to the Sears function based on the local Mach number M:
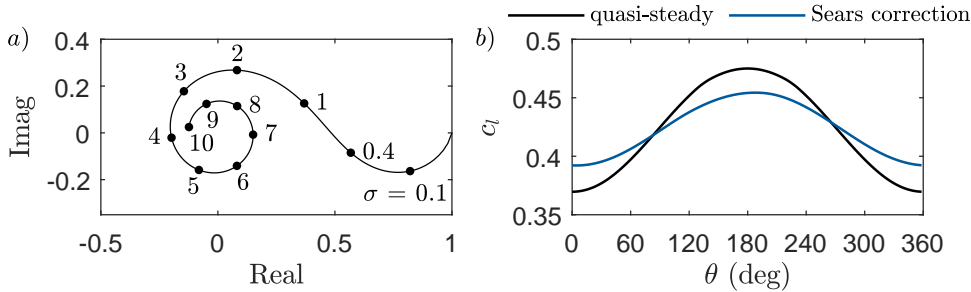
Figure 2.7: a) Real and imaginary parts of the Sears function for subsonic flow. b) Sears correction applied to the 0.75R blade of a rotor at $\alpha = 25°$.

$$\hat{S}(\sigma, M) = \hat{S}_{M=0}\left(\sigma/\zeta^2\right)\left\{J_0\left(\frac{M^2\sigma}{\zeta^2}\right) + iJ_1\left(\frac{M^2\sigma}{\zeta^2}\right)\right\}e^{\left[-i\sigma f(M)/\zeta^2\right]} \tag{2.20}$$

in which the function f is based on the Prandtl-Glauert compressibility factor ζ:

$$f(M) = (1 - \zeta)\ln(M) + \zeta\ln(1 + \zeta) - \ln(2) \qquad \zeta = \sqrt{1 - M^2} \tag{2.21}$$

The Sears function correction is applied to the sectional lift force (0.75R), obtained through BEMT, for a rotor at an angle of attack of $\alpha = 25°$ in figure 2.7b. The quasi-steady results show a variation in lift during a rotation as a result of the varying local angle of attack and dynamic pressure of the blade section. This generates a symmetric distribution, with a maximization of the lift at $\theta = 180°$. The Sears function causes both an amplitude reduction and a phase offset, similar to the correction of Wagner (figure 2.6b). However, since the method is computed in the frequency domain, the initial point ($\theta = 0°$) is also affected.

The aforementioned unsteady loading corrections are applied in this thesis in the predicting of the rotor tonal noise (chapter 8, frequency domain) and effective angle of attack of the rotor-wing system during a reference flight trajectory (chapter 9, time domain).

2.2 ROTOR AEROACOUSTICS

Rotating blades generate aerodynamic noise that can be split into tonal or harmonic noise, generated by repeating fluctuations in pressure due to the blades' rotation, and broadband noise which consists of a non-periodic, random signal. The two contributions will be introduced separately in this section.

2.2.1 HARMONIC NOISE

Tonal noise is observed at frequencies that are multitudes of the frequency of the blade passages. The theoretical prediction of such noise sources follows from the inhomogeneous wave equation that includes the effect of moving bodies. The result is known as the Ffowcs-Williams/Hawkings equation [42]:

$$
\rho'(\mathbf{x},t)c_\infty^2 = \overbrace{\frac{\partial}{\partial t}\int_{S_o}\left[\frac{\rho_\infty V_j n_j}{4\pi R|1-M_r|}\right]_{\tau=\tau^*}\mathrm{d}S(\mathbf{y})}^{\text{thickness noise}}
$$

$$
\underbrace{-\frac{\partial}{\partial x_i}\int_{S_o}\left[\frac{p_{ij}n_j}{4\pi R|1-M_r|}\right]_{\tau=\tau^*}\mathrm{d}S(\mathbf{y})}_{\text{loading noise}}+\underbrace{\frac{\partial^2}{\partial x_i\partial x_j}\int_{V_o}\left[\frac{T_{ij}}{4\pi R|1-M_r|}\right]_{\tau=\tau^*}\mathrm{d}V(\mathbf{y})}_{\text{quadruple noise}}
$$

$$(2.22)$$

in which the acoustic field is presented on the left hand side, denoted by the density perturbation ρ' at observer position $\mathbf{x}$, multiplied by the speed of sound c_∞. On the right hand side of equation 2.22, multiple integrals are carried out over moving bodies at an emission time τ and differentiated in time and space. Each of the integrals on the right-hand side of equation 2.22 represents a force term, corrected for the distance between source and observer R and the Mach number M_r, which is carried out over the moving surface $S(\mathbf{y})$ or the surface velocity $V(\mathbf{y})$. The force terms in equation 2.22 embody different tonal noise sources of rotating blades:

- **Thickness noise** is caused by the volumetric displacement of fluid by the moving blades and can be represented by a monopole source. In equation 2.22 it depends on the blade surface velocity V_j, unit normal vector n_j to the surface and fluid density ρ_∞ at the observer position. The amplitude is proportional to the blade volume and rotational speed. Thickness noise is therefore dominant for high blade speeds [43] and can be mitigated by using thin blades, in particular near the tip region.

- **Loading noise** is due to the blade's surface loading p_{ij}. Loading noise can be represented by a dipole source and is often the dominant tonal noise source for low-speed rotors. A method to mitigate loading noise is to increase the rotor's solidity; for example through more blades, longer blade chords or increased rotor diameter. Loading noise can further be split into steady and unsteady components. The latter is the result of aerodynamic installation effect or non-axial inflow conditions, and is known to be a strong noise source for low-speed rotors [44].

- **Quadruple noise sources** are the result and flow inhomogeneities surrounding the blades, such as turbulence in the wake of the blades or compressibility effects at transonic speeds. Prediction of the quadrople noise sources depends on computing the Lighthill stress tensor T_{ij} [45].

TONAL NOISE MODELLING: HELICOIDAL SURFACE THEORY
The use of low-fidelity tools allows for efficient optimization of the propulsion system and is therefore particularly useful for minimizing the adverse effects on the aerodynamic noise sources of the rotor. Multiple theories are available to predict the tonal noise sources of rotating blades, both in the time and frequency domain. Methods in the frequency domain often give the most elegant solutions due to the redundancy of calculating retarded blade locations and numerical derivatives [46]. A generally applied method here is known

as Helicoidal Surface Theory [47] which is valid for far-field noise predictions and gives a convenient final solution. The derivation starts by adapting the acoustic analogy of Goldstein [48], which is an extension of Ffowcs-Williams/Hawking (equation 2.22) where a moving medium is concerned instead. When neglecting quadruple noise terms Goldstein's acoustic analogy yields:

$$\rho'(\mathbf{x},t)c_\infty^2 = \int_{-T}^{T} \int_{S(\tau)} \left(\rho_0 V_n \frac{\partial G}{\partial \tau} + f_i \frac{\partial G}{\partial y_i} \right) dS(\mathbf{y}) \, d\tau \tag{2.23}$$

in which S are the source surfaces with coordinates $\mathbf{y}$ at a source time τ. V_n the normal component of the airfoil surface velocity and f_i the i-th component of the force that is exerted by the fluid on the airfoil. G is the Green's function in a free space, that depends on the distance R between the observer $\mathbf{x}$ and source $\mathbf{y}$ locations:

$$G = \frac{\delta(t - \tau - R/c_0)}{4\pi R}, \qquad\qquad R = |\mathbf{x} - \mathbf{y}| \tag{2.24}$$

In the work of Hanson [47, 49], equation 2.23 is written in a form where the blade design parameters (such as blade thickness and sweep) appear explicitly. For brevity, the full derivation is not shown, but it deals with the transformation of the integrals of equation 2.23 to an orthogonal helicoidal reference frame in which the rotor axis is aligned with the free stream. The acoustic pressure $p(t)$ is then returned as:

$$p(t) = \sum_{m=-\infty}^{\infty} \sum_{n=-\infty}^{\infty} \left(P_{V,mn} + P_{L,mn} \right) \exp(imB\Omega t) \tag{2.25}$$

in which $P_{V,mn}$ and $P_{L,mn}$ are the thickness and loading source terms for the m-th source harmonic and n-th loading harmonic:

$$\left\{ \begin{array}{c} P_{V,mn} \\ P_{L,mn} \end{array} \right\} = -\frac{2R\rho c_0^2 B \sin\theta_O}{8\pi y(1 - M_x \cos\theta_O)} e^{imB\left(\frac{\Omega R}{c_0} - \frac{\text{sign}(m)|mB-n|\pi}{2} \right)}$$

$$\times \int_{r_{0,hub}}^{1} \underbrace{e^{i(\varphi_0 + \varphi_s)}}_{\substack{\text{phase} \\ \text{delay}}} M_r^2 \underbrace{\left\{ \begin{array}{c} k_x^2 \hat{t}_{b,n} \psi_{V,n} \\ ik_y \frac{\hat{c}_{L,n}}{2} \psi_{L,n} + ik_x \frac{\hat{c}_{D,n}}{2} \psi_{D,n} \end{array} \right\}}_{\text{source terms}} \hat{J}_{|mB-n|} \underbrace{\left(\frac{|m|Br_0 M_t \sin\theta_O}{1 - M_x \cos\theta_O} \right)}_{\text{Bessel function}} dr_0 \tag{2.26}$$

Equation 2.26 consists of an initial term, where M_x is the flight Mach number, and θ_O and y are the angle and vertical distance between the observer position and flight axis. The initial term is multiplied by an integral over the normalized rotor radius r_0 (from hub to tip). The integrand consists of multiple terms in which the first denotes a phase delay, caused by the blade lean ϕ_0 and sweep ϕ_s. The second term shows the thickness and loading source terms. Here, k_x and k_y are wave numbers, $\psi_{V,n}$, $\psi_{L,n}$ and $\psi_{D,n}$ are the source transforms of the blade's thickness and lift and drag forces. $\hat{c}_{L,n}$ and $\hat{c}_{D,n}$ denote the sectional, Fourier transformed, lift and drag coefficient. The final term in the integrand of equation 2.26 concerns the Bessel function of the first kind, which acts as a weighting

function to the blade harmonics. This term can therefore be used to analyze the radiation efficiency of each mode. Values of the Bessel function $\hat{J}_n(x)$ (where n is the order and x is the argument) are presented in figure 2.8.
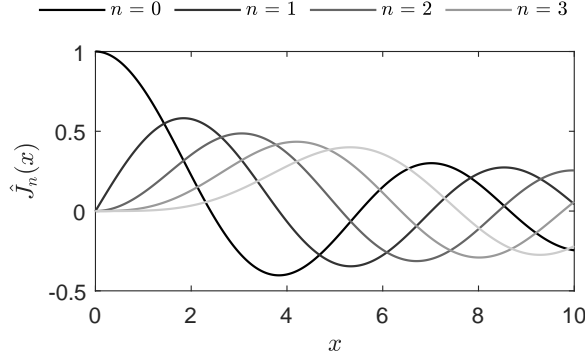
Figure 2.8: Bessel functions of the first kind $\hat{J}_n(x)$ for different orders n.

As shown in figure 2.8, the value of the Bessel function decays rapidly for arguments less than the order of the function (i.e. $|x|<|n|$). For the Bessel function in equation 2.26, low radiation efficiencies are therefore found for [49]:

$$\left| \frac{mBr_0M_t\sin(\theta_O)}{(mB-n)(1-M_x\cos(\theta_O))} \right| < 1 \tag{2.27}$$

in which θ_O is the emission direction ($\theta_O = 0°$ in upstream direction). Hence, in the rotor plane ($\theta_O = 90°$), equation 2.27 reduces to:

$$\left| \frac{mB}{mB-n} \right| r_0M_t < 1, \quad \text{for } \theta_O = 90° \tag{2.28}$$

Equations 2.27 and 2.28 show that the blade count B appears in the low-radiation efficiency criterion. Hence, this design parameter could be exploited to reduce the noise of unsteady loading modes when non-uniform and non-axial inflow conditions are expected. Note that for steady loading, the loading harmonic equals $n = 0$, and the blade count is removed from the criterion.

Recent tonal noise modelling efforts focused on adaptations to include the unsteady loading for pusher propellers by [50, 51], quad rotors [44], contra-rotating open rotors [52] and distributed propellers [53, 54]. The noise ascribed to unsteady loading was shown to be dominant for most noise emission angles for such configurations [44], highlighting its relevance.

2.2.2 Broadband noise
Broadband noise is a type of random noise characterized by pressure fluctuations that are distributed across a wide range of frequencies. This noise can either be result of the blades themselves, i.e. without considering external factors, or by the interaction of the blades with turbulence.

Airfoil self noise

Airfoil self noise describes a family of high-frequency broadband noise sources of airfoils, such as trailing edge scattering, vortex shedding, and laminar and turbulent boundary separation noise. The different airfoil self noise contributions are schematically illustrated in figure 2.9 and are typically scattered at the trailing edge of the airfoil. The broadband self noise of rotating blades can be modelled through various semi-empirical methods such as the Brook-Poke-Marconi [55] or Pegg [56] model.
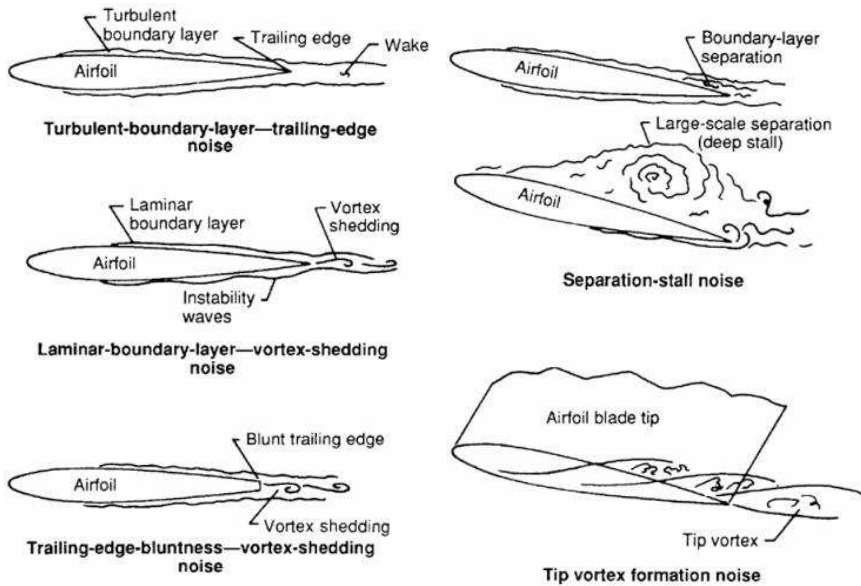
Figure 2.9: Different contributions of airfoil self noise. Figure adpated from [55].

Turbulence ingestion noise

The impingement of turbulent flow leads to stochastic unsteady pressure fluctuations on the leading edge of the blades, generating broadband noise which is typically radiated at lower frequencies compared to airfoil self noise. The ingesting turbulence can originate from various sources, including wakes of the blades themselves (during vertical descend [57] or in a one-after-another configuration [58]), wakes generated by other part of the aircraft such as wings and pylons, or atmospheric turbulence. Since the ingestion can be the result of installation effects, it is expected that, aside from unsteady loading, this is an important noise contribution of installed propulsion systems. Models to effectively predict turbulence ingestion noise based on the turbulence characteristics are available in literature [59, 60].

If the flow scales during ingestion are sufficiently large or the pressure fluctuations vary along the rotor plane, blade-to-blade correlation and amplitude modulation of the pressure fluctuations can occur. This results in the production of spectral humps at multiples of the blade passing frequency which is known as a phenomenon called *haystacking* [61].

2.3 Multi-rotors aerodynamic interactions

EVTOL vehicles typically use a multitude of closely spaced open rotors, either in counter- or co-rotating orientation, that can lead to aerodynamic and acoustic interference along different stages of the flight envelope. In forward flight, the aerodynamic interactions between closely spaced rotors (tip clearance ~ 5% of the radius), can result in a drop in efficiency in the order of 1.5% [62]. This penalty is shown to increase with angle of attack and decreasing thrust but is insensitive to the rotation direction and relative blade phase angle. In hover conditions, the contraction of the rotor stream tube is greatly increased and more pronounced aerodynamic interactions between subsequent rotors are expected. The distance between the rotors has a relatively small influence on their mean thrust coefficient [63–68] but can result in strong temporal variations of the aerodynamic loading [66, 68]. For example, an increase of the thrust fluctuations of up to 250%, compared to a single rotor, was found for a side-by-side rotor configuration with a tip-to-tip spacing of $0.1R$ [68]. This effect is caused by an interaction between the radial velocities in the slipstream, forming an upwash between the individual wakes [64, 68]. Consequently, an overall noise level increase of 3 dB has been reported for side-by-side rotors with rotor spacing of $0.05R$, compared to the same system with a separation distance of $1.0R$, which has been ascribed to the unsteady loading [66–68].

2.3.1 Ground proximity

During vertical take-off and landing, the rotors hover in close proximity to the ground. Such conditions are critical for the safe operation and controllability of the vehicles and have been studied extensively for single rotors [69–71]. The interaction of the rotors with the ground surface creates a wake pattern that deviates from the slipstream model of isolated rotor configurations [72]. In the schematic of figure 2.10, the flow topology of an in-ground-effect rotor is compared to one operated in free hover conditions. By the presence of the ground plane, the rotor slipstream undergoes a rapid deflection resulting in a radially spreading wall jet. The expansion of the rotor wake stretches the tip vortices, thereby increasing vorticity within the vortex core, rendering them more resistant to diffusion. Furthermore, as a result of the lower induced velocity in the center of the rotor wake, the flow stagnates below the rotor hub causing a toroidal separation region [73].

The back pressure of the ground results in a reduction in slipstream velocity. This reduces the separation distances between the rotor's shear layers and increases the blade's local pitch angle for sufficiently low rotor standoff heights z. As a result, an observed increase in the rotor thrust compared to hover conditions is created, which can be approximated using the Cheeseman-Bennett model [75]:

$$\frac{T_{IGE}}{T_{OGE}} = \frac{1}{1 - \frac{1}{16}\left(\frac{R}{z}\right)^2 \left[\frac{1}{1+(V/w_{ind})^2}\right]} \qquad (2.29)$$

in which V is the forward flight speed (parallel to the ground surface) and w_{ind} the induced velocity of the rotor. When considering multi-rotor systems, it has been shown that equation 2.29 fails to accurately predict the thrust enhancement in ground effect conditions [76–78]. An example of this is presented in figure 2.11, which compares the thrust increase prediction of equation 2.29 with measurements of a two-rotor system [76].
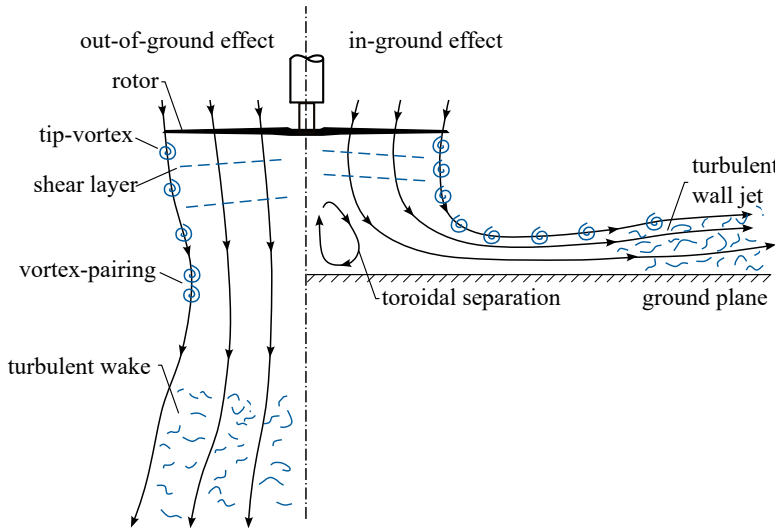
Figure 2.10: Conceptual flow topology of a single rotor in hover (left) and in ground proximity (right), adapted from [69, 74]

Close to the ground (z/R<1)f, the two rotor-system give a greater thrust increase compared to the model. However, for heights exceeding 1 rotor radius, the two-rotor system falls below that of model predictions. This is particularly evident around the height of $z = 2R$, in which the multi-rotor system produces less that 95% of the free-hover thrust. The physical root cause of such non-linear behavior has been ascribed to the onset of global flow recirculation with upward flow between the rotors, known as the fountain flow [77, 78], which under certain conditions causes the turbulent fountain flow to be re-ingested into the rotors [76, 79]. The fountain flow and re-ingestion mechanisms are schematically illustrated in figure 2.12a. The ingestion of the fountain increases the momentum at the inflow and therefore lowers the produced thrust for a fixed rotational speed. On the other hand, studies concerning quad-rotor systems consistently measure an increased thrust compared to the Cheeseman-Bennett model, up to 30% higher than the single rotor value [77, 78]. In this case, there is a central body at which the fountain flow impinges, generating an effective upwash.

The illustration figure 2.12a, presents the symmetric case of the fountain flow, which is re-ingested simultaneously into both rotors. In reality, the re-ingestion is biased to one of the two rotors, and switching of the wake re-ingestion, from one rotor to the other, can occur. This switching cycle is illustrated in figure 2.12b. The timescale associated with this lateral movement of the flow is generally several orders of magnitude larger than the one related to the rotational speed of the rotors [80, 81]. It is therefore conjectured that the unsteadiness is not directly associated with the blade passages and the helical vortices trailing from the blade tips.

eplacements
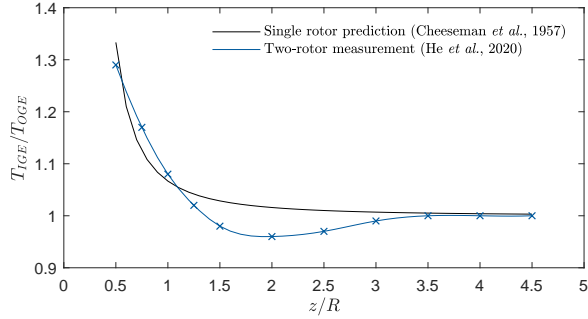
Figure 2.11: Single rotor predictions (equation 2.29) [75] and two-rotor measurements (separated by one rotor diameter, extracted from [76]) in-ground-effect thrust.
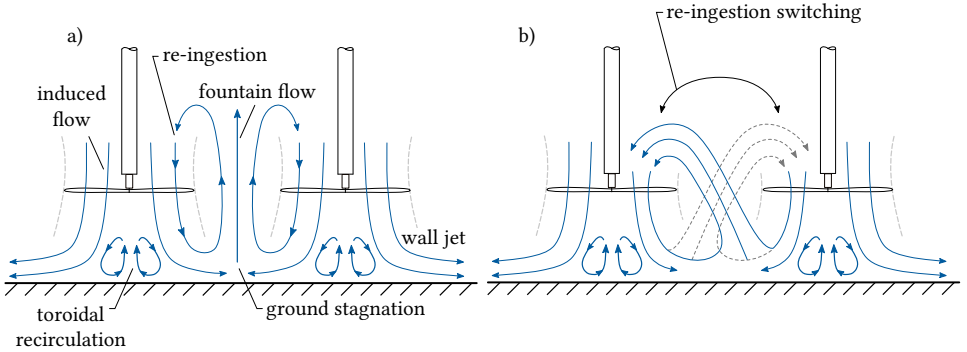
Figure 2.12: a) Conceptual flow topology of the multi-rotor system in ground effect and b) illustration of re-ingestion switching.

Fountain flow unsteadiness in related flows

Low-frequency unsteadiness has been reported in other studies concerning fountain flows. For instance, the rotor-wing interaction of a tilt-rotor configuration in hover produces a similar fountain flow by the back pressure of the wing surface [82]. In a study by Polak *et al.* [83] the effects of the fountain were isolated by the insertion of a physical plane, so-called image plane, between subsequent rotors. This effectively creates a half-span model and thus removed the interaction between the two rotor slipstreams. When the image plane was removed, the height of the fountain increased and it was shown to drift laterally resulting in the "*re-ingestion switching*". These results were also found in a numerical study by Zanotti *et al.* [84]. The occurrence of this phenomenon is reported to be aperiodic [83] at a rate 1-2 orders of magnitude lower than the rotational frequency of the rotors [85]. The switching is believed to be responsible for an intermittent frequency in the acoustic spectrum of tilt-rotors in hover [86]. Valuable observations of two interacting air columns are also made in studies concerning impinging jets, studied for the take-off aerodynamics of STOVL aircraft [87] as well as for a wide range of industrial applications [88]. The location of stagnation point in the foot of the fountain, between the jets, was shown to vary randomly in the lateral direction [89, 90]. Aside from this, variations in the emerging angle of the fountain plume from the wall have been observed [91].

2.4 Installation effects of Over-The-Wing propulsion

Over-The-Wing propulsion presents a disruptive propulsion system layout where the propulsors are positioned over the suction side of the wing, with their axes aligned with the wing's chord line, as schematically illustrated in figure 2.13. This design leverages the interaction between the rotors and the lifting surface to achieve favorable aerodynamic effects and reduced fly-over noise, due to the wing's shielding effect. The current section covers the aerodynamic and aeroacoustic interactions between rotors and the wing surface that occur for Over-The-Wing propulsion.
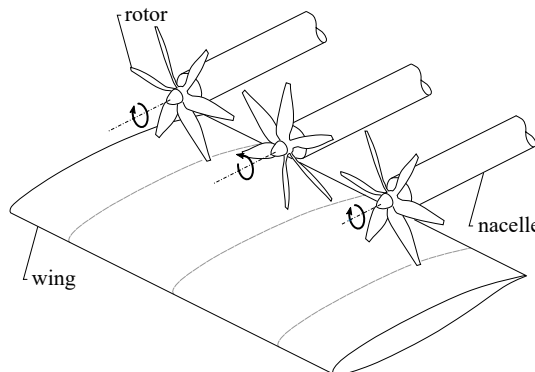
Figure 2.13: Schematic representation of Over-The-Wing propulsion.

2.4.1 Rotor-on-wing aerodynamics

During operation, the rotors provide thrust and induce a flow over the wing, affecting its aerodynamic performance. The main effects are schematically illustrated in figure 2.14a and can be decomposed into inviscid and viscous parts [34].

a)

b)
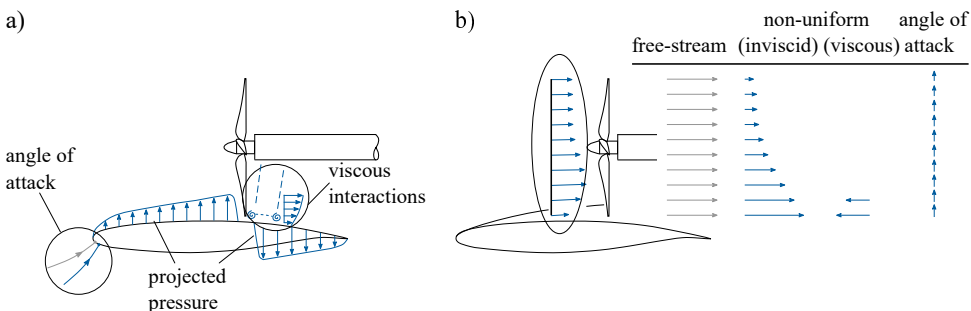
Figure 2.14: Schematic of aerodynamic interactions for Over-The-Wing propulsion. a) Effect of the rotor on wing and b) change in inflow to the rotor by the presence of the wing.

Inviscid effects

As shown in section 2.1, the potential flow induced by the rotor lowers the pressure upstream of the disk by the acceleration of the flow. The static pressure after the disk is increased by the increase of total pressure. When the rotor is positioned over the suction side of the wing, this pressure is projected over the surface, see figure 2.14. Additionally, the accelerated flow upstream of the disk also results in the entertainment of flow from the vertical direction at the wing's leading edge. Consequently, the wing experiences a higher angle of attack than the geometric angle of attack of the system.

These effects impact the aerodynamic efficiency of the wing in cruise conditions, as has been shown by studies concerning single and distributed Over-The-Wing propellers. An increase in the lift-to-drag ratio of 8%, compared to an isolated wing, have been found [92]. This is associated to both a lift increase and (pressure) drag reduction. Such effects on the wing's lift and drag are sensitive to position of the propeller along the wing chord. A propeller position closer to the trailing edge gives the largest increase in the wing's lift, caused by the larger area of reduced surface pressure (increased suction) upstream of the propeller [93]. On the other hand, the drag is shown to be minimized for a propeller position that is located near the maximum airfoil thickness [32, 94]. However, increases in drag due to the propeller's induction have also been noted in literature [95]. Aside from the lift and drag force, Over-The-Wing propulsion increases the yawing, rolling, and nose-down pitching moment [96].

Viscous effects

The propeller induced flow also has an effect on the boundary layer of the wing. Upstream, the propeller moves transition forward [93] but this only takes place when the propeller is relatively close to the natural transition point of the used wing. More significant rotor-induced viscous effects occur downstream of the propellers, in particular when these are positioned upstream of an adverse pressure gradient. Figures 2.15a and b show the axial velocity in such conditions when the propeller is removed and when operated, respectively. These results [97] show that the propeller can trigger flow separation when positioned upstream of a flap. Contributing to this is the thickening of the wing's boundary layer below the propeller [92] and the formation of local momentum deficits, caused by the periodic presence of tip vortices [97]. However, increasing the tip spacing is not an effective mitigation strategy for the separation. Instead, it can be prevented by moving the propeller half a radius forward to force an attachment of the slipstream with the wing [97].

The physics behind the slipstream-wing adherence of the propeller is schematically illustrated in figure 2.15c. After the tip vortex is formed in point A, it moves away from the wing by the contraction of the streamtube in B. Nonetheless, spanwise pressure gradients are also generated, which removes fluid from the center. Subsequently, a mass deficit is formed which entrains the streamtube and tip vortex downwards after point B. The vortex filament is then deformed due to the lower velocity near the wall, resulting in a split in the central segment of the filament. The ends of vortex filaments are re-orientated perpendicular to the wall since no normal velocities can be induced near the wall, and gradually separate from each other as the wake convects downstream.
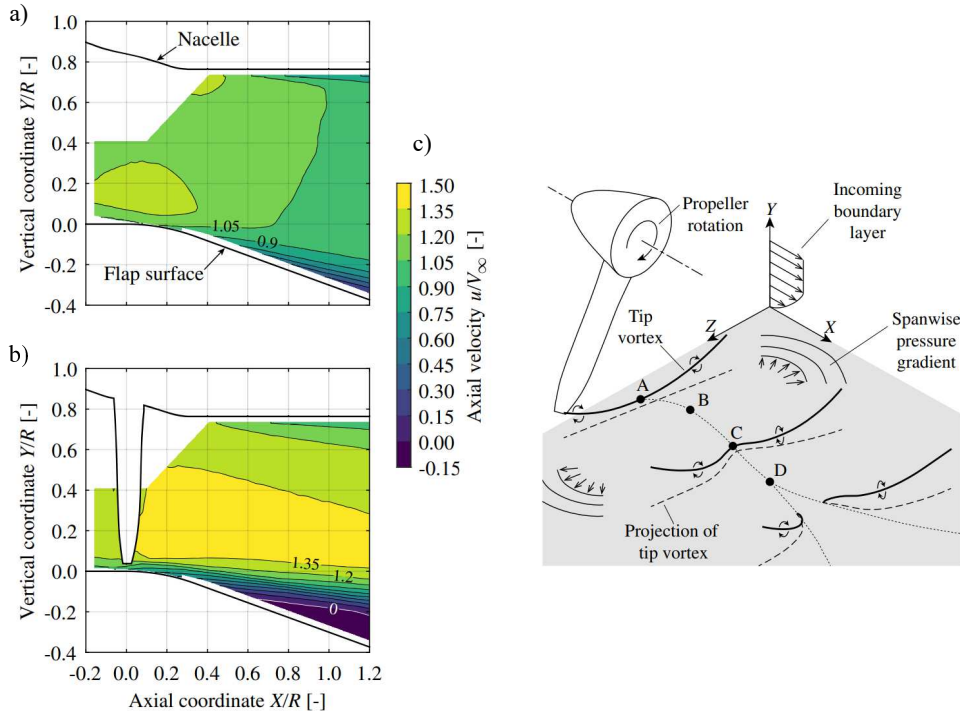
Figure 2.15: Time-averaged axial-velocity distribution and streamlines between the nacelle and the flap surface, a) propeller off and b) propeller on. c) Notional interpretation of the evolution of the tip vortices. The dotted line represents the trajectory of the lowest point of the vortex filament. Figures adapted from [97].

2.4.2 WING-ON-ROTOR AERODYNAMICS

Aside from the aerodynamic effects of the rotor on the wing, the performance of the rotor is also affected due to installation. The interactions primarily affect the inflow of the rotor, resulting in a change in operating conditions compared to free-stream conditions. In figure 2.14b, the inflow is schematically illustrated and decomposed in different contributions [34] that can be expounded on separately. The wing's inviscid flow acceleration is more pronounced near the surface, generating a velocity gradient in the direction normal to the wing surface and leading to non-uniform inflow conditions for the rotor. In contrast, the wing's boundary layer creates a velocity deficit near the surface. Additionally, the combined viscous and inviscid effects of the wing induce a change in the rotor's effective angle of attack. Aforementioned aerodynamic effects of the wing change the rotor's operating conditions and impose unsteady loading on the blades. For a fixed-pitch rotor, the accelerated flow over the wing reduces the effect tip speed ratio and decreases the thrust (recall section 2.1). Moreover, unsteady loading loads of the rotor have been shown to result in propeller efficiency losses up to 16% [92], alongside an expected increase in the tonal component of the propeller's noise signature.

Considering both adverse and beneficial aerodynamic installation effects of Over-The-Wing propeller systems, the aero-propulsive efficiency on the aircraft level is expected to increase compared to an isolated propulsion-wing system. This was shown in a recent study by de Vries *et al.* [98] in which a hybrid-electric regional transport aircraft featuring aft-mounted propellers and an Over-The-Wing–DEP system was compared to a conventional twin-turboprop configuration. The aero-propulsive efficiency is predicted to be increased by 9%, leading to a reduced energy consumption of 5% (although with an uncertainty of ± 5%).

2.4.3 AEROACOUSTICS

Integration of the propulsion system over the wing alters the acoustic signature compared to an isolated system in three ways, as schematically illustrated in figure 2.16.
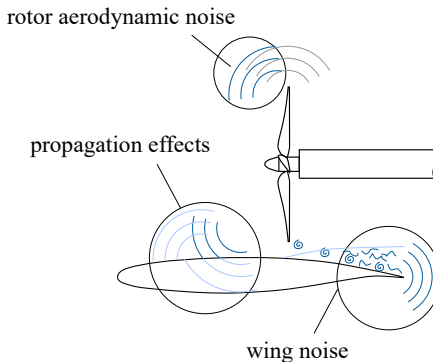
Figure 2.16: Schematic of the aeroacoustic effect for Over-The-Wing propulsion.

First of all, as shown in section 2.4.2, the wing affects the inflow to the rotor resulting in variations in operating conditions of the blades along the azimuth. This potentially results in increased tonal noise amplitudes at the higher harmonics of the blade passing frequency [99, 100]. The wing-induced velocities are greatly affected by the angle of attack, through the increasing circulation as the wing produces more lift, making this effect particularly relevant for the high angles of attack observed in eVTOL flight conditions [22]. Moreover, the generated adverse pressure gradient in these conditions results in rapid growth of the wing's boundary layer and possibly leads to flow separation. Such viscous effects generate a strongly distorted mean inflow, while the ingestion of turbulence elevates the broadband noise levels [101]. When rotors are installed with their axes parallel to a surface, and are operated in high-thrust conditions, an adverse pressure gradient is projected on the surface. This enhances boundary layer ingestion which is reinforced by the passages of blade tips [102]. In addition, energetic flow structures are generated in the separated flow, that are stretched by the pressure gradient at the inflow of the rotor, resulting in strong elevation of the noise levels through blade vortex interaction [102]. The generated vortex structures show resemblance to the formation of inlet vortices during the ground operation of turbo fans or propellers [103, 104] or as found in the propeller-hull interaction for marine applications [105, 106].

Another acoustic effect of Over-The-Wing propulsion, schematically illustrated in figure 2.16, is the affected propagation of acoustic waves coming from the aerodynamic noise sources of the rotor. When an acoustic wave interacts with a finite solid boundary, different propagation effects can occur such as reflection, refraction, absorption, diffraction and scattering. These propagation effects are schematically illustrated in figure 2.17.
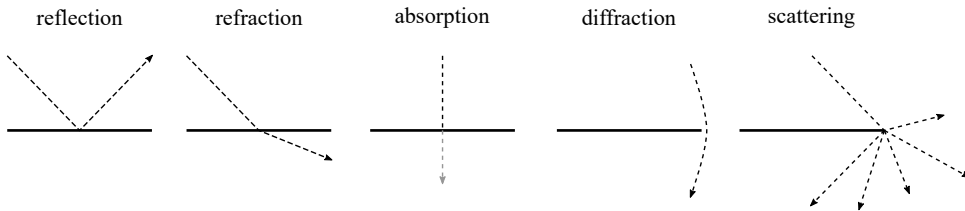
Figure 2.17: Propagation effects of acoustic waves near a finite solid boundary.

To minimize the sound generated during fly-over [16], the rotor noise must be either reflected or absorbed by the wing surface [107], and diffraction should be mitigated. An important consideration here is the Helmholtz number He, which is defined by the ratio between a characteristic length scale (for example the wing chord c) and the acoustic wavelength λ:

$$He = \frac{2\pi c}{\lambda} = kc \tag{2.30}$$

in which k is the acoustic wavenumber. Values of He larger than unity, i.e. acoustic waves that are shorter than the wing chord, indicate acoustic compactness. For rotors, the frequency of interest is typically the BPF. Hence, to prevent effects due to diffraction, a criterium should be set for the ratio between the blade passage frequency and the chord length of the wing:

$$He_{BPF} = \frac{\Omega B}{c_0} c > 1 \rightarrow c > \frac{c_0}{\Omega B} \tag{2.31}$$

Scattering of the tonal noise from the rotor [108] can occur when the rotor blade tips are positioned close to the sharp edge of the wing's trailing edge [109]. This has been shown to increase the radiation efficiency of the low-frequency blade harmonics [51, 109].

Finally, the discussion in section 2.4.1 revealed the physics behind the interaction between the slipstream of the propeller and the wing's boundary layer. As a consequence of this interaction, the turbulent fluctuations downstream of the propeller, at the suction side of the wing, were shown to be increased [97]. This will likely result in an increase in broadband noise compared to an isolated wing. Nonetheless, given the relatively low forward flight speed of eVTOL vehicles, airframe noise is typically less of a concern [110]. Consequently, the rotor aerodynamic noise sources and their affected propagation due to the wing's presence are expected to be the most substantive aeroacoustic effects of Over-The-Wing rotors.

2.5 Challenges

Based on the installation effects of multi-rotor–surface interactions as introduced in sections 2.3 and 2.4, a number of scientific challenges can be identified.

2.5.1 Ground proximity

The thrust of multi-rotor configurations showed non-linear behaviour when interacting with a ground surface which could be detrimental to the controllability of aerial vehicles during take-off, landing, near ground hovering. The existence of the fountain flow has been hypothesized for the variations in thrust, but proof of the mechanism and detailed characterization of the unsteadiness is missing. Moreover, contradictions among experiments carried out by different researchers about the role of rotor spacing, the fountain flow, and the performance of rotor systems in ground effect have been identified by He *et al.* [76]. While two studies, one aimed at rotor-obstacle interaction [111] and another researching a quadrotor configuration [112], reported an increase of the thrust coefficient with a larger rotor spacing, another investigation reported the opposite behavior [113]. Furthermore, studies where fountain-like flows also exist (tilt-rotor-fuselage interaction and twin impinging jets) have identified large-scale instabilities and re-ingestion switching. It is unknown if such effects occur for multi-rotors in ground proximity and how such behaviour relates to the geometric and performance parameters of the system.

2.5.2 Over-The-Wing propulsion

For Over-The-Wing propulsion, the majority of previous investigations dealt with aero-propulsive performance in cruise flight conditions, i.e. a moderate angle of attack is considered and the propellers operate at a relatively high advance ratio. The above conditions do not match those expected for eVTOL flight, where a low advance ratio and a higher incidence will be encountered. The high propulsive thrust conditions of rotors and the low-to-null inflow speed, causes a strong contraction of the stream tube with possible separation regions, determining unexpected viscous interactions with lifting surfaces. Considering the low-speed of the vehicles in the initial stages of the flight envelope, variations in flight conditions could lead to complex transient effects. A generalization of the performance during such operating conditions does not exist and therefore design guidelines are lacking in the public domain. For the aeroacoustic performance in particular, it is unclear how the expected increase in aerodynamic rotor noise relates to the favorable shielding effect.

2.6 Research questions

This thesis aims at the understanding and modeling of critical aerodynamic and aeroacoustic rotor-surface interactions that occur for Over-The-Wing–DEP during vertical take-off. The objective can be split into a number of research questions, that contribute to the scientific challenges established in section 2.5:

1. What is the three-dimensional flow topology around multi-rotors when hovering in ground-proximity and what is the role of the rotor spacing? (chapter 5)

2. Are large-scale fountain instabilities present during near ground hovering and can these be related to the geometrical and performance parameters of the multi-rotor system? (chapter 6)

3. Can the aero-propulsive performance of Over-The-Wing propulsion at incidence be modeled through a single-pass strategy? (chapter 7)

4. What is the effect of the wing on the tonal noise sources of Over-The-Wing rotors? (chapter 8)

5. Do transient aerodynamic flow effects occur during a transition from vertical to horizontal flight? (chapter 9)

To answer these questions, a number of experiments are conducted which are supplemented with results from analytical modeling techniques. The next chapter provides the theoretical background of the conducted experimental measurements.

2

II

Research Methodology

3

EXPERIMENTAL MEASUREMENT TECHNIQUES

THE aerodynamic and aeroacoustic interactions between rotors and surfaces are investigated through experiments, exploiting a wide range of different measurement techniques. In this chapter, the theoretical background for each of the employed techniques is formed. This starts with an introduction to the aerodynamic measurement techniques of integral loading, pressure orifices and velocimetry, in sections 3.1, 3.2 and 3.3, respectively. Furthermore, in section 3.4, techniques and facilities used for the microphone measurements are discussed.

3.1 INTEGRAL LOADING

Force and moment measurements are widely applied in modern wind tunnel test campaigns, and can be used to study the steady-state aero-propulsive forces and assess the performance of rotors and wings. The loads are typically measured using either internal or external balances. Inside the balances, strain gauges are positioned which form the main component used to measure the loads. Strain gauges make use of an uni-axial metallic pad with a wired grid [114], see figure 3.1a. Tension or compression affects the length of the wired grid, which in turn changes the electric resistance. The mechanical strain ϵ is returned from the relative change in resistance $\Delta R/R$ by multiplication with a strain Gauge Factor GF:

$$\epsilon = \frac{\Delta R}{R}\text{GF} \tag{3.1}$$

A typical balance uses a multitude of strain gauges attached to uni-axial flexures to isolate component loads. To allow for accurate measurements of small variations in resistance, the gauges are arranged in a Wheatstone bridge [114] and attached to two sides of a deflecting beam. Figure 3.1b shows a full Wheatstone bridge, consisting of four strain gauges. Nonetheless, half- or quarter-bridges are also available in which some strain gauges are replaced by fixed resistors.

A deflection will cause the resistance of the strain gauges on one side of the beam to increase (R_1 and R_3 in figure 3.1b), while the resistance on the opposing side decreases (R_2
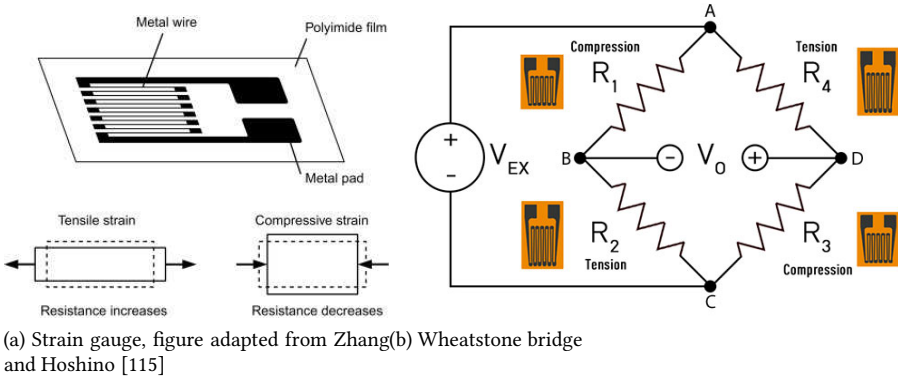
(a) Strain gauge, figure adapted from Zhang (b) Wheatstone bridge
and Hoshino [115]

Figure 3.1: Components for loading measurements

and R_4), generating an imbalance over the bridge. After exciting the circuit by a voltage V_{EX}, the voltage difference over the bridge V_0 yields:

$$V_0 = V_{EX} \left(\frac{R_1}{R_1 + R_3} - \frac{R_2}{R_2 + R_4} \right) \tag{3.2}$$

Calibration of the balance then provides a transfer function between the applied loads and signal voltage.

Strain gauges can be prone to hysteresis caused by either mechanical (due to friction) or temperature variations which should be taken care of during the design and operation. Temperature biases are often compensated for through the Gauge Factor GF or by including a length of temperature-sensitive wire in the electrical circuit [114].

3.2 Pressure orifices

The static pressure over the surface of test geometries, such as wings, can be used to measure pressure forces and identify regions of flow stagnation and separation. These pressure measurements are typically performed through small orifices, drilled perpendicular to the model's surface. Figure 3.2 shows an example of pressure orifices positioned at the center span of a two-dimensional wing profile. The orifices are connected via long thin tubes to a pressure transducer located outside of the wind tunnel model. The pressure transducer measures the pressure difference between the orifices and a reference pressure, typically the ambient pressure. Such pressure difference causes the physical deformation of a membrane which is returned to an electrical signal using strain gauges, recall section 3.1. The measured static pressure p_s in the orifices is typically normalized using the dynamic pressure of the flow, to create the pressure coefficient C_p:

$$C_p = \frac{p_s - p_\infty}{\frac{1}{2} \rho_\infty V_\infty^2} \tag{3.3}$$
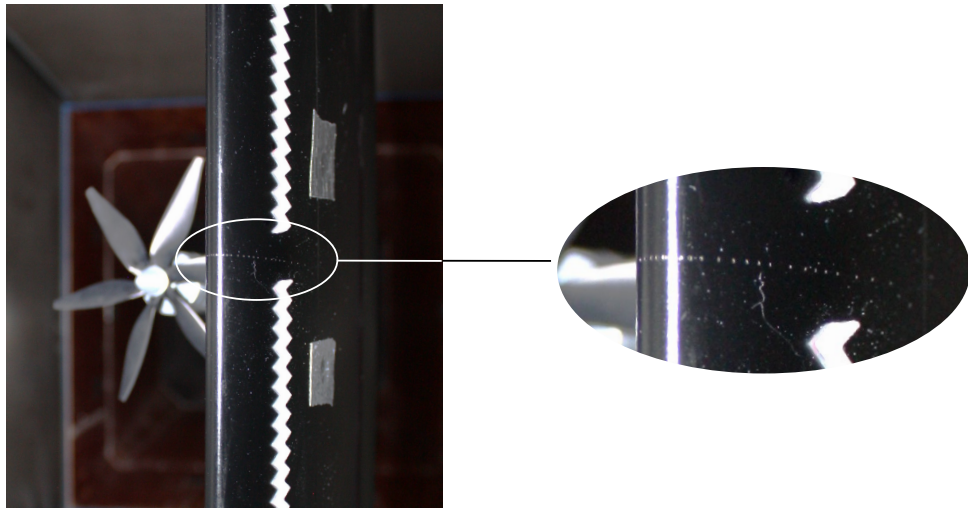
Figure 3.2: Pressure orifices at the mid-span position of a vertically mounted DLR-F15 wing profile.

3

3.3 VELOCIMETRY

Velocimetry is a non-intrusive technique to measure the velocity in fluids and is widely used to study the complex and unsteady aerodynamic interactions generated by rotor-induced flows [116]. The measurements are conducted by seeding the flow with tracer particles that are illuminated by a powerful light source and recorded using one or a system of (high-speed) cameras. Velocity vectors are then returned by computing the displacement of the particles in subsequent images. The basic principles of velocimetry measurements are introduced in this section.

3.3.1 PARTICLES

To measure the flow velocity, a homogeneous distribution of particles in the flow is required. Generally, the tracer particles must obey two main criteria. The first requirement is that the particles accurately follow the flow without affecting the flow's properties. Assuming a very low particle Reynolds number such that viscous terms are dominant, the time response τ_p of a particle due to a sudden step response in acceleration is [117]:

$$\tau_p = d_p^2 \frac{\rho_p}{18\mu_f} \tag{3.4}$$

in which d_p and ρ_p are the particle's diameter and density and μ_f is the dynamic viscosity of the fluid. Table 3.1 present values of the time response of traditional tracer particles (top three rows) for velocimetry in air flows.

To assess the tracking accuracy, the time scale of the flow should be considered as well. For this the particle Stokes number St_p is typically used:

$$St_p = \frac{\tau_p}{\tau_f} \tag{3.5}$$

Table 3.1: Properties of traditional tracer particle & Helium-Filled Soap Bubbles (HFSB).

Tracer material	Diameter [μm]	Density [kg/m^3]	τ_p [μs]
DEHS	1-3	10^3	2
Glycol-water solution	1-3	10^3	2
Vegetable oil	1-3	10^3	2
TiO2	0.2-0.5	1-$4 \cdot 10^3$	0.1-2
HFSB	100-500	1.2-1.4	10

in which τ_f is the characteristic timescale of the flow, found by the ratio between a characteristic length and velocity. Typically a Stokes values below 0.1 yields acceptable tracking characteristics [117].

A second particle criterium is the sufficient scattering of light to be observed in the camera footage. The particle intensity I_p on the camera images scales as follows:

$$I_p \propto \frac{J_I A_O^2 d_p^2}{Z_O d_\tau^2 \Delta X_I^2} \tag{3.6}$$

Equation 3.6 shows that the particle intensity depends on the properties of illumination (light pulse energy J_I and cross-section area ΔX_I^2), the camera objective (objective distance Z_O and aperture A_O) and the particles themselves (particle diameter d_p and particle image diameter d_τ). Note that the light scattering I_p increases with particle diameter d_p, while the tracking fidelity (equation 3.4) decreases, creating a conflict. The tracer particles presented in the top three rows in table 3.1 have densities that are three orders of magnitude larger than air. Hence, to allow sufficient tracking fidelity, their diameter is micrometer scale. The limited scattering properties of such particles confine the measurement domain to planes with an area of 0.1m^2 or relatively small volumes of 50cm^3, with current state-of-the-art hardware.

To increase the size of the particle, and therefore it's scattering characteristics, an efficient strategy would be to reduce the density of the particles. A recent development in the field of velocimetry in gaseous flows is to make use of Helium-Filled Soap Bubble (HFSB) tracer particles. These particles are generated by a nozzle, see figure 3.3, and by controlling the ratio between helium and Bubble Flow Solution (BFS) a difference in density with air of below 0.1 kg/m^3 is achievable [117].

Consequently, particle diameters of $d_p \approx 0.3$ mm are feasible, increasing the scattering by five-orders of magnitude compared to traditional seeding, and allowing for a timescale of $\tau_p = 10$ μs [119]. While HFSBs face challenges regarding seeding density and cannot be applied in high-speed flows by the deformation due to centrifugal forces, the great light scattering characteristics have paved the way to large-scale ($\mathcal{O}(m^3)$) volumetric velocimetry [119–121].

3.3.2 Illumination & Recording
During the measurements, the particles are illuminated by a powerful light source consisting of short pulses separated by Δt. Traditionally, for two-dimensional measurement, the light source consist of a sheet produced by a Nd:YAG or Nd:YLF laser. Nonetheless, with
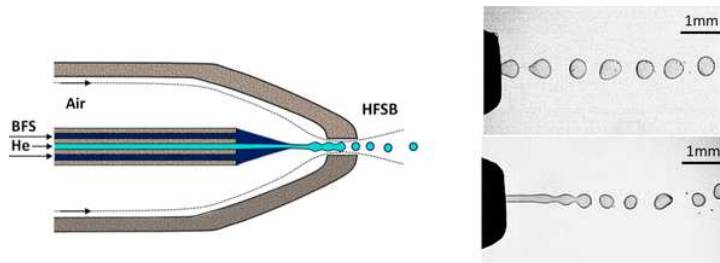
Figure 3.3: Schematic illustration of the bubble generator used in the experiments (left). Shadow visualization of bubbles at the exit of the generator (right) in bubbling (top) and jetting (bottom) regimes. Figure adapted from [118]

the advancements of volumetric flow measurements and HFSBs, high power, pulsed LEDs have gained in popularity [117].

During the illumination pulses, the particles are recorded by CCD or CMOS cameras. Generally, two types of timing schemes are considered: time-resolved and double frame, see figure 3.4a and b, respectively. In time-resolved mode, each recording consists of a single frame and two subsequent images are processed together. Note that this timing scheme is restricted by the allowable Δt, and is therefore only possible for low-speed flows or by using hardware with high repetition rates. Another possibility is to use a double-frame timing scheme in which each recording consists of two frames that are evaluated together. This allows for lower frame rates and longer acquisition times of the cameras for the same Δt, but results in lower temporal resolution with respect to time-resolved measurements.

(a) time-resolved

(b) double-frame
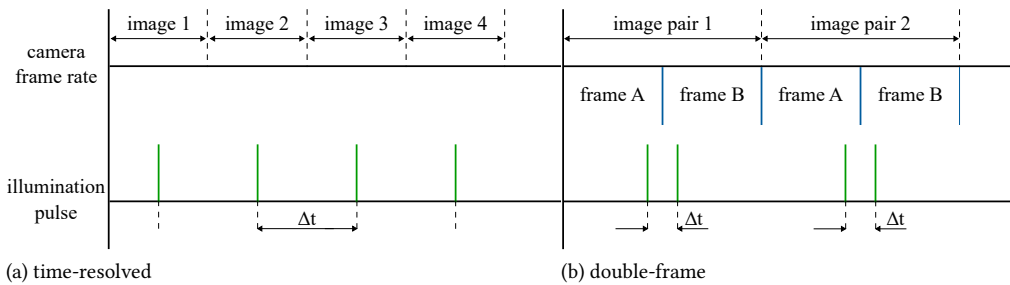
Figure 3.4: Common timing diagrams for velocimetry illumination and recording.

3.3.3 Pre-processing

An example camera recording is presented in figure 3.5a. The image is shown to be disturbed by reflections due to the rotor blades and mounting (indicated by the red dashed lines), and variations in particle intensity are presented. These optical contaminations could result in erroneous vector computation and are typically resolved using a pre-processing procedure.

Levelization deals with subtracting a reference intensity map from the camera footage, which is representative of the background noise [122]. For stationary or slowly moving (variations at a frequency much lower than the acquisition frequency) light reflections or intensity variations, the background can be obtained by performing a sliding average over consecutive frames [123, 124]. For instationary reflections a low- [125] or high-pass [126] frequency filter can be applied. If insufficient temporal information is available for the instationary reflections, background removal cannot rely upon image statistics. Instead, spatial filters can be applied to individual raw images. Such filters generally rely on the fact that particle images have a shorter length scale with respect to the reflections and therefore a filter kernel size that is at least as large as the particle image diameter is required. A popular spatial filter is known as the sliding minimum filter [127]. As a final step in pre-processing, the local particle intensities are generally normalized over (parts of) the spatial domain, to allow for a similar contribution of each particle in the vector computation.

The image in figure 3.5a deals with stationary reflections (highlighted by the vertical red lines) and instationary reflections from the blades (horizontal red lines) that are pre-processed using a high-pass frequency filter [126]. The pre-processed image is presented in figure 3.5b and effectively removes such reflections.

3
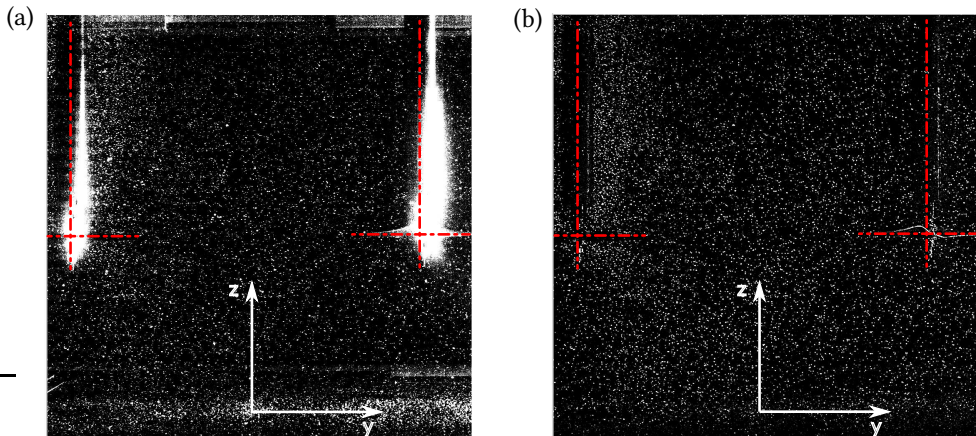
Figure 3.5: (a) Extracted raw footage (1024x1024 pixels) of camera 1 in which LED light reflections of the rotor's support structure and ground plane are visible, (b) similar to (a) but after pre-processing the recording. Positions of the rotor axes and disks are given by the red dotted line.

3.3.4 Vector calculation: Particle Image Velocimetry

In Particle Image Velocimetry (PIV) measurements, two-dimensional velocity vectors are constructed by spatial cross-correlation of consecutive images (by using either a time-resolved or double frame timing scheme). An illustration of the cross-correlation algorithm is presented in figure 3.6.

The correlation maps $R(\mathbf{s})$ of two images are returned through:

$$R(\mathbf{s}) = \int I_1(\mathbf{x}) I_2(\mathbf{x}+\mathbf{s}) d\mathbf{x} \tag{3.7}$$
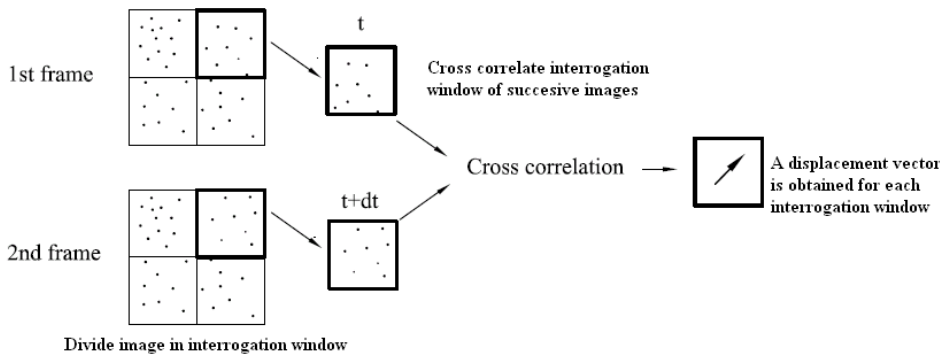
Figure 3.6: Illustration of the cross-correlation algorithm of two-component PIV. Figure adapted from [128].

in which I_1 and I_2 are the recorded intensity maps, separated by Δt. The intensity maps are typically divided into interrogation windows. These are small regions of the image in which multiple ($\mathcal{O}(10)$) particles are present. The example in figure 3.6 shows square interrogation windows, however more advance techniques are available such as window deformation [129] to increase the accuracy in shear regions of the flow.

The cross-correlation map $R(\mathbf{s})$ yields a peak corresponding the average particle displacement $\Delta\mathbf{x}$ between the two intensity maps. The process is carried out for every interrogation window in the image. Overlap between the windows is often used to reduce the vector pitch of the constructed velocity field. Moreover, vector computation generally consists of multiple passes (that include window shifts) [130] during which the interrogation window size is gradually decreased. From the particle image displacement $\Delta\mathbf{x}$ in the image plane, the flow velocity $\mathbf{u}$ in the measurement plane is returned as follows:

$$\mathbf{u} = \frac{\Delta\mathbf{X}}{\Delta t} = \frac{1}{M}\frac{\Delta\mathbf{x}}{\Delta t} \tag{3.8}$$

in which $\Delta\mathbf{X}$ is the physical displacement in the measurement domain and M is the magnification factor of the camera system.

STEREOSCOPIC PARTICLE IMAGE VELOCIMETRY
Two-component velocimetry measurements are subjected to perspective errors which can be significant for large field of views and large out-of-plane velocity values [117]. Stereocopic-PIV (sPIV) [125] is an adaptation to regular two-component PIV and allows for reconstruction of the third velocity component in the measurement plane. For this, a second camera is introduced, which is translated and rotated with respect to the first camera. Since one or both cameras now view the plane from an angle, a Scheimpflug adapter is included to correct the focus plane of the cameras. To reconstruct the velocity components, sPIV relies on a mapping function from the image coordinates to the real world. The mapping function is generated by using a 3D calibration plate and a self-calibration procedure is performed to correct for any errors due to misalignment. These aspects are analogous to three-dimensional velocimetry measurements and are introduced in section

3.3.5. An important consideration in stereoscopic PIV setups is the stereo angle θ, defined as the angle between each camera and the measurement plane's normal direction. Large or small values of θ can lead to errors in the out-of-plane velocity component. Such errors are minimized for a stereo angle of $\theta \approx 45°$ [117].

3.3.5 Vector calculation: Particle Tracking Velocimetry

As an alternative to the reconstruction of velocity vectors through cross-correlation, particle tracking velocimetry (PTV), also known as Lagrangian Particle Tracking (LPT), can be applied. Such algorithms deal with locating individual particles and tracking their displacement through the measurement domain. Velocity vectors are therefore returned at scattered locations through the measurement domain. PTV methods therefore increase the spatial resolution compared to vector reconstruction based on cross-correlation, but are generally less robust.

PTV techniques have been proven to be effective in measuring velocities in large volumes ($> 0.01\text{m}^3$), particularly in combination with Helium-Filled Soap Bubbles as tracer particles. Volumetric measurements require a tomographic imaging system, consisting of at least three cameras, and volumetric illumination. A widely applied 3D-PTV algorithm is known as "*Shake-The-Box*" [131] and is praised for its high computational efficiency, local accuracy and ability to reconstruct velocity vectors in relatively high seeding concentrations for PTV.

Volumetric Lagrangian Particle Tracking: "Shake-The-Box"
The "*Shake-The-Box*" algorithm fits discrete particle positions along their trajectory by a polynomial function that regularizes the particles' position, velocity and acceleration. The algorithm can be split into different parts as illustrated in figure 3.7.
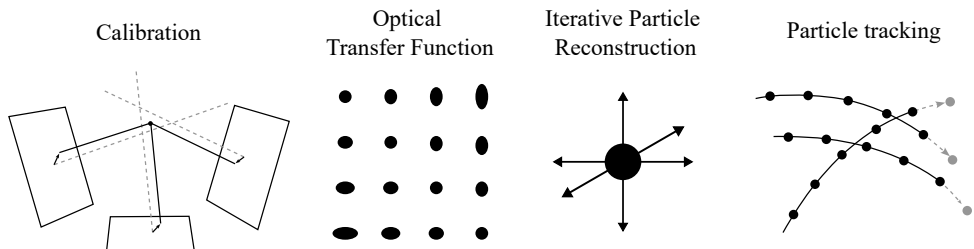
Figure 3.7: Schematic description of the "*Shake-The-Box*" [131] algorithm.

Calibration: The first step is to generate a map between the spatial and image coordinates. This is performed by an optical plate calibration with a known geometry that is recorded from multiple views. Using a pinhole model or a polynomial fit, a mapping function for each camera in the tomographic imaging system is generated. Hence, the mapping function M_i for the i-th camera, relates the spatial coordinates in the measurement domain (X, Y, Z) to the imaging coordinates (x_i, y_i):

$$(x_i, y_i) = M_i(X, Y, Z) \tag{3.9}$$

After this, a self-calibration procedure [132] is performed to compensate for alignment errors, such as inaccuracies in the calibration plate, unstable calibration shift mechanisms and loose mechanical connections of the cameras. Self-calibration is performed by using the particles as a reference and suppressing the calibration disparities. In the procedure, a particle is identified in one of the cameras and potential particle locations in 3D are determined by triangulation, using the images of the other cameras. The disparity vectors are then obtained by re-projecting the particle positions on the images:

$$d_i = \left(d_{ix}, d_{iy}\right) = \left(x_i', y_i'\right) - (x_i, y_i) \tag{3.10}$$

where $\left(x_i', y_i'\right)$ is the projection of the localized particle back to the image of camera i, using the original mapping function M_i. From the disparity vectors, a corrected mapping function $M'(X,Y,Z)$ is determined:

$$M_i'(X,Y,Z) = M_i(X,Y,Z) - d_i(X,Y,Z) \tag{3.11}$$

Optical Transfer Function: Using the (corrected) mapping function, the Optical Transfer Function (OTF) [133] is generated. Instead of assuming a spatially homogeneous mapping function of the voxels to the images, the OTF corrects for the effects of optical distortions (such as blurring) on the reconstruction. To generate the OTF, particle images are fitted with a two-dimensional Gaussian, and averaged over a number of sub-volumes for each camera. As a consequence, information on the particle shape depends both on the particle position and the camera number.

Iterative Particle Reconstruction: After generating the OTF, the particles can be identified and located. The position and intensities of recorded particles can suffer from noise and the influence of overlapping particles. This often leads to slight displacements of the reconstructed particle in relation to the true position. Iterative Particle Reconstruction (IPR) [134] is a technique to overcome such triangulation errors by iteratively updating the reconstructed position by minimizing a residual. IPR deals with the following steps:

1. **Triangulation**: The particles are triangulated in space using the OTF.

2. **Shaking**: Triangulated particles are reconstructed on the image and iteratively translated to minimize the residual with the original image particle, in a process called "*shaking*".

3. **Remove particles**: Particles below a certain intensity threshold are removed from the original image.

4. **Generate residual**: A residual image is generated by back-projection of all identified particle images on the original image.

5. **Repeat**: The loop is repeated with the residual images.

Particle tracking: Particle tracks can then be computed from particle positions of subsequent timesteps. The algorithm deals with an initialization and predicting phase for each track.

In the initialization phase, particle pairs of different timesteps are identified. This is generally resolved by applying a search radius around the particle position or a predictor location based on an input velocity field. After tracks are formed which consist of four particles, the tracks are "initialized".

In the second phase, the initialized particle tracks are fitted using a polynomial function and extrapolated to predict particle positions in the consecutive time steps. This increases computationally efficiency of the "*Shake-The-Box*" algorithm. The predicted particle positions introduce fitting errors, which are corrected by "*shaking*" all predicted positions, similar to IPR. The particles of identified tracks are then removed from the image, and new particles and tracks are triangulated and initialized, before proceeding to the next time step.

3.3.6 Data reduction to Cartesian grid

In PTV, velocity vectors are returned at scattered locations through the measurement domain. Nonetheless, it is typically preferred to analyze the velocity field on a structured grid. Various techniques are available for interpolation of the velocity field to a discretized 3D grid.

The most intuitive approach is to perform a linear interpolation of the scattered velocity data to the grid points, as illustrated left-hand side in figure 3.8. More common, however, is the method of Gaussian Binning, where the impact of the spatial averaging imposed by the size of the bin is minimized by weighing the particles by their distance to respective grid midpoint.

Gaussian Binning and linear interpolation only use velocity information of the particle positions in a single time step. Therefore, it is required for every bin to contain at least one particle.
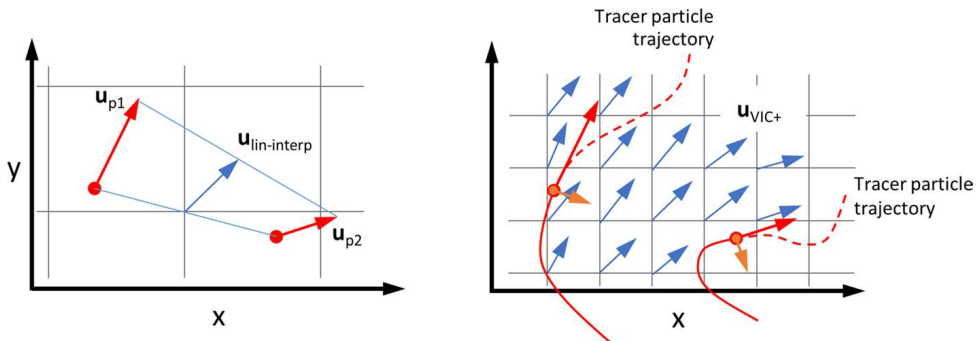

Figure 3.8: Linear interpolation between two PTV velocity measurements (left) and VIC+ interpolation between two PTV particle trajectories (right, the orange vector is Du/Dt). Figure adapted from [135].

To achieve a higher spatial resolution and resolve finer scales in an unsteady flow, the seeding density should therefore be increased. Increasing the seeding density is typically

limited by the seeding system [136] and the ghost particle phenomenon [137]. To prevent the occurrence of ghost particles, the particle per pixel (ppp) cannot exceed a certain value ($ppp = 0.025$ for three-camera systems and $ppp = 0.05$ for four-camera systems [138]). This limitation poses significant challenges in large-scale volumetric velocity measurements with a large depth of field, i.e. exceeding 20 cm.

Fine-scale Reconstruction: VIC+

To enhance the spatial resolution of the reconstructed velocity field, various fine-scale reconstruction methods for 3D-PTV data are available [135, 139]. One such method is Vortex In Cell (VIC+), developed by Schneiders and Scarano [135]. The VIC+ method utilizes not only instantaneous velocity vectors but also the velocity material derivative to increase spatial resolution, as depicted on the right side of figure 3.8. The use of the velocity material derivative ensures that both temporal and spatial information of the flow field is included.

In the initial step of the VIC+ algorithm a 3D structured grid with a grid size of h is defined. As a guideline [135], a grid size that depends on the seeding concentration C can be considered:

$$h = \frac{1}{4}C^{-1/3} \tag{3.12}$$

Equation 3.12 implies that a total of 64 grid points are used for every computed particle track. Dense interpolation of the particle tracks to the Cartesian grid (with size h) is then performed by iteratively minimizing a cost function J:

$$J = J_{\boldsymbol{u}} + \alpha^2 J_{\mathrm{D}\boldsymbol{u}}. \tag{3.13}$$

where α is a weighting coefficient. The cost function J is proportional to the difference between the PTV measurements and the VIC+ results; $J_{\mathbf{u}}$ and $J_{\mathrm{D}\mathbf{u}}$ are defined by equation 3.14 and 3.15, respectively:

$$J_{\mathbf{u}} = \sum_p \left\| \boldsymbol{u}_h\left(\boldsymbol{x}_p\right) - \boldsymbol{u}_m\left(\boldsymbol{x}_p\right) \right\|^2. \tag{3.14}$$

$$J_{D\boldsymbol{u}} = \sum_p \left\| \frac{\mathrm{D}\boldsymbol{u}_h}{\mathrm{D}t}\left(\boldsymbol{x}_p\right) - \frac{\mathrm{D}\boldsymbol{u}_m}{\mathrm{D}t}\left(\boldsymbol{x}_p\right) \right\|^2. \tag{3.15}$$

in which J_u is the relative error in velocity and J_{Du} in acceleration. $\boldsymbol{u}_m$ and $\frac{\mathrm{D}\boldsymbol{u}_m}{\mathrm{D}t}$ are the velocity and velocity material derivative at the particle positions $\boldsymbol{x}_p$ that follow directly from the PTV results. $\boldsymbol{u}_h$ and $\frac{\mathrm{D}\boldsymbol{u}_h}{\mathrm{D}t}$ are the values on the structured grid, at the particle position $\boldsymbol{x}_p$, obtained through a linear interpolator. The material derivative on the grid is defined as:

$$\frac{\mathrm{D}\boldsymbol{u}_h}{\mathrm{D}t} = \frac{\partial \boldsymbol{u}_h}{\partial t} + (\boldsymbol{u}_h \cdot \nabla)\boldsymbol{u}_h \tag{3.16}$$

In the VIC+ algorithm, the velocity and material derivative on the structured grid are derived from the vorticity field ω_h on the same grid. The Poisson equation relates the velocity to the vorticity field:

$$\nabla^2 \boldsymbol{u}_h = -\nabla \times \boldsymbol{\omega_h} \tag{3.17}$$

in which spatial derivatives are determined by center and single-sided finite difference schemes in the algorithm. The temporal derivative of the velocity in equation 3.16 is determined by differentiation of equation 3.17 in time:

$$\nabla^2 \frac{\partial \boldsymbol{u}_h}{\partial t} = -\nabla \times \frac{\partial \boldsymbol{\omega}_h}{\partial t} \qquad (3.18)$$

The temporal derivative of the vorticity in equation 3.18 in turn is obtained from the vorticity and velocity field, and their spatial derivatives, using the vorticity-transport equation:

$$\frac{\partial \boldsymbol{\omega}_h}{\partial t} = (\boldsymbol{\omega}_h \cdot \nabla) \boldsymbol{u}_h - (\boldsymbol{u}_h \cdot \nabla) \boldsymbol{\omega}_h \qquad (3.19)$$

With the velocity and material derivative on the structured grid known, equation 3.13 is minimized using a gradient-based approach and the vorticity field is updated iteratively until a convergence criterion is satisfied.

VIC+ DEMONSTRATION

As a demonstration, results from VIC+ are compared to the velocity field obtained from Gaussian binning, using 3D-PTV data of the slipstream of an isolated rotor ($R = 15.24$ cm) in hover condition as input [33]. The measurement domain (27 dm^3) is sparsely seeded with a seeding concentration of $C \approx 4 \cdot 10^{-4}$ particles mm^{-3}, from which approximately 4000 particle tracks are computed in each time step. The computed particle tracks in this flow field are presented in figure 3.9a.
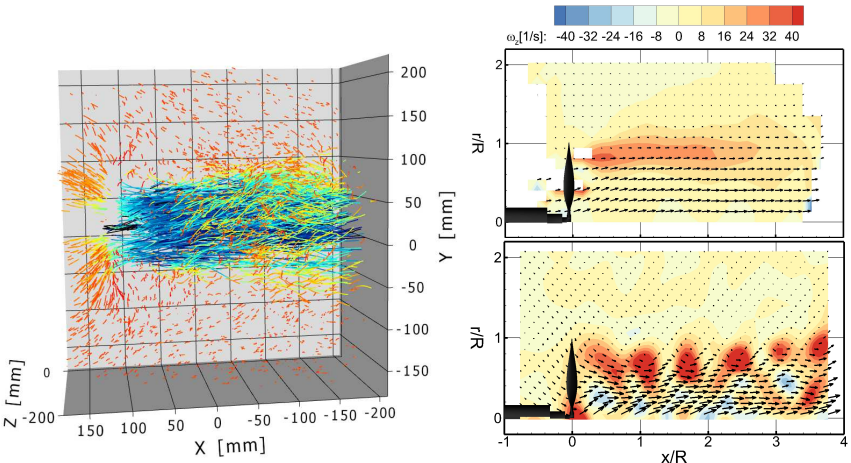
(a) Velocity tracks around an isolated rotor in hover.

(b) Reconstructed vorticity field using Binning (top) and VIC+ (bottom).

Figure 3.9: Demonstration of different data reduction techniques. Data from [33].

To ensure that all cells contain at least one data point in most of the domain, a cubic bin size of $h = 41.2$ mm is required for the instantaneous velocity field when using Gaussian Binning interpolation. Additionally, a 75% overlap factor between subsequent cells is

applied, resulting in a velocity vector spacing of h = 10.3 mm. For the fine reconstruction grid, a grid size of h = 5.15 mm follows from equation 3.12. A comparison of the instantaneous out-of-plane vorticity contours and 2D velocity vectors in the plane through the rotor axis is presented in figure 3.9b.

In the instantaneous vorticity field obtained through Gaussian binning, the tip vortices are returned as a smeared region of high vorticity by the limited spatial resolution. Furthermore, vector data is missing at several locations around the edge of the domain. In contrast, the method of VIC+ enhances the spatial resolution and individual tip vortices can be identified. Dense interpolation by VIC+ also ensures that data are continuous throughout the entire measurement domain.

3.3.7 Measurement error and uncertainty

Considering that PIV systems are quite complex and involve various hardware components, multiple sources of errors (either random or systematic) in the measurements can exist [140]. The sources of errors can be classified as follows:

- **Errors caused by system components**: for example bad particle tracing fidelity, peaklocking [141] (a phenomenon that occurs when the particle image size is comparable to the pixel size, causing a bias error towards integer pixel values) and errors in laser alignment and timing of the recordings.

- **Errors caused by the evaluation techniques**: for example errors in the selection of parameters in the image interrogation algorithm.

The uncertainty of the measurements is defined by the interval around the measured value that is likely to contain the true value within a certain probability [142]. For time-averaged PIV measurements, the uncertainty $\epsilon_{\bar{V}}$ can be estimated statistically:

$$\epsilon_{\bar{V}} = \frac{\sigma_{\bar{V}}}{\sqrt{N}} \tag{3.20}$$

in which $\sigma_{\bar{V}}$ is the standard deviation of the velocity and N is the number of uncorrelated recordings. Advanced methods are also available to estimate the uncertainty apriori [140] or evaluate instantaneous uncertainty [142].

Finally, important performance parameters in PIV systems are the dynamic velocity range DVR and the dynamic spatial range DSR [143]. The dynamic velocity range DVR is defined as the ratio between the maximum and minimum measurable velocities of a given PIV system:

$$DVR = \frac{V_{max}}{\sigma_V} = \frac{\Delta x_{max}}{\sigma_{\Delta x}} \tag{3.21}$$

in which σ is the standard deviation. Instead, dynamic spatial range DSR is determined by the ratio between the maximum and minimum measurable flow wavelength through:

$$DSR = \frac{L}{D_I} \tag{3.22}$$

where L and D_I are the sizes of the sensor and interrogation window, respectively.

3.4 Aeroacoustic measurements

Aeroacoustic measurements are typically performed using microphones in specialized wind tunnel facilities to minimize the influence of reflections and background noise. An important consideration here is the type of test section used.

3.4.1 Wind tunnel test section

Three different test sections can be considered aeroacoustic wind tunnel studies: a closed test section, an open jet facility, and a hybrid test section.

In closed test sections, the flow is geometrically confined and reliable corrections for aerodynamic interference effects are available. Such test sections are therefore preferred when accurate aerodynamic quantities are required [144]. Nonetheless, the wind tunnel walls affect acoustic propagation and the microphones need to be inserted in cavities in the walls. This makes the microphones vulnerable to pressure fluctuations from the turbulent boundary layer and other sources of noise inherent to wind tunnels [145, 146].

Open jet configurations have the advantage that the microphones can be placed outside of the test section. Consequently, the microphones are placed in ambient conditions with no disturbances from the flow. Moreover, since there are no wind tunnel walls, reflections inside the test section are removed. Open jet configurations are usually positioned inside anechoic chambers to reduce the background noise and prevent reflection from external objects and walls.

In hybrid test sections, the wind tunnel walls are fitted with acoustic transparent material such as Kevlar [147] or perforated metallic plates to minimize transmission losses. By doing so, microphones can be placed outside of the test section and reflections of the wind tunnel walls are minimized. Consequently, hybrid test sections are intended to take the aerodynamic advantages of closed test sections with minimal compromises in terms of acoustics. Acoustic corrections are necessary for hybrid test section walls, as acoustic absorption at higher frequencies may occur. Additionally, in cases with strong pressure gradients between external and internal test section conditions, flow permeability may also be present [114].

3.4.2 Microphone measurements

To measure the sound from the wind tunnel's test object, condenser-type microphones are typically used, such as the example presented in figure 3.10a. Condenser-type microphones transfer the pressure waves through electrical energy using the capacitance between a thin metal diaphragm and a fixed backplate, see figure 3.10b.

The diaphragm moves as a consequence of the pressure waves and the relative distance to the backplate varies, forming a variable capacitor. In typical aeroacoustic investigations, multiple microphones are used that either record the noise characteristics at different noise emission angles, to measure the acoustic far-field, or are used in phased-arrays to localize dominant noise sources.

3.4.3 Far-field data processing

The pressure signal from a microphone positioned in the acoustic far-field is generally converted to the Overall Sound Pressure Level (*OASPL*):
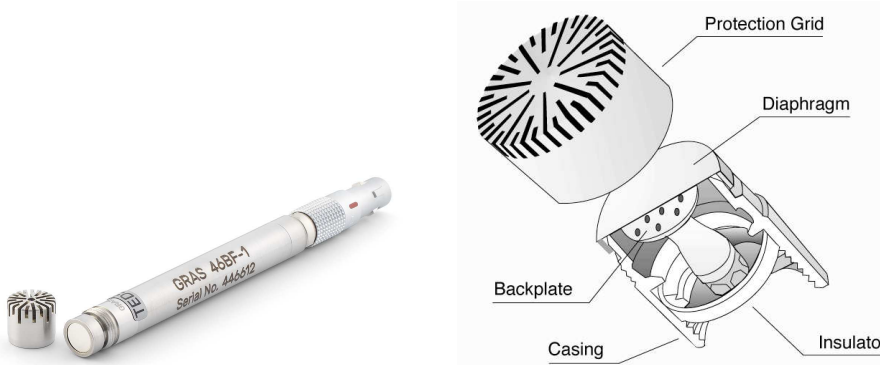
(a) GRAS type 46BF microphone

(b) Main components of condenser-type microphone. Figure adapted from Piezotronics [148].

Figure 3.10: Condenser-type microphone

3

$$OASPL = 20\log_{10}\left(\frac{p_{rms}}{p_{ref}}\right), \qquad\qquad p_{rms} = \sqrt{\frac{1}{N}\sum_{i=1}^{N}p_i^2} \qquad (3.23)$$

where p_{rms} is the root-mean-square of the pressure, as computed from N number of microphone samples. p_{ref} is an acoustic reference pressure that represents the threshold of human hearing (p_{ref} = 20μPa in air).

Frequency spectrum

For a detailed analysis of the acoustic signal, it is general practice to compute a frequency decomposition of the microphone signal by a discrete Fourier transform. To reduce the noise for statistically stationary pressure signals, Welch's method [149, 150] can be applied, by dividing the time signal in M overlapping blocks of K samples when computing the Fourier transform. The ensemble size K is generally a power of two and affects the frequency resolution (equal to the sample rate over the ensemble size K). For the m-th block, the complex pressure amplitudes yield:

$$P_m(f) = \frac{2}{K}\sum_{k=1}^{K}u_k p_k \exp(-2\pi i f k \Delta t) \qquad (3.24)$$

in which f is the frequency, and Δt the sample interval of the microphone signal. Creating such ensembles can lead to a loss of periodicity in the signal, resulting in spectral leakage when computing the discrete Fourier transform. To circumvent this, a window function u_k is included, such as the widely used Hanning window:

$$u_k = C\sin^2\left(\frac{\pi k}{K}\right) \qquad (3.25)$$

Since the results should be consistent with a rectangular window (i.e. $u_k = 1$), the window function includes a coefficient C to normalize the results. To correct the spectral amplitudes, the coefficient C holds [151]:

$$\frac{1}{K} \sum_{k=1}^{K} u_k = 1 \rightarrow C = 2 \tag{3.26}$$

On the other hand, the auto- and cross-power levels are corrected through:

$$\frac{1}{K} \sum_{k=1}^{K} u_k^2 = 1 \rightarrow C = \frac{8}{3} \tag{3.27}$$

After computing the amplitudes for each ensemble m, the contributions are averaged to obtain the frequency spectrum $P(f)$:

$$P(f) = \frac{1}{M} \sum_{m=1}^{M} \frac{1}{2} |P_m(f)|^2 \tag{3.28}$$

The results of the pressure amplitudes are often expressed in the Sound Pressure Level *SPL* through:

$$SPL(f) = 20 \log_{10} \left(\frac{P(f)}{p_{ref}} \right) \tag{3.29}$$

Separation of tonal and broadband noise

As was shown in section 2.2, rotor noise consist of tonal and broadband noise. For aeroacoustic studies, it can be beneficial to split and investigate the two contributions separately. Recall that the tonal noise is deterministic while broadband noise is a random source. Making use of these properties, phased-averaged Fourier transforms [152, 153] can be generated. Then, by averaging over many shaft revolutions the non-periodic, random noise is filtered out of the spectrum. Note that this technique requires information on the rotor position along the azimuth (1P signal). The algorithm is described in [152] and is also presented below:

1. Definition of the trigger times t_j. These are the times when the rotor blades are in a fixed position along the azimuth.

2. Generation of a Fourier transform for each time interval:

$$P_{j,n} = \frac{2}{t_j - t_{j-1}} \int_{t_{j-1}}^{t_j} p(t) \exp\left(-2\pi in \frac{t - t_{j-1}}{t_j - t_{j-1}} \right) dt \tag{3.30}$$

in which $p(t)$ is the microphone signal. Considering that the time interval generated by the trigger times is in general not a power of two, a discrete Fourier transform is computed instead:

$$P_{j,n} = \frac{2}{\tau_{kmax}} \sum_{k=1}^{k_{max}} p(\tau_k) \exp\left(-2\pi in \frac{\tau_k - t_{j-1}}{t_j - t_{j-1}} \right) \tag{3.31}$$

where k and τ are the sample numbers and times in the trigger interval: $t_{j-1} \leq \tau_1 < ... < \tau_{max} < t_j$

3. The discrete Fourier transforms are then averaged over the number of intervals M and complex average C_n is generated:

$$C_n = \frac{1}{M} \sum_{j=1}^{M} P_{j,n} \tag{3.32}$$

When generating the complex average C_n, non-periodic noise will be filtered out. Thus, by averaging over sufficient intervals M, C_n will only contain the tonal, deterministic noise.

4. Finally the auto-power average A_n is generated:

$$A_n = \frac{1}{S} \sum_{j=1}^{S} \frac{1}{2} |P_{j,n}|^2 \tag{3.33}$$

The broadband noise B_n is then found by subtracting the complex average C_n from the auto-power average A_n:

$$B_n = A_n - C_n \tag{3.34}$$

3.4.4 PHASED-ARRAY DATA PROCESSING

When using two-dimensional array of microphones, noise sources can be localized by using the phase difference between each microphone, by a technique known as acoustic beamforming [154, 155]. This allows for separation of different noise sources or the identification of external noise sources contaminating the experiments. For this, the cross-spectral matrix $\mathbf{C}$ is computed from the pressure amplitudes of N microphones [151]:

$$\mathbf{C} = \frac{1}{2} \mathbf{P}\mathbf{P}^*, \qquad\qquad \mathbf{P} = \begin{pmatrix} P_1(f) \\ \vdots \\ P_N(f) \end{pmatrix} \tag{3.35}$$

The asterisk in equation 3.35 denotes the complex conjugate. A steering function $\mathbf{g}$ is then defined which holds information about the propagation of the source to the microphone array. The components g_n of the steering function, are the pressure amplitudes at each microphone for a given reference source. Generally, a monopole source description with unit strength in a uniform meanflow is considered [151]:

$$g_n = \frac{-\exp(-2\pi i f \Delta t_0(\xi, \mathbf{x}_n))}{4\pi \sqrt{(M \cdot (\mathbf{x}_n - \xi))^2 + (1 - M^2)^2 \|\mathbf{x}_n - \xi\|^2}} \tag{3.36}$$

in which $\Delta t_0(\mathbf{x}_n, \xi)$ is the time delay from a search grid point ξ to the coordinates of the n-th microphone $\mathbf{x}_n$. The complex amplitudes a of the sources in ξ result from the minimization of a cost function J:

$$J = \|\mathbf{P} - a\mathbf{g}\|^2 \rightarrow a = \frac{\mathbf{g}^*\mathbf{P}}{\|\mathbf{g}\|^2} \tag{3.37}$$

The source auto-powers then follow from:

$$A = \frac{1}{2} aa^* = \frac{\mathbf{g}^*\mathbf{C}\mathbf{g}}{\|\mathbf{g}\|^4} \tag{3.38}$$

Equation 3.38 is known as conventional beam forming. The source maps obtained from conventional beam forming can be limited in spatial resolution for low-frequencies, leading to overlapping sources. To overcome this issue, deconvolution post-processing techniques [156–158] are often applied.

3

4

EXPERIMENTAL ARRANGEMENTS

T<small>HE</small> experimental techniques as introduced in chapter 3 were used to answer the research questions defined in chapter 2. For the studies, three different experimental arrangements were realized that are introduced separately (sections 4.1, 4.2 and 4.3) in this chapter. In each of the sections, the testing facility, test geometry, operating conditions and measurement parameters of the concerned experimental setups are described.

4.1 MULTI-ROTOR IN GROUND PROXIMITY

A multi-rotor setup was realized at the High-Speed Laboratory at Delft University of Technology to study the aerodynamic interactions in ground proximity (chapters 5 and 6).

4.1.1 ROTOR MODEL

Two counter-rotating rotors were installed with their axes perpendicular to a ground plane, as shown in figure 4.1. The APC-brand rotors are commercially available (model numbers APC 6X4E and APC 6X4EP) and comprise a radius of $R = 76.2$ mm, a pitch of 4 inches and a parabolic tip. Each rotor was driven by a geared in-runner brushless motor (type Hacker, B20 26 L kv2020 + 4:1) operated at a shaft rotation speed of $\Omega = 167$ Hz.

The rotors were not phase-controlled which means that the relative phase difference varied during acquisition. The discrepancy in rotational speed between the rotors is estimated to be equal to 0.25 Hz, resulting in a variation of the phase difference between the rotor blades, over the acquisition duration of the measurement. Hence, in the time-averaged sense, the measurement can be considered as one with a random phase between the blades. The Reynolds number, based on the blade sectional chord length at a nominal radius of 0.75R, was $Re_b = 42,000$ and the tip Mach number was $M_t = 0.22$. The rotors had a thrust coefficient of $C_T = 0.12$ and provided a thrust of $T = 2.14$ N. The rotors were operated in stagnant air representing a hover scenario (thus the advance ratio is $J = 0$). Experiments were performed in an enclosure of 2x3x2 m^3 at conditions of normalized tip-to-tip rotor spacing $S/R = [0.05, 1.0, 2.0]$ and normalized height $H/R = [1.0, 2.0, 3.0, 4.0]$. Experimental conditions are summarized in table 4.1.

This chapter is based on publications [33, 159–162].

Figure 4.1: Multi-rotor setup at High-Speed Laboratory of Delft University of Technology.

Table 4.1: Multi-rotor operating conditions.

Rotor parameters and operation	
Rotation speed Ω [Hz]	167
Number of blades B	2
Radius R [mm]	76.2
(3/4)R rotor blade chord Reynolds number Re_b	42,000
Tip Mach number M_t	0.22
Lateral seperation S/R (tip-to-tip)	0.05-2
Height to ground H/R (disk-to-ground)	1-4
Thrust T [N]	2.14
C_T	0.12

4.1.2 Measurement techniques

To study the flow surrounding the rotor model, both volumetric Lagrangian Particle Tracking (time-averaged flow analysis in chapter 5) and two-component Particle Image Velocimetry (unsteady flow behaviour in chapter 6) were employed.

Lagrangian Particle Tracking

The volumetric velocity measurements covered the flow domain illustrated in figure 4.2. Helium-Filled Soap Bubbles (HFSB) generated under controlled conditions [118] were employed that scatter sufficient light in conditions of volume illumination and imaging. The suitability of this seeding technique for rotorcraft aerodynamics has been recently demonstrated in the study by Wolf *et al.* [163]. Two HFSB generators were utilized producing each approximately 30,000 bubbles per second, with mean diameter of 0.4 mm and nearly neutrally buoyant. The enclosure was seeded for two minutes prior to performing the measurement. The achieved seeding density was approximately 0.01 particles per pixel (ppp) corresponding to a spatial concentration of 0.5 particles/cm^3. The measurement volume was illuminated by a LaVision LED-Flashlight 300 device at a distance of 0.7 m below the measurement volume. Illumination was performed at a rate of 2.0 kHz and the duration of illumination for each pulse (pulse width) was Δt = 50 µs. A tomographic imaging setup

was composed of three high-speed CMOS cameras (Photron *Fastcam* SA1.1) placed outside the enclosure at a distance of 1 m from the measurement region. The cameras subtended a total angle of 38° (see figure 4.2) and were equipped with lenses of focal lengths f = 60 mm (camera 2) and f = 50 mm (cameras 1 and 3), set at numerical aperture $f_\#$ = 16. The resulting measurement volume spanned 20 × 31 × 33 cm^3 (4.3R × 4.0R × 2.6R). System synchronization was obtained with a LaVision Programmable Timing Unit (PTU 8) and each measurement comprises of 2000 recordings for a time duration of 1 s. The object-to-image mapping parameters were obtained with a calibration procedure based on a target recorded at 3 positions separated by 10 cm each. The residual calibration disparity was reduced to less than 0.1 pixels using the volume self-calibration method [132]. An overview of the measurement parameters is presented in table 4.2.
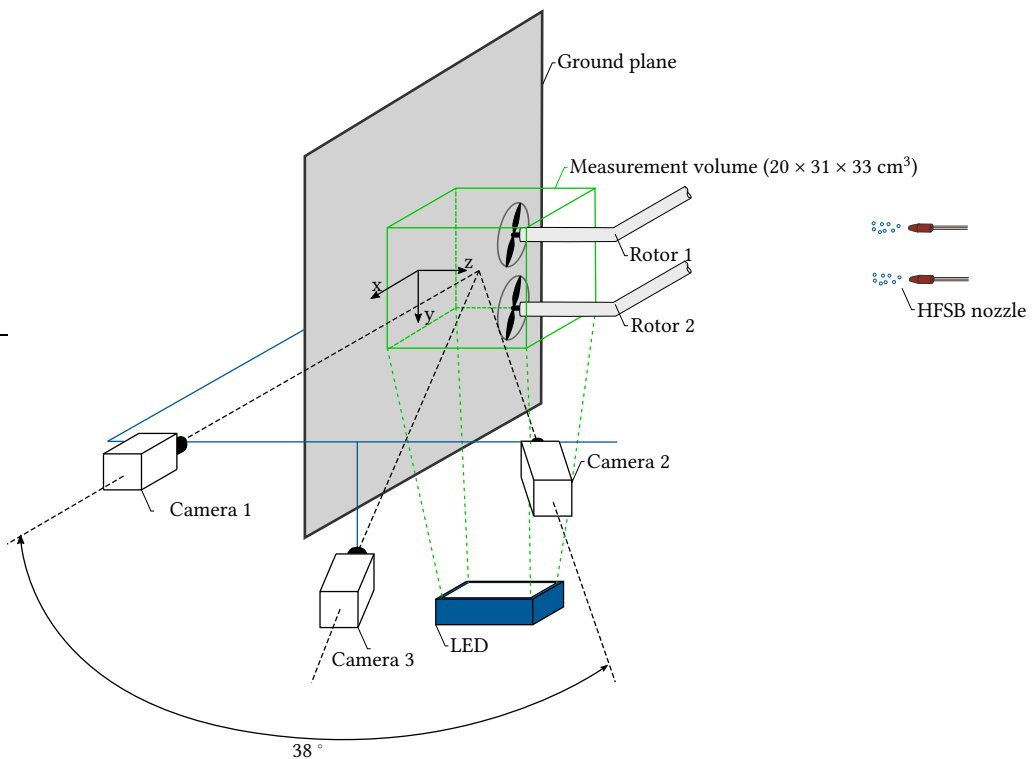
Figure 4.2: 3D schematic of the experimental apparatus, coordinate system and measurement volume. The origin of the coordinate system is at the center location between the two rotors at the ground plane.

The 3D particle motion analysis was performed with the "Shake-The-Box" method [131]. The measurement delivered approximately 8000 particle tracks with a sampling frequency of 2.0 kHz. The maximum particle displacement within a particle track was approximately 20 pixels corresponding to a physical displacement of 6.4 mm. This particle displacement is comparable to other studies using the "Shake-The-Box" method and was shown to be adequate to capture the effect of individual blade passages by the rotors.

Data reduction to a Cartesian grid was performed following two different methods for

Table 4.2: Illumination and imaging conditions for the volumetric flow measurements.

f [mm]	1x 60, 2x 50
$f_\#$	16
Acquisition freq. [Hz]	2000
Sample time [s]	1
Pulse width [μs]	50
ppp	0.01
Field of View (Δx, Δy, Δz)	$20 \times 31 \times 33 \text{cm}^3$

the time-averaged and for the instantaneous velocity fields. Time-average information was gathered in cubic bins of 20 mm size with a 75% overlap factor, yielding a spacing of the velocity vectors of 5 mm. Every bin comprises approximately 10,000 samples. However, the concentration varied across the measurement domain. Nevertheless, a minimum number of 100 samples is set as criterion for a valid measurement.

The instantaneous velocity fields were reconstructed using the vortex-in-cell technique (VIC+) as described by Schneiders *et al.* [135] for 3D scattered particle data; calculations were done in DaVis, with a modified algorithm (VIC#, [164]). The instantaneous velocity field was reconstructed on a grid with h = 7.5 mm spacing between neighboring vectors.

The measurement dynamic spatial range (DSR), defined as the ratio between the largest and the smallest resolvable spatial wavelength, was estimated as the ratio between the domain larger size L and the bin size. Values of DSR = 66 and DSR = 44 are obtained for the time-averaged and instantaneous velocity field, respectively. The dynamic velocity range (DVR) was estimated as the ratio between the maximum and minimum measured tracer velocity and is approximately equal to 360.

The measurement uncertainty ϵ_u for the time-averaged flow field was statistically determined by the ratio between the relevant velocity fluctuations (axial velocity standard deviation) and the square root of the amount of samples per bin. The measurement uncertainty ϵ_u was below 0.5% of the rotor induced velocity in the majority of the domain, except for the shear layers along the boundary of the domain and close to the rotor blades, where it reaches up to $\epsilon_u = 1.5\%$.

PARTICLE IMAGE VELOCIMETRY

Planar PIV velocity measurements were acquired in the domain illustrated in 4.3. The experiment was conducted inside an enclosure of $2 \times 2 \times 3$ m^3 that confines the HFSB used as flow tracers [118]. Any effects of re-circulation in the enclosure are observed at frequencies comparable to the BPF [165] and therefore do not affect the relatively large timescales of interest. Five HFSB generators delivered roughly 150,000 bubbles per second, which were nearly neutrally buoyant and had a mean diameter of 0.4 mm. The enclosure was seeded for two minutes prior to performing the measurement, and resulted in a density of roughly 0.01 particles per pixel (ppp) corresponding to a spatial concentration of 12 particles/cm^2. Laser illumination was provided by a Nd:Yag Continuum Mesa PIV 532-120-M laser. The laser beam was expanded by a cylindrical lens allowing a light sheet thickness of 2 cm. Its effective thickness was estimated using 3D flow data as 8 mm. The

center of the laser sheet was positioned with an offset of 1.5 cm from the propeller axes (in positive x-direction) to avoid shadows from the rotor mounting. Illumination was given with a pulse width of Δt = 150 ns and a rate of 4.0 kHz.
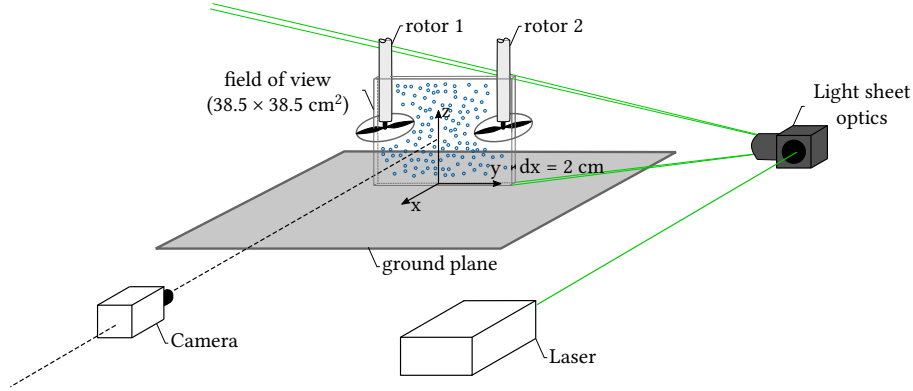
Figure 4.3: 3D schematic of the experimental apparatus, coordinate system and measurement plane.

A high-speed CMOS camera (Photron *Fastcam* SA.5, 1024 px × 1024 px) was used for imaging and placed outside the closed environment at a distance of 1 m from the measurement region. A lens with focal length f = 50 mm, and a numerical aperture set to $f_\#$ = 8 captured a field of view of 38.5×38.5 cm^2 (5R×5R) at a magnification of M = 0.053. Synchronization between the cameras and the laser was obtained with a LaVision Programmable timing unit (PTU X). Each experimental run captured 2.7 s of data (approximately 11,000 recordings) and was repeated six times, thus providing a total of roughly 16 s ($\approx$2750 rotor revolutions) of discontinuous measurements for each of the two configurations. Measurement parameters are summarized in table 4.3.

Table 4.3: Illumination and imaging conditions of the planar velocimetry measurements.

Seeding type	HFSB
Seeding concentration (cm^{-2})	12
Illumination	Nd:Yag Laser
Sheet thickness dx (cm)	2
Pulse width Δt (ns)	150
Repetition rate (Hz)	4000
Camera type	Photron *Fastcam* SA.5 (1024 px × 1024 px)
Objective focal length f (mm)	50
Numerical Aperture $f_\#$	8
Optical Magnification M	0.053
Field of view (cm^2)	38.5 × 38.5
Seeding density ppp	0.01
Number of recordings	6 × 10917
Image analysis	Cross-correlation (24 px × 24 px)

Two pre-processing steps were applied to the raw camera footage before computing PIV-based velocities. First, a minimum time filter was used to eliminate any stationary reflections from the ground plane and support struts of the rotors. Secondly, a sliding minimum filter with a length-scale of 3 pixels was applied, to reduce any unsteady rotor blade-reflections. Planar velocity components were inferred by cross-correlation between subsequent images, with a window size of 24 px ×24 px and an overlap of 75%. This resulted in a vector resolution of 8 mm and a vector spacing of 2 mm. The velocity field was then cropped to a physical domain of 31×27 cm^2. As a final post-processing step, time super sampling with a factor of 5 was applied to improve the quality of the velocity spectra.

The measurement uncertainty ϵ_w for the instantaneous velocity field has been computed using the method of correlation statistics as described by Wieneke [166]. Values of ϵ_w were compared to the induced velocity of a single rotor without a ground plane (w_{ind} = 14.25 m/s). From this follows an average instantaneous uncertainty of approximately 4% of the rotor-induced velocity. Conclusions drawn from these data on the large-scale flow dynamics are not affected by this relatively small uncertainty.

4.2 Performance of Over-The-Wing propulsion

The second experimental setup was used to explore the aerodynamic and aeroacoustic installation effects of the Over-The-Wing propulsion at incidence (chapter 7 and 8).

4.2.1 Wind Tunnel Facility

The experiments were conducted in the closed circuit Aeroacoustic Wind Tunnel (AWT) facility at the Royal Netherlands Aerospace Centre, see figure 4.4. The wind tunnel is positioned in an anechoic chamber ($9 \times 8 \times 6$ m), yielding an absorption rate of 99% above 200 Hz. A closed test section (0.95×0.95 m^2) was used, limiting the turbulence intensity to a maximum of 0.01% at a free-stream velocity of 20 m/s.
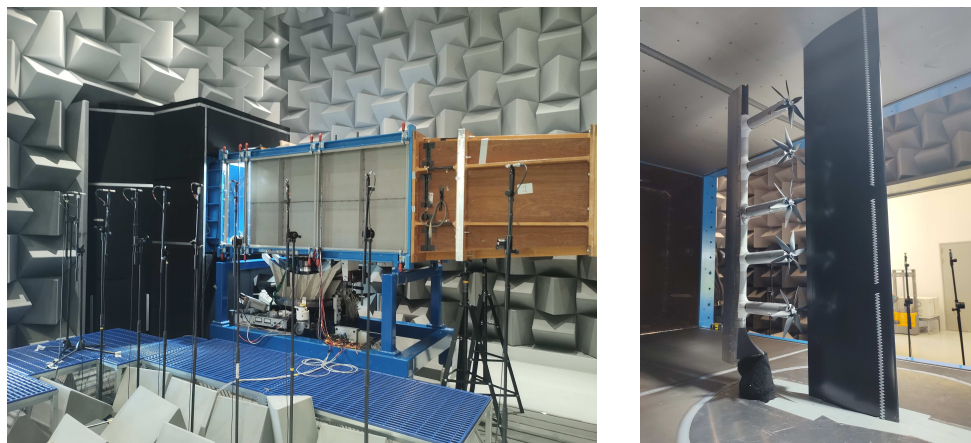

Figure 4.4: Exterior of the 0.95 by 0.95 m^2 test section in the Aeroacoustic Wind tunnel (left) and Rotor-array–wing setup in the test section (right).

4.2.2 Rotor and wing model

A DLR-F15 wing model was mounted vertically on a turntable in the floor of the closed test section, as shown on the right side of figure 4.4. The chord of the wing is 240 mm and transition was fixed at 10% chord by tripping the boundary layer on both the suction and pressure sides. Over the suction side of the wing, a sting was connected to the same turntable as the wing. The sting serves as a support structure for five, span-wise distributed nacelles and aligns each nacelle's axis to the wing's chord direction. Measurements with a single rotor over the wing were also performed. Inside each nacelle, a brushless in-runner motor drives a custom design six-bladed rotor (radius of $R = 63.5$ mm) at a shaft frequency of 383 Hz in counter-rotating orientation. The tip-to-tip separation of each rotor is 0.05 R. The blade design of the rotor is based on a benchmarked version for low-Reynolds application derived from a NACA4412 airfoil [167]. The rotor has been manufactured with CNC out of aluminum with 0.02 mm precision, and cured to avoid material relaxation and oxidation. The test conditions are summarized in table 4.4.

Table 4.4: Over-The-Wing rotor system operating conditions.

Wing chord c (mm)	240
Aspec ratio $A\!R$	4
Shaft frequency (Hz)	383
Number of blades B	6
Rotor radius R (mm)	63.5
Rotor tip gap y_t/R	0.27
Rotor separation z_r/R	2.05
Rotor chord position x_r/c	[0.3, 0.6, 0.9]
Advance ratio J	[0, 0.3, 0.45, 0.6]
Angle of attack α	[-3, 0, 2, 4, 6, 8, 10, 11, 12, 13, 14, 15, 16, 20]
Wing chord Reynolds number Re_c	240,000 - 480,000
(3/4)R rotor blade chord Reynolds number Re_b	$\approx 60,000$
Tip Mach number M_t	0.42
Helmholtz number He $= \frac{2\pi c}{\lambda_{BPF}}$	10.11

4.2.3 Measurement techniques

Integral loading, surface static pressure, velocimetry (two-component and stereoscopic) and acoustic measurement techniques were employed, each will be discussed separately. A schematic overview of the measurement system is provided in figure 4.5a. All measurements (with the exception of PIV) were obtained at an acquisition rate of 4096 Hz and averaged over a time frame of 20 s. Note that the aeroacoustic measurements and sPIV measurements are specific to the single rotor while the 2D2C-PIV measurements are only performed for the distributed propulsion setup.

Integral loads

Rotor thrust and torque were measured on the center rotor. Its brushless motor was mounted to the nacelle using two parallel-mounted uni-axial FUTEK LSB205 load cells
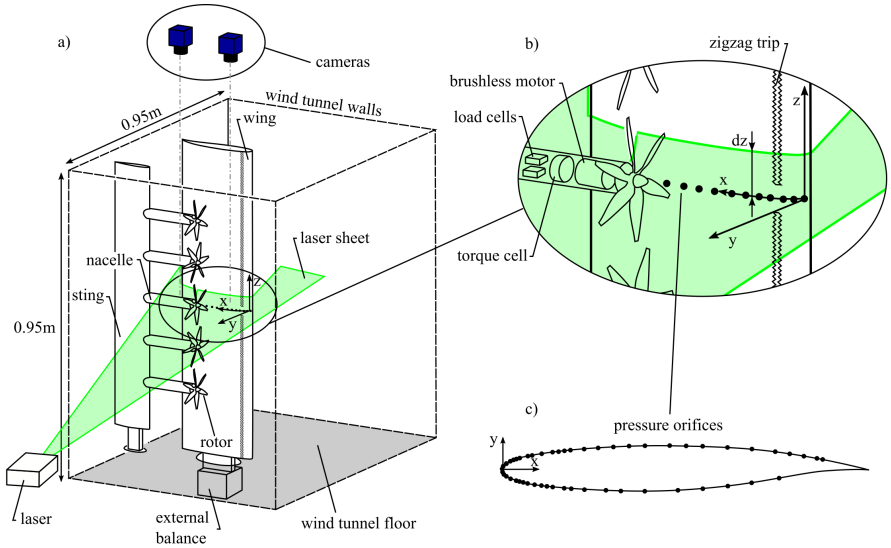
Figure 4.5: 3D schematic of the experimental apparatus and coordinate system, b) zoomed-in plot of the measurement techniques around the center rotor and c) contour of the F15 wing model with location of the static pressure taps.

(Rated Output (RO) of 22.2N with hysteresis of ± 0.1% RO and non-linearity of ± 0.1% RO) and a FUTEK QTA141 torque cell (RO of 1 Nm with hysteresis of 0.5% and non-linearity of 0.2%), see figure 4.5b. The load and torque cells were excited with 7 volts of direct current (VDC) by a single power supply. Repeated measurements for thrust showed an average deviation of 4%. The loads of the wing were measured by a custom-made six-component force balance in the floor of the wing tunnel, see figure 4.5a. In the x- and y-direction, the balance has a capacity of 325 N and 1800 N, respectively. The uncertainty as a percentage of the full load range is 0.80% for the x-direction and 0.13% for the y-direction.

Pressure orifices
The wing's pressure distribution was measured by 59 static pressure taps, fitted in the center span position of the wing below the center rotor. The location of the pressure taps along with the contour of the wing profile is presented in figure 4.5c. The pressures were sampled by a Scanivalve ERAD4000 measurement system with a full range of approximately 100 kPa. Based on the spread in the data of repeated measurements, the experimental uncertainty of the static pressures was found to be ±0.0125 C_p.

Rotor array: 2D2C-PIV
For the measurements concerning the span-wise distributed rotor array, the flow over the suction side of the wing is characterized using 2D2C-PIV. For this, the flow was seeded with DEHS tracer particles (τ_p = 2 μs) that were illuminated by an evergreen laser (200 mJ/pulse) in a sheet of 3mm thickness, see figure 4.5a. Illumination was performed at a rate of 15 Hz and the duration of each pulse (pulse width) was Δt = 25 ns. The center of the laser sheet was positioned with an offset dz in span direction (see figure 4.5b) of 12 mm

from center rotor axis to avoid any shadows from the nacelle. Recording was performed by two sCMOS cameras (Imager sCMOS CLHS) placed outside the section at a distance of 0.8 m from the measurement region. The cameras were equipped with an objective of focal length f = 50 mm, set at numerical aperture $f_\#$ = 8. The resulting field of view spans 36 × 24 cm^2 (6 R × 4 R). System synchronization was obtained with a LaVision Programmable timing unit (PTU X) and each measurement comprised of at least 200 recordings for a time duration of 13 s. An overview of the illumination and imaging conditions is presented in table 4.5.

Table 4.5: 2D2C-PIV illumination and imaging conditions.

Seeding type	DEHS
Particle relaxation time τ_p (μs)	2
Illumination	Evergreen (200 mJ/ pulse)
Sheet thickness δz (mm)	3
Pulse width Δt (ns)	25
Repition rate (Hz)	15
Camera type	2 × Imager sCMOS CLHS
Camera resolution	2560 px × 2160 px
Objective focal length f (mm)	50
Numerical aperture $f_\#$	8
Optical magnification M	0.07
Field of view (cm^2)	36 × 24
Number of recordings	200
Image analysis	Cross-correlation (32 px × 32 px, 75% overlap)
Vector pitch (mm)	1.15

The velocity components were inferred by cross-correlation of two recordings, with a window size of 32 px × 32 px and an overlap of 75%. This resulted in a vector resolution of 2.4 mm and a vector spacing of 1.15 mm. The measurement uncertainty for the time-averaged velocity field is determined by the ratio between the relevant velocity fluctuations (magnitude of the standard deviations) and the square root of the number of statistically independent measurements. This results in an uncertainty of 0.01% of the freestream velocity in the majority of the domain, but locally increases to 6% in shear regions of the flow.

Single rotor: Aeroacoustic measurements

Acoustic measurements were performed for the single rotor configuration inside the anechoic chamber. To avoid reflections of acoustic waves in the wind tunnel, the test section walls were fitted with acoustic transparent walls over a 2 m length. The acoustic transmission losses through the walls are 2 dB over the frequency range of interest, and all experimental results were corrected for this. The noise of the rotor is measured using a microphone array consisting of 64 microphones, see figure 4.6. The array was positioned at a distance of 0.7 m from the center of the test section, and aimed towards the suction side of the wing. Simultaneously, ten free-field microphones record the sound from the

pressure side of the wing to investigate the potential of noise shielding. The free-field microphones are positioned at a distance of 2 m from the center of the test section.
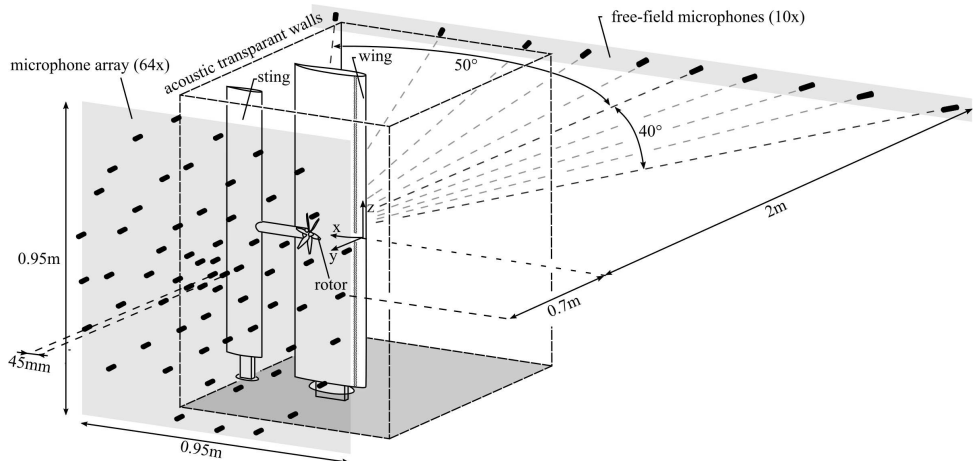

Figure 4.6: 3D schematic of the test section, microphone locations and system of coordinates.

Single rotor: sPIV

The inflow of the single rotor is characterized using stereoscopic Particle Image Velocimetry (sPIV). For this, the acoustic transparent walls were replaced by optical transparent walls. Tracer particles and illumination are identical to that of the 2D2C-PIV setup described above. Recording is performed by two sCMOS cameras (Imager sCMOS CLHS) placed outside the section at a distance of 0.6 m from the center of the measurement region. The camera is equipped with an objective of focal length f = 50 mm, set at numerical aperture $f_\#$ = 8. The resulting field of view spans 19×25 cm^2 ($3\,R \times 4\,R$). System synchronization is obtained with a LaVision Programmable timing unit (PTU X) and each measurement comprises of at least 300 recordings for a time duration of 20 s. An overview of the stereoscopic velocimetry measurement parameters is presented in table 4.6.

The images were processed using an iterative multigrid method [130] with a final interrogation window size of 32px × 32 px and an overlap of 75%. This resulted in a vector resolution of 9.6 mm and a vector spacing of 2.4 mm. The measurement uncertainty for the time-averaged velocity field is determined by the ratio between the relevant velocity fluctuations (magnitude of the standard deviations) and the square root of the number of statistically independent measurements. This results in an uncertainty of 0.0125% of the free-stream velocity in the majority of the domain, but locally increases to 3% in turbulent regions of the flow.

To enable a time-averaged volumetric reconstruction of the velocity field and a surface pressure reconstruction over the wing, the rotor is traversed along the measurement plane, in steps of 10 mm to a maximum displacement of 50 mm ($0.8\,R$) in both positive and negative span-direction.

Table 4.6: sPIV illumination and imaging conditions.

Seeding type	DEHS
Particle relaxation time τ_p (μs)	2
Illumination	Evergreen (200 mJ/ pulse)
Sheet thickness δz (mm)	3
Pulse width Δt (ns)	25
Repition rate (Hz)	15
Camera type	2 × Imager sCMOS CLHS
Camera resolution	2560 px × 2160 px
Stereo angle	35°
Objective focal length f (mm)	50
Numerical aperture $f_\#$	8
Optical magnification M	0.09
Field of view (cm^2)	19 × 25
Number of recordings	300
Image analysis	Cross-correlation (32 px × 32 px, 75% overlap)
Vector pitch (mm)	0.6

4

4.3 EXPERIMENTAL SIMULATION OF TAKE-OFF TRAJECTORY

In the final study of this thesis, the unsteady flow behaviour of the Over-The-Wing rotor system during a reference take-off trajectory is investigated (chapter 9).


Figure 4.7: Outlet of the Open-Jet Facility at Delft University of Technology (left) and experimental setup (right).

4.3.1 Wind Tunnel Facility

The measurements are conducted in the Open-Jet Facility (OJF) at the High-Speed Laboratory at Delft University of Technology. This closed-loop wind tunnel has a large, octagonal outlet of 2.85 m by 2.85 m, that produces a homogeneous jet at speeds between 4 and 35 m/s with 0.5% turbulence intensity. Figure 4.7 shows the outlet of the OJF.

4.3.2 Rotor and wing model

A rotor-wing system is mounted vertically on a Quanser hexapod, see figure 4.8. The hexapod allows for flexibility through the input of time series of the angle of attack. The rotor-wing system is identical to the one introduced in section 4.2.2 and consists of five counter rotating span-wise distributed rotors. The position of the rotor array is fixed at 60% wing-chord with a rotor tip-to-wing clearance of $y_t = 0.27R$.

4.3.3 Lagrangian Particle Tracking

Volumetric velocity measurements cover the spatial domain as illustrated in figure 4.8. The flow is seeded with HFSBs [118] that are illuminated by two LaVision LED Flashlight 300 devices at a distance of 0.6 m from the center of the measurement volume. A tomographic imaging setup is placed at 1.3 m from the model and consists of five high-speed (CMOS) cameras (Photron *Fastcam* SA1.1), equipped with lenses of focal lengths f = 60mm and set at numerical aperture of $f_\#$ = 12. System synchronization is obtained with a LaVision Programmable Timing Unit (PTU 8), and each measurement comprises 5457 recordings for a duration of 1.33 s. An overview of the measurement parameters is presented in table 4.7.
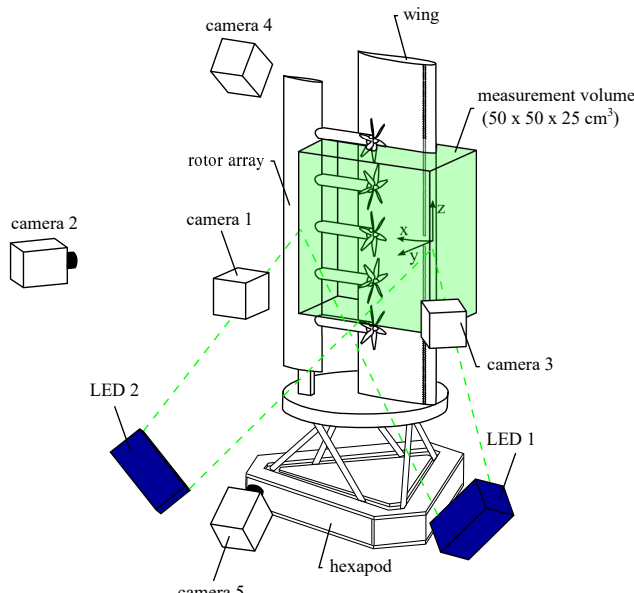
Figure 4.8: 3-D schematic of the experimental apparatus, coordinate system and measurement volume.

Table 4.7: Imaging and recording parameters of the take-off trajectory study.

Seeding type	HFSB
Camera type	5× Photron *Fastcam* SA1.1
Illumination	2× LaVision LED-Flashlight 300
Field of view (Δx, Δy, Δz)	$50 \times 50 \times 25$ cm^3
Repetition rate (Hz)	4000
Objective Focal length f (mm)	60
Numerical Aperture $f_\#$	12
Optical magnification M	0.05
Vector pitch (mm)	9.6

The 3D particle motion analysis is performed with the Shake-The-Box method [131] and delivers approximately 18,000 particle tracks per time step. Data reduction to a Cartesian grid is obtained for each time step, by a sliding average in time over 99 snapshots ($t \approx$ 0.025 s) during which the tracks are gathered in cubic bins of 38 mm size with a 75% overlap factor. Each bin comprises between 200 and 30,000 samples and the resulting velocity field yields a spacing of 9.6 mm between neighboring vectors.

4

III

Results & Discussion

5

Aerodynamic wake interaction in ground proximity

In the initial stages of vertical flight, the rotors produce a significant amount of thrust and will be vertically orientated in close proximity to the ground surface. Consequently, there is an interaction between the rotor's slipstream and the back pressure imposed by ground, which changes the wake organization and performance. The effects of ground proximity flight have been typically well understood for single rotor configurations. Nonetheless, for eVTOL systems, a multitude of rotors closely spaced rotors are used. This results in unexplored aerodynamic effects when hovering in ground effect. More specifically, the role of the rotor separation distance on the three-dimensional flow topology remains poorly understood. Such information is valuable to explain observed differences in mean performance between single- and multi-rotor configurations.

To this purpose, the three-dimensional flow topology of a set of side-by-side rotors is investigated in this chapter. The experimental arrangement as described in section 4.1 is used and velocity field is extracted by making use of Lagrangian Particle Tracking (section 4.1.2). The time-averaged velocimetry results of the side-by-side configuration are compared to the single rotor's flow field in section 5.1. Specific attention is then given to the effect of the rotor-spacing and ground stand-off height in section 5.2. Finally, all results are combined in section 5.3 to create a map of flow regimes for multi-rotors in ground proximity.

5.1 Time-averaged flow fields

When the rotor is operated in close proximity to the ground, the wake expands radially. Figure 5.1 illustrates the difference in the velocity field, by the normalized axial velocity contours w/W_{ind} and 2D velocity vectors scaled by the velocity magnitude, for a single rotor with and without a ground plane. The former is considered at a distance of $2R$ above

This chapter is based on publication [33].

the ground (right plot of figure 5.1). The axial velocities are normalized by the induced velocity of an isolated rotor in hover ($W_{ind} = 14.25$ m/s), which is a constant and used for all results displaying velocity.
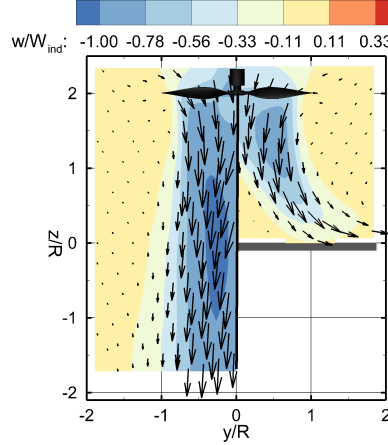
Figure 5.1: Comparison between the normalized time-averaged axial velocity contours and 2D velocity vectors of a single isolated rotor ($y/R < 0$) and a single rotor in ground effect ($y/R > 2$). For the latter, the ground plane is located at $z/R = 0$.

The rotor induces a downward velocity. The non-uniform velocity profile is due to hub wake leading to lower induced velocities along the rotor axis. For the isolated rotor, the slipstream contracts due to the increase in velocity. The maximum axial velocity is found at approximately 2 rotor radii below the rotor disk. Contradictory to this, the wake of a rotor in ground effect expands radially due to the pressure gradient caused by flow stagnation at the ground. Therefore, the axial velocity in the wake of the rotor in ground effect can be significantly lower compared to that of the unbounded rotor. At a certain height this is also noticed at the blade level, which results in an increased local blade angle and an increase in thrust for constant pitch. Also, characteristic for a single rotor in ground effect is the formation of a toroidal flow separation region, or so-called dead air region [73], below the rotor hub near the ground. This is caused by flow stagnation due to the lower velocities in the center of the slipstream and the adverse pressure gradient near the wall.

When a second rotor is introduced, separated for instance by one rotor diameter, a fountain flow emerges. This is illustrated in figure 5.2a, by the axial velocity contours and velocity vectors in the plane through the rotor axes, for $H/R = 2$ and $S/R = 2$. The rotors produce two radial wall jets opposing each other with subsequent stagnation and separation from the wall near the symmetry plane, i.e. $y/R = 0$, where they redirect upward, ultimately generating the fountain pattern. The fountain flow rises above the disk plane in figure 5.2a, also sustained by the favorable pressure gradient determined by the rotor's suction. The wake appears to be mostly re-ingested by rotor 1, and a non-axial inflow condition for rotor 1 is observed. These inflow conditions cause more momentum

to be transferred to the center of the slipstream and reduce the entity of the toroidal separation at the wall from rotor 1. The results in figure 5.2a illustrate that wake interactions in ground proximity occur at larger rotor separations compared to the interactions that take place during hover [168].

(a) $S/R = 2$

(b) $S/R = 1$

(c) $S/R = 0$
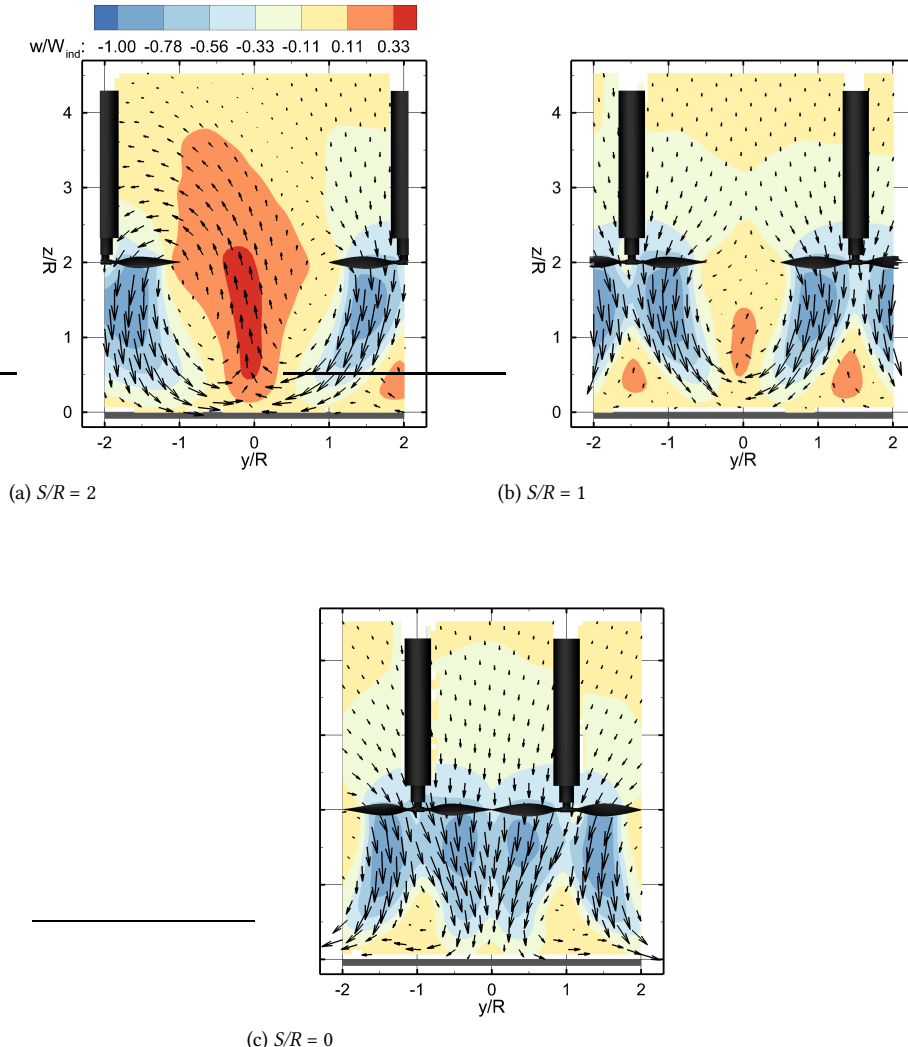
Figure 5.2: Normalized time-averaged axial velocity and 2D velocity vectors in the plane through the rotor axes ($x = 0$) at a rotor height of $H/R = 2$ and different rotor-separations

5.2 Rotor spacing and ground proximity

The primary flow features of the side-by-side rotors are altered by the relative rotor spacing and distance to the ground. The effect of these parameters on the fountain flow, the induced velocity and the Turbulent Kinetic Energy are examined hereafter.

5.2.1 Rotor spacing

By decreasing the lateral distance between the rotors, a stronger interaction between adjacent rotors is expected. However, a reduction of lateral spacing between the rotors is also associated with a decrease in the size of the fountain region for the various test conditions. This is illustrated in figure 5.2 by the axial velocity for $S/R = 1$ (b) and $S/R = 0.05$ (c), remaining a constant height of $H/R = 2$. This can therefore be compared to the case of $S/R = 2$, as presented in figure 5.2a.

Placing the rotors closer together, i.e. $S/R = 1$, means that the radial wall jets collide before they move parallel to the ground plane and more momentum is transferred out-of-plane rather than being re-directed upwards. This condition decreases the extent of the fountain flow which is visible for the plot of $S/R = 1$, see figure 5.2b. The fountain flow, in this case, remains confined between the ground and the height of the rotor disks. Due to flow stagnation of the fountain flow, two recirculation regions are formed between each rotor wake and the tip of the fountain flow. No re-ingestion takes place and a symmetric flow field is produced in which each of the two wakes represent the wake of a single rotor in ground effect. This means that the toroidal separation regions near the ground are also present.

A different mechanism takes place when the rotor spacing is further reduced to $S/R = 0.05$. At this rotor separation distance, there is mutual induction of the individual rotor wakes, caused by the Coandă-effect [68]. This happens before the wake interacts with the ground plane and therefore no fountain is created. A flow field with lower induced velocities between the rotor axis is present due to the increased limitations of radial wake expansion in this region. Around the center of the domain close to the ground, i.e. ($y/R = 0$, $z/R = 0$), the wake moves laterally outwards. A greater effect is observed on the separation regions below the rotor hub, which have now become separated from the ground. The shape of the separation region has been changed and only a single node is observed here. Similar to the case of $S/R = 1$, no wake re-ingestion occurs and a symmetrical mean velocity field is found.

To show the three-dimensional evolution of the streamwise velocity component in the wake, the axial velocity contours w/W_{ind} and 2D velocity vectors are extracted in the (x,y)-plane at varying heights of $z/R = [0.3, 1.0, 1.7]$ and are presented in figure 5.3. At few positions, data are missing due to optical blocking from the rotor's support. Also low particle intensity in the pre-processed images near the ground plane, i.e. $z/R = 0.3$, causes some local data drop-out.

From the axial velocity extracted at the $z/R = 1.7$ plane, the top row of figure 5.3, it is possible to identify the effect on induced velocity near the rotor blades which will have a direct influence on the rotors' performance. For the closest rotor spacing considered, i.e. $S/R = 0.05$, a non-axisymmetric wake profile for each of the two rotors is apparent; in the region between the rotor axes, there is a clear reduction in the axial velocity. Increasing the rotor spacing to $S/R = 1$ prevents any interaction between the two rotor wakes and
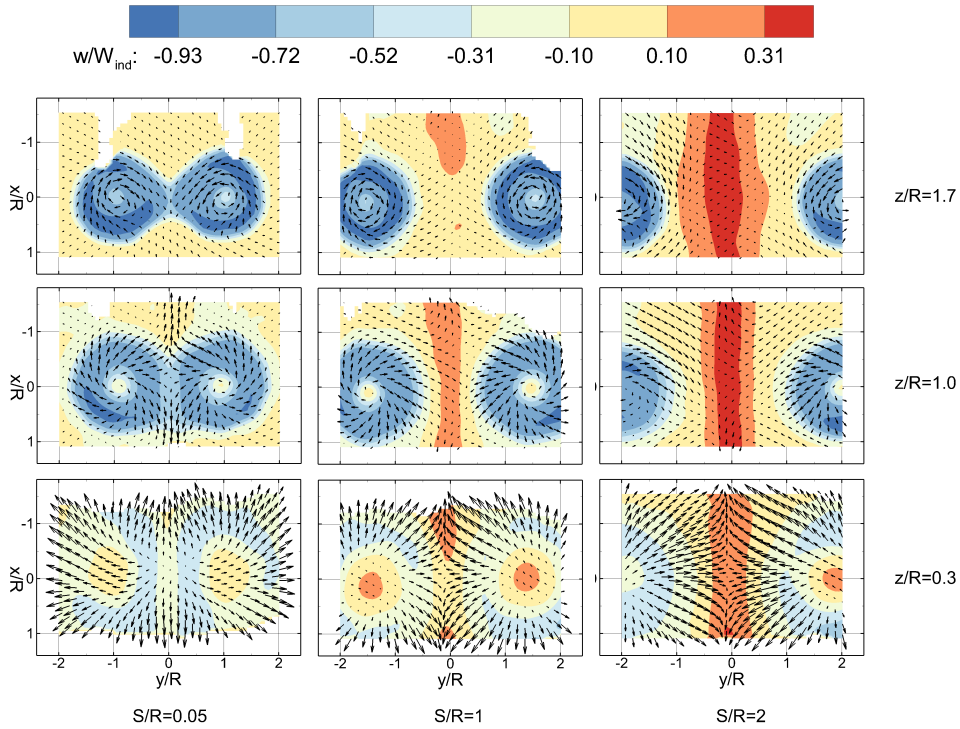
Figure 5.3: Normalized time-averaged axial velocity and 2D velocity vectors extracted at z/R = 0.3, z/R = 1.0 and z/R = 1.7 for the different values of the rotor spacing and H/R = 2.

an axisymmetric induced velocity profile is restored. The fountain flow is also apparent between the two wakes but not affecting the rotor wake itself. When considering the larger rotor separation distance of S/R = 2, top right image of figure 5.3, the similarity of the two individual wakes is removed. Here, in the wake of rotor 1 for S/R = 2, rather than the typical swirl around the axis of rotation, the velocity vectors are directed towards the center of the wake. Moreover, in the flow field surrounding the wake of the rotors, a stronger lateral component of the velocity is visible for S/R = 2, indicated by the larger velocity vectors, when compared to the other rotor separation distances. The velocity vectors are in the direction of a region between the rotors and the fountain flow and are ascribed to a low-pressure region.

Following the wake in streamwise direction to a height of z/R = 1.0, as presented in the middle row of figure 5.3, the radial expansion of the slipstream becomes apparent. This results in stronger mutual induction of the wakes for S/R = 0.05. Moreover, due to the fact that one rotor wake obstructs the wake expansion of the other rotor, there is a strong velocity component in x-direction along y/R = 0, indicated by the large vectors. For S/R = 1, at this height in the wake, the fountain flow becomes apparent between the rotor wakes, see the middle plot of figure 5.3. However, there is little effect on the wake profile. For S/R = 2, the wake of rotor 1 has very weak radial velocities ascribed to the re-ingestion

of the fountain. For this largest rotor spacing, the fountain is also considerably narrower compared to close to the blades, as it was in the plot of z/R = 1.0, see top right of figure 5.3.

Close to the ground plane at z/R = 0.3, the bottom row of figure 5.3, the wake from the rotor has much lower axial velocity caused by the increase in static pressure. The axial velocity is transferred to velocities along the radial component, indicated by the larger vectors, which form the radial wall jets. In the case of S/R = 0.05, a single wall jet is directed outward along the center of the combined wake. For the S/R = 1 and S/R = 2, two radial walls jets are formed. The stagnation line is clearly visible by the positive axial velocity and the collision of the two rotor wall jets. However, for S/R = 1, there are higher axial velocities and lower radial velocities as the wall jet approaches the stagnation line. One should note that the stagnation line between the propellers has a slight offset towards the negative y/R-bound, which can be the cause of a minor misalignment of the setup or small geometric differences between the rotor blades.

Apart from the apparent differences in the mean velocity field, the velocity fluctuations are also influenced by the lateral spacing of the rotors. The unsteady flow behavior is statistically described by the normalized Turbulent Kinetic Energy, $TKE = 0.5\left(\overline{u'^2} + \overline{v'^2} + \overline{w'^2}\right)/U_{tip}^2$. Its spatial distribution is illustrated in figure 5.4.
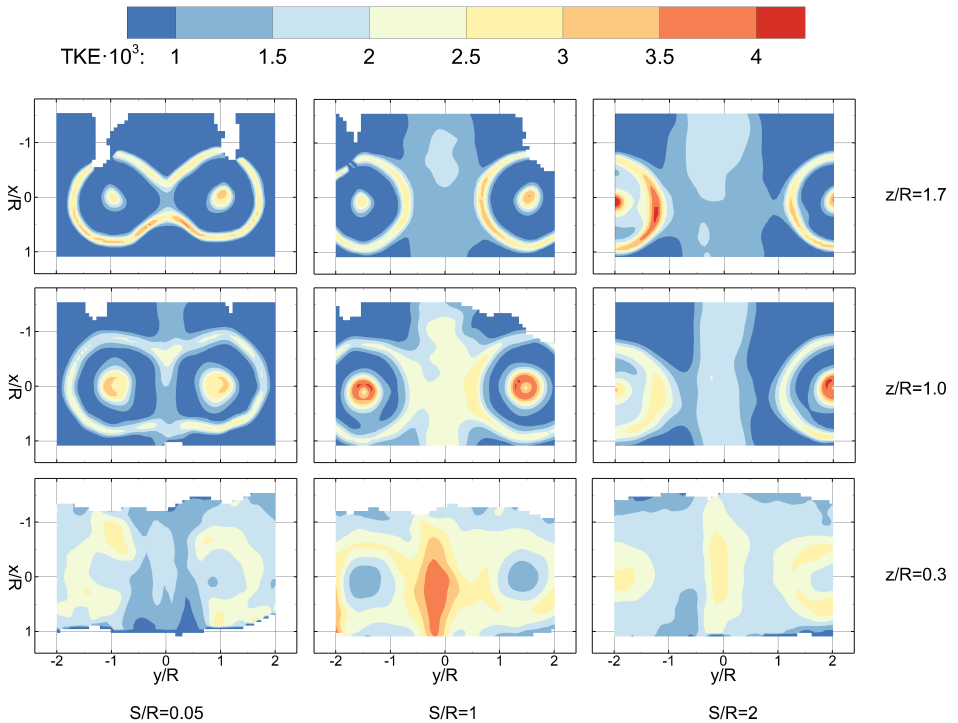

Figure 5.4: Three dimensional distribution of normalized Turbulent Kinetic Energy extracted at z/R = 0.3, z/R = 1.0 and z/R = 1.7 for the different values of the rotors spacing and H/R = 2.

Fluctuations are concentrated along the tip vortex path and hub region, at z/R = 1.7.

Regarding S/R = 0.05, there is a clear mutual induction of the tip vortex path creating a horseshoe-like TKE distribution in this plane. This loss of the structure of the tip vortices between the wakes complies with both experimental [68] and numerical studies [169] on side-by-side rotors out of ground effect. For the case of S/R = 1, the TKE values along the tip vortex path are similar compared to S/R = 0.05 but there are also relatively large values of TKE between the rotors in the fountain flow region. At the largest rotor separation distance of S/R = 2, the effect of flow re-ingestion on the velocity fluctuations becomes notable. Higher TKE levels are found in the wake of rotor 1 which is more severely subject to flow re-ingestion. This is visible along the tip vortex path and in the inner part of the slipstream. Regions of high TKE near the blades can indicate regions of unsteady loading, more pronounced force fluctuations and broadband noise emissions [170].

The magnitude of the TKE decreases gradually for all rotor spacings due to viscous dissipation, which is visible in the z/R = 1.0 plane. Aside from the higher magnitude, overall TKE distribution looks similar to what is observed near the blade. However, the TKE has increased in the fountain flow as well as below the rotor hub due to flow stagnation. Regarding z/R = 0, the overall levels of the TKE have increased but are distributed more uniformly in this plane. TKE between the rotors for S/R = 0.05 is low, while for rotor spacings of S/R = 1 and S/R = 2 there are typically higher values of TKE along the stagnation line. This is especially visible for S/R = 1, where higher TKE values are found near the stagnation line region compared to S/R = 2.

5.2.2 Ground proximity

Proximity to the ground induces an earlier deflection of the slipstream towards the wall jet. A more powerful interaction is therefore expected to occur in the region in between the rotors and with possibly more prominent effects of the fountain flow. Figure 5.5 illustrates such effects when H/R is varied from 1 to 3 maintaining a constant rotor spacing S/R of 2. Hence, the effect of the rotor height can therefore be analyzed by comparing this to figure 5.2a. At the lowest rotor height H/R = 1, there is a clear reduction of the induced velocity compared to the same system at H/R = 2, see figure 5.2. Varying the rotor height does not alter the absolute height of the fountain flow. The re-ingestion of the ejected wall jet appears to be biased towards rotor 1, although the flow induced by both rotors appears to be similar. This can be explained by the fact that the process of wake re-ingestion happens further away from the rotors due to the constant size of the fountain flow. Consequently, the inflow conditions to rotor 1 are undisturbed and axial creating slipstream characteristics that are similar for rotor 1 and rotor 2 and comparable to the single rotor case. Even though the velocities are lower below the rotor disk, the flow does not stagnate here but is rather in the direction towards the fountain. This in turn can be caused by the stronger wall jet at the inner region of the two wakes caused by the sub-atmospheric pressure of the fountain flow [171].

When higher rotor heights are considered, H/R = 3, the fountain flow decreases slightly in size but the process of flow re-ingestion happens closer to the rotor blades compared to what is observed in H/R = 1. This creates a more pronounced non-axial direction of inflow to the rotors. Similar to the case of H/R = 2, see figure 5.2a, an increase in induced velocity in the center of the wake is found. Flow re-ingestion is again biased towards rotor 1 which creates a flow field that is highly asymmetric. Similar to the case of H/R = 2 the

toroidal separation region at the ground is missing for rotor 1 and is visible for rotor 2. A recirculation zone is present between rotor 1 and the fountain at $(y/R, z/R)$ = (-0.75, 1.25).


(a) H/R = 1   (b) H/R = 3
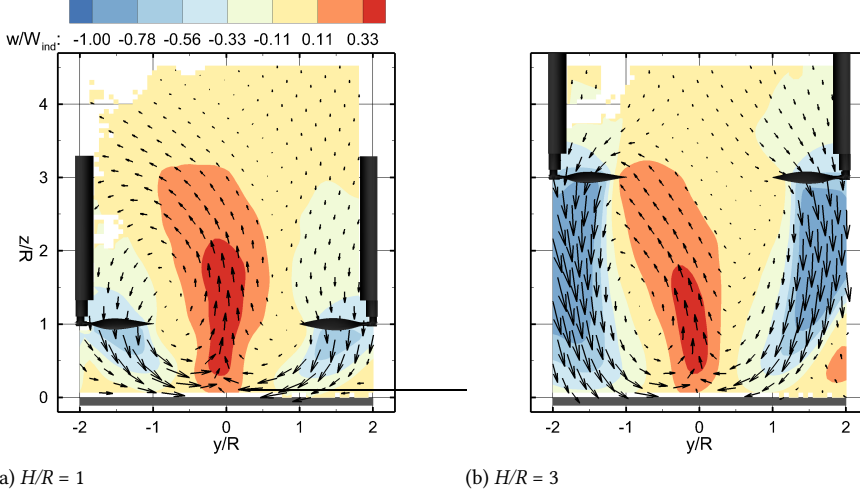
Figure 5.5: Normalized time-averaged axial velocity and 2D velocity vectors in the plane through the rotor axes (x = 0) for S/R = 2.

5.3 Summary of identified flow regimes

The results of sections 5.2.1 and 5.2.2 can be combined to identify different flow regimes. These flow regimes can be placed on a map consisting of rotor spacing along the x-axis and rotor height along the y-axis, as presented in figure 5.6. From a high-level perspective, three different flow patterns have been identified within the parameter space that has been considered. One should note that the exact position of the boundaries between the different flow regimes are unknown and could change for different blade loading.

For close rotor spacing, S/R = 0.05, the wakes of the rotors move towards one another due to the Coandă-effect. Hence, there is a flow attachment of the wakes before they interact with the ground. The combined wake then attaches to the ground and no fountain is generated. The induced velocity below the hub is still low and therefore the flow stagnates here. However, only a single node is created which is separated from the ground. The high momentum at the inner part of the combined wake is also pushed out and flows below the separation regions towards the boundaries of the measurement domain. In this state the induced velocity between the rotor axes is lower compared to the outer part of the combined wake which could result in a stronger influence of the thrust increase but can also offset unsteady loading on the blades. By increasing the rotor spacing, the Coandă-effect is lost and the two separated rotor wakes interact with the ground plane. The wakes expand by the increase in pressure close to the ground and interact over a stagnation line. Over this stagnation line the fountain flow is generated which size is determined by the rotor spacing. If the wakes interact before the wall jet flows parallel to the ground plane,

most of the momentum is pushed out-of-plane. Consequently, for smaller rotor spacings and larger rotor heights, the fountain stays below the rotor disks. The individual wakes therefore strongly resemble the characteristics of a single rotor in ground effect.

At the largest rotor spacing investigated in the current study, the wall jet can develop over the ground plane. The wall jets interact head-on in the saddle point which increases the size of the fountain. This increases the chance for the fountain to rise above the rotor disk which has a dramatic effect on the slipstream characteristics. By re-ingestion the inflow becomes highly non-axial which could increase unsteady loading on the blades and reduce the efficiency. More momentum is transferred to the center of the wake in the re-ingestion state. A consequence of the more uniform velocity distribution is the absence of a toroidal separation region above the ground. Furthermore, there is entrainment of air in the region between the rotors and the fountain which causes re-circulation.
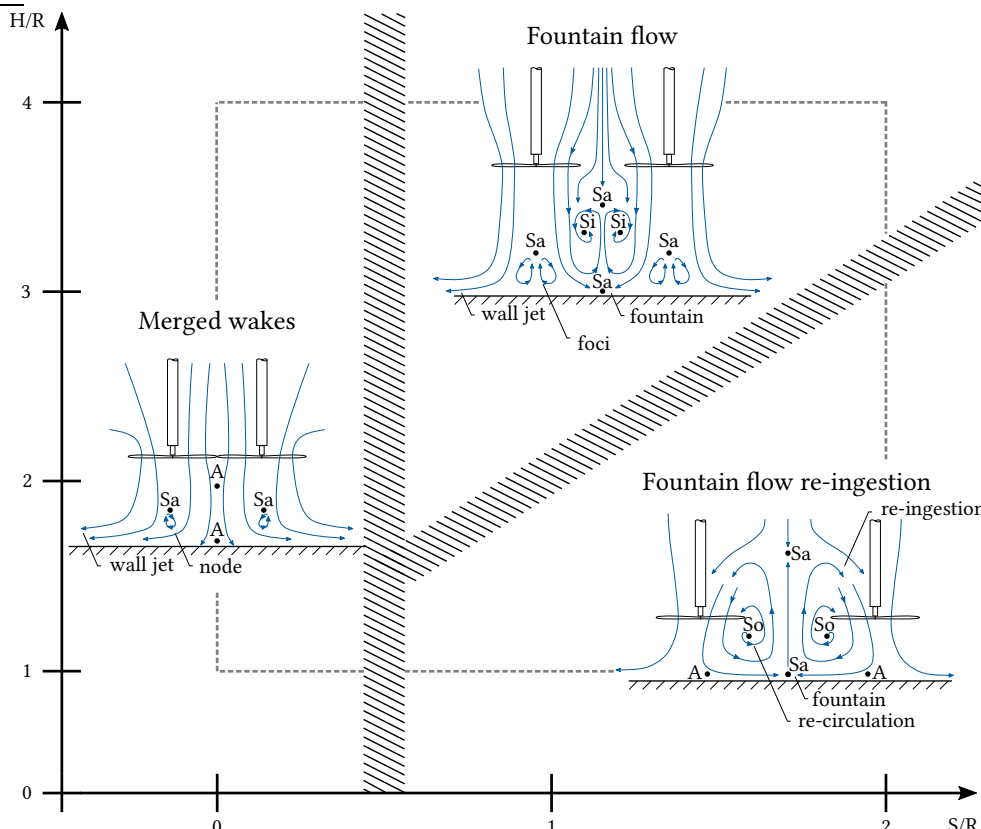

Figure 5.6: Observed flow regimes for a multi-rotor in ground effect as a function of rotor height and rotor spacing with relevant flow features and critical points. Point A indicates a flow attachment point, So is a source, Si is a sink and Sa is a saddle point. The grey dotted box represents the domain of the parameter space that was investigated.

5.4 Conclusion

Different flow regimes for a side-by-side rotor in ground effect depend on a combination of rotor spacing and height over the ground plane. In closely spaced rotors, with a tip-to-tip spacing close to zero, the individual rotor wakes move laterally towards one another by the Coandă effect and form a combined wake before they interact with the ground plane. By increasing the rotor separation to tip-to-tip spacings of at least one rotor radius, an upward flow component known as the fountain flow is created over a line between the two rotors. The height of this fountain flow increases with increasing rotor separation. This can result in the fountain flow to rise above the rotor disk where it is re-ingested into the rotors. However, planar symmetry between the two rotors is lost since the wake re-ingestion is biased towards one of the rotors. In this wake re-ingestion state, the inflow conditions to the rotors are affected which results in an increase in the amount of the unsteadiness near the rotor blades. This could introduce additional thrust fluctuations and broadband noise components. Moreover, wake re-ingestion increases the induced velocity of the rotor, which is especially noticeable in the center of the wake.

Decreasing the rotor height reduces the induced velocity effectively for the multi-rotor system. However, the observed fountain height is indifferent for the rotor stand-off distances observed in this study. At large rotor spacing and small rotor height the fountain flow reaches a sufficient height over the rotor disk to be re-ingested relatively axially. The effects of the flow re-ingestion are most pronounced where the height of the fountain flow is comparable to the height of the rotors.

5

6

Unsteady flow behaviour in ground proximity

I N the mean flow analysis of chapter 5, wake re-ingestion was shown to be biased towards one of the rotors, which violates the symmetry condition between the two rotors. Underlying in the time-averaged velocity field are rich temporal phenomena, in particular for the fountain re-ingestion regime, determining a location switch of re-ingestion from one rotor disk to the other, multiple times during acquisition. As a consequence, varying inflow conditions are imposed on the rotors, adversely affecting the safety, aerodynamic performance and noise emissions. The time scale related to the unsteadiness was two orders of magnitude larger than the blade passing frequency, and therefore the dynamics must be caused by another mechanism. Being able to predict such time scales as a function of the geometrical characteristics of the multi-rotor system allows one to predict the loss of performance and maneuverability issues and relate them to changes in the acoustic footprint.

In this chapter, the unsteady flow behavior of rotors in ground proximity is elucidated. The same rotor setup as used in chapter 5 is considered (described in section 4.1) and Lagrangian Particle Tracking and two-component PIV techniques (see section 4.1.2) are used to characterize the unsteadiness and associated time-scales. This information is then used to find a relation between the spatial-temporal description of the flow dynamics and system parameters of the rotors.

In section 6.1, a description of the flow field is presented and the unsteady phenomenon of re-ingestion is introduced on temporarily resolved data. In section 6.2, a modal analysis by means of Proper Orthogonal Decomposition (POD) is conducted to discuss the spatial and temporal properties of the flow in detail. Results from the modal analysis are then used in section 6.3 to create a low-order representation of the re-ingestion switching mechanism.

This chapter is based on publication [159].

6.1 Flow field analysis

6.1.1 Three-dimensional flow topology

Observations of the unsteady flow behavior of the multi-rotor system in ground proximity, based on the instantaneous and mean flow fields, are described in this chapter. An illustration of the fountain phenomenon is shown in figure 6.1a, for a ground stand-off distance of four radii. Shown are the instantaneous velocity magnitude (blue) and positive axial velocity iso-surfaces (red); the velocity has been normalized by w_{ind} is adopted for all results displaying normalized velocity.
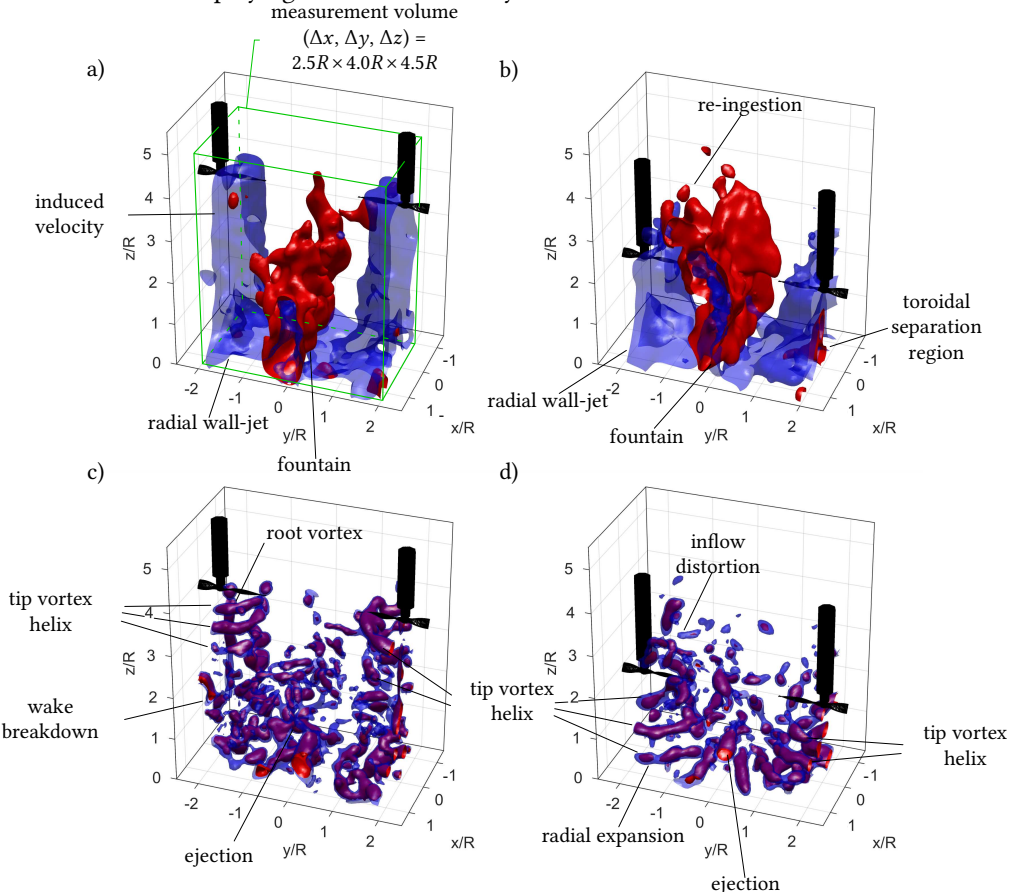
Figure 6.1: a) Iso-surfaces of normalized velocity magnitude V/w_{ind} = 0.5 (blue) and w/w_{ind} = 0.25 (red) for H/R = 4 and b) H/R = 2. c) Iso-surfaces of $\lambda_2 = -60000\,s^2$ (blue) and $\lambda_2 = -90000\,s^2$ (red) for H/R = 4 and d) similar iso-surfaces for H/R = 2. The measurement volume is illustrated by the green box in a).

In figure 6.1a, the rotor slipstreams develop two wall jets that stagnate near the ground plane. The collision of these jets along the stagnation line between the rotors results in the fountain flow, highlighted by the red iso-surfaces, and reaches up to 3 rotor radii in height. When the ground stand-off distance is reduced to two rotor radii, the fountain remains similar in height (figure 6.1b) by the balance between the increase of stagnation

pressure with reduced height (for constant thrust) and the reduced inflow to the rotor by the presence of the ground. In this case, the fountain reaches above the rotor disk and is inclined towards the left-sided rotor 1. Furthermore, the toroidal separation region in the center of the wake has increased, as is particularly visible in the wake of rotor 2 not being affected by a re-ingestion. The rotor wake involves tip/root-vortices of the blades, as well as the blade section wakes. Due to the relatively high-loading in the hover scenario, the tip-vortices are the dominant flow features carried to the fountain where they are ejected from the ground. This is confirmed by computing the λ_2-criterion, which is visualized for both ground stand-off distances in figures 6.1c and 6.1d. In figure 6.1c, the path of the blade tip vortices is clearly visible close to the blade. They are visible for wake ages up to 3-4 rotor revolutions before break down occurs. Even though the helical structure of the wake is lost after this, coherent structures are still present close to the ground and even within the upward fountain flow. A different phenomenon is present in figure 6.1d for $H/R = 2$, where the wake expands before the vortices break down. Consequently, the vorticity is increased by vortex stretching, similar to what is found for a single rotor in ground proximity [69]. This is likely to be the reason why larger vortex structures are present in the fountain for the lower ground stand-off distance. Furthermore, since the fountain reached above the rotor disk, coherent structures get re-ingested into rotor 1 (at the time instant of the instantaneous field in figure 6.1d). Note that the direction of re-ingestion was observed changing back-and-forth from rotor 1 to rotor 2. This re-ingestion switching occurred at a relatively large timescale, in comparison to 1 s acquisition period of the 3D data. In order to further focus on the plane of the fountain switching, we proceed with the 2D dataset for a more detailed analysis of the velocity distribution. The choice to switch to planar velocimetry data is justified by the limited out-of-plane motions in the fountain plume.

6.1.2 Velocity field statistics

The RMS of the axial and lateral velocity fluctuations of the 2D velocity measurements are presented in figure 6.2 for both ground stand-off distances.
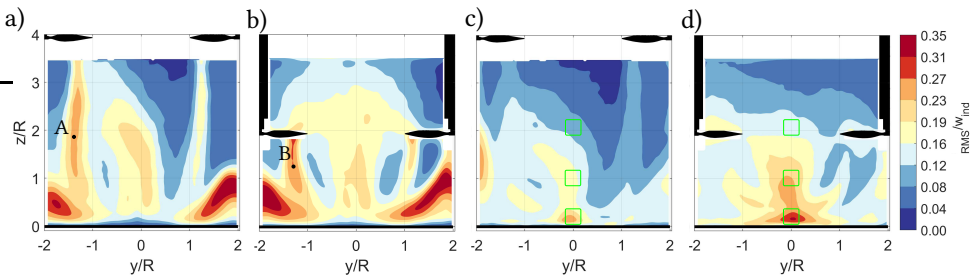
Figure 6.2: RMS of velocity fluctuation in axial direction, for a) $H/R = 2$ and b) $H/R = 4$, and lateral direction, for c) $H/R = 2$ and d) $H/R = 4$. Green rectangles denote the regions where the vectors are extracted for generating figure 6.3.

In the axial direction, the most intense fluctuations are found in the separation regions below each rotor, see figures 6.2a and 6.2b. The fluctuations are also intense along the boundaries of the slipstream, caused by the tip vortices, see points A and B in these fig-

ures. Moreover, the fluctuations are stronger in the slipstream of the rotor that re-ingests the fountain flow, which is expected due to the turbulence ingestion. The strongest fluctuations in the lateral direction are found in the stagnation points near the ground (figures 6.2c and 6.2d). For the lower rotor ground stand-off distance, the fluctuations comprise a larger magnitude and exhibit a larger extent into the fountain flow.

6.1.3 Fountain flow dynamics
In order to examine the relation between the fountain flow unsteadiness and the *BPF*, the pre-multiplied spectrum of the lateral velocity fluctuations is computed, at different heights within the fountain. For the calculation of the spectra, roughly 330,000 samples are collected. These are divided into ensembles of 2^{13} samples and processed using the Welch method (50% overlap) and a Hanning window to reduce any spectral leakage. This results in a frequency resolution of 2.44 Hz (0.015 *BPF*). The pre-multiplied spectra are presented in figure 6.3 for three heights and both ground stand-off distances. All energy spectra are dominated with a broadband hump at lower frequencies compared to the *BPF*. Particularly, in figure 6.3a, which is extracted close to the stagnation point near the ground, the fluctuations are energetic at frequencies one-to-two orders of magnitude lower than the *BPF*. Higher up within the fountain, towards $z/R = 1.0$ and $z/R = 2.2$, figures 6.3b and 6.3c respectively, the energy distribution shifts towards slightly higher frequencies by the increase in turbulent fluctuations after the collision of the two opposing wall-jets. As was discussed in section 6.1, the intensity of the velocity fluctuations increases when re-ingestion takes place (indicated by the arrows in figure 6.3).

6
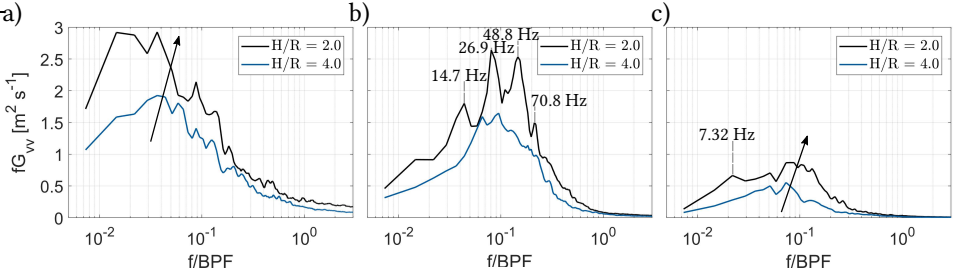
Figure 6.3: Pre-multiplied energy spectra of the lateral velocity fluctuations in the centre of the fountain flow, for $H/R = 2$ and $H/R = 4$, and at heights of a) $z/R = 0.2$, b) $z/R = 1.0$ and c) $z/R = 2.2$.

Furthermore, the spectra corresponding to $H/R = 4$ are relatively smooth in comparison to the spectra from the case of $H/R = 2$. The latter comprises distinct peaks at multitudes of approximately 7 Hz in figure 6.3b, thus indicating that the flow unsteadiness for the $H/R = 2$ case is distinctly different. The occurrence of these spectral peaks are later shown to be related with the re-ingestion switching of the fountain flow.

6.1.4 Re-ingestion switching cycle and timescale
After having shown the occurrence of a low-frequency unsteadiness in the fountain flow structure, the time-resolved flow field will aid in identifying the spatial-temporal dynamics of this unsteadiness. For the case of $H/R = 2$, re-ingestion occurs at certain time instances (recall figure 6.1 and its discussion), while other time instances are characterized by the

absence of re-ingestion. During these latter instances, the fountain can occasionally reach locations significantly higher than the rotors' height. Two sequences in figure 6.4 (top and bottom rows) show these two different scenarios using sliding averaged results. The length of each sequence is 113 ms, corresponding to an approximate frequency of 8.8 Hz, comparable to the frequency at which the dominant flow fluctuations were identified in section 6.2.
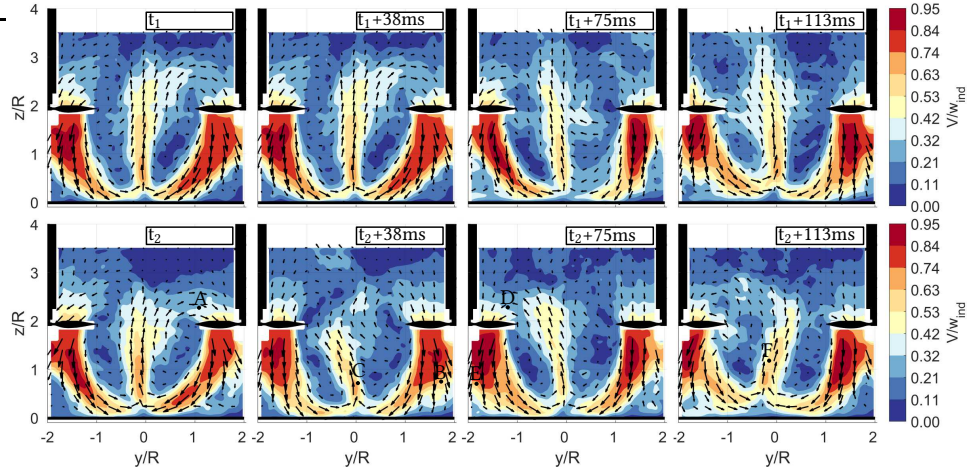
Figure 6.4: Normalized velocity magnitude contours V/w_{ind} and 2D velocity vectors of two time sequences of sliding averages (ensembles of 100 samples/0.25s), with a temporal increment of $dt = 0.0375$s. The top row series is statistically-independent from the bottom one, with $t_2 = t_1 + 1.7$ s.

The top sequence in figure 6.4 starting at t_1 captures a relatively stable fountain flow reaching above the rotor disks. Hence, the phenomenon of fountain flow re-ingestion, by one of the two rotors, is minimal. Contradictory to this is the statistically-independent time sequence starting at t_2, shown at the bottom. In the first frame, the fountain leans towards the right rotor, where re-ingestion takes place at point A. At $t_2 + 38$ ms, this results in an increase in momentum at point B and the fountain directs towards the left rotor, see point C. In the subsequent frame $t_2 + 75$ ms, re-ingestion takes place in point D and more momentum towards the center of the wake is found in point E. Finally, the fountain re-orientates back towards the right rotor, visible in point F. Within a full measurement acquisition period, several similarly looking switching cycles were observed.

The occurrence of the two different flow states described above (fountain flow eruption above the rotor disk and re-ingestion switching) closely resembles a "*bimodal*" behavior of a fountain flow associated with impinging, twin jets [90, 91] and is suggested to be caused by the orientation of vortical structures in the turbulent wall jet [91]. On that note, the re-ingestion switching cycle as illustrated in figure 6.4 (bottom) is not present for each sequence investigated along the measurement. Although not shown here for brevity, intermittent intervals of stable re-ingestion to either rotor are also present. On average, this happens more often for rotor 1 compared to rotor 2, which causes the slight inclination of the fountain to rotor 1 when computing the time-averaged results in chapter 5. Given

the unstable nature of the fountain and the low-Reynolds number regime in which the rotor blades are operated, the bias is expected to be caused by minor discrepancies in the geometrical/performance parameters between the two rotors. Nonetheless, re-ingestion is still seen to switch along the loop presented at the bottom of figure 6.4 during the majority of the acquisition period.

To quantify the re-ingestion switching, a timescale can be assigned for the case of $H/R = 2$. By following a particle trajectory during re-ingestion, the reciprocal of its velocity is integrated along a path s to compute the convective flow-around time. Note that the velocity $V(s)$ and trajectory length s depend on the system parameters of ground stand-off distance H and rotor thrust T. The resultant flow-around time is approximately $T_{conv} \approx 0.1$ s and corresponds to a frequency of $f_{conv} = 1/T_{conv} \approx 10$ Hz. This value is in the same order as the energy content at 7 Hz (and multiples of that) within the spectra of the lateral velocity fluctuations (figure 6.3). Furthermore, the flow-around time is representative of the fountain switching to the other rotor and back, see figure 6.4. Note that the velocity $V(s)$ and trajectory length s depend on the system parameters of ground stand-off distance H and rotor thrust T. Hence, for a given ground stand-off distance, and therefore constant trajectory length s, the convective frequency f_{conv} is expected to increase with an enhancement of the thrust.

Next, the cycle of re-ingestion switching is explored in further detail in sections 6.2 and 6.3, with a modal analysis to identify its underlying spatial-temporal flow structures.

6.2 MODAL DECOMPOSITION OF THE UNSTEADY FLOW FIELD

It has now been established that the fountain flow re-ingestion can cause a dynamic cycle of switching. The goal is now to identify the energetic dynamic features that sustain this cycle. This is achieved through a reduced-order POD analysis. The low-order flow field representation is presented in this chapter, and is used in section 6.3 to formulate a dynamic flow description of the re-ingestion switching cycle.

6.2.1 APPLICATION OF CLASSICAL POD

A POD decomposition is performed using data corresponding to all six acquisition periods for the condition of $H/R = 2$. Thus, the total space-time data consists of $m \approx 65,000$ temporal snapshots, corresponding to roughly 16 s of data. Spatially, the data of the full field-of-view is employed. For the POD, the formulation of [172] is adopted, known as the classical POD review provided by [173]. Considering that the amount of snapshots m exceeds the spatial rank of the data ($n \approx 40,000$), the classical approach is favored so that ensemble averaging in time can be performed, e.g. see [174, 175]. The decomposition deals with the velocity fluctuations only, computed as:

$$\mathbf{u}'(\mathbf{x},t) = \mathbf{u}(\mathbf{x},t) - \overline{\mathbf{u}}(\mathbf{x}), \quad t = t_1, t_2, ..., t_m. \tag{6.1}$$

The velocity fluctuations are decomposed in a set of temporal coefficients, $a_i(t)$, and spatial modes, $\phi_i(\mathbf{x})$, where i is the mode number. A full reconstruction of a single instantaneous field, using all n POD modes, is then generated through:

$$\mathbf{u}'(\mathbf{x},t) = \sum_{i=1}^{n} a_i(t)\phi_i(\mathbf{x}). \tag{6.2}$$

In order to solve for the POD modes and temporal coefficients, an eigenvalue problem is constructed with the spatial modes $\phi_i(\mathbf{x})$ defined as the eigenvectors of the covariance matrix, or two-point correlation tensor, $\mathbf{R}$, following:

$$\mathbf{R}\phi_i = \lambda_i \phi_i, \quad \lambda_1 \geq \dots \geq \lambda_n. \tag{6.3}$$

The covariance matrix $\mathbf{R}$ is generated using ensemble-averaging in time, following:

$$\mathbf{R} = \langle \mathbf{u}'(\mathbf{x},t)\,\mathbf{u}'\left(\mathbf{x}'',t\right)\rangle, \tag{6.4}$$

where the double-prime is used to denote separations in space. In equation 6.3, λ_i denotes an ordered sequence of eigenvalues. By indicating the total resolved kinetic energy with E, equal to the sum of the eigenvalues, the relative energy fraction of each spatial mode ϕ_i is equal to:

$$\widetilde{\lambda}_i = \frac{\lambda_i}{\sum_{k=1}^{n} \lambda_k} = \frac{\lambda_i}{E}. \tag{6.5}$$

Finally, the temporal coefficients $a_i(t)$ can be computed by projecting the original data on the spatial modes, according to:

$$a_i(t) = \int \mathbf{u}'(\mathbf{x},t)\,\phi_i(\mathbf{x})\,\mathrm{d}\mathbf{x}. \tag{6.6}$$

6.2.2 ENERGY DISTRIBUTION AND SPATIAL POD MODE SHAPES

Data reduction using the spatial POD ranks the modes according to their relative energy contribution to the total resolved energy in the flow domain. Figure 6.5 presents the relative energy fraction and cumulative energy for each mode. The system is relatively low-dimensional, given that 70% of the total resolved energy is captured in less than 100 modes. The energy fraction of the first five modes are 7.0%, 4.8%, 4.3%, 3.9% and 3.3%, respectively.
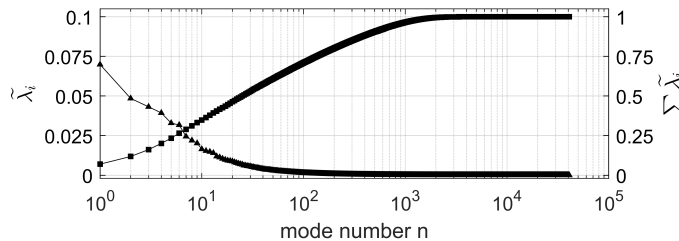
Figure 6.5: Energy fraction and cumulative energy as function of POD mode number n.

Figure 6.6 presents the first five POD mode shapes, split by their lateral and axial velocities. A sketch is included in the most right column to show the contribution of each mode to the time-averaged flow field by highlighting the primary flow features. We now proceed with a brief discussion of each mode.

In the discussion of figure 6.4 (top), an intermittent appearance of the fountain rising above the rotor disk was identified. Since no re-ingestion takes place in that case, the flow
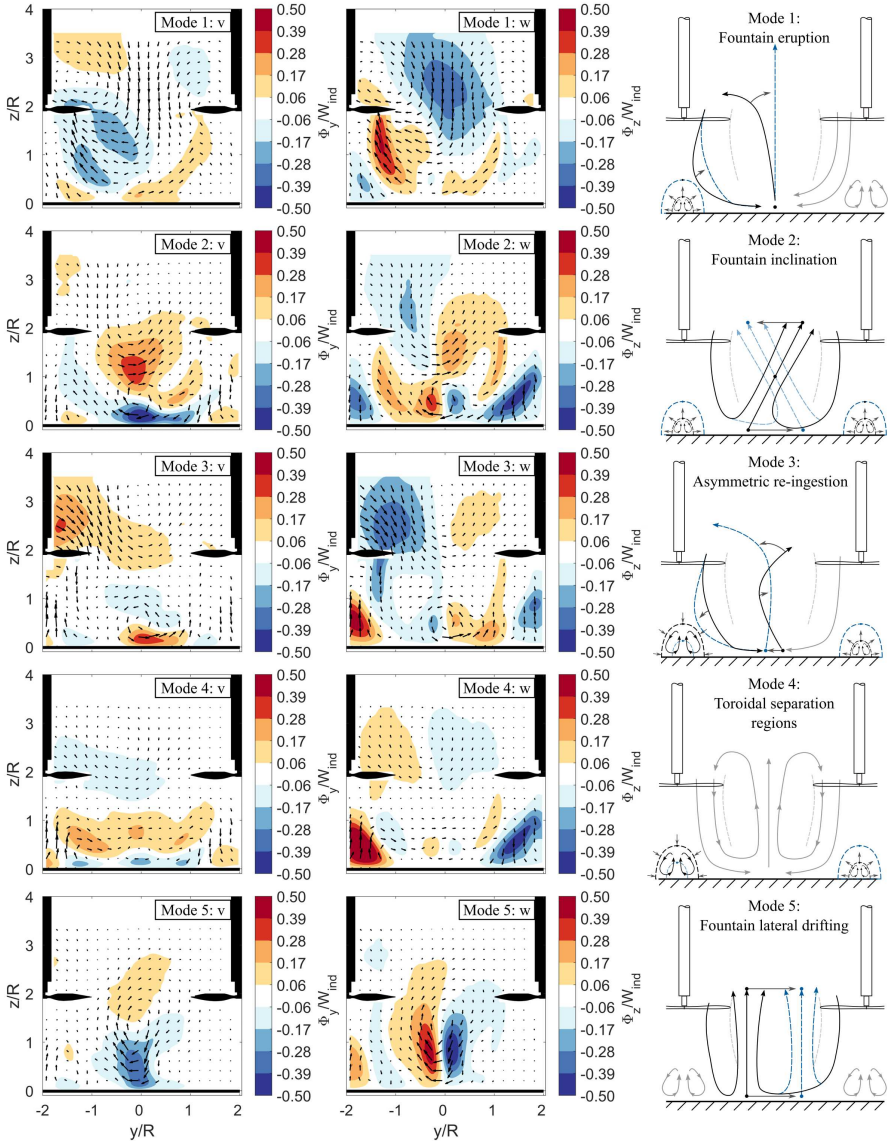
Figure 6.6: POD mode shapes (v (left column) and w (middle column) component). The right column shows the contribution of the mode to the flow field when the time coefficient decays from positive unity (black streamlines) to negative unity (blue streamlines).

field is relatively symmetric with a large vertical velocity magnitude between/above the rotors. Mode 1 in figure 6.6 is representative of this flow state. A sideways inclination of the fountain is captured by mode 2 and predominantly shows activity below the rotor disk. When the associated temporal coefficient would decrease from a positive value to a

negative one, the fountain will change inclination from the left rotor to the right. There is also an activity in the axial direction near the wall, showing a relation with the two toroidal separation regions. These two regions simultaneously grow/shrink in size. Similar to mode 1, mode 3 comprises an asymmetric mode shape. Here, most of the energy is contained at the inflow and toroidal separation region of rotor 1. Again, as for mode 2, we see an increase of the separation regions below rotor 1 when re-ingestion goes to the other rotor. Mode 4 contains most of the activity in the axial motions within the separation regions. These motions have opposite sign for the regions associated with rotors 1 and 2, e.g., one separation region grows while the other one shrinks, and vice versa. Finally, mode 5 represents a lateral drifting of the entire fountain column, where a positive time coefficient is associated with the fountain being closer to the left rotor. When time is retained in the analysis, the zero-mean temporal coefficient of each POD mode signifies the degree of activity of the mode, during the measurement time. Temporal coefficients are analysed next to show the dynamic behaviour and mode coupling.

6.2.3 Temporal POD coefficients

The temporal coefficients are inferred from projecting the raw data back on the POD modes. Recall that 6 different acquisition periods were used to compute the POD modes. Hence, the corresponding time coefficient of each mode consist of 6 independent segments, which are presented in figures 6.7a and 6.7b for modes 1 and 2, respectively.
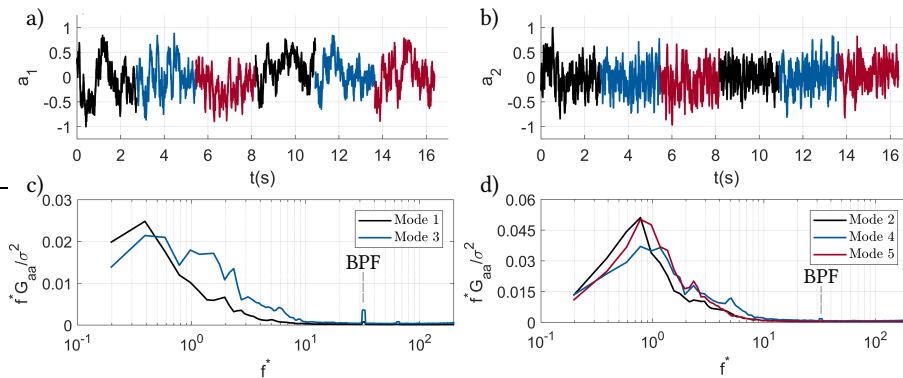
Figure 6.7: Temporal POD coefficient of a) mode 1, a_1, and b) mode 2, a_2. c) Pre-multiplied energy spectra of the temporal coefficients of modes 1 and 3, and d) modes 2, 4 and 5. The frequency has been normalized by the convective frequency, i.e. $f^* = f/f_{conv}$.

A simple visual inspection of the a_1 and a_2 time series in figures 6.7a and 6.7b already reveals that mode 1 resides at a lower frequency in comparison to mode 2. This is further explored by computing the energy spectra of the temporal mode coefficients. Pre-multiplied energy spectra, normalized with the resolved energy per mode, are shown in figure 6.7c for both modes 1 and 3, and in figure 6.7d for modes 2, 4 and 5. All spectra were computed with ensemble averaging each of the 6 segments of data, of which each segment itself was first split into bins of 2^{11} samples long (yielding a spectral resolution of $df \approx 2$ Hz). Note that the abscissa has been normalized with the convective frequency, thus $f^* = f/f_{conv}$ (recall section 6.1).

Overall, the energy content resides at low frequencies compared to the *BPF*, as was already noted in the spectra of the raw, lateral velocity fluctuations presented in figure 6.3. Most interestingly, modes 2, 4 and 5 comprise a similar spectral distribution, concentrated around the convective frequency. This indicates that these modes are linked to the flow recirculation cycle. The coupling between these three modes is investigated in section 6.3 through a more detailed analysis of the temporal coefficients.

6.3 Dynamic flow description

Having identified the re-ingestion switching in section 6.1, here a physical description of this cycle and its underlying features will be presented. This will start by an analysis on the coupling between the modes that describe this mechanism.

6.3.1 Modal coupling

The temporal coupling between modes 2, 4 and 5 is first confirmed by plotting a magnitude of the linear coherence for every combination of two temporal mode coefficients in the range $n = 1$ to 6. First, the linear coherence was computed between temporal coefficient a_i and a_j, following:

$$\gamma^2(f) = \frac{|G_{a_i a_j}(f)|^2}{G_{a_i a_i}(f) G_{a_j a_j}(f)} \tag{6.7}$$

Here $G_{a_i a_i}(f)$ is the energy spectrum of temporal coefficient $a_i(t)$, and $G_{a_i a_j}(f)$ is the cross-spectrum of mode coefficients $a_i(t)$ and $a_j(t)$. The spectral coherence is calculated using windows of 2^{11} samples, similar to how the energy spectra of figure 6.7 were generated. The coherence indicates the fraction of energy corresponding to the coherent fluctuations in $a_i(t)$ and $a_j(t)$; note that γ^2 is a normalized quantity, thus $0 \leq \gamma^2 \leq 1$. When averaging γ^2 over a frequency domain of interest, that is the rate of the re-ingestion switching loop ($0.75 f_{conv} \leq f \leq 1.25 f_{conv}$), the resultant magnitude $\overline{\gamma^2}$ is obtained and its amplitude is plotted in figure 6.8. Here, coherence values between 0.3 and 0.5 are found across the convective frequency domain for the coupling between modes 2, 4 and 5. The coherence-magnitudes between the other mode combinations remain below 0.25.
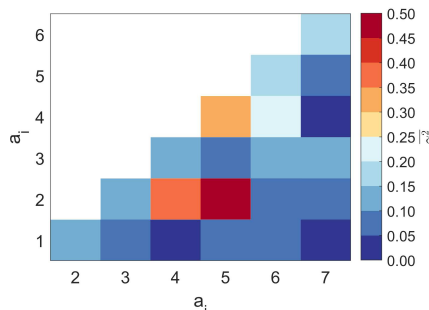

Figure 6.8: Coherence magnitude $\overline{\gamma^2}$ for combinations of temporal mode coefficients, taken as the average coherence value over $0.75 f_{conv} \leq f \leq 1.25 f_{conv}$.

The relations between modes 2, 4 and 5 is further examined in the time domain by computing the cross-correlation between each of the temporal coefficients of these modes. The results in figure 6.9 show a correlation and anti-correlation peak in the proximity of a lag of $\tau = 0$ s. The zoomed-in plot of figure 6.9 reveals a similar shape of the cross-correlation signal for each of the three mode combinations. First of all, this is characterized by a correlation value of approximately 0.3 at a positive lag, indicated by τ_i. Secondly, by the orthogonality definition in the modal decomposition, a zero correlation value for $\tau = 0$ s is found. Finally, a weaker but present anti-correlation value is visible at a negative lag, i.e. $\tau < 0$.
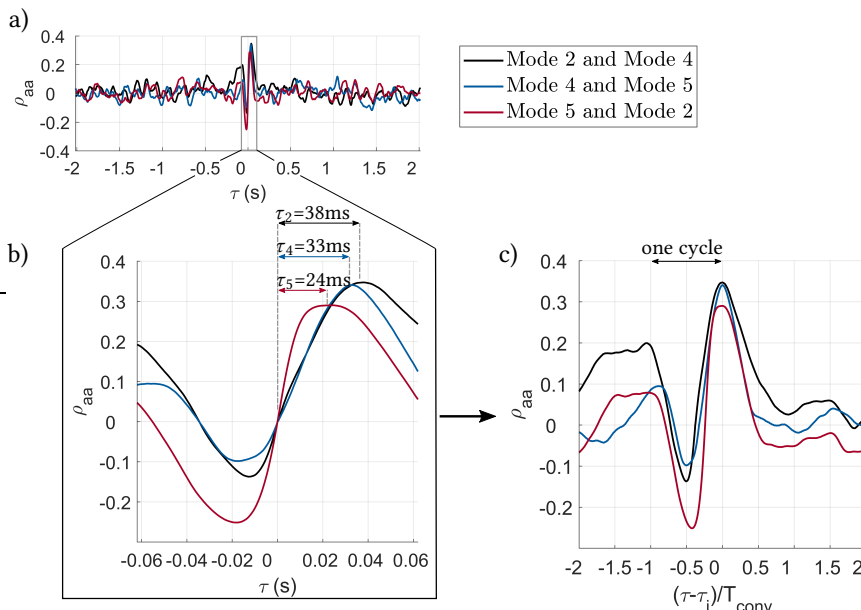
Figure 6.9: a) Overview and b) zoomed-in plot of the temporal cross-correlation coefficient, and corresponding lags for modes 2, 4 and 5. c) Same as a) and b) but subtraction of lags in b) and normalization of lag τ by T_{conv}.

The sum of the lags τ_i, effectively creating a loop from mode 2 back to 2 while passing modes 4 and 5, closely resembles the flow-around time introduced in section 6.1, i.e. $\sum \tau_i = 94$ ms $\approx T_{conv}$. Hence, these modes represent successive, energetic events that occur along the re-ingestion cycle. This apparent cyclic behavior is also confirmed by translation of the cross-correlation signals. By subtracting the lag τ_i from figure 6.9b and normalizing τ by the flow-around time T_{conv} (resulting in figure 6.9c). The anti-correlation of each of the mode combinations is now shifted towards a value of 0.5. Moreover, a second positive correlation peak also becomes apparent for a lag value of -1, indicating similar behavior between the modes which is a complete cycle ahead of the dominant correlation peak. The physical interpretation of the combination of modes 2, 4 and 5 and the meaning of their relative lag τ_i will become clear from a low-order reconstruction presented next.

6.3.2 Low-order reconstruction

The reduced-order flow with its energetic features will allow for a description of dynamic flow features that are part in establishing the cycle of re-ingestion switching. The coupling between these modes is reconstructed using a pseudo time coefficient b_i, based on a harmonic wave of frequency f_{conv}, over a time interval of $0 \leq t \leq 1.75 T_{conv}$, following:

$$b_i = \sin(2\pi f_{conv} t + \psi_i), \quad 0 \leq t \leq 1.75 T_{conv} \tag{6.8}$$

Here the relative phase offset ψ_i between the time coefficients b_i is based on the sum of the cross-correlation lag τ_i between the modes:

$$\psi_i = 2\pi f_{conv} \sum_i \tau_i, \quad i \in \{2, 4, 5\} \tag{6.9}$$

Figure 6.10 presents the adapted time coefficients b_i computed from equation figure 6.8. The original temporal coefficients a_i, derived directly from the time-resolved velocity field, have a different shape than what is presented in figure 6.10. However, the purpose of using the pseudo time coefficients b_i is to show how the modes statistically combine during the flow re-ingestion cycle.
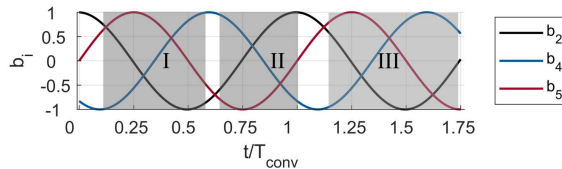
Figure 6.10: Pseudo time coefficients b_i used for the low-order reconstruction. Intervals I, II and III indicate the time domains for velocity field-reconstructions in figure 6.11a, b and c, respectively.

Sticking to the temporal simplification of harmonic waves, the velocity field can be reconstructed by the sum of the spatial modes 2, 4 and 5, multiplied by their corresponding time coefficient b_i, such that:

$$\widehat{\mathbf{u}}(\mathbf{x}, t) = \overline{\mathbf{u}}(\mathbf{x}) + \sum_i b_i(t) \phi_i(\mathbf{x}), \quad i \in \{2, 4, 5\} \tag{6.10}$$

By examining the reconstructed velocity field $\widehat{\mathbf{u}}$, three successive events can be identified within the trajectory of re-ingestion. These events are investigated independently by the definition of spatial and temporal subdomains in the reconstructed velocity field $\widehat{\mathbf{u}}$, denoted by I, II and III. These time interval are highlighted by the grey zones in figure 6.10. The spatial subdomains of I, II and III are based on a trajectory of re-ingestion to rotor 1, which is split-up into three parts. These spatial subdomains, alongside the corresponding time series of the reconstructed velocity field $\widehat{\mathbf{u}}$, are presented in figure 6.11a, b and c.

The three sequential events of figure 6.11a, b and c present the core mechanism of the flapping of the fountain and the re-ingestion switching. Subdomain I, illustrated in figure 6.11a, shows three successive snapshots. The first of which, at $t/T_{conv} = 0.11$, presents the emerging fountain from the ground with an inclination towards the left. The fountain is then convected upwards and re-ingested into rotor 1 in the final snapshot at $t/T_{conv} = 0.58$.
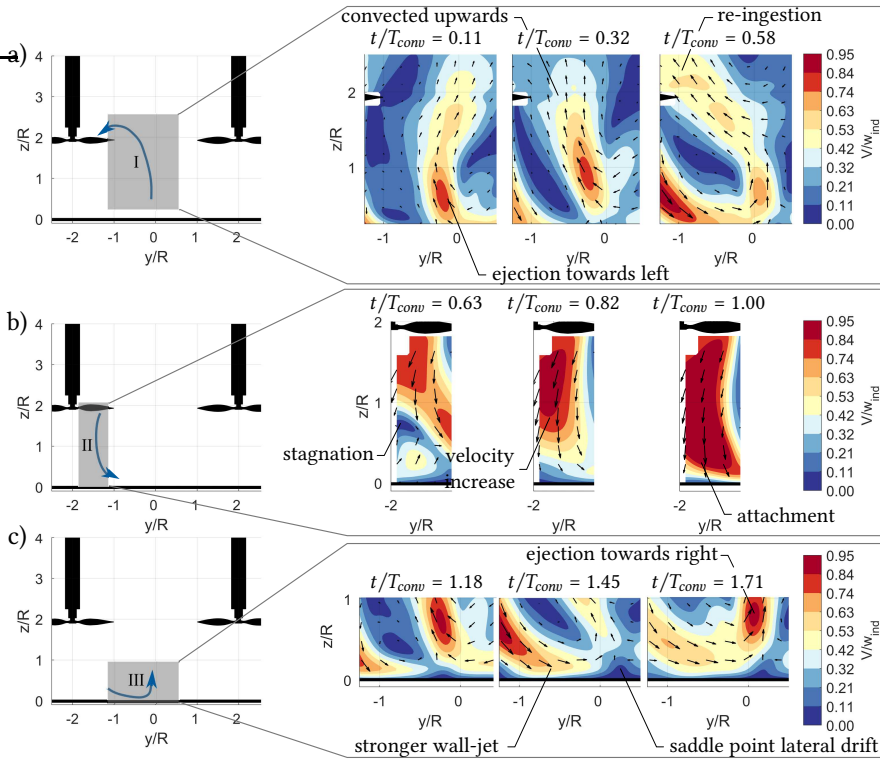
Figure 6.11: Normalized velocity magnitude contours V/w_{ind} of the reconstructed velocity field $\hat{u}$, visualized along the trajectory of re-ingestion to highlight successive critical events. a) Convection of ejected structures to the inflow of rotor 1, b) dynamic pressure increase in the wake and c) lateral drifting of the saddle point. The left plot in (a,b,c) illustrates the spatial domain, based on the trajectory of re-ingestion (blue arrow), corresponding to the time intervals of figure 6.10.

After re-ingestion, the momentum in the slipstream increases, as shown in figure 6.11b. Stagnation in the center of the slipstream, as indicated in the left snapshot, is removed and an attachment of the wake to the ground positions itself laterally below the rotor axis, at $t/T_{conv} = 1.00$. With more lateral momentum in the wall jet, the foot of the fountain drifts towards the right, see figure 6.11c. After this, ejection from the ground is inclined towards the right rotor, and the cycle is repeated in mirrored orientation. Each of the three events in figure 6.11 also resembles the results of the time-resolved flow field analysis in figure 6.4.

One should note that, by the bias of the time-averaged flow field, the cycle of re-ingestion towards the right rotor is less pronounced. However, the same dynamic features are present. Moreover, as noted in section 6.1, intervals of stable re-ingestion to either rotor are also found, which means that re-ingestion does not switch after every flow-around cycle. During these intervals, the stronger wall-jet is not able to push the foot of the fountain far enough towards the other rotor for the switch to occur. For completeness, the re-ingestion switching cycle, along with the corresponding (statistical) delays between

the events, are schematically represented in figure 6.12.

In the schematic of the re-ingestion loop of figure 6.12, the first three events show the observations as seen in figure 6.11a and b. In the fourth event of figure 6.12, the fountain is seen to drift towards the right, as seen by the middle snapshot in figure 6.11c. This completes the loop after a time delay of T_{conv} from the first event. After this follow two possibilities: Either the cycle is repeated with the same orientation but with a more pronounced inclination of the fountain, or the stagnation point has drifted far enough to the subsequent rotor to allow the re-ingestion to switch, effectively repeating the loop in mirrored orientation.
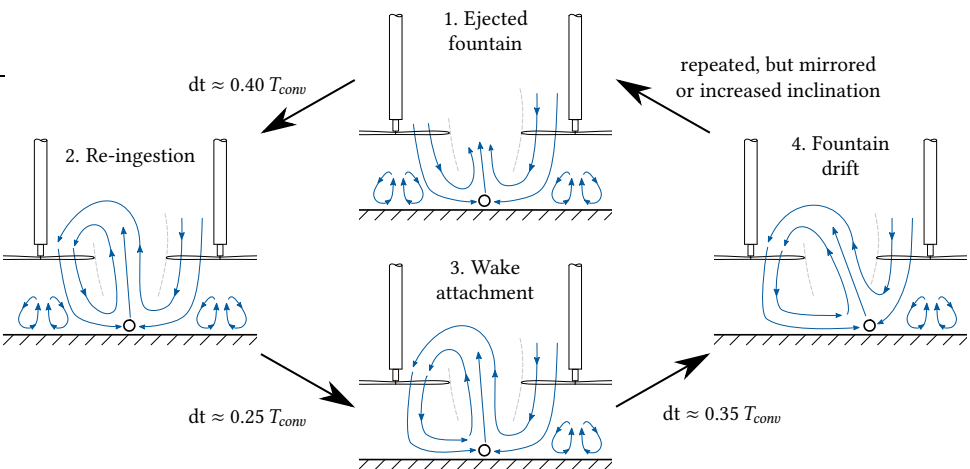
Figure 6.12: Schematic representation of events during the re-ingestion of the fountain column.

6.4 Conclusion

Coherent structures are shown to be ejected from the ground in the fountain produced by the two-rotor system in ground proximity. For lower ground stand-off distances, these structures rise above the rotor disks where they are re-ingested into one of the two rotors. During the re-ingestion, velocity fluctuations are increased in the fountain, resulting in more pronounced side-by-side drifting of the column. These dynamics are observed at an intermittent frequency, which is related to the convective frequency of the re-ingestion loop. Consequently, this intermittent frequency depends on the system parameters (ground stand-off distance and rotor thrust) through the height of the fountain and its characteristic velocity.

Different dynamic features of fountain inclination, toroidal separation regions and fountain lateral drifting are returned as individual POD modes and responsible for establishing the cycle of re-ingestion switching. These POD modes are coupled with a statistical delay. A reconstruction with only the few relevant modes shows that when the fountain is inclined towards one of the rotors, a non-axial inflow condition is created in which more momentum is transferred to the center of the rotor slipstream. Consequently, the wake does not separate in the center of the wake close to the ground but attaches to the wall.

With more lateral momentum in the wall jet, the fountain drifts towards the subsequent rotor. After this, the re-ingestion either switches towards the other rotor, or re-ingestion is maintained to the same rotor with a shallower angle.

A second regime of the fountain is also present along certain time intervals, with reduced lateral fluctuations. Here, the fountain emerges vertically from the ground and re-ingestion is minimized. This apparent bimodal behavior is similar to observations on twin impinging jets, indicating a relationship with the orientation of the coherent structures in the turbulent wall jet.

6

7

Aero-propulsive performance of Over-The-Wing propulsion

After the initial stages of take-off, which has been the topic of chapters 5 and 6, the rotors will hover without any effect of the ground surface. For tilt-wing vehicles, the hover phase is quickly followed by a transition phase, in which the dominant lift force gradually changes from propulsive thrust to the wing's circulation. In this part of the flight envelope, the operating conditions are characterized by low advance ratios and high angles of attack, determining wings operating close to stall. This marks a regime that is radically different from traditional propeller-wing aerodynamic studies. For the Over-The-Wing propulsion system in particular, the effect of a high angle of attack on the aerodynamic interactions and aero-propulsive performance is unknown. As a consequence, design guidelines for Over-The-Wing propulsion at incidence are missing in the public domain.

The formulation of such guidelines requires low-fidelity predictive tools to efficiently vary parameters related to the geometry and aerodynamic performance of the rotor and wing of these systems. Existing low-fidelity tools for integrated propulsion systems [32, 93, 176–178] typically employ iterative schemes to include the coupling between propulsors and lifting surfaces. Although such methods are computationally efficient, the iteration scheme obscures the impact of the dominant design parameters.

In the current chapter, a semi-analytical model to study and predict aerodynamic interactions of OTW propulsion is formulated, with a focus on the effect of the system's angle of attack and the interpretability of the final expression. The thrust-lift interactions are parameterized as a function of the geometric and operating parameters of the rotor-array and wing, and, by employing a single-pass strategy, such design properties appear explicitly in the formulation. Wind tunnel experiments (described in section 4.2) provide insight into the flow topology of OTW propulsion and its interaction with the lifting surface, and

This chapter is based on publication [160].

yield data to validate the model. This chapter is organized as follows. In section 7.1, a hypothesis of the dominant rotor-wing aerodynamic interactions is introduced from which the aero-propulsive model is derived. The general flow features of the rotor-wing system are then introduced from experimental velocimetry and pressure orifices data in section 7.2. Finally, in section 7.3, the model performance trends are analyzed and compared to integral loading data.

7.1 Model description

A model is proposed for describing the thrust and lift performance of an Over-The-Wing propulsion system. Thrust force T is here defined as the integral loading over the rotor disk, acting parallel to the rotor axis. Lift force L is defined as the force perpendicular to the flow direction, generated by the wing only. These two forces are both schematically illustrated in figure 7.1, and are modeled by adopting the superposition principle of the wing and rotors-induced effects. The effect of the rotor induction on the wing's drag is not included in the aero-propulsive model.
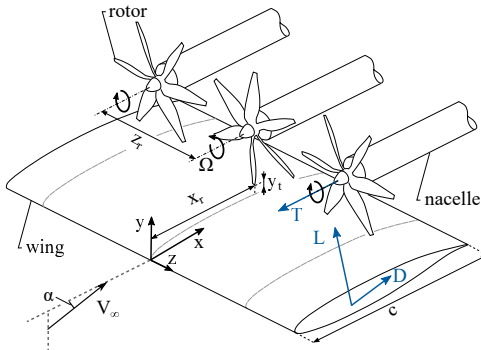
Figure 7.1: Schematic representation of Over-The-Wing propulsion with relevant system parameters and definition of aero-propulsive forces.

The modeling approach itself first considers the wing's influence on the rotor system. A prediction of the rotor-array thrust is obtained by taking the flow pattern over the isolated wing into account, resulting in an effective advance ratio that is combined with the isolated rotor performance trend ($C_{T,iso}$-J). Secondly, the predicted rotor thrust is used to generate the flow properties inside the rotor-array's streamtube. Finally, the influence of the rotor-array on the wing's lift force is considered. The lift force is obtained from a formulation that includes the lift of the isolated wing, with in addition the changes induced by the rotor-induced flow in proximity to the suction side of the wing. Hence, a low-order model of aero-propulsive forces is obtained by considering a one-way rotor-array–wing interaction. To enhance the interpretability of the formulation, the modelling approach is not advanced using an iterative procedure of rotor-wing interaction effects. A schematic illustration of the model's flow diagram and outline of this chapter is presented in figure 7.2. Here, the output is the system performance in terms of the installed rotor thrust coefficient (C_T) and wing lift coefficient (c_l). For this, the model requires an advance ratio J and system angle of attack α as well as the geometric parameters of the rotor-wing sys-
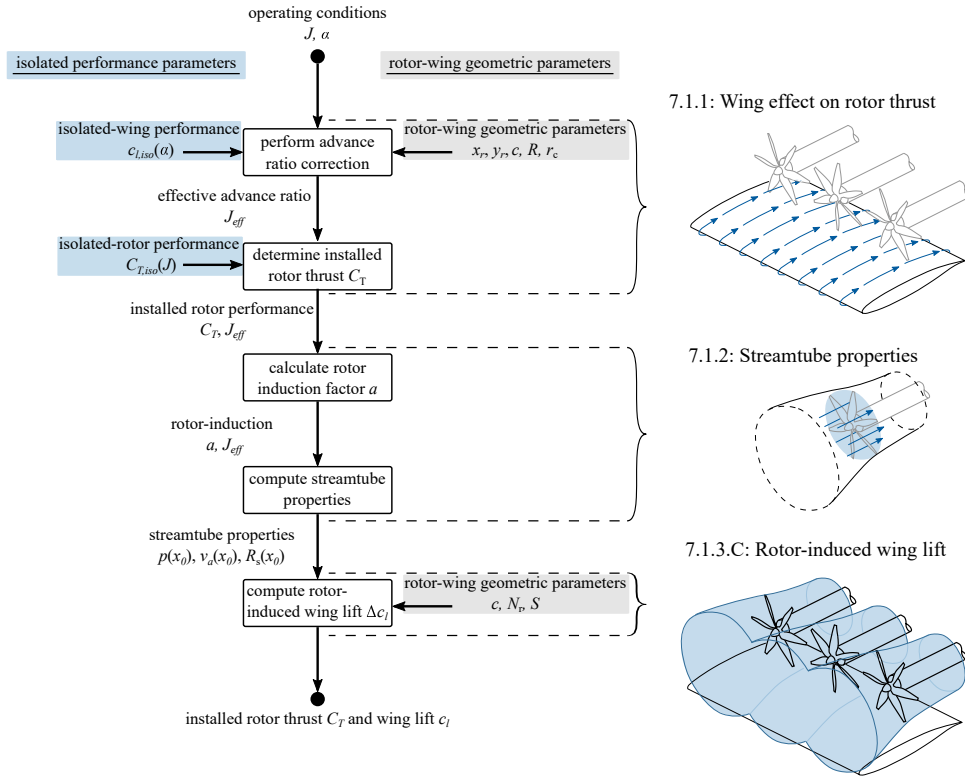
Figure 7.2: Flow diagram of the aero-propulsive model.

tem. In addition, aerodynamic performance characteristics of the *isolated* wing and rotors are used. The wing's aerodynamic performance comes in through the lift coefficient as a function of the angle-of-attack, while the isolated rotor's performance is included through a thrust coefficient as a function of the advance ratio.

7.1.1 WING EFFECT ON ROTOR THRUST

When neglecting stall on the rotor blades, which is generally valid for the vehicle's design conditions, the thrust coefficient C_T exhibits a linear dependence on the advance ratio for fixed-pitch rotors. The slope $\frac{\mathrm{d}C_T}{\mathrm{d}J}$ and base $C_{T,h}$ of this relation is specific for each rotor design. Since the thrust of the isolated rotor is often known a priori, or can be computed with relative ease, these are defined as performance variables equation 7.1.

$$C_T = \frac{\mathrm{d}C_T}{\mathrm{d}J}J_{eff} + C_{T,h} \tag{7.1}$$

Here C_T is the thrust coefficient of the installed rotor, and J_{eff} is the effective advance ratio taking into account the wing-induced velocity. Note that, while a linear relation for $C_T(J)$ is used, other functional forms are permitted in case the linear dependency does

not apply to the specific rotor geometry and/or operating regime being considered. A modeling strategy is proposed next in order to compute J_{eff}.

Advance ratio correction

To model the effective advance ratio, the parameterized geometry of figure 7.3a is used. Here, the rotor disk with diameter $D = 2R$ is centered at the position of the rotor axis (x_r, y_r). The velocity distribution captured by the rotors can be decomposed into axial and non-axial components. The former is further split into the uniform (spatial average), and non-uniform (wing proximity) contribution, see figure 7.3b. Since the focus of the current work is to predict the steady (time-averaged) loads of fixed pitch rotors, only the uniform, axial component of the inflow needs to be considered. The zero-mean non-uniform and the non-axial inflow components predominantly yield azimuthal variations in blade loading, and are primarily relevant to the rotor's far-field acoustics. Note that, for extreme angles of attack and/or high advance ratios, non-axial inflow could result in elevated steady thrust [179, 180]. Such conditions, however, fall outside the investigated parameter space. Additionally, considering that the wing deflects streamlines for OTW-propulsion, flow angularity at the rotor is reduced compared to an isolated configuration.
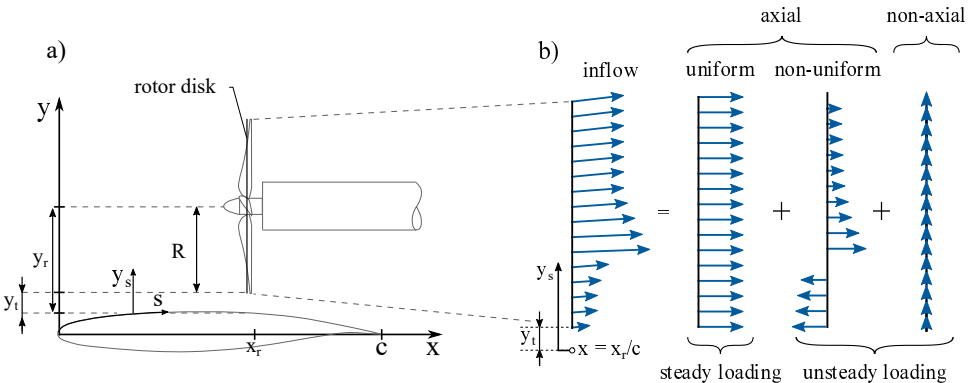
Figure 7.3: a) 2D system of coordinates and b) decomposition of inflow field at the disk plane.

In the model, the wing aerodynamics are split into an inviscid and viscous contribution. The inviscid part accounts for the axial velocity increase by the circulation distribution over the wing's profile. A viscous contribution accounts for leading-edge separation over the wing, occurring at large angles of attack. Other viscous effects, such as the rapid increase in boundary layer thickness along the adverse pressure gradient region are disregarded, as this only affects rotors that are installed with minuscule tip gaps, i.e. $y_t < \delta_{99}$ (not considered in the present work).

Contributions from inviscid and viscous flow effects to the isolated rotor's advance ratio J are modeled with two correction factors, J_Γ and J_{SL}, respectively. This will yield the effective advance ratio, according to:

$$J_{eff} = J \cdot J_\Gamma \cdot J_{SL} \tag{7.2}$$

The correction factors J_Γ and J_{SL} are derived as a function of the geometric and performance parameters of the rotor-wing system, with a focus on interpretability and general-

a)   b)   c)
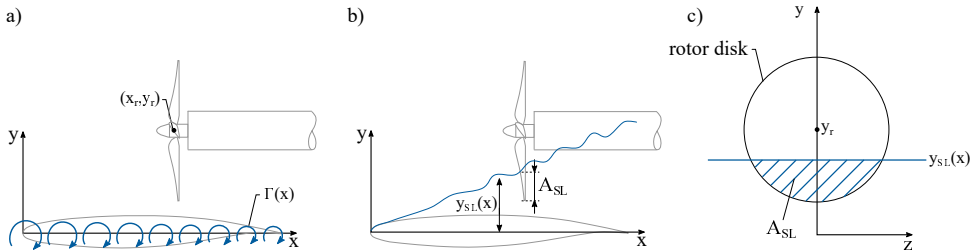
Figure 7.4: Schematic of the modelling strategies for the effective advance ratio, a) the (inviscid) velocity increase by the circulation distribution $\Gamma(x)$ and b) the (viscous) boundary layer separation at large angles of attack and c) definition of the ratio of boundary layer ingestion.

ity of the model. A simplified description is presented in the next sections. For additional details the reader is directed to Appendix A.1.

Inviscid: Wing's circulation

The axial induced velocity in a reference point r by a set of vortex filaments $\Gamma(s)$ can be found by integration of the Biot-Savart law [181]. The advance ratio correction, by the wing's circulation J_Γ, is then defined as the induced axial velocity, averaged over the rotor disk:

$$J_\Gamma = \frac{V_{\Gamma,x}}{V_\infty} = \underbrace{\frac{1}{\pi R^2} \int_A \frac{\widehat{\boldsymbol{n}_x}}{V_\infty} \overbrace{\int_s \frac{\Gamma(s)}{4\pi} \frac{\boldsymbol{s} \times \boldsymbol{r}}{|\boldsymbol{r}|^3} \, \mathrm{d}\boldsymbol{s}}^{\text{axial induction by vortex filaments}} \, \mathrm{d}A}_{\text{disk-average}} \tag{7.3}$$

For an airfoil, the bound vortex filaments typically lie along its contour, making the integration of equation 7.3 rather cumbersome. The problem is modeled by making use of thin airfoil theory, with a parabolic distribution of vortex filaments $\Gamma(x)$ along the chord line, as schematically illustrated in figure 7.4a. The strength of the vorticity source $\Gamma(x)$ depends on the lift coefficient of the wing:

$$\Gamma(x) = \frac{3}{4} c_l V_\infty c \left(1 - \frac{x^2}{c^2} \right) \tag{7.4}$$

A second simplification is made by extracting the axial induction only at the center point of the rotor disk, i.e. the rotor axis (x_r, y_r), which corresponds with sufficient accuracy to the disk-averaged value (relative error below 1%). The simplified expression for J_Γ becomes:

$$J_\Gamma \approx \frac{1}{2\pi V_\infty} \int_0^c \frac{\Gamma(x) y_r}{(x_r - x)^2 + y_r^2} \, \mathrm{d}x \tag{7.5}$$

which can be integrated analytically.

Viscous: Shear layer ingestion

Wing stall is implemented by considering that flow separation occurs abruptly at the leading edge when the angle of attack exceeds a given stall angle α_c. Consequently, the advance ratio needs to be corrected to account for the fraction of the rotor's area affected by separated flow ingestion, A_{SL}:

$$J_{SL} = 1 - f(\alpha,\alpha_c) \overbrace{\left(1 - \frac{V_{SL}}{V_\infty}\right)}^{\substack{\text{momentum} \\ \text{deficit}}} \overbrace{\frac{A_{SL}}{\pi R^2}}^{\substack{\text{ratio of} \\ \text{ingestion}}} , \quad f(\alpha,\alpha_c) = \begin{cases} 0, & \alpha < \alpha_c \\ 1, & \alpha \geq \alpha_c \end{cases} \tag{7.6}$$

In the equation above $f(\alpha,\alpha_c)$ is a stall criterion and V_{SL} is the local velocity in the separated region. A_{SL} is modeled assuming a span-wise homogeneous shear layer, oriented tangential to the free-stream direction (see figure 7.4b). Experimental data (later presented in figure 7.11) showed that the shear layer height at the position of the rotor was underpredicted. Therefore, the modeled shear layer profile was adjusted by applying a steeper slope, with a factor of $\left(\frac{11}{8}\right)$ compared to the free-stream. The area A_{SL} is obtained by integration (equation 7.7) and schematically illustrated in figure 7.4c.

$$A_{SL} = \int_{y_r - R}^{y_{SL}} \sqrt{(y - y_r)^2 + R^2} \, \mathrm{d}y \tag{7.7}$$

To complete the model, the stall angle α_c is found by using an empirical relation as a function of the wing's nose radius to chord length r_c/c [182].

It is worth noting that the model exhibits abrupt separation at the leading edge, differing from the gradual progression of separation from trailing to leading edge, as observed for an isolated wing as the angle of attack increases. Experimental results (later presented in figure 7.8) revealed that, for Over-The-Wing propulsion, separation occurs more abruptly due to the formation of a flow reversal region between the rotor and wing, indicating that the model accurately captures the observed separation mechanism of the installed system.

7.1.2 Streamtube properties

For modeling the wing's lift force, the influence of the rotor-induced flow field must be taken into account. Using the actuator disk model, the rotor's induction factor a, defined as the induced velocity v_a normalized by the free-stream velocity, can be written as a function of the local advance ratio J_{eff} and the installed rotor's thrust coefficient C_T:

$$a = \frac{v_a}{V_\infty} = \frac{(J_\Gamma \cdot J_{SL})}{2}\left(\sqrt{\frac{8 C_T R^2}{S_d J_{\text{eff}}^2} + 1} - 1\right) \tag{7.8}$$

Following a similar approach as in the work of Veldhuis [32], the rotors can be modeled by a uniform distribution of doublets of strength Δp over the disk surfaces (as shown in figure 7.5a). Considering that a span-wise distributed array of rotors is used in the current work, the doublets are instead re-distributed on a rectangular surface with height $\mathrm{d}y = 2R$ and width $\mathrm{d}z = 2N_r R$ (here N_r is the number of rotors considered), see figure 7.5b.
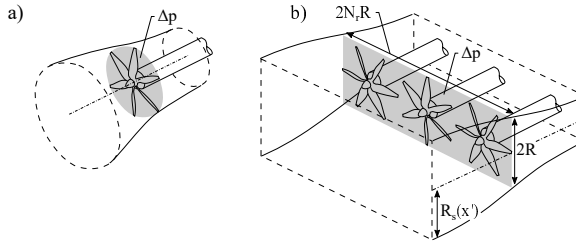
Figure 7.5: Schematic of the projected pressure doublets with strength Δp on a) a single rotor disk and b) a rectangular disk surface as considered in the aero-propulsive model.

It can then be shown (see section A.2 for a detailed derivation) that for rotor numbers of $N_r \geq 5$, the streamwise distribution of streamtube quantities approaches the two-dimensional solution ($N_r = \infty$):

$$p\left(x'\right) = \frac{\Delta p}{\pi} \tan^{-1}\left(\frac{R}{x'}\right)$$

$$\frac{v_a\left(x'\right)}{V_\infty} = a\left(\frac{x'}{\sqrt{x'^2}} + 1 - \frac{2}{\pi}\tan^{-1}\left(\frac{R}{x'}\right)\right) \tag{7.9}$$

$$\frac{R_s\left(x'\right)}{R} = \frac{1+a}{1 + a\left(\frac{x'}{\sqrt{x'^2}} + 1 - \frac{2}{\pi}\tan^{-1}\left(\frac{R}{x'}\right)\right)}$$

in which x' denotes the streamwise distance from the rotor's disks, i.e $x' = x - x_r$. The relations of equation 7.9 are used to predict the lift increase by rotor induction, as is introduced in the next section.

7.1.3 Rotor-induced wing lift

Three separate rotor-induced aerodynamic effects on the lift-generating mechanism of the wing are considered in the model (illustrated in figure 7.6). Firstly, a contraction of the rotor's streamtube causes an effective upwash near the wing's leading edge leading to a lift enhancement $\Delta c_{l,\alpha}$. Secondly, inside the streamtube, the pressure varies compared to the surroundings. This pressure is projected on the wing surface resulting in $\Delta c_{l,p}$, see figure 7.6b. Finally, if the wing has camber, this causes the streamtube to deflect downwards, creating an additional lift component $\Delta c_{l,tv}$, as shown in figure 7.6c.

The lift increase compared to the isolated wing is modelled by superimposing each of the three rotor-induced flow effects:

$$\Delta c_l = \Delta c_{l,a} + \Delta c_{l,p} + \Delta c_{l,tv} \tag{7.10}$$

A simplified derivation of the aero-propulsive model is now presented in the next sections, for additional details the reader is referred to appendix A.2.

Effective angle of attack

The axial velocity increase v_a in the rotors' streamtubes results in a vertical induced velocity v_i, see figure 7.6a. This generates an effective upwash at the wing's leading edge,
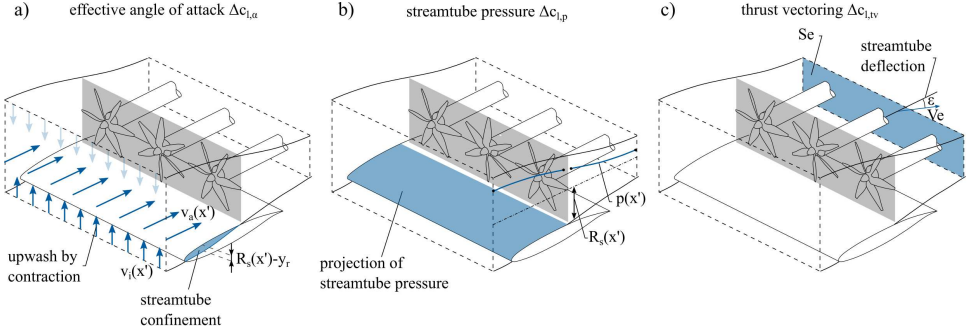
Figure 7.6: Schematic of interactions of the rotors' two-dimensional streamtube on wing's lift, a) upwash by streamtube contraction b) the streamtube pressure and c) the streamtube deflection

resulting in an increase in lift by $\Delta c_{l,\alpha}$. The increase of angle of attack $\Delta \alpha$ by the rotor-induced flow is modeled by the resulting angle between the inflow vectors of the installed configuration and the geometric angle of attack, and by considering the affected span of the wing:

$$\Delta c_{l,\alpha} = \overbrace{2\pi}^{\substack{\text{lift} \\ \text{slope}}} \overbrace{\Delta\alpha}^{\substack{\text{increase} \\ \text{angle of} \\ \text{attack}}} \overbrace{\frac{2N_r R}{S}}^{\substack{\text{affected} \\ \text{span}}} = 2\pi \cos^{-1}\left(\frac{\mathbf{a}\cdot\mathbf{b}}{|\mathbf{a}||\mathbf{b}|}\right)\frac{2N_r R}{S}, \quad \mathbf{a} = \begin{bmatrix} \frac{v_a(-x_r)}{V_\infty} + \cos(\alpha) \\ \frac{v_i(-x_r)}{V_\infty} + \sin(\alpha) \end{bmatrix}, \quad \mathbf{b} = \begin{bmatrix} \cos(\alpha) \\ \sin(\alpha) \end{bmatrix}$$

(7.11)

in which $\mathbf{a}$ is the two-dimensional normalized inflow vector of the installed configuration and $\mathbf{b}$ of the isolated wing. The vertical induced v_i follows from v_a (equation 7.9) by the conservation of mass:

$$\frac{v_i\left(x'\right)}{V_\infty} = C_1 \frac{\mathrm{d}\frac{v_a(x')}{V_\infty}}{\mathrm{d}x'}R$$

(7.12)

Here, C_1 is a correction factor used to account for the confined streamtube by the presence of the wing. The confinement leads to a higher-than-predicted axial velocity in the streamtube, further reducing the static pressure around the leading edge of the wing, and increasing vertical-induced velocity v_i. The correction for this is formulated as a power function of the overlap between the predicted rotors' free-contraction at the position of the leading edge (i.e. $R_s(-x_r)$) and the wing's surface height y_r (see figure 7.7 for the definition of variables), normalized by the rotor radius:

$$C_1 = \max\left(1, c_0\left(\frac{R_s(-x_r)-y_r}{R}\right)^{c_1}+1\right) = \max\left(1, 60\left(\frac{R_s(-x_r)-y_r}{R}\right)^{\frac{5}{2}}+1\right)$$

(7.13)

The coefficients c_0 and c_1 are obtained by fitting the experimental results of the effective angle of attack. The experimental results of the effective angle of attack are presented

in section 7.3 and the details of the fitting process are described in appendix A.2.2. Even though the coefficients c_0 and c_1 are based on experimental data, the relation of equation 7.13 is universally applicable to Over-The-Wing propulsion systems. Nonetheless, to ensure consistency, the coefficients should be tuned through a more comprehensive training database which includes variations in vertical rotor positioning.
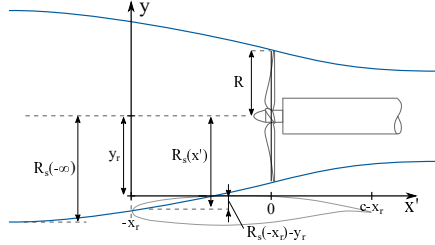

Figure 7.7: Schematic of the overlap between the streamtube and wing surface, and the definition of the variables to compute $\Delta c_{l,\alpha}$ and $\Delta c_{l,p}$.

STREAMTUBE PRESSURE

The rotors' suction leads to a reduction in pressure in front of the disk, while the pressure is increased downstream. The generated lift coefficient $\Delta c_{l,p}$ due to this effect is predicted by integrating the pressure in streamwise direction:

$$\Delta c_{l,p} = \overbrace{\frac{2N_r R}{S}}^{\substack{\text{affected} \\ \text{span}}} \overbrace{\frac{2}{\rho V_\infty^2 c}}^{\substack{\text{lift} \\ \text{normalization}}} \int_{-x_r}^{1-x_r} p^* \left(x' \right) dx', \quad \text{for} \quad \frac{\lim\limits_{x' \to -\infty} R_s \left(x' \right)}{y_r} = \frac{R(a+1)}{y_r} > 1 \quad (7.14)$$

in which $p^* \left(x' \right)$ is the projected streamtube pressure over the wing surface, see figure 7.7 for the range of integration. Equation 7.14 therefore only holds when the pressure is overlapping the with the wing surface, explaining the criterion on the right hand side where the limit function highlights the maximum streamtube radius, also illustrated in figure 7.7. The pressure $p^* \left(x' \right)$ is based on the relation for the free-streamtube pressure $p \left(x' \right)$, recall equation 7.9, and in addition includes a correction $g(x', y_r)$ that accounts for the reduced pressure due to the streamtube confinement, using Bernoulli's principle:

$$p^* \left(x' \right) = p \left(x' \right) - \overbrace{\frac{\rho}{2} \left(v_a \left(x' \right) + V_\infty \right)^2 \left(1 - \left(g \left(x', y_r \right) \right)^2 \right)}^{\text{effect of streamtube confinement}}, \quad g \left(x', y_r \right) = \frac{R_s \left(x' \right)}{y_r} \quad (7.15)$$

Considering that $\Delta c_{l,p}$ is based on the overlap between streamtube height and wing contour, only the upstream region in the integral of equation 7.14 is considered in the aeropropulsive model. Modeling of the lift reduction by the pressure increase downstream of the rotor-array relies on the streamtube-wing attachment point, which is determined by complex viscous interactions [97]. Moreover, since the attachment point is moved further

downstream for rotors in high-thrust conditions, the effect of the projected pressure is expected to be dominated by the upstream contribution.

For the second term in equation 7.15, the averaged values (in the upstream direction) of the induced velocity v_a and streamtube height R_s are considered. This reduces the complexity of the integral of equation 7.14. Details of the derivation and the final expression for $\Delta c_{l,p}$ are described in appendix A.2.3.

Thrust vectoring
The third aerodynamic effect is the deflection of streamtube in vertical direction, providing a form of thrust vectoring. The lift increase by slipstream deflection $\Delta c_{l,tv}$ follows from a momentum balance using a streamtube deflection angle ϵ, and the velocity V_e and area S_e at the exit of the streamtube, see figure 7.6:

$$\Delta c_{l,tv} = \frac{2S_e \left(V_e - V_\infty\right)^2 \varepsilon}{V_\infty^2 c}, \quad \varepsilon = \varepsilon_w \overbrace{\left(1 - \frac{x_r}{c}\right)}^{\substack{\text{rotor} \\ \text{position}}} = \frac{2c_{l,0}c}{\pi S}\left(1 - \frac{x_r}{c}\right) \tag{7.16}$$

The deflection angle ϵ is set to be equal to the one of the isolated wing under $\alpha = 0°$, i.e. ε_w, with a weighting (as a function of rotor position) to account for effectiveness as a thrust vectoring device. Note, that V_e and S_e in equation 7.16 indicate the streamtube velocity and cross-sectional surface in the downstream extend and can be found by taking the limit of equation 7.9 to $x' \to +\infty$.

7.1.4 Applicability range
Several assumptions are made in the derivation of the aero-propulsive model, confining the parameter space over which the method is applicable. An overview of this parameter space, consisting of both geometrical and performance conditions, is provided in table 7.1. The origin of the limitation is included in the third column here. Note that the lift part of the model has a more confined applicability range.

Finally, any (steady) aerodynamic rotor-to-rotor effects are not included and the lift model is only applicable when the flow at the leading edge of the wing is attached. Recall that the calculation of $\Delta c_{l,\alpha}$ includes a correction for streamtube confinement. Excluding this correction affects the predicted lift for aft-mounted rotors at low advance ratios, resulting in a reduction exceeding 15% within the examined parameter space. On a related note, the interactions between the rotor and wing induction are modeled using a single-pass approach, without requiring additional iterations of the aero-propulsive model. An analysis, presented in appendix A.3, showed that additional iterations lead to a minor reduction (up to 5%) in the aero-propulsive forces. This minor increase in accuracy therefore does not justify the additional complexity and obscurity of repetitive computations.

7.1.5 Experimental validation
To validate the model, a number of experiments were conducted with an array of 5 rotors above an airfoil for a wide range of angles of attack, advance ratios and three rotor positions along the chord. The extracted data consisted of the center rotor and wing loads, and flow measurements through 2D2C-PIV and pressure orifices. The experimental setup and measurement techniques were described in section 4.2.

Table 7.1: Parameter space of the aero-propulsive performance model

Parameter	Value	Origin
Free-stream Reynolds number Re_c	$> 250,000$	Laminar separation not included in model.
Free-stream Mach number M	< 0.3	Incompressible flow assumed for equations 7.9 and 7.15.
Advance ratio J	$0 < J \leq J_{T0}$	Hover and negative thrust conditions cannot be applied in equation 7.9.
Rotor chord-wise position x_r/c	$0.1 \leq x_r/c \leq 0.9$	Equation 7.5 fails to predict wing-induced velocities at leading- and trailing edge.
Rotor tip gap y_t	$> \delta_{99}$	Boundary layer ingestion not included in the model.
Rotor spacing z_r/R	< 1.5 (lift)	Required for the 2D-streamtube
Number of rotors N_r	≥ 5 (lift)	formulation of equation 7.9.

7.2 Results

7.2.1 Flow field statistics

The general flow features of the rotor-wing system are investigated by considering three levels of inclination for a fixed rotor position of $x_r/c = 0.6$, namely zero angle of attack, an angle of attack of 8° which positions the rotor in a strong adverse pressure gradient, and the early onset of stall at $\alpha = 12°$. The time-averaged velocity magnitude contours and two-dimensional velocity streamlines in the plane with an offset of $0.2R$ in the spanwise direction from the center rotor's axis are presented in figure 7.8. The top row presents results with the rotors removed. Evidently, the acceleration of the flow over the wing's suction side is relatively moderate for $\alpha = 0°$, but increases for $\alpha = 8°$ due to the enhanced circulation of the wing. Inclination of the wing to $\alpha = 12°$, in figure 7.8c, shows that the boundary layer separates close to the leading edge, which marks the onset of stall.

When proceeding to the case of a low thrust condition ($J = 0.6$), an increase of velocity appears over the wing (see figures 7.8d and 7.8e). The flow is primarily accelerated downstream of the disk, leaving the upstream region largely unaltered. Nonetheless, for $\alpha = 8°$, the induced flow of the rotors causes separation from the wing at roughly $0.8c$ chord (compare figure 7.8b and figure 7.8e) by the entrainment of flow towards the slipstream. The result for the early stall condition in figure 7.8f shows that the limited suction of the rotors prevents the boundary layer from reattaching. By reducing the advance ratio to $J = 0.3$, the rotors' thrust increases, leading to a stronger contraction of the rotor's streamtube and higher induced velocities, both upstream and downstream of the disks. The flow topology, relative to the lower thrust conditions of $J = 0.6$, changes significantly when changing the system's angle of attack. For $\alpha = 8°$ in figure 7.8h, the pressure jump over the rotor disk increases the adverse pressure gradient imposed by the wing and causes the flow to separate. As a consequence, the rotor ingests flow from downstream of the disk leading to stagnation upstream of the disk. By a combination of this stagnation and the
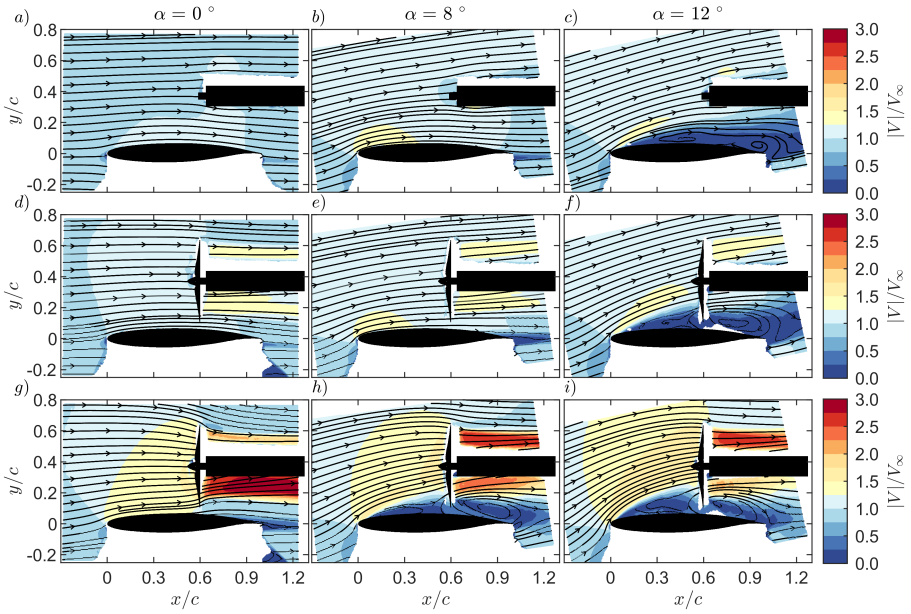
Figure 7.8: Normalized velocity magnitude contours and 2D streamlines for $\alpha = 0°$, $\alpha = 8°$ and $\alpha = 12°$ for the rotors-off case (a-c), $J = 0.6$ (d-f) and $J = 0.3$ (g-i). The rotor position is fixed at $x_r/c = 0.6$.

contraction of the slipstream, the flow over the wing separates close to the leading edge. This phenomenon remains unchanged with a further increase in the geometric angle of attack, since the data for $\alpha = 12°$ presents a similar flow topology, see figure 7.8i. However, in this case, the shear-layer height in the upstream region of the rotors has grown by the larger geometric angle of attack.

Another characteristic of the flow that manifests itself strongly for the $J = 0.3$ case is an in increase in flow angle upstream of the wing ($x < 0$ & $y < 0$) with respect to the rotors-off conditions (compare figures 7.8(a-c) to figures 7.8(g-i)). This behavior was included in the aero-propulsive model and will be discussed in more detail in section 7.3.1.

The effect of the rotors on the wing's pressure distribution is shown by the results of the static pressure measurements, in figure 7.9. Note that in this case the pressures are extracted directly below the center rotor axis at the wing's surface, without the offset in span-wise direction as used to generate figure 7.8.

For $\alpha = 0°$ in figure 7.9a, the rotors-off data have comparable pressure distributions, on the suction and pressure sides. When including the rotors, the flow accelerates, leading to a lower static pressure upstream of the disk. Downstream of the disks, the total pressure increases, leading to an increase in static pressure on the wing. These effects are noticeable for $J = 0.3$ in particular. The occurrence of a suction peak for $J = 0.3$ and the increase in pressure on the pressure side, are effects that are consistent with the observed increase in flow angle, as was observed in figures 7.8(g-i).

Similarly, the pressure profiles for $\alpha = 8°$, presented in figure 7.9b, show an increase of the suction peak up to $C_p \approx -3$ and a stagnation point on the pressure side that moves
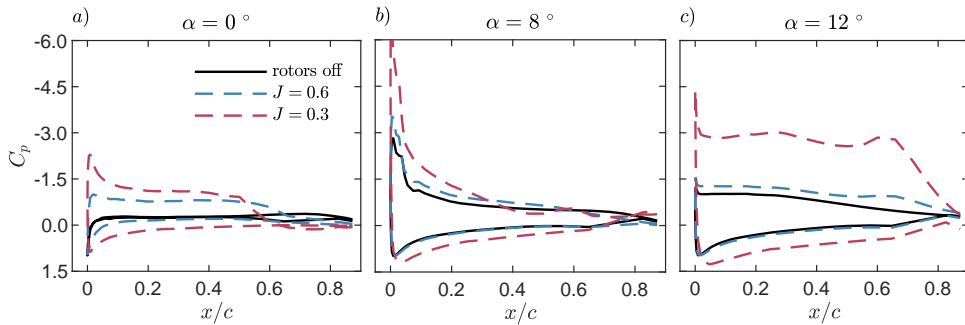
Figure 7.9: Pressure coefficient C_p along the wing's contour for the rotors-off condition, J = 0.6 and J = 0.3, a) α = 0°, b) α = 8° and c) α = 12°. The rotor position is fixed at x_r/c = 0.6.

towards the trailing edge by the rotor-induced flow. However, in the vicinity of the rotor, i.e. x_r/c = 0.6, the results are different than those for α = 0°. That is, for the inclined system at an advance ratio of J = 0.3, a small pressure plateau at x_r/c = 0.5 hints upon the occurrence of flow separation. The pressure jump just downstream at the rotor disk location is now reduced in magnitude (figure 7.9a) and is ascribed to the re-circulation bubble downstream of the disk, as seen in figure 7.8h.

Finally, in the separated flow region that occurs at α = 12°, seen in figure 7.9c, the pressure plateau is visible at x/c = 0.1, for the rotors-off condition. For the installed configuration, the pressure plateau starts at the same chord-wise position but the pressure is reduced depending on the advance ratio and therefore the rotors' thrust delivered. Note that even though the separation point at the wing is maintained, the effective angle of attack is enhanced and therefore the flow curvature increases with respect to the rotors-off condition. Additionally, the rotors' suction also deflects the shear layer which further increases the flow curvature after separation has occurred. As a consequence of these effects, the difference between the installed and rotors-off pressure distribution is more substantial for this angle of attack, and therefore the largest increase in lift is expected in post-stall conditions.

7.2.2 Boundary layer separation

In the previous section, it was shown that the rotors operated in low thrust conditions (J = 0.6) were not able to delay the boundary layer separation from the wing's leading edge. In addition, for high thrust conditions, the rotors caused a region of flow reversal between the rotor and wing, leading to local flow separation upstream. These effects are described in more detail now, by evaluating boundary layer profiles along the wing's chord for a relatively fine discretization of the angle of attack.

Figure 7.10 presents the axial velocity profiles, extracted at different chord-wise positions along the wing. For α = 4° (figure 7.10a), the decrease in J causes an increase in axial velocity while maintaining the same profile shape as the rotors-off condition. This persists until $x/c \approx 0.5$, where the axial velocity close to the wing is reduced due to the pressure jump that occurs over the rotor disk for J = 0.3. Thereupon, separation downstream of the rotor for this advance ratio is also observed. When the system is inclined to α = 8°
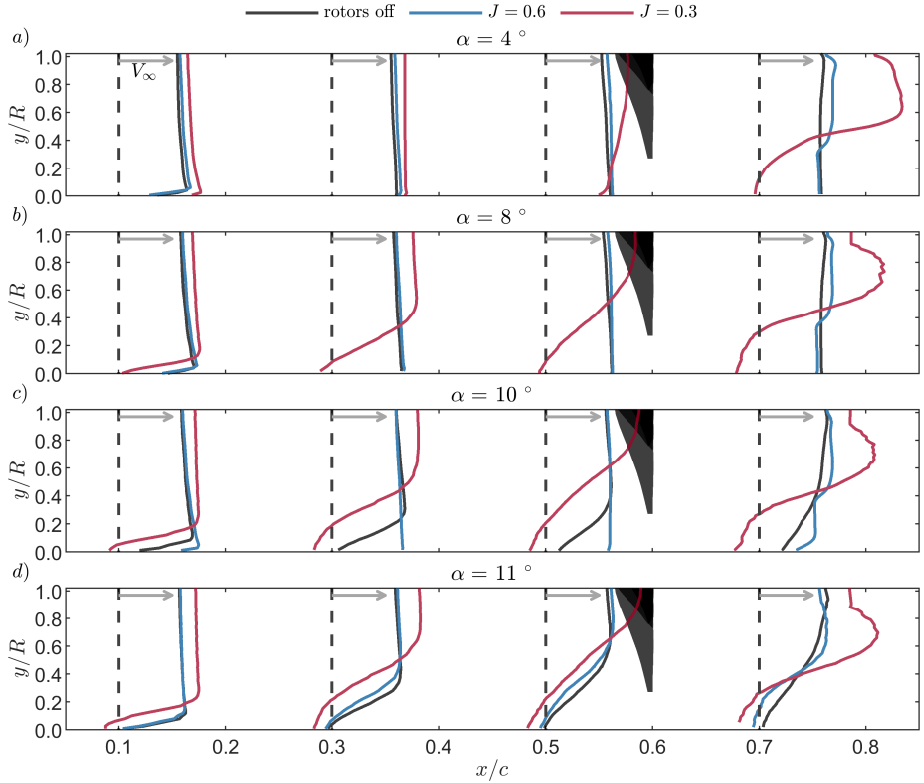
Figure 7.10: Axial velocity profiles upstream of the rotor extracted at $x/c = 0.1$, $x/c = 0.3$, $x/c = 0.5$ and $x/c = 0.7$ for a) $\alpha = 4°$, b) $\alpha = 8°$, c) $\alpha = 10°$ and d) $\alpha = 12°$. The rotor position is fixed at $x_r/c = 0.6$, the blade is shown by the black surface. To provide an indication of the velocity magnitude of the profile, a grey arrow is shown with its length being representative of the free-stream velocity magnitude.

in figure 7.10b, the rotor-induced separation is moved further upstream, and occurs from $x/c \approx 0.3$ onwards. Further inclination, in figures 7.10c and 7.10d, has no further effect on the flow topology of the data corresponding to $J = 0.3$. In contrast, when the rotors produce limited thrust ($J = 0.6$), they are able to delay flow separation over the wing. Around the isolated wing stall angle of $\alpha = 10°$ (figure 7.10c), the boundary layer remains thinner than the rotors-off condition. This reduction in separation is noticeable both upstream and downstream of the rotor array. This delay in separation disappears again for larger angle of attach, as shown for $\alpha = 11°$ in figure 7.10d.

The effect of the rotors on the location of the separation point and the shear layer profile during ingestion is shown by the distribution of the normalized shear layer height, as presented in figure 7.11. The shear layer height is identified from the velocity field as the maximum of the vertical derivative of the velocity magnitude, i.e. $y_{SL} = \max(\mathrm{d}V/\mathrm{d}y)$. For the rotor-off conditions, the shear layer adheres to a rather linear profile as a function of the chord-wise coordinate x, the slope of which increases with the angle of attack. With

the rotors operating at $J = 0.6$, the flow is still attached for $\alpha = 10°$, as shown in figure 7.11a. For the larger values of α, the data for this advance ratio show a similar linear function of the boundary layer thickness as the rotors-off condition, although with an increased slope, see figures 7.11b and c. Moreover, the separation point is unaffected by the rotors for this advance ratio. The increased suction of $J = 0.3$ generates a thicker, parabolic shape for the boundary layer thickness, which is independent of α. Based on these experimental results, an approximate, linear, function for the shear layer ingestion height is implemented model (recall the discussion on equations 7.6 and 7.7).
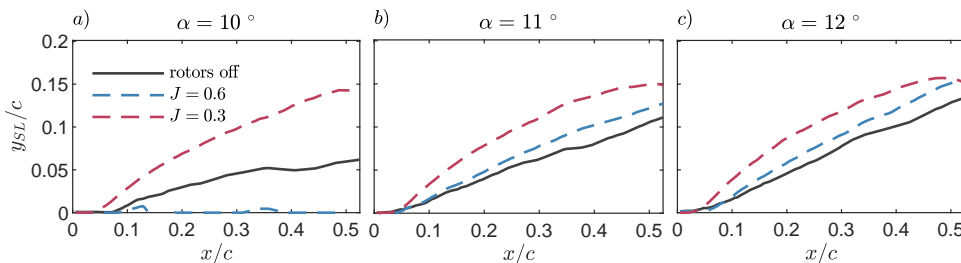

Figure 7.11: Normalized shear layer height y_{SL}/c for a) $\alpha = 10°$, b) $\alpha = 11°$, and c) $\alpha = 12°$. The rotor position is fixed at $x_r/c = 0.6$.

7.3 MODEL VALIDATION & PERFORMANCE TRENDS

Trends in the aero-propulsive performance of the wing–rotor-array system are now described, and compared between the empirical observations and the model predictions. First, we start with a validation of the modeled flow features (section 7.3.1), after which the propulsive thrust and wing lift augmentation are covered in sections 7.3.2–7.3.3.

7.3.1 ROTOR-INDUCED EFFECTS

In section 7.1.3, three rotor-induced flow features were introduced that form the foundation of the lift part of the aero-propulsive model. Both the presence of the upwash ($\Delta c_{l,\alpha}$) and thrust vectoring ($\Delta c_{l,tv}$) sources of lift, and their dependence on rotor positioning, are validated with the experimental PIV data. Note that validation of the projected streamtube pressure ($\Delta c_{l,p}$) is excluded here, as the other rotor-induced lift-generating contributions affect the experimental wing pressure values, making direct comparison unreliable. Nonetheless, a simplified comparison, for a condition where the effects of the other lift-contributions are minimized, is included in appendix A.4.

Recall that the upwash is generated by the rotor contraction upstream of the wing. To validate this flow feature, the system's inflow angle is extracted from a quarter wing chord upstream of the wing and averaged over a vertical length of half a wing chord ($x/c = -0.25$, $y/c = [-0.25, 0.25]$) using the measured velocity fields. This sample domain is outside of the stagnation region of the wing, and small variations in the horizontal position gave consistent results. The change in inflow angle, $\Delta\alpha$, due to the rotors induction is taken by subtracting the rotors-off inflow angle from the value of the installed configuration.
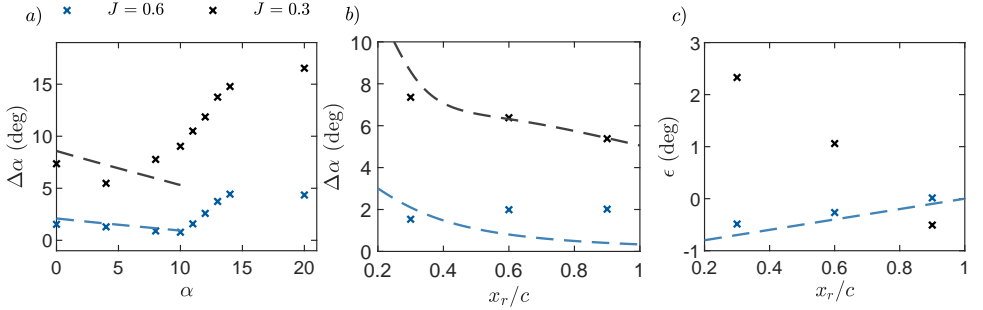
Figure 7.12: Comparison between modelled (dashed lines) and measured (markers) rotor-induced flow features, a) the increase in inflow angle $\Delta\alpha$ compared to the rotors-off condition (extracted at $(x/c, y/c)$ = (-0.25, [-0.25, 0.25])) for x_r/c = 0.3, as a function of α, b) the increase in inflow angle $\Delta\alpha$ for α = 0° as a function of rotor positioning and c) the averaged angle of the rotor slipstream ϵ extracted at x/c = 1.05.

In figure 7.12a, the generated upwash as a function of the geometric angle of attack for a rotor position of x_r/c = 0.3 is considered. This rotor position was chosen to eliminate the effect of the confined streamtube (recall the discussion on the correction factor C_1 in section 7.1.3). The results show positive values of $\Delta\alpha$, corresponding to an increase in the angle of attack by operation of the rotors. Experimental data of the low-advance ratio of J = 0.6, indicated by the solid lines, present a decreasing trend with α until reaching the stall angle of α = 12°. After this, the value of $\Delta\alpha$ increases gradually, reaching a plateau of $\Delta\alpha \approx 5°$. The trend for J = 0.3, is comparable to that of J = 0.6, although the positive slope of $\Delta\alpha$ occurs at a lower value of α, caused by the generation of the flow reversal between rotors and wing, as was shown in figure 7.8h. The significant increase in the effective angle of attack in post-stall conditions can be explained by the flow non-uniformity that is generated by the ingestion of the shear layer. Such conditions cause an abrupt increase in rotor-induction in the lower half of the rotor-array and therefore more fluid is entrained around the wing's leading edge.

Predictions of $\Delta\alpha$ only concern conditions where the flow at the leading edge is attached (i.e. $\alpha \leq 10°$). As such, the modeled relations for $\Delta\alpha$ are shown by the dashed lines up to α = 10° and show a similar decreasing trend with α, although with an initial overestimation for J = 0.3.

In figure 7.12b, the increase in inflow angle $\Delta\alpha$ is shown for different chord-wise rotor positions and α = 0°. The experimental data show a constant value for J = 0.6 and a linear decreasing trend with rotor position for J = 0.3.

For J = 0.6, the rotor vertical position exceeds the predicted streamtube height, and no correction takes place (i.e. C_1 = 1 in equations 7.12 and 7.13). Nonetheless, the modelled results show a lower value of $\Delta\alpha$ for the mid and aft-mounted rotor. Note that a rotor also induces a flow outside of the streamtube, by its vortex system [34]. Such complex effects are not included in the model but could explain the discrepancies in low-thrust conditions.

Another lift contribution in the aero-propulsive model is the deflection of the rotors' slipstreams by the wing's contour (i.e. $\Delta c_{l,tv}$). This effect is validated by tracking the slipstream boundaries (localized using the extreme values of the vertical derivative of the velocity magnitude, i.e. dV/dx), and taking the average position of the top and bottom

boundary. Then, the local angle of the streamtube is fitted by a linear function and extracted at $x/c = 1.1$. Finally, the streamtube angle directly behind the disk (at $x/c = x_r/c + 0.15$) is removed from this value, to obtain the deflection angle ϵ. The slipstream deflection angle ϵ is presented in figure 7.12c for $\alpha = 0°$ and shows large differences between the lower and higher advance ratio. The higher advance ratio of $J = 0.6$ shows a negative ϵ, corresponding to the slipstream being deflected downwards. For lower advance ratio of $J = 0.3$, the deflection angle ϵ is positive, due to the slipstream separation (see figures 7.8g and 7.10a). Note that the modelled slipstream deflection is independent of the advance ratio and resembles the results for $J = 0.6$.

7.3.2 PROPULSIVE THRUST

Results of the rotor's thrust coefficient C_T as a function of the angle of attack α are presented in figure 7.13 for the three chord-wise rotor positions, and $J = 0.3$ and $J = 0.6$. Here, the mean of repeated experimental results are presented by the markers while the hatched area resembles the repeatability of independent load measurements.

For the installed configuration, the thrust is reduced with respect to the isolated rotor for most of the concerned angles of attack. Below $\alpha = 12°$, a downward trend with inclination is visible. The slope of this trend increases for a more forward-positioned rotor and with the advance ratio J. The model results, shown by the solid lines, capture these effects. This indicates that the loss in thrust can be attributed to the increasing circulation of the wing.
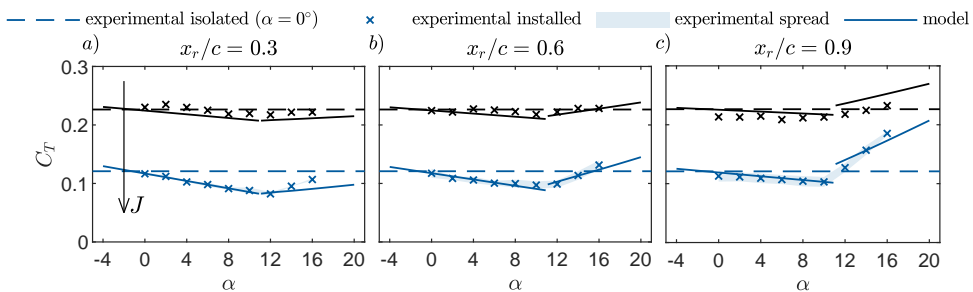
Figure 7.13: Center rotor's thrust coefficient C_T for a) $x_r/c = 0.3$, b) $x_r/c = 0.6$ and c) $x_r/c = 0.9$. Experimental results have been averaged over repeated measurements. The spread in the values of the installed configuration is shown by the translucent surfaces. The solid lines present the modelled trends. The different colors indicate different values of the advance ratio; $J = 0.3$ (black) and $J = 0.6$ (blue)

Around the stall angle of the wing, i.e. $\alpha = 10°$, the thrust increases again. Placing the rotor further towards the trailing edge increases the amount of re-ingestion, having a larger effect on the thrust augmentation. Since the stall criterion is a singularity in the model, this is also returned in the thrust predictions while the measurements show a smoother pattern along stall conditions. The model slightly under-predicts the slope of the thrust in these conditions. This can be attributed to the increase in shear layer height by the operation of the rotors (recall figure 7.11). This increment as a result of the re-ingestion region is not included in the model.

7.3.3 Wing lift

The lift increase of the wing by the rotor-induced flow is presented in figure 7.14. For the predictions, the lift increase by rotor induction Δc_l is combined with the isolated wing's lift coefficient c_l (obtained through the Viterna and Corrigan model [183]).
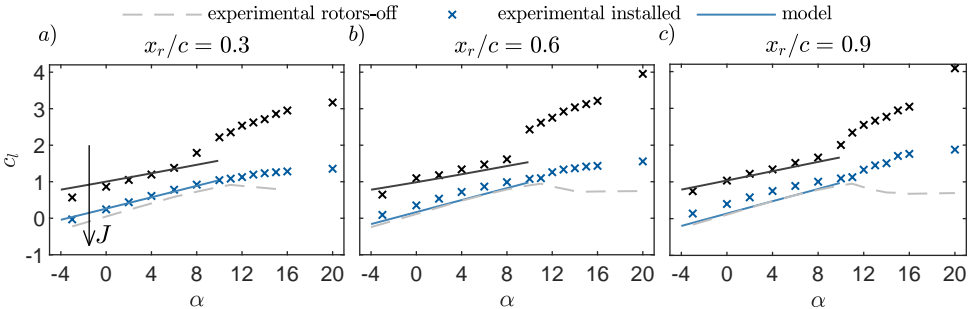

Figure 7.14: Wing's lift coefficient c_l for a) x_r/c = 0.3, b) x_r/c = 0.6 and c) x_r/c = 0.9. The solid lines present the modelled trends. The different colors indicate different values of the advance ratio; J = 0.3 (black) and J = 0.6 (blue). The rotors-off condition is shown by the grey line for Re_c = 480,000.

In figure 7.14, the rotors-off condition shows the lift curve with the well-known features; a linear regime up until the stall angle of α = 12°, after which the lift is reduced. Operation of the rotors increases the lift for each of the investigated chordwise rotor positions, advance ratios and angles of attack. This lift enhancement decreases with the advance ratio J, as shown by the trend arrow in figure 7.14a.

In the pre-stall regime of the lift curve, i.e. α < 12°, the results of the wing with rotors installed show a reduced slope compared to the rotors-off condition. This is caused by the fact that the rotor's thrust is reduced with inclination, therefore reducing the induced flow as well. Considering the chord-wise position of the rotor, the aft-mounted rotor, i.e. x_r/c = 0.9 in figure 7.14c, shows an increase in c_l by 10% compared to the forward rotor position of x_r/c = 0.3. The lift enhancement compared to the rotors-off conditions is abruptly amplified once the stall angle is reached. This is ascribed to the increase in the effective angle of attack (figure 7.12).

The model predictions, for pre-stall conditions, show a comparable increase in lift and a similar reduction of the slope for J = 0.3. Nonetheless, the lift increase for the mid and aft-positioned rotor is slightly underestimated for J = 0.6. For these conditions, the rotor vertical position y_r exceeds the modeled streamtube height $R_s\left(x'\right)$, i.e. the wing is located outside the rotors' streamtubes and the model predicts only a marginal lift increase. In reality, rotors induce flow outside of the streamtube region by their vortex systems [32]. Such complex vortex-induced velocities are not considered in the model but can contribute to the lift of Over-The-Wing propulsion in low-thrust conditions [34], explaining the observed discrepancies.

To show the variations with rotor positioning more clearly, the lift increase Δc_l as a function of the rotor position x_r/c is presented in figure 7.15 for a moderate (α = 0°) and high angle of attack (α = 6°). Here, the modeled contributions to the lift have been decomposed to highlight the effect of the different aerodynamic features.

In figure 7.15, the measurements show variations in lift coefficient with chord-wise rotor position x_r/c of up to 10%. For moderate inclination of $\alpha = 0°$ in figure 7.15a, a max-imization of the lift for a mid-positioned rotor is found while the rotor positioned closest to the leading edge gives the lowest lift enhancement. Instead, for the higher inclination (figure 7.15b) a linear behavior with rotor position is found, in which the lift for the aft-mounted is 18% higher than for the forward-mounted rotor.
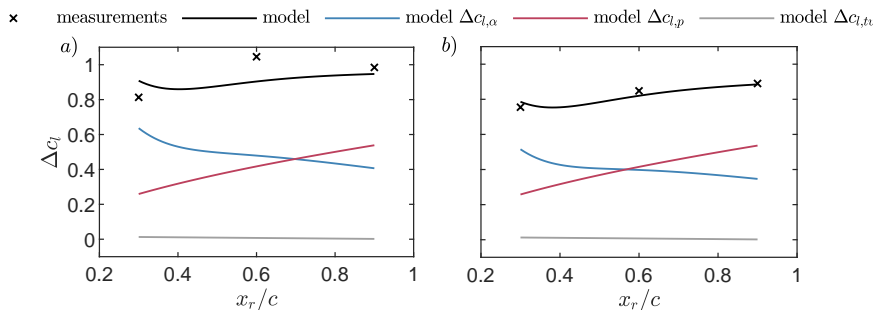

Figure 7.15: Difference in lift coefficient Δc_l compared to the isolated wing and decomposition of the model components, as a function of rotor spacing, for $J = 0.3$ and a) $\alpha = 0°$ and b) $\alpha = 6°$.

The predictions show an increase in lift coefficient with rotor position x_r, although a local enhancement in lift around $x_r/c = 0.3$ due to the effective angle of attack is also observed. The decomposition of the modeled components shows that the lift increase due to the projected pressure distribution $\Delta c_{l,p}$ and the increase in the effective angle of attack $\Delta c_{l,\alpha}$ are comparable in magnitude for a mid-mounted rotor. For a forward-mounted rotor, $\Delta c_{l,\alpha}$ clearly becomes the dominant term, while for the aft-mounted rotor, the lift is prevailed by the reduced pressure due to rotor suction. $\Delta c_{l,\alpha}$ is however, more strongly reduced by inclination than $\Delta c_{l,p}$, which could explain varying trends with α observed in the experimental data. The predicted increase in lift due to streamtube deflection $\Delta c_{l,tv}$ shows to be negligible for the used airfoil, due to the limited amount of camber.

7.3.4 Wing drag

The wing's drag coefficient c_d is presented in figure 7.16. Note that this force was not included in the aero-propulsive model. Nonetheless, the results show a distinctly different pattern with the angle of attack α. Note that only the drag of the wing profile is included in figure 7.16; the additional drag component due to the rotor array [96, 98] is excluded. For moderate angles of attack $\alpha < 4°$ the drag coefficient of the wing is comparable to that of the rotors-off condition. The drag slope increases with the advance ratio J when the rotors are operated. Drag is minimized for a rotor position at 60% chord. This rotor position also shows a drag reduction ($\Delta c_d = -0.015$) with respect to the rotors-off conditions for $\alpha < 0°$. The rotors positioned at $x_r/c = 0.9$ gives the largest value of the drag, as a result of the maximum suction that is applied at the region where the wing thickness reduces. At high angles of attack ($\alpha > 8°$), and in the post-stall regime ($\alpha > 12°$) in particular, the drag coefficient is significantly increased compared to the rotors-off condition. In these conditions, the drag is maximized for rotor positions towards the trailing edge.
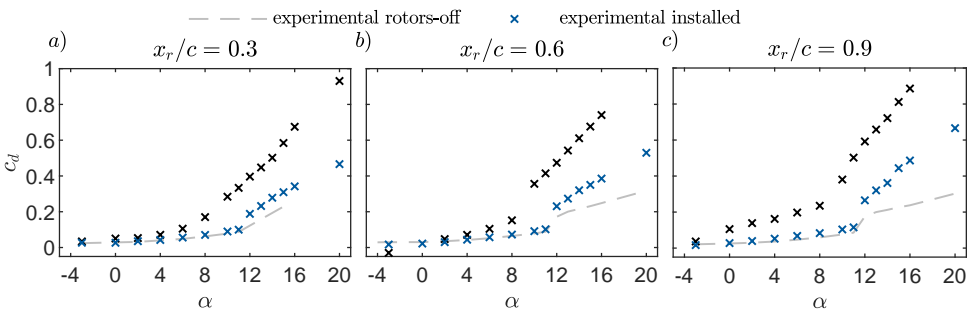
Figure 7.16: Wing's drag coefficient c_d for a) $x_r/c = 0.3$, b) $x_r/c = 0.6$ and c) $x_r/c = 0.9$. The different colors indicate different values of the advance ratio; $J = 0.3$ (black) and $J = 0.6$ (blue). The rotors-off condition is shown by the grey line for $Re_c = 480,000$.

7.4 Conclusion

The installed rotor's thrust is modeled through the definition of an effective advance ratio, determined by the inviscid velocity increase by the wing's circulation and the predicted momentum deficit by shear layer ingestion. Model predictions and experimental data present a similar reduction in thrust when positioned over the suction side of the wing. The difference compared to the isolated rotor depends on a combination of the advance ratio, angle of attack and the chord-wise position over the wing. In the pre-stall regime, the thrust is reduced most significantly for the rotor position near the wing's leading edge. Around the wing's stall angle, the rotor operated thrust conditions showed to energize the boundary layer resulting in a delay of leading-edge separation by approximately 1 degree. Increasing the thrust was shown to be unsuccessful in increasing this delay by the formation of a flow-reversal region due to the adverse pressure gradient generated by the rotors. As a consequence, around the wing's stall angle, the thrust is increased by the ingestion of the separated boundary layer.

The rotors' induced flow affects the wing's lift through a generated upwash, the projection of the streamtube pressure on the wing's surface and the deflection of the streamtube. In the pre-stall regime, these effects increase lift but reduce the lift slope compared to the rotors-off conditions. The reduced slope is the result of the reduction of thrust by the increasing circulation provided by the wing and the decreasing contribution of the rotor-induced upwash with geometric inclination. For most of the investigated parameter space, the aft-mounted rotor showed the highest value of the lift, up to 10% higher than the forward-mounted rotor. The model predicts the general trends of the lift curve but discrepancies are found for the low thrust conditions due to the induced velocities outside the streamtube. Although the effect of the rotors on the leading edge separation is marginal, an abrupt increase in lift was observed once separation occurred. This is the result of an additional increase in the rotor-induced upwash while maintaining the separation point at the same position along the wing's chord as for the rotors-off condition.

8

Aeroacoustics of Over-The-Wing propulsion

The aero-propulsive performance model of chapter 7 is based on the definition of an effective advance ratio, from which the mean rotor's thrust can effectively be predicted. Considering that only the steady part of the rotor loads was of interest, any effect of flow angularity or non-uniformity was disregarded. In reality, the inflow to the rotor blades will vary in time by the inclination of the rotor-wing system and the non-uniform flow imposed by the wing. This creates unsteady loading on the blades, which is known to be a strong noise component of low-speed rotors. It is currently unknown how this expected increase in noise of the rotor compares to the favorable shielding effect of the wing.

In this chapter, the effective advance ratio, as derived in chapter 7, will be extended and written in blade section coordinates. This creates a non-axial and non-uniform inflow, required to predict the unsteady loading. Information on the blade loading is then used to compute the far-field acoustics using Helicoidal Surface Theory. The results of the model are validated against experimental measurements of a single Over-The-Wing mounted rotor.

The outline of this chapter is as follows. In section 8.1 the blade sectional advance ratio and the analytical modeling techniques are introduced. The aeroacoustic characteristics of the setup are then presented in section 8.2 using experimental data. Moreover, flow regimes excluded in the model are identified and the relative importance of tonal and broadband noise is quantified. Then, in section 8.3, the model results are compared to the measurements, and a parametric study is performed on the chord-wise rotor position.

8.1 Tonal noise modelling techniques

In chapter 7, a model for the steady propulsive thrust by a rotor in the vicinity of the wing was introduced. An effective advance ratio was defined based on the (inviscid) axial velocity increase by airfoil circulation and the (viscous) separated boundary layer ingestion. To model the aerodynamic performance, these phenomena were accounted for by an average

---

This chapter is based on publication [161].

change of the rotor disk inflow. For noise modeling, the rotor azimuth-dependent blade loading is required and hence both the non-uniform and non-axial contributions to the inflow of the rotor should be included, see figure 8.1a.

The inclusion of the non-uniform and non-axial inflow is achieved by an extension of the advance ratio correction model introduced in chapter 7, while maintaining the same base flow lying at its foundation. First of all, the contributions of the inviscid and viscous flow features are modeled for both the axial V_x and non-axial velocity V_y as a function of the wing-normal coordinate y, for a given rotor position (x_r, y_r). Then, the inflow velocity components $V_x(y)$ and $V_y(y)$ are transferred to the cylindrical coordinate frame (r,θ) of the rotor disk, as is shown in figure 8.1b. For a full rotation, the axial $V_{ax}(r,\theta)$ and tangential $V_\theta(r,\theta)$ inflow velocity is prescribed at each blade section, see figure 8.1c. This includes the local rotational velocity of the blade section itself as well. The derivation of the axial $V_{ax}(r,\theta)$ and tangential $V_\theta(r,\theta)$ velocities are section in section 8.1.1 and 8.1.2, respectively.
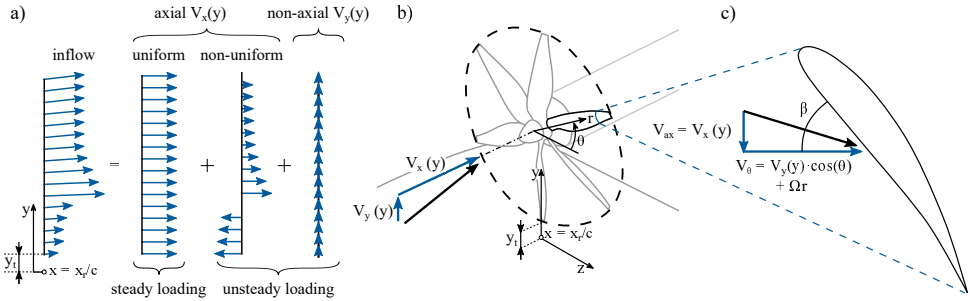
Figure 8.1: a) Decomposition of the inflow at the rotor position (x_r, y_r), b) horizontal V_x and vertical velocity V_y components at the inflow of the rotor and c) definition of axial V_{ax} and tangential velocity V_θ of the blade section at (r,θ).

8

8.1.1 Axial inflow velocity

Inviscid: Circulation

Recall from section 7.1 that the axial induced velocity by the wing's circulation is computed by integration of Biot-Savart's law [181]:

$$V_\Gamma(r) = \int_s \frac{\Gamma(s)}{4\pi} \frac{s \times r}{|r|^3} ds \tag{8.1}$$

Under the assumption that a parabolic source strength distribution of bound vortex filaments lies along the wing's chord line, see figure 8.2a, the distribution of circulation Γ in chord-wise direction x for thin airfoils reads:

$$\Gamma(x) = \frac{3}{4} c_l V_\infty c \left(1 - \frac{x^2}{c^2} \right) \tag{8.2}$$

Substituting equation 8.2 in equation 8.1, and transferring to blade coordinates, reduces the equation for the axially induced velocity $V_{\Gamma,x}$ at the rotors disk to:

$$V_{\Gamma,x}(r,\theta) = \frac{1}{2\pi} \int_0^c \frac{\Gamma(x)(y_r + r\sin\theta)}{(x_r - x)^2 + (y_r + r\sin\theta)^2} dx \tag{8.3}$$

which can be solved analytically. The exact solution can be found in appendix B.1.
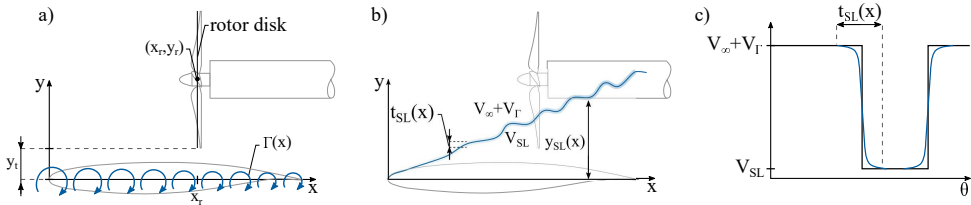
Figure 8.2: Schematic of the modelling of the a) velocity increase by wing's circulation, b) the ingestion of the separated boundary layer and c) variations in blade inflow velocity during a rotation through the shear layer.

VISCOUS: SHEAR LAYER INGESTION

At a critical angle of attack α_c (found by using an empirical relation as a function of the wing's nose radius to chord length r_c/c [182]), the wing's boundary layer separates at the leading edge. The shear layer height y_{SL} is modeled by a linear function parallel to the free-stream direction (see figure 8.2b):

$$y_{SL}(x) = x\tan(\alpha) \tag{8.4}$$

and imposes a jump in velocity when a blade section enters the separated flow region. The blade section transitioning into the separated flow region is modeled by an approximation of the Heaviside step function h in which the slope corresponds to the shear layer thickness t_{SL}, as is shown in figure 8.2c.

$$h(r,\theta) = \frac{1}{1 + e^{-c_1\left(\frac{y_{SL}(x_r)}{y_r + r\sin\theta} - 1\right)}}, \quad c_1(x_r) = \frac{2R\ln\left(\frac{1}{0.99} - 1\right)}{t_{SL}(x_r)}, \tag{8.5}$$

in which c_1 is a coefficient based on the shear layer thickness t_{SL}, see figure 8.2b. Using the self-similar solution of Görtler [184] describing a planar free shear layer, the thickness t_{SL} can be approximated by [185]:

$$t_{SL}(x_r) = \frac{x_r}{\sigma_{SL}\sqrt{2\pi}} \tag{8.6}$$

where σ_{SL} is the empirical spreading parameter [186, 187]. Assuming a thin shear layer gives $\sigma_{SL} = 13.5$.

By the inclusion of a stall criterion $f(\alpha,\alpha_c)$ and defining V_{SL} as zero, the relation C_{SL} corrects the blade sectional axial advance ratio when the blade section enters the shear layer region, i.e. $R\sin(\theta) < y_{SL}(x)$:

$$C_{SL}(r,\theta) = 1 - f(\alpha,\alpha_c)h(r,\theta), \quad f(\alpha,\alpha_c) = \begin{cases} 0, & \alpha < \alpha_c \\ 1, & \alpha \geq \alpha_c \end{cases} \tag{8.7}$$

The axial inflow velocity $V_{ax}(r,\theta)$ is then found as the combination of the free-stream, inviscid and viscous contributions:

$$V_{ax}(r,\theta) = \left(\cos\alpha V_\infty + V_{\Gamma,x}(r,\theta)\right)C_{SL}(r,\theta) \tag{8.8}$$

8.1.2 Tangential inflow velocity

The tangential inflow velocity is defined as the axial velocity. In this case however, the vertical component $V_{\Gamma,y}$ of the wing's circulation is considered:

$$V_{\Gamma,y}(r,\theta) = \frac{1}{2\pi} \int_0^c \frac{\Gamma(x)(x_r - x)}{(x_r - x)^2 + (y_r + r\sin\theta)^2}\,\mathrm{d}x \tag{8.9}$$

By the inclusion of the shear layer correction term C_{SL}, the free-stream velocity and the rotational velocity of the blades, the tangential inflow $V_\theta(R,\theta)$ returns:

$$V_\theta(r,\theta) = \cos\theta \left(\sin\alpha V_\infty + V_{\Gamma,y}(r,\theta)\right) C_{SL}(r,\theta) + r\Omega \tag{8.10}$$

8.1.3 Unsteady blade loading

The inflow field is discretized in azimuthal and radial direction to obtain the rotor loads. The step size should be sufficiently small to model the blade transitioning into to the separated flow region, i.e. $\Delta\theta < t_{SL}/R \approx 0.02\pi$. For each azimuthal position of the blade in the non-uniform flow field, the loads are computed using Blade Element Momentum Theory (BEMT) [27]. This gives a distribution of local blade lift and drag coefficients, that are transformed to the frequency domain, resulting in $\hat{C}_{L,QS}$ and $\hat{C}_{D,QS}$.

Then, following a similar approach as the work of van Arnhem *et al.* [39], a correction for the unsteady aero-propulsive forces is applied (reducing the amplitude and causing a phase delay), by multiplication of the complex local lift $\hat{C}_{L,QS}$ coefficient by the Sears function $\hat{S}$ [40].

$$\hat{C}_L(r,\sigma) = \hat{C}_{L,QS}(r,\sigma)\hat{S}(r,\sigma) \tag{8.11}$$

In equation 8.11, σ is the reduced frequency that defines the degree of unsteadiness of the aero-propulsive forces, given by the loading harmonic n, the local blade chord c_b and the induced velocity of the isolated rotor V_{iso}:

$$\sigma = \frac{n\Omega c_b}{2V_{iso}} \tag{8.12}$$

8.1.4 Helicoidal Surface Theory

The complex blade sectional lift and drag coefficients are used as an input to predict the rotor noise emission, using Helicoidal Surface Theory. This model was developed by Hanson [47] and extended [49] to include unsteady loading effects. For the m-th noise harmonic and n-th loading harmonic, the complex-valued pressure amplitude for the thickness-, lift- and drag noise components are approximated by equation 8.13:

$$\begin{Bmatrix} P_{Vmn} \\ P_{Lmn} \\ P_{Dmn} \end{Bmatrix} = -\frac{2R\rho c_0^2 B \sin\theta_O}{8\pi y (1 - M_x \cos\theta_O)} e^{imB\left(\frac{\Omega R}{c_0} - \frac{\text{sign}(m)|mB-n|\pi}{2}\right)}$$

$$\times \int_{r_{0,hub}}^1 M_r^2 e^{i(\varphi_0 + \varphi_s)} \hat{J}_{|mB-n|} \left(\frac{|m|Br_0 M_t \sin\theta_O}{1 - M_x \cos\theta_O} \right) \begin{Bmatrix} k_x^2 \hat{t}_{b,n} \psi_{V,n} \\ ik_y \frac{\hat{c}_{L,n}}{2} \psi_{L,n} \\ ik_x \frac{\hat{c}_{D,n}}{2} \psi_{D,n} \end{Bmatrix} dr_0 \qquad (8.13)$$

In equation 8.13 $\hat{C}_{L,n}$ and $\hat{C}_{D,n}$ are the n-th complex lift and drag coefficient. ψ_{Vn}, $\psi_{L,n}$ and $\psi_{D,n}$ denote the spatial distribution of the volume, lift and drag surface sources for each loading harmonic. For the lift and drag surface forces, a parabolic distribution over the blade section chord is assumed, which resembles the pressure distribution at large angles of attack.

The thickness sources term $\psi_{V,n}$ is determined by the normalized thickness of the displaced fluid along the blade $H(X)$ (in which X is the normalized blade chord coordinate from -1/2 (leading edge) to 1/2 (trailing edge)). At large angles of attack, the flow can separate at a given chord-wise position X_s over the blade, see figure 8.3a.
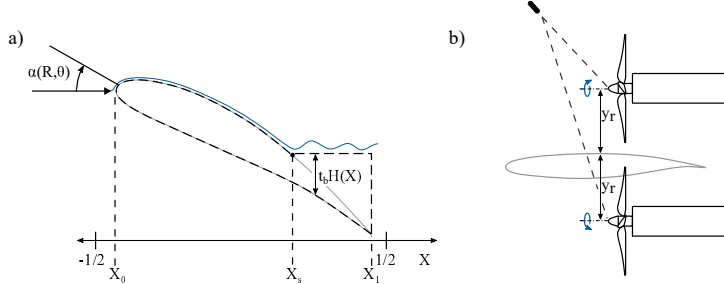
Figure 8.3: Schematics of noise source model features: a) Normalized blade thickness distribution $H(X)$ under large angles of attack and b) image-source model.

The separation point X_s is approximated by a bipolar linear function of the current angle of attack of the blade section α, the angle at which the flow separates at the trailing edge (α_0) and at the leading edge (α_1):

$$X_s(\alpha, \alpha_0, \alpha_1) = \max\left(\min\left(X_1, f\right), X_0\right), \quad f = \frac{(\alpha_1 - \alpha)(X_0 - X_1)}{\alpha_0 - \alpha_1} \qquad (8.14)$$

The values of α_0 and α_1 were found to be 10° and 20° respectively, for the considered blade geometry and operating conditions.

Due to the variations in blade angle of attack during a rotation, $H(X)$ also varies along the azimuth. Consequently, the thickness noise spatial distribution ψ_{Vn} is found by integration of the Fourier transform of $H(X)$:

$$\psi_{Vn} = \int_{-1/2}^{1/2} \widehat{H}_n(X) e^{ik_x X} dX \qquad (8.15)$$

For the case of the isolated rotor, without interference with the airfoil, the computed loads and the tonal noise predictions were compared with experimental data, which showed good agreement (see appendix B.3) validating the computational chain.

Figure 8.4 shows a decomposition of rotor noise in its thickness and loading noise component for the first blade-passing frequency harmonic of the isolated rotor for an advance ratio of $J = 0.3$ and $J = 0.6$. This shows that in upstream directions, i.e. $90° < \theta_o < 270°$, the thickness noise is dominantly contributing, whereas in the downstream direction, loading noise exceeds the thickness noise.
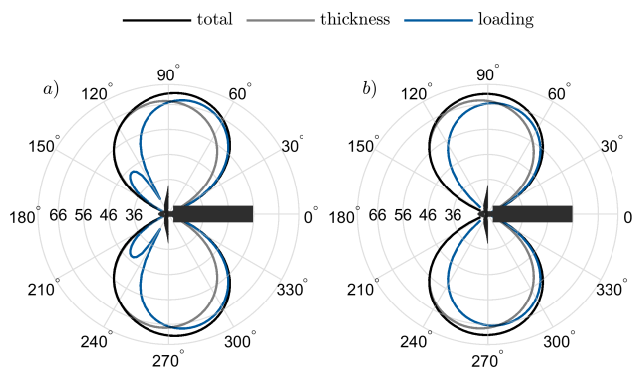
Figure 8.4: Modelled directivity pattern of the 1st *BPF* and contributions of the thickness and loading noise for the isolated rotor for a) $J = 0.3$ and b) $J = 0.6$.

8

To account for the reflection of acoustic waves by the wing's surface, the image-source model [188] is included. In this approach, a second noise source is mirrored along the (x,z)-plane and translated to a vertical position of $y = -y_r$. The predicted tonal noise of the integrated rotor is then the superposition of the original noise source (computed by equation 8.13) and its mirrored counterpart, see figure 8.3b. In the current work, the vertical offset between the real and image rotor axis is approximately equal to one wavelength of the first blade-passing frequency ($2y_r/\lambda_{BPF} \approx 1.1$), indicating that constructive interference may lead to an increase in noise for the first and second blade-passing frequencies.

Note that application of the image-source model is only possible under restrictive conditions. First of all, the wing's chord should be larger than the wavelength of the first blade-passing frequency, which is met for the conditions in this study ($c/\lambda_{BPF} \approx 1.6$). Secondly, the image-source model does not hold when the rotor is operated close to an edge, due to diffraction of acoustic waves [189]. Since both the tip-gap ($0.27\,R$) and rotor–trailing-edge distance ($(c - x_r)/\lambda_{BPF} \approx 1.1$, for most of the concerned conditions) is large in the current work, such effects are not expected to occur. Nonetheless, analytical formulations are available to include such acoustic installation effects [189].

Finally, it is important to note that, by using the image-source model, only the noise above the rotor-wing system can effectively be predicted. The model does not consider the shielding properties or scattering effects of the wing, meaning that noise predictions below the pressure side of the wing are not included.

8.1.5 Experimental validation

To validate the model, experiments were conducted with a single rotor above an airfoil for a wide range of angles of attack, advance ratios and three rotor positions along the chord. The extracted data consist of the rotor thrust and torque and microphone measurements towards both the suction and pressure side of the wing. Additionally, the flow was characterized using stereoscopic-PIV and pressure orifices. During the flow measurements, the rotor was traversed in span direction to generate a time-averaged volumetric flow reconstruction and surface pressure contours over the wing. The experimental setup and measurement techniques were described in section 4.3.

8.2 Aeroacoustic characteristics

The aeroacoustic properties of the Over-The-Wing rotor system will be elucidated by analysis of the experimental data. The difference in noise emission compared to the isolated rotor, the relative contributions of tonal and broadband noise and the effect of varying operating conditions through the advance ratio and angle of attack are investigated. A fixed rotor position along the wing's chord of $x_r/c = 0.3$ is considered. The role of the rotor position on noise emissions are covered in more detail in section 8.3, along with a comparison to model predictions.

8.2.1 Installed rotor noise

The effect of the wing on the rotor noise is shown by comparison of the experimental data from the isolated and installed rotor. Noise spectra are generated using Welch's method by dividing the microphone data into blocks of 4096 samples with 50% overlap, yielding a frequency resolution of 10 Hz. Furthermore, a Hanning window is applied to mitigate spectral leakage and all results are scaled to an observer distance of 1 m from the rotor hub. The noise spectra in the rotor plane ($\theta_O = \pm 90°$), obtained by bi-linear interpolation of the *SPL* values from the microphones, are presented in figure 8.5 for an advance ratio of $J = 0.6$, where a relatively low amount of thrust is provided by the rotor and $J = 0$, corresponding to hover conditions.

For cruise conditions (figure 8.5a) the results for the isolated rotor, shown by the solid gray lines, exhibit a dominant peak at the first *BPF*. The higher harmonics of the *BPF* show a strong reduction (> 20 dB) in sound pressure amplitude and fall below the broadband noise floor after the fourth harmonic. Note that also several weak spectral peaks occur at the shaft frequency (1/6th *BPF*) and its harmonics, attributed to a slight imbalance in the rotor-motor combination.

For the rotor-installed configuration, spectra are plotted for the suction side ($\theta_O = 90°$) and the pressure side ($\theta_O = 270°$). For the former, an increase in the tonal and high frequency (> 4 *BPF*) broadband noise levels is observed. The first *BPF* increases by approximately 3 dB, while the second and third harmonic attain up to 10 dB higher noise levels. On the pressure side however, noise shielding by the wing reduces the 1st *BPF* with 10 dB. Furthermore, the high-frequency broadband noise is also lower when compared to the isolated rotor.

The dashed lines show the installation noise component, i.e. the set-up's noise emission without the rotor installed. Comparison of the spectra, and an analysis using noise
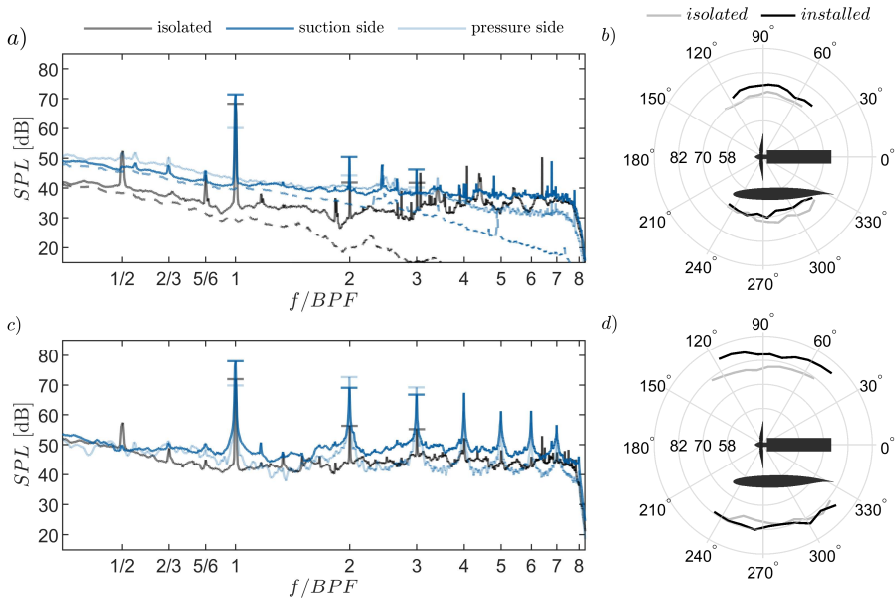
Figure 8.5: Noise spectra in the rotor disk plane without inclination ($\alpha = 0°$) for a) $J = 0.6$ and c) $J = 0$ for $x_r/c = 0.3$. The horizontal lines in the spectra highlight the sound pressure levels of the first three blade-passing frequency harmonics. The dashed lines in the spectra of a) are the results with the rotor removed. b) and d) show the directivity pattern of the $OASPL$ (for $f = BPF \cup [2\ BPF\ , \infty)$) for $J = 0.6$ and $J = 0$, respectively.

source localization techniques [151, 154], showed that low-frequency broadband noise ($f < 2BPF$) for the installed configuration is dominated by an external noise source of the wind tunnel configuration. Instead, for the high frequencies ($f > 3BPF$), a moderate increase in broadband noise is observed when the rotor is active.

The overall noise level ($OASPL$) is obtained by integration of the spectra (without applying a frequency weighting filter) for the BPF and all frequencies exceeding $f \leq 2BPF$. This frequency range is chosen to isolate the external noise source of the closed wind tunnel configuration. The directivity pattern of the $OASPL$ is plotted in figure 8.5b. At each of the observer angles on the suction side, the installed rotor shows larger values than the isolated rotor's data, in particular in the upstream direction ($\theta_O = 115°$). The $OASPL$ values on the pressure side show a reduction in noise up to 5 dB which is found in the downstream direction in particular. In the upstream direction ($\theta_O = 240°$) the shielding effect is limited since the isolated and installed configuration show a comparable value of the $OASPL$.

At hover conditions (figure 8.5c), the isolated rotor's tonal noise increases to 72 dB. Moreover, an elevation in broadband noise is apparent which is attributed to flow separation occurring over a part of the span of the rotor blades near the root. The increase in the tonal noise by the insertion of the wing is more severe for $J = 0$ compared to the results of $J = 0.6$ (figure 8.5a). In particular, the higher harmonics exhibit a strong increase (> 15 dB). Moreover, the rotor harmonics for the installed condition are characterized by broadband humps in the neighboring frequencies, indicative of a form of haystacking. While the tonal

and broadband noise is reduced in the pressure side's direction, an unexpected increase of the second and third harmonics of the *BPF* compared to the suction side's value is seen here. Note that these harmonics are more sensitive to variations in inflow conditions and installation effects than the first *BPF* [190].

The noise directivity pattern in figure 8.5d shows more noise radiated in the forward direction ($\theta_O = 115°$) and backward ($\theta_O = 60°$), due to the increase in broadband noise. Isolated and installed rotor's emissions in the wing's pressure side direction are comparable in magnitude for this advance ratio. The benefit of shielding is therefore negated by the increased rotor noise levels. Installation effects are greater at hover ($J = 0$) conditions than at cruise conditions ($J = 0.6$). To explain the mechanism behind this, the measured velocity fields of the two conditions are presented in figure 8.6a and b. At the zero advance ratio, rotor thrust is higher, leading to a stronger pressure jump and contraction of the rotor disk streamtube. Consequently, the velocity field shows a region of flow reversal between the rotor and wing, as indicated by the streamlines below the rotor tip. The Turbulent Kinetic Energy *TKE* in figure 8.6c and d reveal a great flow unsteadiness at the inflow of the rotor for $J = 0$, indicating intermittent separation of the wing's boundary layer. This explains the observed haystacking and elevated tonal components through blade-vortex interaction [102].
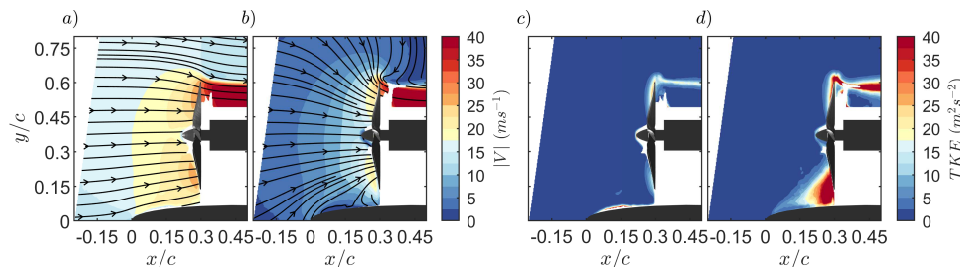
Figure 8.6: Velocity magnitude contours $|V|$ and 2D velocity streamlines for a) $J = 0.6$ and b) $J = 0$ and Turbulent Kinetic Energy *TKE* contours for c) $J = 0.6$ and d) $J = 0$.

8.2.2 Effect of angle of attack

During transition from vertical to horizontal flight, angles of attack around stall are encountered. The effect of angle-of-attack on rotor noise is presented for a high ($J = 0.6$, figure 8.7a & b) and low-advance ratio ($J = 0.3$, figure 8.7 c & d). One should note that the steady loads of the rotor are also affected by the inclination of the rotor-system but this falls outside the scope of the current work.

Inspection of figure 8.7a shows that the first *BPF* tone remains unaltered until $\alpha = 10°$. Broadband levels are dramatically elevated for $\alpha = 12°$, which marks the condition where the boundary layer of the wing separates near the leading edge. The first blade-passing frequency harmonic is reduced by 5 dB for this angle of attack.

The effect of angle of attack on noise directivity is presented in figure 8.7b by plotting the *OASPL*. No significant changes are exhibited, until reaching the stall angle. An increase in sound pressure level is observed in all directions but occurs most profoundly in the upstream radiation direction $\theta_O = 120°$.
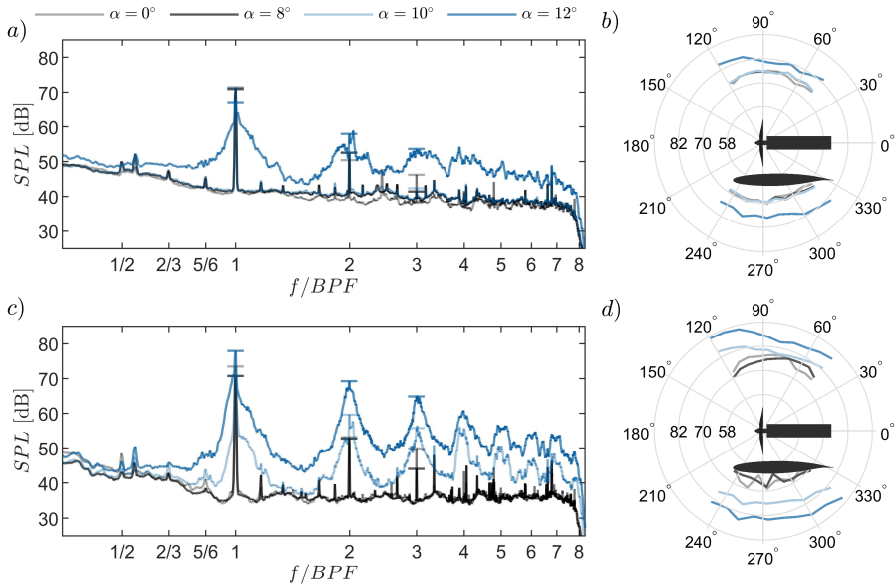
Figure 8.7: Noise spectra in the rotor disk plane ($\theta_O = 90°$) for increasing inclination for a) $J = 0.6$ and c) $J = 0.3$ for $x_r/c = 0.3$. b) and d) show the directivity pattern of the $OASPL$ (for $f = BPF \cup [2\,BPF, \infty)$) for $J = 0.6$ and $J = 0.3$, respectively.

Figure 8.7c shows the spectra for a reduced advance ratio ($J = 0.3$), where the rotor generates more thrust, representative of close-to-vertical flight conditions. In this case, for an angle of attack increase from $\alpha = 0°$ to $\alpha = 8°$, the BPF noise level exhibits a slight reduction, which can be attributed to decreased blade loading. At $\alpha = 10°$ and $12°$, close to the wing's stall angle an augmentation of the broadband noise around the BPF harmonics is seen. The $OASPL$ directivity in figure 8.7d increased sound pressure levels in the upstream direction $\theta_O = 120°$ for these cases by turbulent ingestion.

To investigate the source mechanism of the observed spectra for $J = 0.3$, the flow topology and surface pressure are plotted for the various angles of attack in figure 8.8. The velocity magnitude and streamlines are extracted in the (x,y)-plane, at an offset from the rotor hub of $dz = 0.2c$.

For $\alpha = 0°$ (figure 8.8a) the pressure distribution is mirror symmetric about $z = 0$ plane, where the absolute value of pressure is 25% higher in the mid-span position compared to the edges of the domain. In chord-wise direction, a low-pressure region is found upstream, induced by the rotor. The velocity streamlines clearly show the contraction of the rotor's stream tube, both on the wing's surface and the extracted velocity field slice. By increasing the wing angle of attack, the flow accelerates over the suction side and consequently, the static pressure over the wing decreases as is shown in figure 8.8b. The higher inflow velocity at the rotor disk leads to a decreased thrust (recall chapter 7), which is also manifested in a reduced contraction of the streamlines. The inclination of the rotor also results in an increase in thrust for the advancing side ($z < 0$) compared with the retreating side ($z > 0$) of the rotor disk. As a consequence, the pressure distribution exhibits mirror-asymmetry
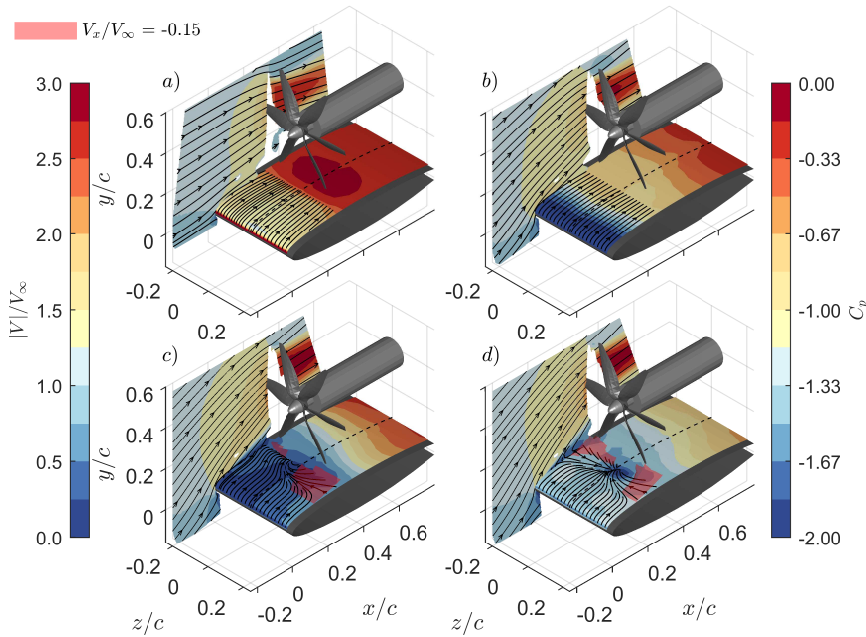
Figure 8.8: Pressure coefficient C_p contours over the wing's surface in the (x,z)-plane and projected 2D streamlines extracted at $dy = 0.025c$, normalized velocity magnitude $|V|/V_\infty$ and 2D velocity streamlines in the (x,y)-plane at $dz = -0.2c$ and iso-surfaces of stream-wise velocity of $V_x = -0.15V_\infty$ for a) $\alpha = 0°$, b) $\alpha = 8°$, c) $\alpha = 10°$ and d) $\alpha = 12°$ for $x_r/c = 0.3$ and $J = 0.3$.

8

about the projected rotor axis.

Figure 8.8c for $\alpha = 10°$, shows a further reduction of the pressure in front of the rotor due to the flow acceleration around the leading edge. However, below and slightly in front of the rotor a low-pressure region is found, entraining fluid from span-wise directions, which lifted upwards and expelled into the rotor disk. Consequently, the flow stagnates as it approaches the rotor and separates from the wing as indicated by the vertical velocity slices. The spatial extent of the reversed flow region is shown by the red iso-surfaces. This shows that the air is primarily entrained from the positive span coordinate. Such flow topology creates a highly disturbed inflow, explaining the significant tonal noise increase.

A further increase in the angle of attack in figure 8.8d, marks the early stages of stall for the used wing profile. In this case, the rotor's suction is not sufficient to delay the boundary layer separation indicated by the higher surface pressures at the leading edge. Flow is entrained inside the separated boundary layer from spanwise and downstream directions towards a low-pressure region slightly upstream of the rotor. The reversed flow iso-surfaces, in this case, are mirror symmetric around $z = 0$ and fill the area between the rotor disk and wing's surface. Note that the stagnation region as a result of the complex aerodynamic interaction between the rotor and the wing is not included in the proposed model.

8.2.3 Contributions of tonal and broadband noise

It was shown that the presence of the wing alters both the tonal and broadband noise created by the rotor. Considering the aeroacoustic model only computes the tonal noise, it is therefore valuable to examine the relative share of this to the overall sound pressure level. By computing phased-averaged noise spectra, the broadband noise is filtered out [152, 153]. The tonal overall sound pressure level can then be computed by integration of the phase-locked spectra. Subsequently, the contribution of the broadband noise follows by subtracting the tonal noise from the microphone auto-powers. The resulting tonal and broadband overall sound pressure level in the rotor plane, are presented in figure 8.9 as a function of the angle of attack α.
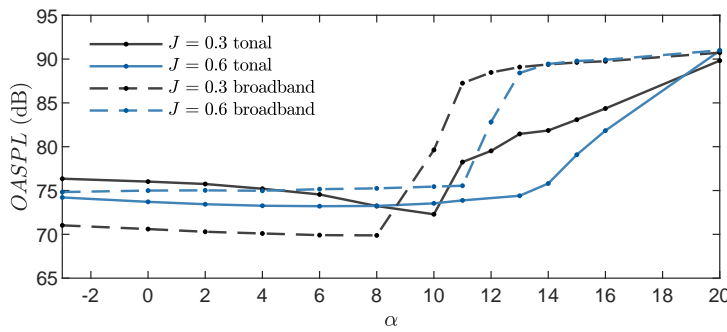
Figure 8.9: *OASPL* in the rotor disk plane, obtained by integration of the tonal and broadband spectra, using microphone data from the wing's suction side direction. Displayed are data from a rotor position of $x_r/c = 0.3$ as a function of the angle of attack α.

From this follows that the tonal and broadband noise are within approximately 3 dB of each-other in the pre-stall regime, for angles up to $\alpha = 10°$. A supplementary analysis using noise source localization techniques (not shown here for brevity) confirmed that rotor self-noise is the dominant broadband noise source under these condition. For the lower advance ratio of $J = 0.3$, the rotor loads are higher and therefore the contribution of tonal noise is greater than that of broadband noise. For $J = 0.6$ the opposite is observed. As expected, the broadband noise becomes dominant in early stall conditions, leading to an increase in the order of 10 dB.

8.3 Model results

In this section, the model predictions, which are limited to the tonal components, are compared to the measurements. This starts with a comparison of the wing-induced flow field, which is used as a steady inflow distortion in the aeroacoustic chain.

8.3.1 Velocity field

The experimentally obtained wing-induced flow field is extracted from data of the isolated wing. The data are then sampled at the position of the rotor ($x_r = 0.3$) and decomposed in axial V_{ax} and azimuthal V_θ components, which are presented in figure 8.10a and b, re-

spectively. The inflow velocities of the model, as defined by equations 8.8 and 8.10 are presented in figure 8.10d and e, for the same conditions.
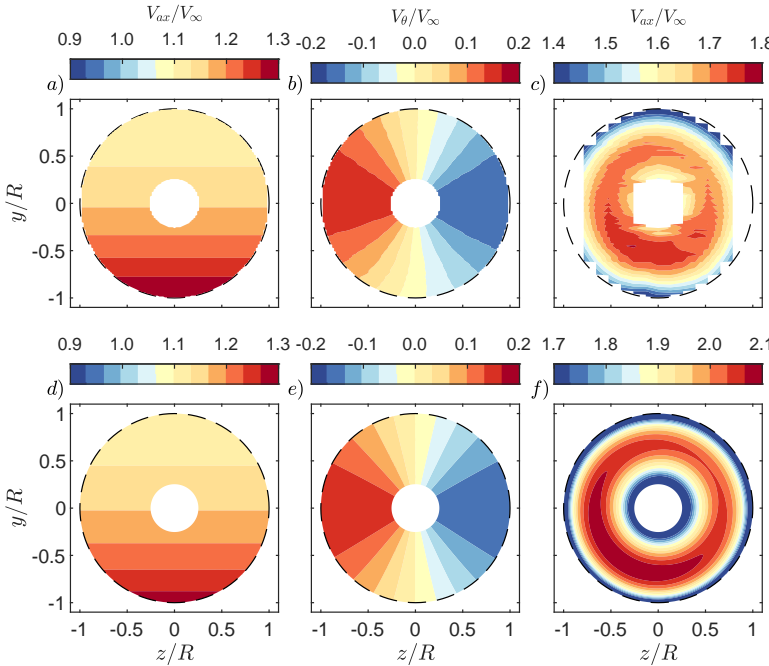
Figure 8.10: Normalized velocities in the rotor plane for $x_r/c = 0.3$, $y_r/R = 0.27$ and $\alpha = 8°$. The top row presents the experimental data of a) axial and b) azimuthal velocity of the isolated wing extracted at $x/c = 0.25$, and c) axial velocity of the rotor-wing system for $J = 0.3$ extracted slightly upstream of the disk at $x/c = 0.25$. The bottom row presents the model predictions for similar conditions.

Both the experimental and modeled results show the expected increase in axial velocity compared to the free-stream conditions, as shown in figure 8.10a and d. The model captures the axial velocity distribution with an overprediction in the magnitude of the wing-induced velocity by 10%. The measured and modeled azimuthal induced velocity by the wing are in good agreement, as is shown in figure 8.10b and e. The distribution shows an increase in azimuthal velocity on the advancing side and a reduction on the retreating side of the rotor.

The measured inflow velocity of the installed configuration, with the rotor operated at $J = 0.3$, is presented in figure 8.10c. It is extracted upstream of the rotor disk at $x/c = 0.25$, approaching the disk being limited by the optical blockage of the blades. The combination of the steady inflow distortion of the wing and the rotor-induced flow generates velocity distribution that is maximized in the lower-left and minimized in the top-right quadrant of the rotor disk.

The model velocity distribution is the superposition of the predicted wing and the (non-uniform) rotor-induced flow field. Note that the rotor-induced velocities from BEMT are solely defined at the rotor disk, hence the predicted velocity field, as presented in figure 8.10f, is extracted at the rotor position of $x/c = 0.3$. To account for this, the contour

levels have been corrected by a factor of 0.85 for the estimated streamtube contraction rate
[32], based on the displaced extracted frame and the effective thickness of the rotor disk.
The analytical axial induced velocity shows a similar distribution as the measurements
(compare figure 8.10c and figure 8.10f), with extreme values in the lower-left and top-right
quadrants. This validates the azimuthal variations in inflow conditions that are predicted
in the model.

8.3.2 Rotor loads

The wing-induced acceleration of the flow reduces the steady loads for the fixed-pitch
rotor. The measured and predicted values of the rotor's thrust and torque coefficients
are indicated by the markers for different advance ratios and varying angles of attack in
figure 8.11. Here, the modeled steady thrust and torque are computed by averaging the
loads over one rotor rotation and presented by the solid lines. A similar trend for thrust
is captured by the model in figure 8.11a, although a slight under-prediction up to 5% is
observed. When the angle of attack of the rotor-wing system increases, the rotor's thrust
is reduced due to the wing's circulation accelerating the flow towards the rotor. This effect
is more pronounced when the advance ratio is increased. Beyond the isolated wing's stall
angle of 12°, the thrust is increased, resulting from the ingestion of the low-momentum
boundary layer. The rotor's torque coefficient, as shown in figure 8.11b, shows a similar
trend as the thrust curve. In this case, the model results provide a closer match to the
measured values.
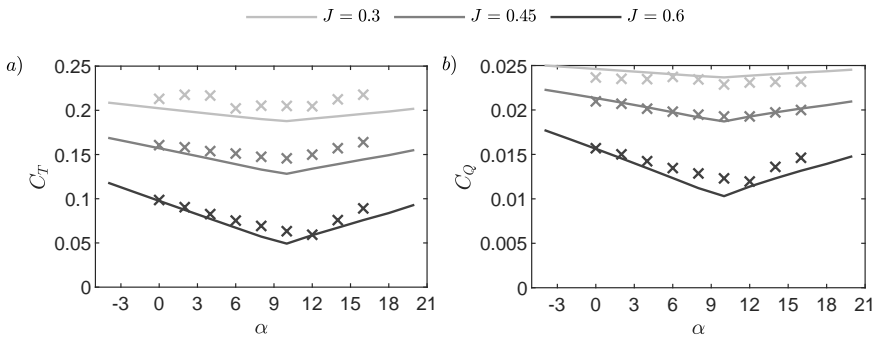
Figure 8.11: Steady installed rotor's thrust coefficient C_T and torque coefficient C_Q as a function of the angle of
attack for x_r/c = 0.3. The measurements are given by the markers, while the computed loads are shown by the
solid lines.

In figure 8.12, the predicted distribution of the thrust coefficient over the rotor disk,
normalized by the isolated rotor thrust distribution, is presented for increasing angle of
attack and an advance ratio of J = 0.6. For this advance ratio, the largest relative variations
in thrust are expected from the model. An increase is observed in the variation of thrust
along the azimuth with increasing angle of attack. For α = 8° in figure 8.12b, the thrust
is reduced over the entire disk with a minimal value found in the lower right quadrant of
the disk. However, the strongest variations in thrust are found for α = 14° in figure 8.12c.
Here the thrust partly recovers by the fact that the wing's circulation is reduced compared
to α = 8°. Moreover, for the current rotor position, a limited region of the boundary layer

ingestion on the lower side of the disk generates enhanced thrust levels. Such abrupt changes in thrust adversely affect the tonal components of the rotor's acoustics, which is shown in the following sections.
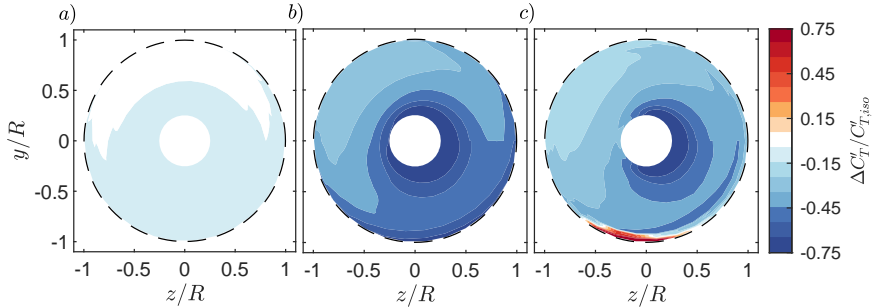
Figure 8.12: Model predictions of the blade in-plane sectional thrust distribution with respect to an isolated rotor without inclination ($\Delta C'_T = C'_T - C'_{T,iso}$), for $x_r/c = 0.3$ and $J = 0.6$, for a) $\alpha = 0°$, b) $\alpha = 8°$ and c) $\alpha = 14°$.

8.3.3 NOISE HARMONICS

To validate the model noise predictions, the experimental and modeled directivity patterns of the first *BPF* are presented in figure 8.13 for the same conditions as were presented in figure 8.12. Phased locked spectra [152, 153] are used in this case, strongly attenuating the broadband noise. For $\alpha = 0°$ and $\alpha = 8°$, in figure 8.13a and b respectively, both the experimental and model results show the expected directivity pattern in which the emitted noise is maximized in the rotor disk plane, i.e. $\theta_O = 90°$ and good agreement is obtained. Differences between modeled and measured values are below 2 dB over the greater part of measured directivity pattern. Some discrepancies are evident towards the downstream directions $\theta_O = 60°$ in figure 8.13b. The experimental results show strong variations with chord-wise rotor position for this emission direction and therefore the differences are associated with interference effects. A satisfactory resemblance between modeled and experimental results is found, showing a significant increase in tonal noise in forward and backward directions when the detached boundary layer is ingested (figure 8.12c).
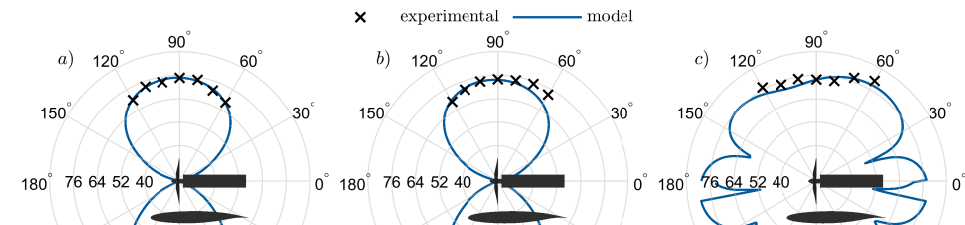
Figure 8.13: Experimental and modeled directivity pattern of the first *BPF* of the installed rotor for $x_r/c = 0.3$ and $J = 0.6$, for a) $\alpha = 0°$, b) $\alpha = 8°$ and c) $\alpha = 14°$

The first three measured and modeled noise harmonics, relative to the isolated rotor at $\alpha = 0°$ ($\Delta SPL = SPL - SPL_{iso}$), are presented in figure 8.14 for $\alpha = 8°$ and $\alpha = 14°$. The

modeled results without the inclusion of the image source are also presented here, to remove the effect of the reflection as assessed from simple geometrical acoustics (ray-theory) arguments.

Note that the experimental spectra of the isolated rotor could not be generated through phase-averaging since the position of the shaft throughout acquisition was not available. Nonetheless, the broadband noise was found to have a negligible effect on the amplitude of the first two blade-passing frequency harmonics for the isolated rotor. Despite that, generating spectra without phase-averaging reduces the tonal amplitudes due to small variations in rotational velocity during acquisition. This loss was found to be a constant 2 dB (results presented in appendix B.4) and all isolated rotor spectra have been corrected for this when computing the ΔSPL.

For $\alpha = 8°$ in figure 8.14a, in the disk plane (center column), the experimental results show an increase in the SPL of the first and second BPF by 3 and 7 dB respectively, compared to the isolated rotor. The model (blue line) shows a similar elevation of the harmonic noise levels and predicts the values within an accuracy of 3 dB. Moreover, the model predicts a stronger effect on the third harmonic, which is increased by 14 dB. Reliable experimental values for this frequency have not been obtained due to the presence of broadband noise in the isolated rotor's spectral values.
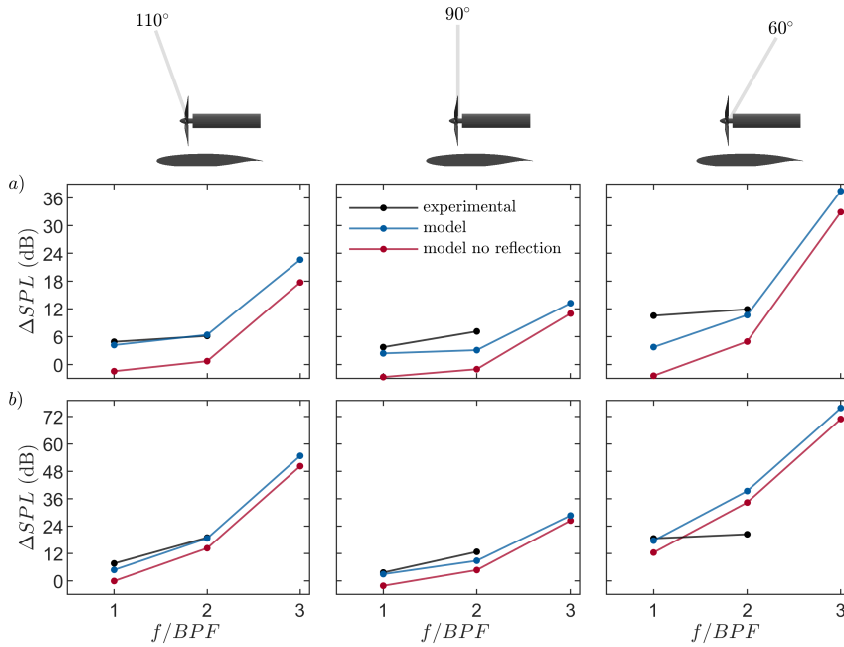
Figure 8.14: Difference between the tonal components of the installed rotor and the isolated rotor at $\alpha = 0°$ (i.e. $\Delta SPL = SPL - SPL_{iso}$) for $x_r/c = 0.3$ and $J = 0.6$ in which a) $\alpha = 8°$ and b) $\alpha = 14°$.

The predicted effect of the reflection due to the presence of the wing is evaluated by comparison of the red (rotor aerodynamic noise) and blue line (rotor aerodynamic noise and reflection). It is clear that the first and second BPF are primarily elevated due to the

reflection since the installed rotor's aerodynamic noise is in fact slightly lower (<1 dB) than that of the isolated rotor due to the reduction in steady loads. The third harmonic, however, exhibits a stronger dependence on the wing's aerodynamic effect, where the aerodynamic noise is increased by 7 dB compared to the isolated rotor. When considering up and downstream observer positions (left and right columns of figure 8.14a), effects due to unsteady loading are expected to be more pronounced. This is reflected in the model results by a noticeable increase in the second and third blade-passing frequency harmonics. A good match between experimental results and predictions is found, except for an under-estimation of the first BPF by approximately 8 dB for $\theta_O = 60°$. For post-stall conditions (figure 8.14b), ΔSPL values for the second and third harmonics are elevated compared to the attached flow conditions. Similar results are again found for the experimental results and model predictions, with discrepancies below 3 dB for most of the results. However, a signification over-prediction is present for $\theta_O = 60°$, for the second blade-passing frequency.

Figure 8.15 compares the rotor noise that is radiated over the suction side (black solid line) with the noise that is radiated towards the pressure side of the wing (blue dashed line). Only the aerodynamic effect of the wing is accounted for here, i.e. reflections from the image-source model are excluded. For $\alpha = 8°$, in figure 8.15a, the discrepancies between radiated noise towards the upper and lower sides are restricted to angles close-to-parallel to the rotor axis in downstream direction. In contrast, figure 8.15b illustrates that when the rotor ingests the shear layer, such discrepancies are primarily observed closer to the rotor disk plane. Notably, local noise minima are found around $\theta_O = 60°$ and $\theta_O = 250°$.
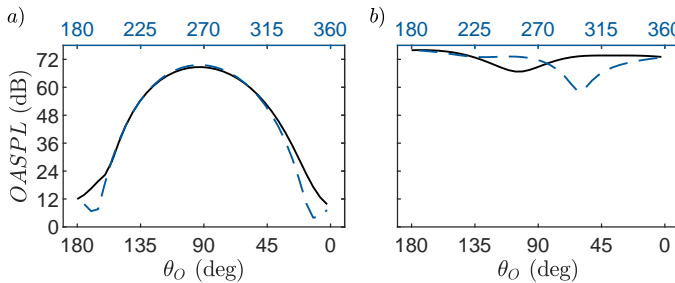
Figure 8.15: Comparison between the modeled $OASPL$ (obtained from the first three BPF-harmonics) over the suction (with the exclusion of reflections) and pressure side for $x_r/c = 0.3$ and $J = 0.6$ in which a) $\alpha = 8°$ and b) $\alpha = 14°$.

8.3.4 Effect of rotor positioning

So far, a fixed rotor position was of $x_r/c = 0.3$ was considered. To investigate the effect of rotor positioning along the wing's chord, the $OASPL$, generated from the first three blade-passing frequency harmonics, are presented in figure 8.16 for $\alpha = 8°$.

The result for $\theta_O = 75°$ is presented in figure 8.16a. The experimental data for this observer angle is shown by the markers. While the model underestimates the tonal noise increase for the forward-positioned rotor by 1.5 dB, both model and experimental data show that the tonal noise is minimized for a mid-chord positioned rotor for this emission
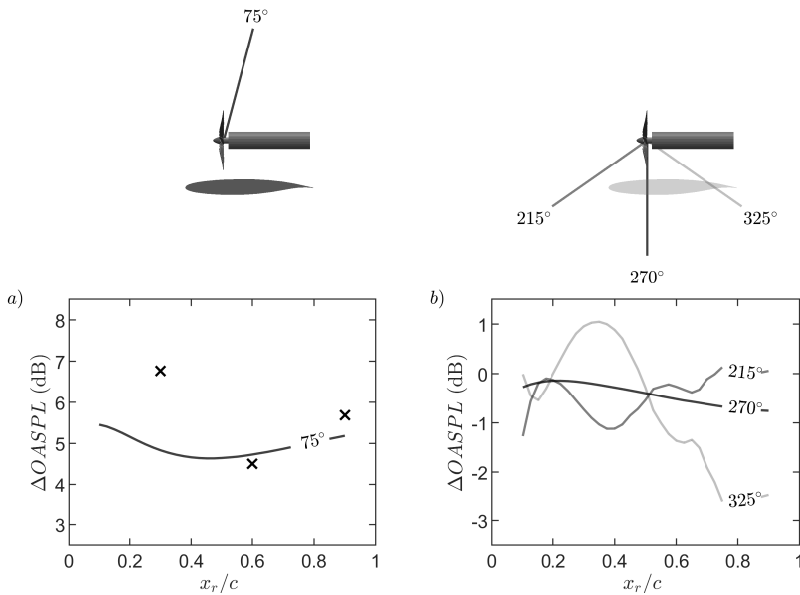
Figure 8.16: Predicted tonal $\Delta OASPL$ levels with respect to the isolated rotor (for $\alpha = 0$ °), for different rotor positions along the chord for $\alpha = 8$ ° and $J = 0.6$. a) Results for an observer position of $\theta_O = 75°$ in which the crosses show the experimental results (obtained from the first three BPF-harmonics) averaged over $\theta_O = 75 \pm 5°$. b) The predicted values on the pressure side of the wing, in which only the aerodynamic effect of the wing is considered.

8

direction. This can be explained from the fact that the rotor's steady loads in the pre-stall regime are higher for a more aft-mounted rotor (as was shown in chapter 7), while the variation in loading along the azimuth typically decreases through the circulation distribution along the wing's chord. Nonetheless, as was shown in figure 8.14, the increase in noise for observer positions near the disk plane is primarily the result of constructive interference and therefore variations with chord-wise positioning are limited.

More relevant is to investigate the rotor noise that is radiated towards the wing. Predictions for such observer angles are presented in figure 8.16b. In this case, the image source below the wing is removed, hence only the aerodynamic effect of the wing on the rotor noise is considered. The result in the rotor disk plane ($\theta_O = 270°$), shows a reduction between 0 and 1 dB with respect to the isolated rotor. However, note that the steady loads of the rotor are also reduced up to 35% for these operating conditions. While variations with rotor position are marginal, tonal noise variations are slightly enhanced for a front-mounted rotor.

The effect of the unsteady loading (and therefore rotor positioning) is increased by considering directivity angles closer towards the direction of the rotor shaft, for example $\theta_O = 325°$. These results show a maximization of the noise for a rotor positioned around 40% chord with variations up to 4 dB. The data of $\theta_O = 215°$ show an observer direction at which the thickness noise outweighs the loading noise for the used rotor geometry (recall

figure 8.4). In this direction variations with chord position are lower again since the effect of unsteady loading is suppressed.

8.4 CONCLUSION

The modeled steady inflow distortion and distribution of the rotor-induced flow field correspond to that of the aerodynamic measurements. The resulting rotor loads in the pre-stall regime show a reduction in thrust for each blade sectional position with respect to the isolated rotor. Nonetheless, gradual variations in loading along the blade's azimuth are found which depend on the geometric angle of attack and rotor position along the wing. In these conditions, the model predictions and experimental results both show a similar increase (3 - 7 dB) of the tonal noise of the first two blade-passing frequency harmonics with respect to the isolated rotor, or observer positions in the rotor disk above the wing. The model predictions show that the tonal noise due to unsteady loading is minimal for these emission angles, and the observed increase in sound pressure level is primarily due to the reflections from the wing. Instead, the third harmonic exhibits a greater dependency on the aerodynamic effect of the wing and is elevated up to 14 dB. While the wing reflects the noise of the rotor at the suction side, the measurements show a reduction in tonal noise up to 10 dB and the broadband noise floor with respect to the isolated rotor below the wing.

In post-stall conditions, more rapid variations in rotor loads along the azimuth are found, during which the wing's shear layer is ingested. This results in a stronger elevation of the tonal components around the wing's suction side in the normal direction, up to 12 dB for the first two-blade passing harmonics.

A parametric study of the experimental results and model predictions, for pre-stall conditions, shows that tonal noise above the rotor is minimized for a mid-chord rotor position. For emission directions downstream, where the effects due to unsteady loading are more pronounced, the model predicts a maximization of the noise for a rotor positioned at 40% chord and variations with rotor positioning of up to 4 dB. Although the model accurately captures the trend behavior with rotor positioning, discrepancies exist between predicted and measured noise values in the downstream direction, where unsteady loading effects are more pronounced. Moreover, the experimental results show that for low-advance ratios and angles of attack close to the wing's stall angle, the intermittent formation of a flow-reversal region between the rotor and wing leads to an additional increase in rotor noise by blade-vortex-interaction. Such effects are not included in the model which explains part of the observed under-estimates.

9

Experimental simulation of take-off trajectory

In chapter 7, the aerodynamic interactions were investigated through velocimetry and pressure orifices at fixed positions along the span, under quasi-steady operating conditions. However, the advance ratio and angle of attack will change continuously throughout the flight envelope, potentially leading to transient aerodynamic effects that could impact the performance. Additionally, the highly unsteady and rotational nature of the rotors' slipstreams may introduce complex three-dimensional interactions not captured by the planar measurements.

The aim of this chapter is to investigate the three-dimensional flow topology during a tilt-wing take-off maneuver. For this, time series of the wind-tunnel operating conditions, that correspond to a reference trajectory, are defined in section 9.1. The rotor-wing system is then operated in dynamic conditions for the wind-tunnel velocity and geometric angle of attack, during which the flow is characterized using Lagrangian Particle Tracking employing Helium-Filled Soap Bubbles. The presented results of the experiments include an analysis of the time-averaged flow field in section 9.2 and the instantaneous flow field during crucial stages of the flight envelope in section 9.3. In the final part of section 9.3, the results obtained for the dynamic operating conditions are compared with quasi-steady measurements to identify transient aerodynamic effects.

9.1 Operating conditions

A reference eVTOL tilt-wing flight envelope is chosen from literature [22] and scaled according to the wing chord length. Figure 9.1a presents the vertical H and horizontal S displacement of the vehicle during the scaled reference flight path. Note that the flight path is not a pure vertical take-off trajectory but rather a steep ascent profile.

Time series of the angle of attack α and free-stream velocity V_∞ for the considered rotor-wing system (the same system as used in chapter 7) are then found by using the loading measurements which have been obtained for a wide range of angles of attack

This chapter is based on publication [162].
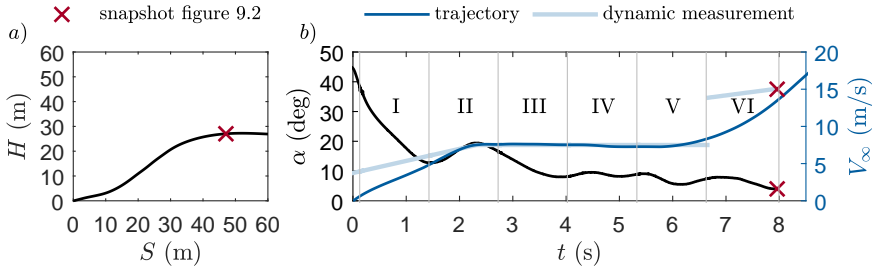
Figure 9.1: a) Reference trajectory of eVTOL flight envelope. b) Time series of the angle of attack and free-stream velocity and the discretization of the measurements. The transparant blue line shows the actual wind-tunnel velocity during the measurements. The red marker shows the conditions of the extracted flow field in figure 9.2.

and rotor advance ratios [160]. A constant rotational velocity of the rotors is assumed here, and a thrust-to-weight ratio of 0.8 is chosen to obtain realistic acceleration values. Details on the process from trajectory to wind tunnel conditions can be found in appendix C. The corresponding time series of the wind-tunnel free-stream velocity and geometric angle of attack along the trajectory are presented in figure 9.1b, by the black and blue lines, respectively. The time series show large values of the angle of attack, in particular in the initial two seconds of take-off. Nonetheless, the flight velocity is low here. After acceleration, the flight velocity reaches a plateau between two and six seconds, during which the angle of attack is gradually decreased. The final two seconds of the maneuver show the transition towards cruise; whereupon flight speed increases again and a further reduction in the angle of attack is observed.

9.1.1 Experimental arrangement

The experimental setup was presented in section 4.3. The measurements are split into seven successive measurements (of 1.33 s) over the time series of the flight trajectory, see figure 9.1b. Note that there are some discrepancies between the trajectory defined and measured values of the free-stream velocity V_∞, which includes a discontinuity between the sixth and seventh measurements. This is a result of the limited acceleration of the wind tunnel. Nonetheless, the timescales along the continuous part of the experimental time series are comparable to that of the trajectory-based operating conditions. For a number of operating conditions that lie along the flight trajectory, quasi-steady measurements are conducted as well, as presented in table 9.1.

Table 9.1: Operating conditions of the quasi-steady measurements.

measurement index	J	V_∞ [m/s]	α [deg]
a	0.154	7.5	8
b	0.154	7.5	12
c	0.154	7.5	20
d	0.308	15	4

9.2 Time-averaged flow topology

The time-averaged flow field is presented for a fixed operating condition of $V_\infty = 15$ m/s ($J = 0.154$) and $\alpha = 4°$ (measurement index d in table 9.1). The position of this operating condition along the flight envelope can be found in figure 9.1. An overview of the measurement domain is presented in figure 9.2a and covers the complete suction side of the wing. Moreover, half a chord's length is measured both upstream and downstream of the wing. The red iso-surfaces in figure 9.2a show that the measurement domain stretches a length of roughly two rotor diameters in both positive and negative span direction from the center rotor. Around the center rotor, multiple planes are extracted to investigate span-wise variations in the flow.
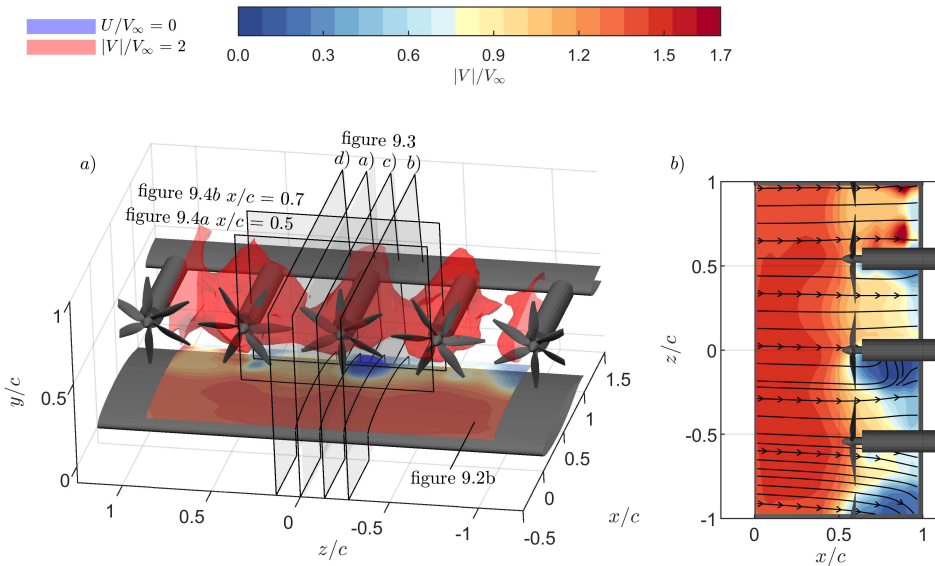
Figure 9.2: Extracted time-averaged flow field ($t = 1.33$s, ≈ 3000 blade passages) for a constant $\alpha = 4°$ and $V_\infty = 15$ m/s ($J = 0.154$) (see figure 9.1 for flight position and conditions). The red and blue iso-surfaces highlight regions of high momentum and flow stagnation, respectively. a) Overview of measurement domain and extracted planes, b) normalized velocity magnitude contours and 2D streamlines extracted at $dy = 0.05c$ from the wing's surface.

Figure 9.2b shows the velocity magnitude and 2D streamlines extracted at a constant offset of $dy = 0.05c$ from the wing's surface. High-velocity values are found upstream of the rotors, but the flow stagnates as it approaches the chord-wise position of the rotor array. Considering the span-wise variations upstream, velocities are higher along the axis of the rotors. Downstream of the rotor array, intermittent regions of separation are found along the span. Such regions are located around the position of the rotor axis. Note that, at the lower edge of the domain ($z/c = -1$, $x/c = 1$) the flow is turned in the negative span-wise direction, as a result of the high pressure in the separation region at the edge of the rotor array.

To investigate the variations in span in more detail, the velocity is extracted in the (x, y)-plane in figure 9.3 for different span positions. At the span position of the center

rotor axis (i.e. $z = 0$) in figure 9.3a, a pronounced separation region downstream of the disk is found, as was already identified in chapter 7. The velocity slice between two streamtubes is extracted in figure 9.3b and shows a reduction in the size of the separation region. The high-velocity region along the vertical position of the rotor axes indicates that the wakes of subsequent rotors merge. Such behaviour of closely spaced rotors was already identified in chapter 5.
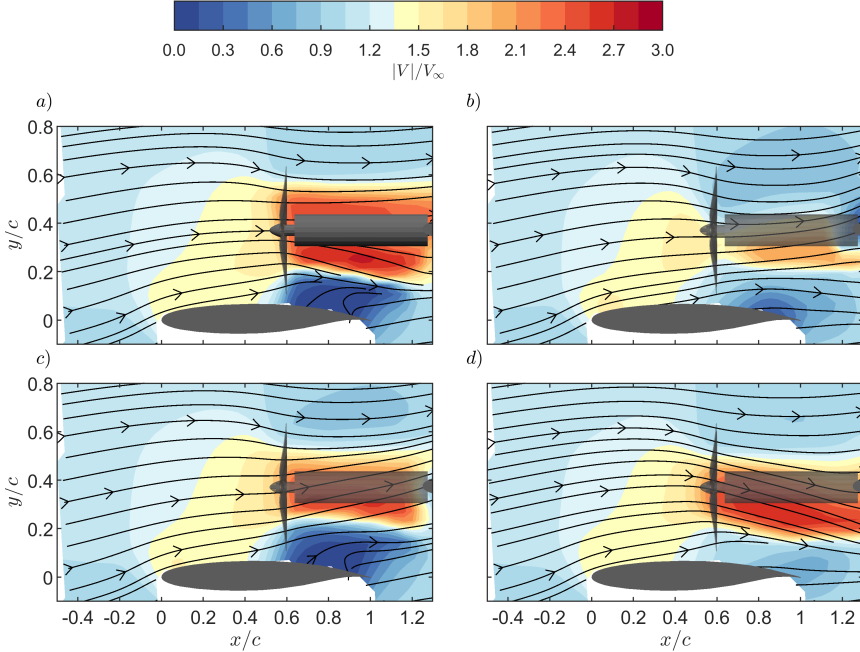
Figure 9.3: Time-averaged normalized velocity magnitude contours and 2D streamlines for $\alpha = 4°$ and $V_\infty = 15$ m/s ($J = 0.154$). Slices taken at different span-wise positions; a) through the rotor axis ($z = 0$), b) between two rotors ($z = -z_r$), c) at the advancing size of the blade ($z = -R/2$) and d) at the retreating side of the blade ($z = R/2$)

Figures 9.3c and d show the velocity in the wake of the center rotor, extracted at the advancing ($z = -R/2$) and retreating side ($z = R/2$). Different behavior is observed here. The wake extracted in figure 9.3c is pushed upwards while the wake of the retreating side of the blade in figure 9.3d generates a downwash. This has an effect on the separation region, which is removed for the retreating side of the rotor streamtube. Instead, for the advancing side (figure 9.3c), the separation region is comparable to what was found below the rotor axis position (figure 9.3a).

The effect of rotational direction is shown more clearly by the extracted velocity slice in the (z,y)-plane in figure 9.4. Note that the geometry of the rotors is also shown here and includes a given phase angle between each rotor. During the experiments, this phase difference was random and slowly varied in time to obtain a converged mean flow. Figure 9.4a shows the plane extracted $0.1c$ upstream of the rotor array to highlight the inflow to the rotors. The contours show circular patches of high velocity, due to the suction of the rotors. These circular patches are connected, at the height over the rotor axis, caused by

the interaction of the streamtubes of subsequent rotors [97]. The rotor rotation direction is indicated by the blue arrows. The combined swirls of the streamtubes generate a downwash on one side of the center rotor ($z/c = 0.25$). Instead, on the other side of the rotor (see $z/c = -0.25$), the combination of the upwards-moving swirl in the streamtubes and the downward entrainment from outside the streamtube, generates a flow region with low vertical velocity.
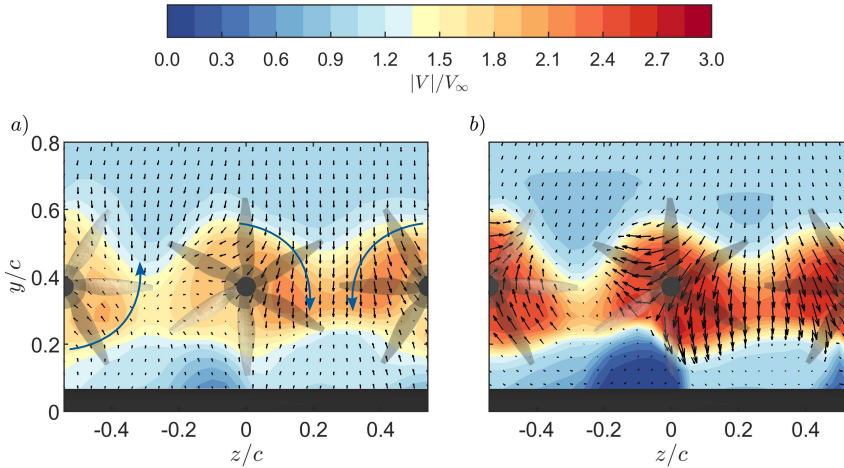

Figure 9.4: Time-averaged normalized velocity magnitude contours and 2D velocity vectors for $\alpha = 4°$ and $V_\infty = 15$ m/s ($J = 0.154$). Slices taken at different chord-wise positions; a) upstream of the rotor array $x/c = 0.5$ and b) downstream of the rotor array $x/c = 0.7$.

9

The rotor-to-rotor effects are also present downstream of the array, as shown by the velocity vectors extracted at $x/c = 0.7$ in figure 9.4b. Noticeable here are the highly deformed streamtubes as a consequence of the close rotor spacing. Furthermore, the downwash generated between the two rotors, at $z/c = 0.25$, has grown in magnitude compared to the upstream extracted velocity field. Effects of the combined swirl direction of subsequent rotors are also present on the surface of the wing, since rotor-induced separation is only found at the side of the center rotor where the combined swirl moves upward (i.e. $z < 0$).

9.3 Flow physics along trajectory

Results are now extracted at four points along the flight trajectory, indicated by the markers in figure 9.5a and operating conditions shown in figure 9.5b and table 9.1. The velocity field around the rotor-wing system at these four positions, under dynamic operating conditions, is presented in figure 9.5 by the normalized velocity magnitude contours and velocity vectors in a vertical plane ($z = 0.45c$) and over the surface of the wing ($dy = 0.05c$).
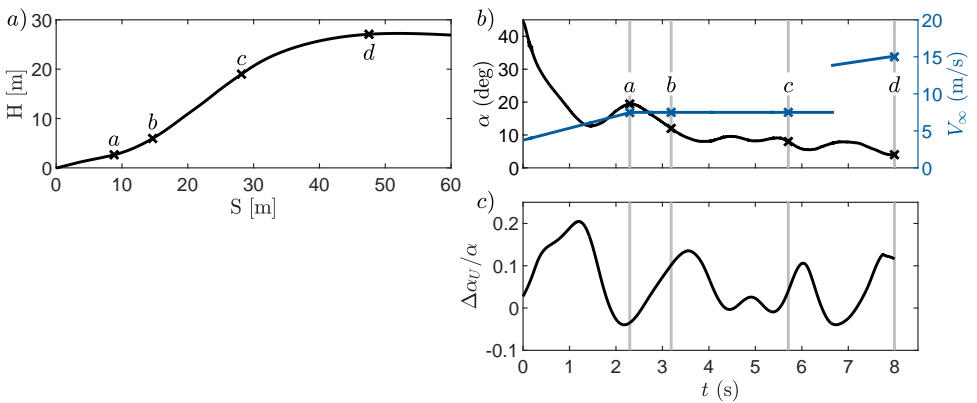
Figure 9.5: a) Reference trajectory of eVTOL flight envelope with extracted points as shown in figures 9.6 and 9.7. b) Operating conditions of the reference points and c) normalized difference between the geometric angle of attack and predicted effective angle of attack (equation 9.3) of a thin airfoil during the eVTOL flight envelope.

9
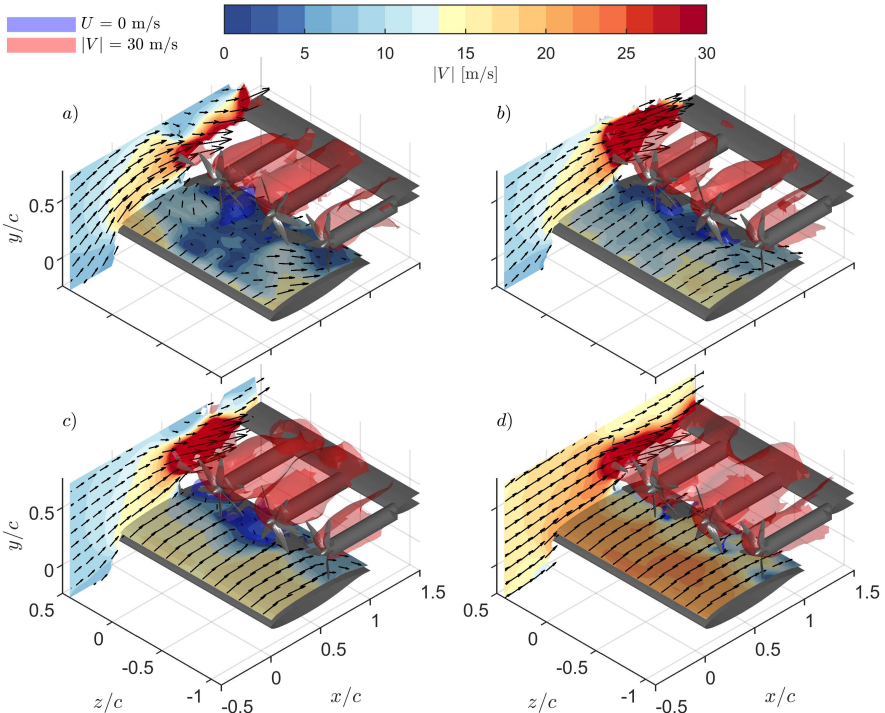
Figure 9.6: Time-averaged ($t = 0.025s$, ≈ 57 blade passages) flow field obtained with dynamic operating conditions. The operating conditions of (a-d) are presented in table 9.1 and figure 9.5. Plotted are the velocity magnitude contours and 2D vectors extracted at $dy = 0.05c$ from the wing's surface and at $z/c = 0.425$.

Figure 9.6a shows the extracted flow field during the initial stages of the flight envelope when the slope of the trajectory is gradually increased (figure 9.5a). Consequently, the high angle of attack leads to flow separation near the leading edge, as indicated by the flow near the wing's surface. Separation is maximized around the center of the measurement domain. In both negative and positive span direction, the flow around the leading edge is more attached and flow is entrained from the center span.

The data in figure 9.6b are extracted at the onset of the climb phase. Here, the angle of attack is decreased to $\alpha = 12°$, reducing the separation in the center span of the wing. Nonetheless, the flow still separates around the chord position of the rotor array, which is most apparent for the center rotor.

In figure 9.6c, the end of the climb phase is reached and the angle of attack is further reduced compared to figure 9.6b, resulting in better flow attachment and increased velocity around the leading edge. The lower angle of attack does not affect the rotor-induced separation downstream of the disk, however. Finally, figure 9.6d considers the flight condition when cruise altitude is reached. The free-stream velocity is increased to $V_\infty = 15$ m/s, and the angle of attack reduced to $\alpha = 4°$. The lower thrust reduces the rotor-induced separation around the position of the propulsors, although local regions of separation are still present. Upstream of the rotor disk, variations in span direction are decreased for this condition.

9.3.1 PREDICTION OF TRANSIENT EFFECTS

To predict the occurrence of transient aerodynamic effects, a time scale of the flow should be defined. Considering the complexity of the propulsion system, with associated aerodynamic interactions, the definition of such a quantity is cumbersome. Given that the rotors are operated at a fixed rotational speed, a simplification is made by excluding their effect on the aerodynamic time scale. Hence, classical theory of thin airfoils is employed to predict where transient effects are to be expected. Recall (section 2.1) that from the theory of Wagner [37], the unsteady angle of attack response $\alpha_U(t)$ of a thin airfoil depends on the initial angle of attack α_0, the rate of change of the geometric angle of attack $\frac{d\alpha}{dt}$ and the Wagner function $\psi(t)$:

$$\alpha_U(t) = \alpha_0 + \int_0^t \frac{d\alpha}{dt}\psi(t)dt \tag{9.1}$$

The Wagner function $\psi(t)$ can be approximated by equation 9.2, and is a function of the flight speed V_∞ and wing chord c.

$$\psi(t) = 1 - 0.165\exp(0.0910V_\infty t/c) - 0.335\exp(0.6V_\infty t/c) \tag{9.2}$$

The difference between the predicted unsteady angle of attack $\alpha_U(t)$ and the quasi-steady (geometric) angle of attack $\alpha(t)$ is then found by:

$$\Delta\alpha_U(t) = \alpha_U(t) - \alpha(t) = \alpha_0 + \int_0^t \frac{d\alpha}{dt}\psi(t)dt - \alpha(t) \tag{9.3}$$

The found unsteady angle of attack $\Delta\alpha_U(t)$ for the reference flight envelope is normalized using the time series of the geometric angle of attack $\alpha(t)$ and presented in figure 9.5c. Values that deviate from zero could indicate the presence of transient aerodynamic effects.

Primarily positive values of $\Delta\alpha_U(t)$ are found, indicating that the effective angle of attack is higher than obtained through quasi-steady measurements. The average value of $\Delta\alpha_U(t)$ is 6% of the geometric angle of attack, with local maxima between 20% and 10%.

9.3.2 Comparison with quasi-steady measurements

The data from the dynamic experiment (figure 9.6) are now compared with the quasi-steady results, for the same operating conditions. The results are presented in figure 9.7 by the velocity magnitude and 2D vectors over the surface of the wing.
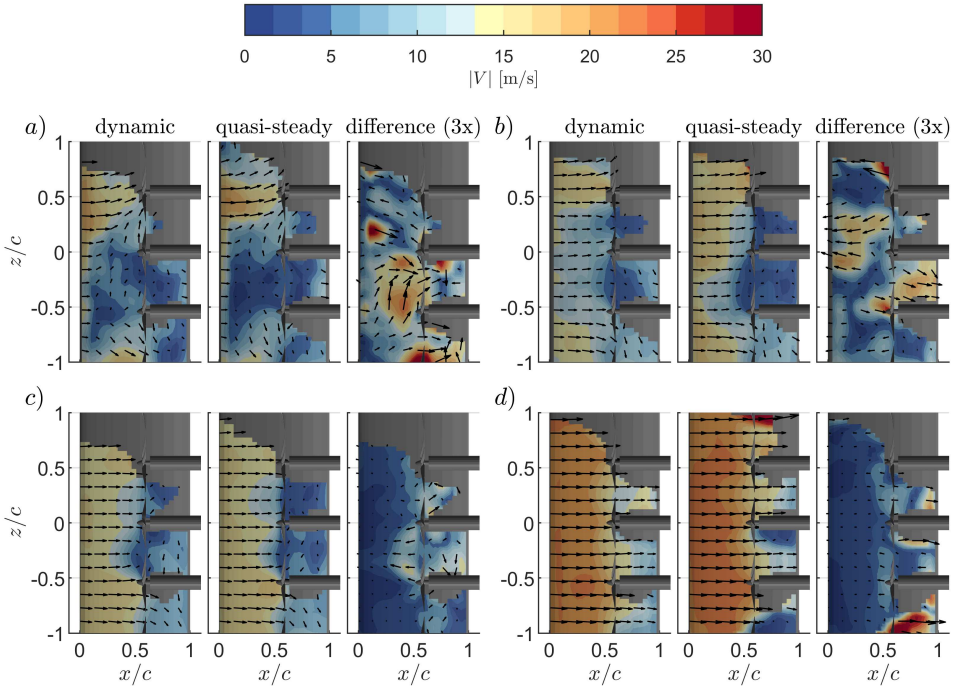
Figure 9.7: Comparison between the flow field obtained from quasi-steady and dynamic operating conditions. Plotted are the velocity magnitude contours and 2D vectors extracted at $dy = 0.05c$ from the wing's surface. The operating conditions of (a-d) are presented in table 9.1 and figure 9.5. The difference between the quasi-steady and dynamic flow fields has been multiplied by a factor of 3 and is presented in the third column for each of the conditions of (a-d).

Each subplot of figure 9.7 contains results for dynamic (similar to figure 9.6) and quasi-steady conditions, and the difference between the two (i.e. dynamic minus quasi-steady results) multiplied by a factor of three. For the conditions of figure 9.7a, the unsteady angle of attack (figure 9.5c) was 3.5% lower than the geometric angle of attack. When examining the contours upstream of the rotors in figure 9.7a, the results confirm this hypothesis, since the flow during the dynamic measurements is more attached. Instead, for figures 9.7b, c and d, an increase in the effective angle of attack was expected from equation 9.3. In the contours of figures 9.7b and c, more pronounced separation takes place. For figure 9.7b, this occurs at the leading edge while in figure 9.7c the increased separation is

primarily found near the chord-wise position of the rotors. Figure 9.7d, marks a condition where the flow is still attached. Instead, the effective angle of attack during the dynamic measurements appears to be lower due to reduced velocity compared to the quasi-steady measurements. Note that for each of subplots of figure 9.7, discrepancies between dynamic and quasi-steady results are present downstream of the rotor array, which could suggest that this region is more sensitive to such transient effects.

9.4 CONCLUSION

The operating conditions of the Over-The-Wing propulsion system during a reference trajectory have been found using experimental loading measurements, which were used to simulate a steep ascend take-off trajectory. The dynamic measurements capture the three-dimensional aerodynamic interactions of all encountered angles of attack and free-stream velocities that occur along the unsteady maneuver, thereby demonstrating an efficient approach to measuring complex aerodynamic phenomena. An analysis of the time-averaged velocity field showed that the most pronounced variations in the span direction are found downstream of the rotor disks. The combined swirl of the wakes produced by the counter-rotating rotor array generates alternating regions of downwash and low vertical velocity between the rotors. The downwash mitigates the rotor-induced flow separation behind the disk.

The flow is characterized by high angles of attack and leading edge separation during the initial stages of the flight envelope. A velocity field snapshot obtained under dynamically varying conditions and one where a fixed angle of attack has been prescribed, show a similar flow topology. However, variations in the position of the separated flow regions suggest a change in the effective angle of attack for the dynamic measurements. The behavior is linked to the classical theory of the unsteady angle of attack for thin airfoils, but a more detailed analysis is required to conclude this.

9

IV

Final remarks

10

Conclusions & Recommendations

10.1 Conclusions

The main objective of this thesis was defined as follows:

> ***Understand the key aerodynamic rotor-surface interactions, and their performance impact, of Over-The-Wing propulsion for vertical flight***

The presented studies contribute to this goal through the experimental investigation and the low-order modelling efforts of fundamental rotor-surface interactions. Conclusions related to the sub-goals outlined in chapter 1 are now discussed separately.

10.1.1 Aerodynamic rotor-surface interactions

Two types of multi-rotor–surface interactions were considered in this thesis. The first concerned the near ground hovering where the effect of the wing was disregarded. Subsequently, interactions between (distributed) rotors and the lifting surface in an Over-The-Wing orientation were investigated. The interactions were characterized experimentally, employing Lagrangian particle tracking velocimetry and helium-filled soap bubbles as tracer particles. This technique has demonstrated its effectiveness in providing quantitative information on the large-scale unsteady flow organization surrounding the rotors.

Rotors operating in ground proximity, investigated in chapters 5 and 6, flow stagnation between the wall jets generated by side-by-side rotors generates a fountain-like flow pattern over a line between the two rotors. Lowering the ground-standoff distance results in the ingestion of the fountain into one of the rotors and pronounced lateral drifting of the column. These dynamic features occur at an intermittent frequency, which was found to be related to the convective time scale of the re-ingestion loop and therefore depend on system parameters (ground stand-off distance and rotor thrust) through the height of the fountain and its characteristic velocity. Aforementioned unsteady flow features impose a significant effect on the inflow, which can lead to fluctuations in thrust at frequencies of two orders of magnitude lower than the *BPF*. This can be detrimental to the controllability

during the ground operation of multi-rotor vehicles. Moreover, the intermittent ingestion of coherent structures originating from the fountain, combined with the unsteady loading on the blades result in an expected increase in the acoustic footprint as these systems approach the ground.

For distributed rotors operating parallel to lifting surfaces, in an Over-The-Wing configuration (chapters 7, 8 and 9), the rotor induction affects the flow separation from the wing at large angles of attack. In low-thrust conditions such effects are favorable, as the rotors' suction energizes the boundary layer, resulting in a marginal delay of leading-edge separation. Instead, for low-advance ratios, as observed in hover or during the transition towards cruise, the rotors induce separation leading to flow re-circulation between the rotor-tip and wing surface. The likelihood of such rotor-induced separation is further increased through the adverse pressure gradient under inclination, in combination with the low-Reynolds number encountered during vertical flight. On that note, chapters 5 and 9 have shown that the combined swirl of the wakes produced by closely spaced counter-rotating rotors can generate a downwash between a set of rotors that could be utilized to increase the slipstream-wing adherence behind the disks.

The investigated rotor-surface interactions have revealed that confined rotor-systems in vertical flight conditions (inclined with the flight direction and/or operated at high thrust levels) have the tendency to generate unsteady, recirculating flow patterns leading to re-ingestion. This generates elevated noise levels through spectral broadening and turbulence ingestion as well as increased fluctuations of the rotor loads. A careful design of the propulsion system and flight mission is therefore required to mitigate such adverse effects. Considering that the flow patterns are dominated by viscous interactions, experimentation is essential in providing the required data in this process.

Aside from enhanced thrust levels and higher angles of attack compared to cruise flight, the operating conditions for tilt-wing vehicles gradually change during take-off. The low speed in the initial stages of flight could lead to long aerodynamic time scales and consequential transient effects during swift changes in the angle of attack. The thesis outcomes presented in chapter 9 have shown that a variation in the effective angle of attack is observed during a steep take-off trajectory when compared to quasi-steady measurements. This affects the flow separation over the suction side of the wing at large angles of attack. The behaviour is linked to the classical theory for thin airfoils but a more detailed analysis, supported by loading and acoustic measurements, is required to validate this connection and to study the performance impact.

10.1.2 Performance installation effects

Based on experimental observations, it is shown that Over-The-Wing distributed propulsion for vertical flight brings both beneficial and adverse aerodynamic and aeroacoustic coupling effects.

Effects of the wing on the rotors are primarily adverse, due to the inviscid velocity increase by the wing's circulation resulting in a steady-inflow distortion at the rotor inflow. For a fixed-pitch rotor this results in a reduction of the steady-thrust for a constant rotational speed as well as azimuthal variations in the rotor loads. The associated noise increase by unsteady loading is primarily radiated downstream, and increases with inclination. Around the disk plane, the noise elevation compared to the isolated rotor is

primarily the result of acoustic reflections from the wing's surface. One must note that the acoustic sources of the considered rotor geometry were dominated by thickness noise. For a more slender rotor blade, or lower tip-Mach numbers, the relative contribution of unsteady loading noise to the acoustic signature is expected to increase. Moreover, the installed rotor noise was compared with an isolated rotor for a fixed rotational speed. The reduction in thrust by the presence of the wing means that the rotor-noise increase during operating is therefore underestimated.

Below the wing, noise shielding reduces the first *BPF* by 10 dB when compared to the isolated rotor, highlighting the capability to reduce noise during fly-overs. This, combined with the noise increase by unsteady loading and reflections over the suction side of the wing, results in a complex noise directivity pattern. Adequate mission planning of the take-off procedure is therefore required to steer the dominant noise sources from the suction side away from populated areas, where minimizing noise pollution is essential.

Concerning the aerodynamic installation effects, rotor-induction increases the wing-lift but reduces the lift slope for a constant advance ratio. Although the effect of the rotors on the leading edge separation is marginal, an abrupt increase in lift is observed once separation occurred. As a consequence, the wing does not stall, providing a notable safety advantage.

The rotor position can be adjusted to mitigate adverse installation effects, optimizing the performance of Over-The-Wing propulsion. Based on experimental results of the installed thrust, lift and emitted rotor tonal noise sources, a rotor position towards the trailing edge is most favorable. On the other hand, the shielding potential is higher for a mid-positioned rotor, and a rotor towards the trailing edge increases the likelihood of acoustic scattering of the blade harmonics and gave the largest drag penalty of the wing. Additionally, considering that the occurrence of flow reversal is related to the boundary layer properties of the wing, such effects are more significant for aft-mounted rotors. The ideal rotor position is thus a trade-off between the aforementioned effects and depends on specific requirements of the propulsion system. Finding the optimal trade-off necessitates the exploration of a broader parameter space than typically addressed during experiments and therefore requires the use of computationally efficient prediction tools or surrogate models.

10.1.3 Low-order modelling

Aerodynamic rotor-surface interactions are inherently unsteady, exhibiting complex dynamics that can impact the overall system performance. A reduced-order representation of these interactions enables the identification of energetic dynamic features that sustain unsteady flow cycles. These models can be inferred from experimental data using modal decomposition techniques, such as Proper Orthogonal Decomposition (POD), by coupling different modes with a statistical delay. This approach has been successfully applied to characterize the coherent structures and feedback loop during near-ground hovering of multi-rotor systems (chapter 6).

The understanding of aerodynamic interactions facilitates the development of performance models. Low-fidelity performance tools allow for efficient variation of geometric and performance parameters of the propulsion system for optimization purposes and can support the formulation of design guidelines. A semi-analytical prediction tool for the

aero-propulsive performance is proposed, which is applicable for fixed-pitch rotors positioned over thin wings, with tip gaps exceeding the wing's boundary layer. The method employs a single-pass strategy and, as a consequence, the dominant design properties, i.e. the relative position and size of the rotor-wing system and the isolated system performance parameters, appear explicitly in the final formulation. Steady installed rotor thrust is predicted correctly through the definition of an effective advance ratio, and the inclusion of the isolated rotor loads. For the unsteady thrust and torque of the rotor, a similar approach is taken by definition of a blade-sectional advance ratio correction. The azimuthal and radial variation in loads and the corresponding aerodynamic noise sources can then be predicted through existing, computationally efficient, analytical methods.

Modelling of the wing lift-force is performed by the superposition of lift-producing rotor-induced flow effects. This approach allows for the isolation of individual components of the lift force leading to additional insights into the installed system performance. The model accurately predicts the lift force for forward-positioned rotors but requires a correction for the streamtube confinement by the wing for aft-mounted rotors. Even though this correction is based on experimental velocimetry data, it is universally applicable to Over-The-Wing propulsion systems. Additional discrepancies in the predicted lift arise for low-thrust conditions, caused by the increasing importance of the induced velocities outside the streamtube by the rotors' vortex systems. Such complex interactions cannot be modelled by a low-order approach and require the inclusions of empirical relations based on experimental data.

The employed analytical performance modeling techniques disregard viscous effects and therefore do not include the observed rotor-induced separation and the resulting flow re-ingestion. The performance impact of flow re-ingestion requires experimental data or high-fidelity simulations; however, since this is an off-design condition, effective prediction of the onset of such effects is of greater concern.

10.2 Recommendations for future work

Several possible research directions for future work can be suggested based on the studies presented in this thesis.

10.2.1 Flow reversal prediction and mitigation

Flow reversal between rotor and wing surface has been identified in chapter 7 and 8 leading to adverse effects in terms of noise, blade force fluctuations and reduced leading-edge separation delay authority in high-thrust conditions. A predictive model for such flow effects is valuable for prevention and allows for the identification of dominant system parameters. Additionally, advanced flow control mitigation strategies can be applied to prevent flow reversal and re-ingestion, which are required to enable Over-The-Wing propulsion for vertical flight. A few suggestions regarding this with increasing complexity are briefly enumerated:

1. **Reducing the tip gap** could minimize the interaction between the (low pressure) upstream and (high pressure) downstream regions of the rotor streamtube, potentially reducing the flow reversal phenomenon.

2. **Inclusion of a slat to the wing profile** could be used to generate a more energetic boundary layer which is less sensitive to separation.

3. **Include a physical obstruction between rotor and wing surface**. This could be a full duct or half duct for example.

When proven effective, separation delay in high thrust conditions is expected which could make Over-The-Wing propulsion very effective during low-speed loitering. For these flight conditions, it is also valuable to investigate any hysteresis effects in the separation delay mechanism.

10.2.2 TRANSIENT AERODYNAMIC EFFECTS

A reference tilt-wing take-off trajectory was simulated experimentally in chapter 9. The preliminary results included a comparison between results obtained through dynamic and quasi-steady operating conditions. To conclude on this, a more detailed analysis, ideally supplemented using loading and acoustic data, is required. Furthermore, the aerodynamic timescales were based on classical theories of thin two-dimensional airfoil. eVTOL vehicles generally employ fixed-pitch rotors that vary in rotational velocities through out the flight mission while interacting with such surfaces. This requires new theories regarding the aerodynamic timescales.

The investigated unsteady maneuver deals with gradual changes in the angle of attack and flight speed during a steep ascent trajectory. During operation, certain flight maneuvers exhibit shorter timescales with respect to this. Examples are the interactions with gusts in urban environments or a sudden evasion procedure. Moreover, during the vertical landing, there is generally an abrupt increase in the rotational speed of the rotors to reduce the descent speed, which could also lead to transient effects.

10.2.3 UNSTEADY LOADING AND BROADBAND NOISE

In chapter 8, the tonal aerodynamic noise sources of rotors were investigated and a low-order model of the inflow was generated. Validation of the tonal noise sources is required for directivities closer to the rotor axis, in which the effects of unsteady loading are more severe. Considering that all installed rotors are inherently affected by steady inflow distortions, it is also important to investigate ways to mitigate the resulting adverse effects. This could be achieved through innovative blade design, such as modifying the blade sweep to dephase the unsteady loads in radial direction, thereby reducing interaction tones.

Finally, broadband and tonal noise contributions were found to be comparable in magnitude for the studied rotor. The model should therefore be extended by inclusion of turbulent ingestion and airfoil self-noise for a complete prediction and analysis of the aerodynamic noise sources of the installed rotor.

10

A

APPENDIX: DERIVATION OF AERO-PROPULSIVE MODEL

The derivation of the aero-propulsive model as used in chapter 7 is given here.

A.1 DERIVATION OF THE THRUST MODEL

Each of the different terms in the thrust model will be derived separately.

A.1.1 CIRCULATION

The induced velocity by circulation is approached by the integration of the bound vorticity of the wing. The wing's circulation Γ_{tot} based on the lift coefficient c_l reads:

$$\Gamma_{tot} = \frac{c_l V_\infty c}{2} \tag{A.1}$$

It is assumed that the circulation Γ_{tot} forms a parabolic distribution along the wing's chord, from which the circulation distribution $\Gamma(x)$ follows:

$$\Gamma(x) = \frac{3}{2}\left(1 - \left(\frac{x}{c}\right)^2\right)\Gamma_{tot} = \frac{3}{4}c_l V_\infty c\left(1 - \left(\frac{x}{c}\right)^2\right) \tag{A.2}$$

The induced velocity by the two-dimensional bound circulation distribution is then computed by the integration of Biot-Savart law. For the horizontal induced velocity $V_{\Gamma,x}$ at a rotor position (x_r, y_r) this reads:

$$\frac{V_{\Gamma,x}}{V_\infty} = -\frac{1}{2\pi V_\infty}\int_0^s \frac{\Gamma(x)\left(\frac{y_r}{c} - \frac{y_\gamma(s)}{c}\right)}{\left(\frac{x_r}{c} - \frac{x_\gamma(s)}{c}\right)^2 + \left(\frac{y_r}{c} - \frac{y_\gamma(s)}{c}\right)^2}\mathrm{d}s = -\frac{c}{2\pi V_\infty}\int_0^1 \frac{\gamma(x)y_r}{\left(x_r - x_\gamma\right)^2 + y_r^2}\mathrm{d}x_\gamma \tag{A.3}$$

In which s is defined as the line of the vorticity distribution, given by the x- and y-coordinates x_γ and y_γ, respectively. The vorticity source is considered as a horizontal line (i.e. $y_\gamma = 0$), which returns the right-hand side of equation A.3. Then, by substitution

of equation A.2 in equation A.3 and working out the integral, the final expression for the normalized axial induced velocity yields:

$$
\frac{V_{\Gamma,x}}{V_\infty} = \frac{3c_l}{8\pi c^2}
$$
$$
\left(x_r y_r \ln\left(\frac{x_r^{\,2} + y_r^2}{(c - x_r)^2 + y_r^2} \right) + \left(x_r^{\,2} - y_r^{\,2} - c^2 \right) \left(\tan^{-1}\left(\frac{x_r - c}{y_r} \right) - \tan^{-1}\left(\frac{x_r}{y_r} \right) \right) - y_r c \right)
$$

(A.4)

A.1.2 Shear layer ingestion

At sufficiently large angles of attack, the wing's boundary layer will separate. The correction for the effect is given by J_{SL}:

$$
J_{SL} = 1 - f(\alpha, \alpha_c)\left(1 - \frac{V_{SL}}{V_\infty} \right)\frac{A_{SL}}{\pi R^2}
$$

(A.5)

For simplicity, the velocity below the shear layer is assumed to be zero, i.e. $V_{SL} = 0$. The function $f(\alpha, \alpha_c)$ in equation A.5 is a stall criterion which has the form of:

$$
f(\alpha, \alpha_c) = \frac{(\alpha - \alpha_c)}{2\sqrt{((\alpha - \alpha_c))^2}} + \frac{1}{2}, \quad \alpha_c = 0.818\sqrt{\frac{r}{c}}
$$

(A.6)

The area A_{SL}, can then be found by integrating the rotor disk area below the shear layer height:

$$
A_{SL} = \int_{y_r - R}^{y_{SL}} \sqrt{(y - y_r)^2 + R^2}\,\mathrm{d}y
$$

(A.7)

in which $y_{SL}(x)$ corresponds to the shear layer height of the isolated wing, at the chordwise position of the rotor x_r:

$$
y_{SL}(x) = \left(\frac{5}{4} \right) x_r \tan(\alpha)
$$

(A.8)

Integration of equation A.7 and substitution in equation A.5 leads to the exact expression of J_{SL}:

$$
J_{SL} = 1 - \left(\frac{(\alpha - \alpha_c)}{2\sqrt{((\alpha - \alpha_c))^2}} + \frac{1}{2} \right)
$$
$$
\left(\frac{y_{SL}(x) - y_r}{\pi R^2}\sqrt{R^2 - (y_{SL}(x) - y_r)^2} + \frac{1}{\pi}\tan^{-1}\left(\frac{y_{SL}(x) - y_r}{\sqrt{R^2 - (y_{SL}(x) - y_r)^2}} \right) + \frac{1}{2} \right)
$$

(A.9)

A.2 Derivation of the lift model

For the derivation of the lift model, the streamtube properties for a distributed rotor array are introduced first. After this, the different terms in the lift model are derived separately.

A.2.1 STREAMTUBE PROPERTIES FOR DISTRIBUTED ROTORS

Using the approach of Veldhuis [32], the rotor disks are modeled as uniform distributions of pressure doublets with strength $\Delta p = p_2 - p_1$. Here, p_1 indicates the pressure in a point directly in front and p_2 directly after the rotor disk. Considering a reference point r at a given distance l_r from the rotor disk, the pressure in r is found by:

$$p_r = \frac{\Delta p}{4\pi} \int_S \frac{\partial}{\partial n}\left(\frac{1}{l_r}\right) \mathrm{d}S \quad \text{for } l_r > 0 \tag{A.10}$$

in which S is the surface of the distribution of pressure doublets. Rather than a circular disk, the rotor array is modeled by a rectangular surface with length $2N_r R$ and width $2R$. Considering a reference point in the center of the streamtube (i.e. $y = 0$, $z = 0$, and $n = x$), the pressure returns:

$$p_r = \frac{\Delta p}{4\pi} \int_{N_r R}^{N_r R} \int_{-R}^{R} -\frac{x}{\left(x^2 + y_1^2 + z_1^2\right)^{\frac{3}{2}}} \mathrm{d}y_1 \mathrm{d}z_1 \tag{A.11}$$

Solving the integral of equation A.11 returns the stream-wise distribution of pressure $p(x)$ for a rectangular streamtube:

$$p(x) = \frac{\Delta p}{\pi} \tan^{-1}\left(\frac{N_r R^2}{x\sqrt{\left(N_r^2 + 1\right)R^2 + x^2}}\right) \tag{A.12}$$

The axial-induced velocity $v_a(x)$ upstream and downstream of the disk then follows directly from the result equation A.12 and the momentum equation [32]:

$$\frac{v_a(x)}{V_\infty} = a\left(\frac{x}{\sqrt{x^2}} + 1 - \frac{2}{\pi}\tan^{-1}\left(\frac{N_r R^2}{x\sqrt{\left(N_r^2 + 1\right)R^2 + x^2}}\right)\right) \tag{A.13}$$

in which:

$$a = \frac{\Delta p}{2\rho V_\infty^2} \tag{A.14}$$

Considering $N_r = 5$, the term withing brackets in equations A.12 and A.13 reduces to:

$$\frac{N_r R^2}{x\sqrt{\left(N_r^2 + 1\right)R^2 + x^2}} \approx \frac{R}{x} \quad \text{for } N_r \geq 5 \tag{A.15}$$

Consequently, the stream-wise distribution of pressure $p(x)$ and induced velocity $v_a(x)$ approaches the two-dimensional solution:

$$p(x) = \frac{\Delta p}{\pi} \tan^{-1}\left(\frac{R}{x}\right)$$
$$\frac{v_a(x)}{V_\infty} = a\left(\frac{x}{\sqrt{x^2}} + 1 - \frac{2}{\pi}\tan^{-1}\left(\frac{R}{x}\right)\right) \tag{A.16}$$

Finally, by the continuity equation and the result of equation A.16, the height of the two-dimensional streamtube $R_s(x)$ yields:

$$\frac{R_s(x)}{R} = \frac{1+a}{1+a\left(\frac{x}{\sqrt{x^2}}+1-\frac{2}{\pi}\tan^{-1}\left(\frac{R}{x}\right)\right)} \tag{A.17}$$

Equations A.16 and A.17 are then used to derive the expressions for the rotor-induced lift components, which are introduced in sections A.2.2, A.2.3 and A.2.4.

A.2.2 Effective angle of attack

The increase in lift by the effective angle of attack $\Delta c_{l,\alpha}$ follows from the difference between the predicted installed and the isolated wing's inflow angle $\Delta\alpha$:

$$\Delta c_{l,\alpha} = \overbrace{2\pi}^{\substack{\text{lift}\\\text{slope}}} \overbrace{\Delta\alpha}^{\substack{\text{increase}\\\text{angle of}\\\text{attack}}} \overbrace{\frac{2N_rR}{S}}^{\substack{\text{affected}\\\text{span}}} = 2\pi\cos^{-1}\left(\frac{\mathbf{a}\cdot\mathbf{b}}{|\mathbf{a}||\mathbf{b}|}\right)\frac{2N_rR}{S} \tag{A.18}$$

in which the term on the right side corrects the result for the affected span region of the wing. The two-dimensional velocity vectors $\mathbf{a}$ and $\mathbf{b}$ are for the installed configuration and isolated wing respectively, at the wing's leading edge:

$$\mathbf{a} = \begin{bmatrix} \frac{v_a(-x_r)}{V_\infty}+\cos(\alpha) \\ \frac{v_i(-x_r)}{V_\infty}+\sin(\alpha) \end{bmatrix}, \quad \mathbf{b} = \begin{bmatrix} \cos(\alpha) \\ \sin(\alpha) \end{bmatrix} \tag{A.19}$$

Substitution of equation A.19 in equation A.18, applying the small-angle approximation for α, gives the expression for $\Delta\alpha$:

$$\Delta\alpha = \cos^{-1}\left(\frac{\left(1-\frac{\alpha^2}{2}\right)\frac{v_a(-x_r)}{V_\infty}+\alpha\frac{v_i(-x_r)}{V_\infty}+1}{\sqrt{\left(\frac{v_a(-x_r)}{V_\infty}+1-\frac{\alpha^2}{2}\right)^2+\left(\frac{v_i(-x_r)}{V_\infty}+\alpha\right)^2}}\right) \tag{A.20}$$

The axial induced velocity v_a upstream of the disks follows from equation A.16, resulting in:

$$\frac{v_a(x)}{V_\infty} = -\frac{2a}{\pi}\tan^{-1}\left(\frac{R}{x}\right) \quad \text{for } x < 0 \tag{A.21}$$

By the acceleration in the axial direction, the flow will be entrained from the vertical direction by a velocity v_i, which follows from the law of continuity:

$$\frac{v_i(x)}{V_\infty} = C_1\frac{d\left(\frac{v_a(x)}{V_\infty}\right)}{dx}R = C_1\frac{2aV_\infty R^2}{\pi(x^2+R^2)} \quad \text{for } x < 0 \tag{A.22}$$

In equation A.22 the coefficient C_1 is used to correct the results for the blockage of the wing, limiting the contraction of the streamtube in high thrust conditions, as illustrated in figure A.1a.
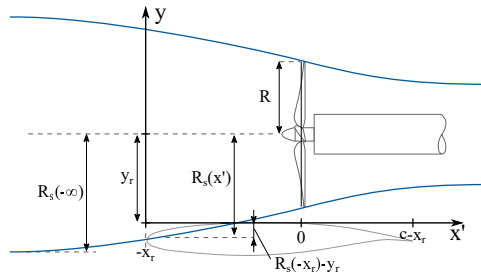
Figure A.1: Schematic and definition of the variables of the rotor-induced upwash v_i correction (C_1) by the confined streamtube contraction.

This results in a higher axial velocity and lower static pressure upstream of the disk than the predictions of equation A.16, which concern a free contraction of the streamtube. Consequently, this effect is expected to generate a greater upwash at the wing's leading edge, and scales with the overlap between the free-contraction stream tube height R_s and the vertical rotor position y_r:

$$C_1 = f\left(\frac{R_s(-x_r) - y_r}{R}\right) \approx c_0 \left(\frac{R_s(-x_r) - y_r}{R}\right)^{c_1} + 1 \tag{A.23}$$

A power function is then formed using the expression of the overlap region, as shown on the right side of equation A.23. The final expression for C_1 is found by minimization of the L_2-norm between the predicted and measured upwash (as used to generate figures 7.12a and b). During the minimization, only integer values for c_0 are considered, while c_1 uses both integers and half-integers:

$$C_1 = \max\left(1, \; 60\left(\frac{R_s(-x_r) - y_r}{R}\right)^{\frac{5}{2}} + 1\right) \tag{A.24}$$

A.2.3 STREAMTUBE PRESSURE

The effect of the projected streamtube pressure is only considered when the maximum streamtube height R_s exceeds the vertical rotor spacing y_r. The effect of this pressure on the lift of the wing $\Delta c_{l,p}$ is computed through:

$$\Delta c_{l,p} = \overbrace{\frac{2N_r R}{S}}^{\substack{\text{affected} \\ \text{span}}} \overbrace{\frac{2}{\rho V_\infty^2 c}}^{\substack{\text{lift} \\ \text{normalization}}} \int_{-x_r}^{1-x_r} p^*\left(x'\right) \mathrm{d}x', \quad \text{for} \quad \frac{\lim\limits_{x' \to -\infty} R_s\left(x'\right)}{y_r} = \frac{R(a+1)}{y_r} > 1 \tag{A.25}$$

in which $p^*\left(x'\right)$ is the projected streamtube pressure over the wing surface. This pressure is based on the relation for the streamtube pressure $p\left(x'\right)$ (equation A.16) and includes a correction due to the effect of the streamtube confinement (recall figure A.1). The streamtube confinement leads to a reduction in effective streamtube height, leading to an increase in axial velocity. $g\left(x', y_r\right)$ corrects the axial velocity to find v^*:

$$v^* \left(x' \right) = \left(v_a \left(x' \right) + V_\infty \right) g \left(x', y_r \right) = \left(v_a \left(x' \right) + V_\infty \right) \frac{R_s \left(x' \right)}{y_r}, \quad \text{for } \frac{R_s \left(x' \right)}{y_r} > 1 \quad \text{(A.26)}$$

The correction function $g \left(x', y_r \right)$ is defined as the ratio between the free-contraction $R_s \left(x' \right)$ and confined contraction streamtube height y_r. Using Bernoulli's equation, the pressure $p^* \left(x' \right)$ yields the free-contraction stream tube pressure (equation A.16) and a second term that includes the streamtube confinement effect:

$$p^* \left(x' \right) + \frac{\rho}{2} \left(v_a \left(x' \right) + V_\infty \right)^2 g \left(x', y_r \right)^2 = p \left(x' \right) + \frac{\rho}{2} \left(v_a \left(x' \right) + V_\infty \right)^2 \quad \text{(A.27)}$$

$$p^* \left(x' \right) = p \left(x' \right) - \frac{\rho}{2} \left(v_a \left(x' \right) + V_\infty \right)^2 \left(1 - g \left(x', y_r \right)^2 \right) \quad \text{(A.28)}$$

Equation A.28 is then integrated during which the integrals are split, and only the upstream part of the rotor's streamtube is considered:

$$\int_{-x_r}^{1-x_r} p^* \left(x' \right) \mathrm{d}x' \approx \int_{-x_r}^{0} p \left(x' \right) \mathrm{d}x' - \int_{-x_r}^{0} \frac{\rho}{2} \left(v_a \left(x' \right) + V_\infty \right)^2 \left(1 - g \left(x', y_r \right)^2 \right) \mathrm{d}x' \quad \text{(A.29)}$$

The first term of equation A.29 is found by integrating equation A.16:

$$\int_{-x_r}^{0} p \left(x' \right) \mathrm{d}x' = \frac{\Delta p}{\pi} \left(\frac{1}{2} R \ln \left(\frac{R^2}{R^2 + x_r^2} \right) + x_r \tan^{-1} \left(\frac{R}{-x_r} \right) \right) \quad \text{(A.30)}$$

The second term of equation A.29 is further simplified by defining the axial velocity and rotor contraction as the averaged value of the free-stream condition and the rotor disk:

$$v_a \left(x' \right) + V_\infty \approx \frac{\lim\limits_{x' \to -\infty} v_a \left(x' \right) + v_a (0)}{2} + V_\infty = V_\infty \left(\frac{a}{2} + 1 \right) \quad \text{(A.31)}$$

$$R_s \left(x' \right) \approx \frac{\lim\limits_{x' \to -\infty} R_s \left(x' \right) + R_s (0)}{2} = R \left(\frac{a}{2} + 1 \right) \quad \text{(A.32)}$$

This reduces the second term of equation A.29 to:

$$-\int_{-x_r}^{0} \frac{\rho}{2} \left(v_a \left(x' \right) + V_\infty \right)^2 \left(1 - g \left(x', y_r \right)^2 \right) \mathrm{d}x' \approx -\int_{-x_r}^{0} \frac{\rho V_\infty^2}{2} \left(\frac{a}{2} + 1 \right)^2 \left(1 - \left(\frac{R}{y_r} \left(\frac{a}{2} + 1 \right) \right)^2 \right) \mathrm{d}x'$$

$$\approx \frac{x_r \rho V_\infty^2}{2} \left(\frac{a}{2} + 1 \right)^2 \left(1 - \left(\frac{R}{y_r} \left(\frac{a}{2} + 1 \right) \right)^2 \right)$$

$$\text{(A.33)}$$

Substituting equations A.29 and (A.30) in equations (A.33) and (A.25), gives the final expression of $\Delta c_{l,p}$:

$$
\Delta c_{l,p} = \frac{2N_r R}{Sc}
$$
$$
\left(\frac{4a}{\pi} \left(\frac{1}{2} R \ln \left(\frac{R^2}{R_1^2 + x_r^2} \right) + x_r \tan^{-1} \left(\frac{R}{-x_r} \right) \right) + x_r \left(\frac{a}{2} + 1 \right)^2 \left(1 - \left(\frac{R}{y_r} \left(\frac{a}{2} + 1 \right) \right)^2 \right) \right)
$$

(A.34)

A.2.4 Thrust vectoring

From a momentum balance, the lift increase due to a stream tube deflection by ϵ yields:

$$
\Delta c_{l,tv} = \frac{2S_e (V_e - V_\infty)^2 \sin(\varepsilon)}{V_\infty^2 c}
$$

(A.35)

In the aero-propulsive model, the angle ϵ is based on the flow deflection by the isolated wing ϵ_w under $\alpha = 0°$, and it is assumed that this depends linearly on the position of rotor along the wing's chord:

$$
\varepsilon = \epsilon_w \left(1 - \frac{x_r}{c} \right) = \frac{2c_{l,0}c}{\pi S} \left(1 - \frac{x_r}{c} \right)
$$

(A.36)

The streamtube cross-sectional surface S_e and velocity V_e are extracted by taking the limit of the streamtube contraction R_s and velocity V_a:

$$
S_e = 2N_r R \lim_{x' \to \infty} \left(2R_s \left(x' \right) \right) = 4N_r R^2 \frac{1+a}{1+2a}
$$

(A.37)

$$
V_e = \lim_{x' \to \infty} \left(V_a \left(x' \right) \right) + V_\infty = (2a+1)V_\infty
$$

(A.38)

Substitution of equation A.36, equation A.37 and equation A.38 in equation A.35 and assuming small angles for ϵ, results in the final expression of the lift increase by slipstream deflection $\Delta c_{l,tv}$:

$$
\Delta c_{l,tv} = \frac{64N_r R^2 (1+a)a^2 c_{l,0}}{(1+2a)\pi S} \left(1 - \frac{x_r}{c} \right)
$$

(A.39)

A.3 Validation of the single-pass strategy

The mutual interference of rotors and wing has been modelled using a single-pass strategy. To validate this approximation, predictions are compared to results obtained from running the same model over multiple iterations. These iterations are performed by including the rotor-induced lift (equation 7.10) in the circulation distribution of the wing (equation 7.4) and re-computing the effective advance ratio (equation 7.2). The found thrust C_T and lift coefficient c_l for different iterations i, normalized by the single-pass results, are presented in figure A.2.

The results presented in figure A.2 correspond to the rotor position that exhibited the greatest deviation between the single-pass (iteration 1) and the converged results, within
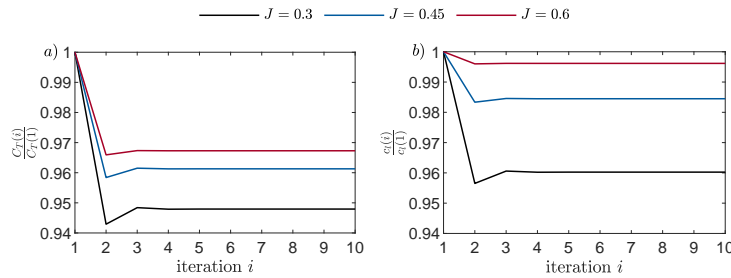
Figure A.2: Predicted a) thrust and b) lift coefficient for different iteration numbers, normalized by the single-pass results ($i = 1$), for $x_r/c = 0.3$, $y_r/R = 0.27$ and $\alpha = 8°$.

A

the investigated parameter space. Both thrust and lift values converge after the third iteration and show a reduction compared with the single-pass results of up to 5%, dependent on the advance ratio.

A.4 Validation of projected streamtube

Validation of the projected streamtube mechanism $\Delta c_{l,p}$ is performed by comparison with the experimental pressure distribution below the rotor axis. It is important to note that other rotor-induced lift-generating contributions also impact the experimental pressure values of the wing (effective angle of attack, thrust vectoring). To minimize these effects, the validation is based on data for the aft-positioned rotor, without inclination ($x_r/c = 0.9$ and $\alpha = 0°$). Figure A.3 displays the experimental and modeled (by equation 7.15) rotor-induced pressure distribution for $J = 0.3$ and $J = 0.6$.
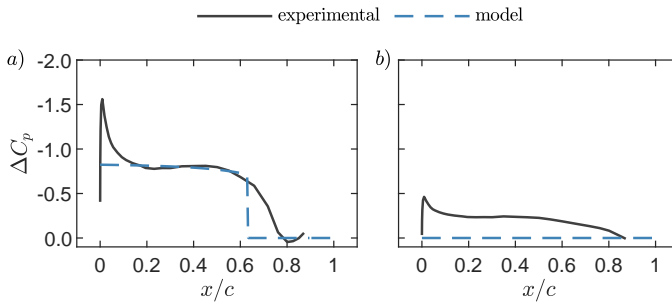
Figure A.3: Predicted rotor-induced pressure distribution ($\Delta C_p = C_p - C_{p,wing}$) over the suction side for $x_r/c = 0.9$, $y_r/R = 0.27$ and $\alpha = 0°$, a) $J = 0.3$ and b) $J = 0.6$.

For $J = 0.3$ in figure A.3a, a good match is observed between the experimental and modeled pressure distributions. However, discrepancies are noted near the leading edge due to the rotor-induced increase in the angle of attack in the experimental results. Furthermore, closer to the rotor ($0.6 < x/c < 0.9$) the model does not capture any rotor-induced pressure reduction because the rotor height exceeds the streamtube height, i.e. $R_s(x')/y_r < 1$. This limitation also applies to $J = 0.6$ in figure A.3b, where the modeled rotor-induced pressure distribution equals zero, leading to an under-prediction compared to the experimental value. This discrepancy is tied to the induced velocities of the rotors' vortex systems, which are not considered in the model.

B

APPENDIX: AEROACOUSTIC MODELLING

The exact term of the inflow model as used in chapter 8 and the validation of the isolated rotor loads and tonal noise are given here.

B.1 EXACT TERMS OF INDUCED VELOCITY BY CIRCULATION

The exact expressions for $V_{x,\Gamma}(r,\theta)$ and $V_{\Gamma,y}(r,\theta)$ can be obtained by integration of equation 8.3 and equation 8.9, respectively. After integration, the result can be found in equations B.1 and B.2.

$$
\begin{aligned}
V_{\Gamma,x}(r,\theta) = \frac{3c_l V_\infty}{8\pi c^2} \Bigg(& x_r(y_r + r\sin\theta)\ln\left(\frac{x_r^2 + (y_r + r\sin\theta)^2}{(c - x_r)^2 + (y_r + r\sin\theta)^2}\right) \\
& + \left(x_r^2 - (y_r + r\sin\theta)^2 - c^2\right)\left(\tan^{-1}\left(\frac{x_r - c}{(y_r + r\sin\theta)}\right) - \tan^{-1}\left(\frac{x_r}{(y_r + r\sin\theta)}\right)\right) \\
& - (y_r + r\sin\theta)c\Bigg)
\end{aligned}
$$

$$(B.1)$$

$$
\begin{aligned}
V_{\Gamma,y}(r,\theta) = \frac{3c_l V_\infty}{16\pi c^2} \Bigg(& \left(c^2 - x_r^2 + (y_r + r\sin\theta)^2\right)\ln\left(\frac{x_r^2 + (y_r + r\sin\theta)^2}{(c - x_r)^2 + (y_r + r\sin\theta)^2}\right) \\
& + 4x_r(y_r + r\sin\theta)\left(\tan^{-1}\left(\frac{x_r - c}{(y_r + r\sin\theta)}\right) - \tan^{-1}\left(\frac{x_r}{(y_r + r\sin\theta)}\right)\right) + 2x_r c + c^2\Bigg)
\end{aligned}
$$

$$(B.2)$$

B.2 ISOLATED ROTOR LOADS VALIDATION

The measured and modeled isolated rotors thrust and torque coefficients are presented in figure B.1. The model captures the general shape of the isolated rotor's performance

trends and predicts the thrust and torque with sufficient accuracy. Some discrepancies are found for the thrust predictions, but these fall within or are close to the experimental uncertainty.
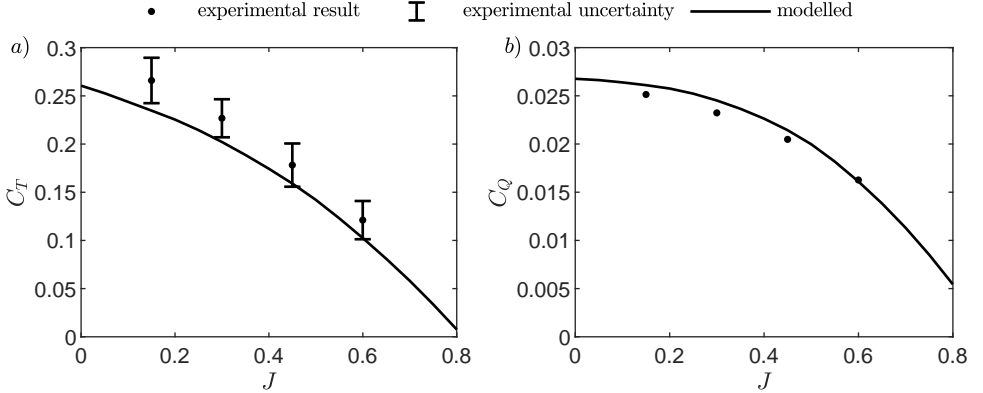
Figure B.1: Modelled and measured isolated rotor's a) thrust coefficient C_T and b) torque coefficient C_Q as a function of the advance ratio J.

B.3 Isolated rotor tonal noise validation

The modeled tonal components of the isolated rotor are presented together with the isolated rotor spectra in figure B.2a. The noise spectra are generated using Welch's method by dividing the microphone data in segments of 2^{12} samples with 50% overlap, giving a frequency resolution of 10 Hz. This shows that the first two blade harmonics fall within an accuracy of 1.5 dB, while the model underpredicts the higher harmonics.
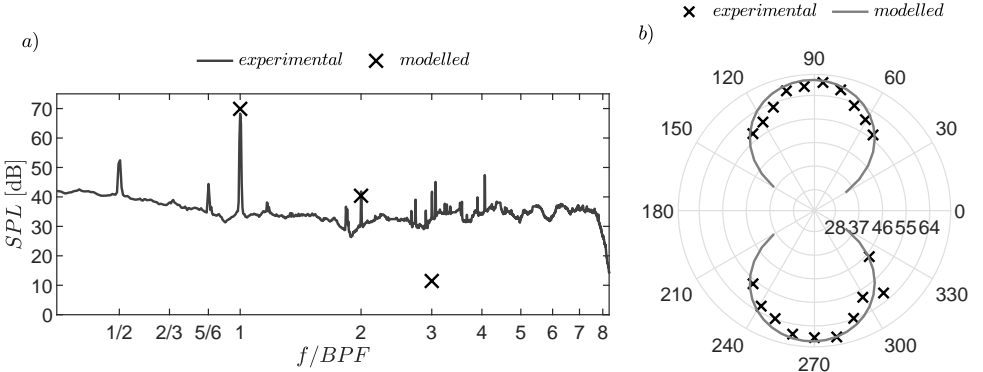
Figure B.2: Noise characteristics of the isolated rotor, showing (a) experimental spectra and modeled tonal noise harmonics, and (b) noise directivity of the first blade passing frequency (*BPF*).

The directivity pattern of the first *BPF* in figure B.2b shows the expected distribution of the source in both the model prediction and experimental results. Discrepancies between the predictions and measurements reach a maximum of 3 dB for some observer directions.

B.4 Phase-averaged spectra

Spectra generated without phase-averaging, i.e. using a fixed sample count per window which is not synchronized with the rotor revolutions, can lead to reduced tonal amplitudes due to minor fluctuations in rotational velocity during data acquisition. This effect was observed by comparing the experimental phase-averaged tonal values with the acoustic spectrum as obtained using Welch's method, by dividing the same microphone data into segments of 2^{12} samples with 50% overlap. The results are presented in figure B.3 and show a consistent reduction in tonal values for the first 4 *BPF*s of approximately 2 dB.
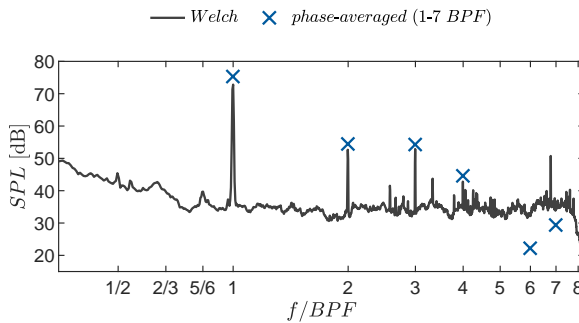
Figure B.3: Comparison between experimental tonal values obtained through Welch's method and phase-averaged spectra, for a microphone in the rotor disk plane (θ_O = 90°) and J = 0, α = 0° and x_r/c = 0.3.

C

APPENDIX: REFERENCE FLIGHT TRAJECTORY

To obtain the flight conditions that correspond to the reference flight trajectory of chapter 9, time is first discretized. For each time step t_i, a vertical and horizontal force balance is created by using the experimental rotors' thrust $T(V_\infty, \alpha)$ and wing lift $L(V_\infty, \alpha)$ and drag $D(V_\infty, \alpha)$.

C.1 FORCE BALANCE

In figure C.1, the definition of the considered aero-propulsive forces along a reference flight path (H,S) are given. Note that the wing's normal $f_{w,N}$ and axial force $f_{w,A}$ depend on the lift L and drag D of the wing only.
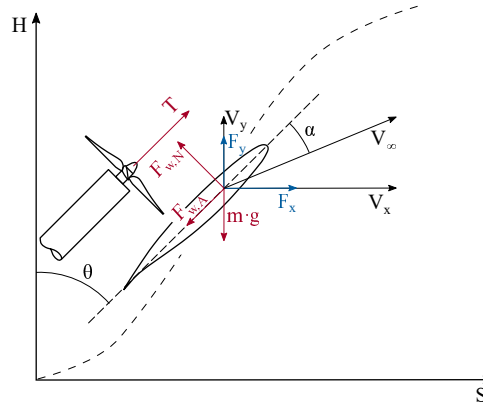
Figure C.1: Definition of the force- (blue) and velocity-vectors (black) of the Over-The-Wing rotor system.

Under the assumption that all forces have the same origin, the horizontal f_x and vertical force f_y on the rotor-wing system for a time-step t_i is given by equations C.1 and C.2:

$$F_x(t_i) = \sin\Big(\theta(t_i)\Big) \cdot T\Big(V_\infty(t_i), \alpha(t_i)\Big) - \sin\Big(\theta(t_i)\Big) \cdot F_{w,N}\Big(V_\infty(t_i), \alpha(t_i)\Big)$$
$$+ \cos\Big(\theta(t_i)\Big) \cdot F_{w,A}\Big(V_\infty(t_i), \alpha(t_i)\Big) - mg \quad \text{(C.1)}$$

$$F_y(t_i) = \cos\Big(\theta(t_i)\Big) \cdot T\Big(V_\infty(t_i), \alpha(t_i)\Big) - \cos\Big(\theta(t_i)\Big) \cdot F_{w,N}\Big(V_\infty(t_i), \alpha(t_i)\Big)$$
$$- \sin\Big(\theta(t_i)\Big) \cdot F_{w,A}\Big(V_\infty(t_i), \alpha(t_i)\Big) \quad \text{(C.2)}$$

in which θ is the rotor-wing tilt-angle and m is a given reference mass. The wing's normal $f_{w,N}$ and axial force $f_{w,A}$ are given by:

$$F_{w,N}(V_\infty, \alpha) = \sin(\alpha) \cdot L(V_\infty, \alpha) + \cos(\alpha) \cdot D(V_\infty, \alpha) \quad \text{(C.3)}$$

$$F_{w,A}(V_\infty, \alpha) = \cos(\alpha) \cdot L(V_\infty, \alpha) - \sin(\alpha) \cdot D(V_\infty, \alpha) \quad \text{(C.4)}$$

C.2 Accounting for unsteady effects

For each time-step the angle of attack is corrected using the theory of Wagner [37]:

$$\alpha_U(t) = \alpha_0 + \Delta\alpha_U(t) = \alpha_0 + \int_0^t \frac{d\alpha}{dt} \cdot \psi(t)dt \quad \text{(C.5)}$$

$$\psi(t) = 1 - 0.165\exp(0.0910Vt/c) - 0.335\exp(0.6Vt/c) \quad \text{(C.6)}$$

C.3 Time-marching scheme

The values for $\alpha(t_i)$ and $V_\infty(t_i)$ are then found through the following time-marching scheme:

Table C.1: Time-marching scheme to obtain dynamic operating conditions.

For each time step t_i
1. Compute T, $F_{w,N}$ and $F_{w,A}$ for α_i and $V_{\infty,i}$ (equations C.3 and C.4)
2. Compute F_x and F_y (equations C.1 and C.2)
3. Compute the accelerations and update the position
4. Change θ to match the direction of flight
5. Find α_{i+1} and $V_{\infty,i+1}$ and correct for unsteadiness (equation C.5)

Along the trajectory, a fixed rotation velocity of the rotors of $n = 383$ Hz is assumed. Hence the rotor advance ratio J is directly related to the free-stream velocity V_∞, i.e. $J = V_\infty/(nD)$. Moreover, a thrust-to-weight ratio of 0.8 is considered.

BIBLIOGRAPHY

REFERENCES

[1] Adu-Gyamfi, B. A., and Good, C., "Electric aviation: A review of concepts and enabling technologies," *Transportation Engineering*, Vol. 9, 2022, p. 100134. doi: 10.1016/j.treng.2022.100134.

[2] Straubinger, A., Rothfeld, R., Shamiyeh, M., Büchter, K.-D., Kaiser, J., and Plötner, K. O., "An overview of current research and developments in urban air mobility–Setting the scene for UAM introduction," *Journal of Air Transport Management*, Vol. 87, 2020, p. 101852. doi: 10.1016/j.jairtraman.2020.101852.

[3] Thipphavong, D. P., Apaza, R., Barmore, B., Battiste, V., Burian, B., Dao, Q., Feary, M., Go, S., Goodrich, K. H., Homola, J., et al., "Urban air mobility airspace integration concepts and considerations," *2018 Aviation Technology, Integration, and Operations Conference*, 2018, p. 3676. doi: 10.2514/6.2018-3676.

[4] Bauranov, A., and Rakas, J., "Designing airspace for urban air mobility: A review of concepts and approaches," *Progress in Aerospace Sciences*, Vol. 125, 2021, p. 100726. doi: 10.1016/j.paerosci.2021.100726.

[5] Cohen, A., and Shaheen, S., "Urban Air Mobility: Opportunities and Obstacles," *International Encyclopedia of Transportation*, 2021, pp. 702–709. doi: 10.1016/B978-0-08-102671-7.10764-X.

[6] Goyal, R., Reiche, C., Fernando, C., Serrao, J., Kimmel, S., Cohen, A., and Shaheen, S., "Urban Air Mobility (UAM) Market Study," Tech. Rep. HQ-E-DAA-TN63717, NASA, 2018. URL https://ntrs.nasa.gov/citations/20190001472.

[7] EASA, "Study on Societal Acceptance of Urban Air Mobility in Europe," Tech. rep., European Union Aviation Safety Agency and McKinsey & Company, 2021. URL https://www.easa.europa.eu/sites/default/files/dfu/uam-full-report.pdf.

[8] Biehle, T., "Social Sustainable Urban Air Mobility in Europe," *Sustainability*, Vol. 14, 2022, p. 9312. doi: 10.3390/su14159312.

[9] Borer, N. K., Patterson, M. D., Viken, J. K., Moore, M. D., Bevirt, J., Stoll, A. M., and Gibson, A. R., "Design and Performance of the NASA SCEPTOR Distributed Electric Propulsion Flight Demonstrator," *16th AIAA Aviation Technology, Integration, and Operations Conference*, American Institute of Aeronautics and Astronautics, 2016, p. 3920. doi: 10.2514/6.2016-3920.

[10] Volocopter, "VoloCity air taxi aircraft standing at an airport field," https://www.volocopter.com/, 2023. [Online; accessed November 15, 2024].

[11] Sciences, A. F., "Aurora Flight Sciences Pegasus PAV," https://evtol.news/aurora/, 2024. [Online; accessed November 15, 2024].

[12] Aviation, J., "Joby Aviation S4 2.0," https://www.jobyaviation.com/, 2019. [Online; accessed November 15, 2024].

[13] Airbus, "Acubed Vahana," https://evtoldatabase.org/app/aircraft/show.php?aircraft_id=1, 2024. [Online; accessed November 15, 2024].

[14] Wick, A. T., Hooker, J. R., and Zeune, C. H., "Integrated Aerodynamic Benefits of Distributed Propulsion," *53rd AIAA Aerospace Sciences Meeting*, American Institute of Aeronautics and Astronautics, 2015, p. 1500. doi: 10.2514/6.2015-1500.

[15] Lee, T., Ni, T., and Lin, G., "Aerodynamics and Flowfield of Distributed Electric Propulsion Tiltwing During Transition With Deflected Trailing-Edge Flap," *Journal of Fluids Engineering*, Vol. 146, 2024. doi: 10.1115/1.4063934.

[16] Broadbent, E., "Noise shielding for aircraft," *Progress in Aerospace Sciences*, Vol. 17, 1976, pp. 231–268. doi: 10.1016/0376-0421(76)90009-9.

[17] Müller, L., Kozulovic, D., Hepperle, M., and Radespiel, R., "The influence of the propeller position on the aerodynamics of a channel wing," *Deutscher Luft-und Raumfahrt Kongress*, 2012, pp. 784–792.

[18] Alba-Maestre, J., van Reine, K. P., Sinnige, T., and Castro, S. G. P., "Preliminary Propulsion and Power System Design of a Tandem-Wing Long-Range eVTOL Aircraft," *Applied Sciences*, Vol. 11, 2021, p. 11083. doi: 10.3390/app112311083.

[19] Alba-Maestre, J., Beyne, E., Buszek, M., Cuadrat-Grzybowski, M., Montoya Santamaria, A., Poliakov, N., Prud'homme van Reine, K., Salvador Lopez, N., Schoser, J., and Wadia, K., "Midterm Report—Multi-Disciplinary Design and Optimisation of a Long-Range eVTOL Aircraft," Tech. rep., Delft University of Technology, 2021. doi: 10.5281/zenodo.5576104.

[20] Bacchini, A., and Cestino, E., "Electric VTOL configurations comparison," *Aerospace*, Vol. 6, No. 3, 2019, p. 26. doi: 10.3390/aerospace6030026.

[21] Leishman, J., *Principles of Helicopter Aerodynamics*, Cambridge Aerospace Series, Cambridge University Press, 2016. URL https://books.google.nl/books?id=uscAMQAACAAJ.

[22] Chauhan, S. S., and Martins, J. R. R. A., "Tilt-Wing eVTOL Takeoff Trajectory Optimization," *Journal of Aircraft*, Vol. 57, 2020, pp. 93–112. doi: 10.2514/1.C035476.

[23] Panish, L., and Bacic, M., "Tiltwing eVTOL Transition Trajectory Optimization," *Journal of Aircraft*, 2024, pp. 1–13. doi: 10.2514/1.C037862.

[24] Lilium, "Lilium Jet (7-seater)," https://evtol.news/lilium-gmbh-lilium-jet-7-seater, 2024. [Online; accessed December 11, 2024].

[25] Lilium, "Technology Blog," https://lilium.com/newsroom-detail/technology-behind-the-lilium-jet, 2021. [Online; accessed April 19, 2022].

[26] Liu, Y., and Gao, C., "Assessing Electric Vertical Take-Off and Landing for Urban Air Taxi Services: Key Parameters and Future Transportation Impact," *Sustainability*, Vol. 16, No. 11, 2024, p. 4732. doi: 10.3390/su16114732.

[27] Glauert, H., "Airplane Propellers," Springer Berlin Heidelberg, 1935, pp. 169–360. doi: 10.1007/978-3-642-91487-4_3.

[28] Gur, O., and Rosen, A., "Comparison between blade-element models of propellers," *The Aeronautical Journal*, Vol. 112, 2008, pp. 689–704. doi: 10.1017/S0001924000002669.

[29] Vries, O. D., "Fluid dynamic aspects of wind energy conversion," Tech. Rep. AGARD-AG-243, Advisory Group for Aerospace Research and Development, 1979.

[30] Prandtl, L., and Betz, A., *Vier abhandlungen zur hydrodynamik und aerodynamik*, Universitätsverlag Göttingen, 1927.

[31] Shen, W. Z., Sørensen, J. N., and Mikkelsen, R., "Tip Loss Correction for Actuator/-Navier–Stokes Computations," *Journal of Solar Energy Engineering*, Vol. 127, 2005, pp. 209–213. doi: 10.1115/1.1850488.

[32] Veldhuis, L., "Propeller wing aerodynamic interference," Ph.D. thesis, Delft University of Technology, 2005.

[33] Dekker, H. N. J., Ragni, D., Baars, W. J., Scarano, F., and Tuinstra, M., "Aerodynamic Interactions of Side-by-Side Rotors in Ground Proximity," *AIAA Journal*, Vol. 60, 2022, pp. 4267–4277. doi: 10.2514/1.J061105.

[34] de Vries, R., "Hybrid-Electric Aircraft with Over-the-Wing Distributed Propulsion: Aerodynamic Performance and Conceptual Design," Ph.D. thesis, Delft University of Technology, 2022. doi: 10.4233/uuid:ef87dc11-e7b2-4726-a41f-28588d64c58d.

[35] Ramasamy, M., Johnson, B., and Leishman, J. G., "Turbulent Tip Vortex Measurements Using Dual-Plane Stereoscopic Particle Image Velocimetry," *AIAA Journal*, Vol. 47, 2009, pp. 1826–1840. doi: 10.2514/1.39202.

[36] McAlister, K. W., "Rotor Wake Development During the First Revolution," *Journal of the American Helicopter Society*, Vol. 49, 2004, pp. 371–390. doi: 10.4050/JAHS.49.371.

[37] Wagner, H., "Dynamischer auftrieb von tragflugeln," *Zeitschrift für angewandte Mathematik und Mechanik*, 1925.

[38] Jones, R. T., "Operational treatment of the nonuniform-lift theory in airplane dynamics," Tech. Rep. NACA-TN-667, National Advisory Committee for Aeronautics (NACA), 1938.

[39] van Arnhem, N., de Vries, R., Sinnige, T., Vos, R., Eitelberg, G., and Veldhuis, L. L. M., "Engineering Method to Estimate the Blade Loading of Propellers in Nonuniform Flow," *AIAA Journal*, Vol. 58, 2020, pp. 5332–5346. doi: 10.2514/1.J059485.

[40] Sears, W. R., "Some Aspects of Non-Stationary Airfoil Theory and Its Practical Application," *Journal of the Aeronautical Sciences*, Vol. 8, 1941, pp. 104–108. doi: 10.2514/8.10655.

[41] Amiet, R. K., "Compressibility Effects in Unsteady Thin-Airfoil Theory," *AIAA Journal*, Vol. 12, 1974, pp. 252–255. doi: 10.2514/3.49212.

[42] Williams, J. E. F., and Hawkings, D. L., "Sound generation by turbulence and surfaces in arbitrary motion," *Philosophical Transactions of the Royal Society of London. Series A, Mathematical and Physical Sciences*, Vol. 264, 1969, pp. 321–342. doi: 10.1098/rsta.1969.0031.

[43] Greenwood, E., Brentner, K. S., Rau, R. F., and Gan, Z. F. T., "Challenges and opportunities for low noise electric aircraft," *International Journal of Aeroacoustics*, Vol. 21, 2022, pp. 315–381. doi: 10.1177/1475472X221107377.

[44] Roger, M., and Moreau, S., "Tonal-Noise Assessment of Quadrotor-Type UAV Using Source-Mode Expansions," *Acoustics*, Vol. 2, 2020, pp. 674–690. doi: 10.3390/acoustics2030036.

[45] Lighthill, M. J., "On sound generated aerodynamically I. General theory," *Proceedings of the Royal Society of London. Series A. Mathematical and Physical Sciences*, Vol. 211, No. 1107, 1952, pp. 564–587.

[46] Glegg, S., and Devenport, W., *Aeroacoustics of low Mach number flows: fundamentals, analysis, and measurement*, Academic Press, 2017.

[47] Hanson, D. B., "Helicoidal Surface Theory for Harmonic Noise of Propellers in the Far Field," *AIAA Journal*, Vol. 18, 1980, pp. 1213–1220. doi: 10.2514/3.50873.

[48] Goldstein, M. E., *Aeroacoustics*, Mc Graw-Hill: New York, NY, USA, 1976, 1976.

[49] Hanson, D. B., "Near-field frequency-domain theory for propeller noise," *AIAA Journal*, Vol. 23, 1985, pp. 499–504. doi: 10.2514/3.8943.

[50] Brouwer, H., "Analytical Method for the Computation of the Noise from a Pusher Propeller," *16th AIAA/CEAS Aeroacoustics Conference*, American Institute of Aeronautics and Astronautics, 2010, p. 3848. doi: 10.2514/6.2010-3848.

[51] Roger, M., Acevedo-Giraldo, D., and Jacob, M. C., "Acoustic versus aerodynamic installation effects on a generic propeller-driven flying architecture," *International Journal of Aeroacoustics*, Vol. 21, 2022, pp. 585–609. doi: 10.1177/1475472X221107372.

[52] Moreau, S., and Roger, M., "Advanced noise modeling for future propulsion systems," *International Journal of Aeroacoustics*, Vol. 17, 2018, pp. 576–599. doi: 10.1177/1475472X18789005.

[53] Zarri, A., de Prenter, F., Casalino, D., Avallone, F., and Ragni, D., "Tip-on-Tip Interaction Noise Modeling for Distributed Propellers," *DICUAM 2024*, 2024.

[54] De Prenter, F., Zarri, A., and Casalino, D., "Low-cost computational modeling of aeroacoustic interactions between adjacent propellers," *30th AIAA/CEAS Aeroacoustics Conference (2024)*, 2024, p. 3069. doi: 10.2514/6.2024-3069.

[55] Brooks, T., Pope, D., and Marcolini, M., "Airfoil self-noise and prediction," Tech. Rep. L-16528, NASA, 1989.

[56] Pegg, R. J., "A summary and evaluation of semi-empirical methods for the prediction of helicopter rotor noise," Tech. Rep. NASA-TM-80200, NASA, 1979.

[57] Yu, Y. H., "Rotor blade–vortex interaction noise," *Progress in Aerospace Sciences*, Vol. 36, 2000, pp. 97–115. doi: 10.1016/S0376-0421(99)00012-3.

[58] Stokkermans, T. C. A., Usai, D., Sinnige, T., and Veldhuis, L. L. M., "Aerodynamic Interaction Effects Between Propellers in Typical eVTOL Vehicle Configurations," *Journal of Aircraft*, Vol. 58, 2021, pp. 815–833. doi: 10.2514/1.C035814.

[59] Buck, S., Oerlemans, S., and Palo, S., "Experimental Validation of a Wind Turbine Turbulent Inflow Noise Prediction Code," *AIAA Journal*, Vol. 56, 2018, pp. 1495–1506. doi: 10.2514/1.J056134.

[60] Raposo, H., and Azarpeyvand, M., "Turbulence ingestion noise generation in rotating blades," *Journal of Fluid Mechanics*, Vol. 980, 2024, p. A53.

[61] Blake, W. K., *Mechanics of flow-induced sound and vibration, Volume 2: Complex flow-structure interactions*, Academic press, 2017.

[62] de Vries, R., van Arnhem, N., Sinnige, T., Vos, R., and Veldhuis, L. L., "Aerodynamic interaction between propellers of a distributed-propulsion system in forward flight," *Aerospace Science and Technology*, Vol. 118, 2021, p. 107009. doi: 10.1016/j.ast.2021.107009.

[63] Shukla, D., and Komerath, N., "Low Reynolds number multirotor aerodynamic wake interactions," *Experiments in Fluids*, Vol. 60, 2019, p. 77. doi: 10.1007/s00348-019-2724-3.

[64] Shukla, D., and Komerath, N., "Multirotor drone aerodynamic interaction investigation," *Drones*, Vol. 2, 2018, p. 43. doi: 10.3390/drones2040043.

[65] Ramasamy, M., "Measurements comparing hover performance of single, coaxial, tandem, and tilt-rotor configurations," *AHS 69th Annual Forum*, Vol. 31, 2013, p. 32.

[66] Ning, Z., "Experimental investigations on the aerodynamic and aeroacoustic characteristics of small UAS propellers," Ph.D. thesis, Iowa State University, 2018.

[67] Lee, H., and Lee, D. J., "Rotor interactional effects on aerodynamic and noise characteristics of a small multirotor unmanned aerial vehicle," *Physics of Fluids*, Vol. 32, 2020, p. 47107. doi: 10.1063/5.0003992.

[68] Zhou, W., Ning, Z., Li, H., and Hu, H., "An experimental investigation on rotor-to-rotor interactions of small UAV propellers," *35th AIAA applied aerodynamics conference*, 2017, p. 3744. doi: 10.2514/6.2017-3744.

[69] Lee, T. E., Leishman, J. G., and Ramasamy, M., "Fluid dynamics of interacting blade tip vortices with a ground plane," *Journal of the American Helicopter Society*, Vol. 55, 2010, p. 22005. doi: 10.4050/JAHS.55.022005.

[70] III, J. I. M., and Leishman, J. G., "Vortical sheet behavior in the wake of a rotor in ground effect," *AIAA Journal*, Vol. 55, 2017, p. 24. doi: 10.2514/1.J054498.

[71] Nathan, N. D., and Green, R. B., "The flow around a model helicopter main rotor in ground effect," *Experiments in Fluids*, Vol. 52, 2012, pp. 151–166. doi: 10.1007/s00348-011-1212-1.

[72] Landgrebe, A. J., "The wake geometry of a hovering helicopter rotor and its influence on rotor performance," *Journal of the American Helicopter society*, Vol. 17, 1972, pp. 3–15. doi: 10.4050/JAHS.17.4.3.

[73] Fradenburgh, E. A., "The helicopter and the ground effect machine," *Journal of the American Helicopter Society*, Vol. 5, 1960, pp. 24–33. doi: 10.4050/JAHS.5.4.24.

[74] Hanson, L., Jawahar, H. K., Vemuri, S. S., and Azarpeyvand, M., "Experimental investigation of propeller noise in ground effect," *Journal of Sound and Vibration*, Vol. 559, 2023, p. 117751. doi: 10.1016/j.jsv.2023.117751.

[75] Cheeseman, I. C., and Bennett, W. E., "The effect of the ground on a helicopter rotor in forward flight," Tech. Rep. No. 3021, Aeronautical Research Council, 1957.

[76] He, X., and Leang, K. K., "Quasi-Steady In-Ground-Effect Model for Single and Multirotor Aerial Vehicles," *AIAA Journal*, Vol. 58, 2020, pp. 5318–5331. doi: 10.2514/1.J059223.

[77] Sanchez-Cuevas, P., Heredia, G., and Ollero, A., "Characterization of the aerodynamic ground effect and its influence in multirotor control," *International Journal of Aerospace Engineering*, Vol. 2017, 2017. doi: 10.1155/2017/1823056.

[78] Sharf, I., Nahon, M., Harmat, A., Khan, W., Michini, M., Speal, N., Trentini, M., Tsadok, T., and Wang, T., "Ground effect experiments and model validation with Draganflyer X8 rotorcraft," *2014 International Conference on Unmanned Aircraft Systems (ICUAS)*, 2014, pp. 1158–1166. doi: 10.1109/ICUAS.2014.6842370.

[79] Conyers, S. A., Rutherford, M. J., and Valavanis, K. P., "An empirical evaluation of ground effect for small-scale rotorcraft," *2018 IEEE International Conference on Robotics and Automation (ICRA)*, 2018, pp. 1244–1250. doi: 10.1109/ICRA.2018.8461035.

[80] Healy, R., McCauley, J., Gandhi, F., Sahni, O., and Mistry, M., "A Computational Investigation of Side-by-Side Rotors in Ground Effect," *Proceedings of the 77th VFS Annual Forum (Virtual)*, 2021.

[81] Healy, R., McCauley, J., Gandhi, F., and Sahni, O., "A Computational Examination of Side-by-Side Rotors in Ground Effect," *Journal of the American Helicopter Society*, Vol. 68, 2023, pp. 32007–32024. doi: 10.4050/JAHS.68.032007.

[82] Maisel, M. D., *The history of the XV-15 tilt rotor research aircraft: from concept to flight*, National Aeronautics and Space Administration, Office of Policy and Plans, 2000.

[83] Polak, D. R., Rehm, W., and George, A. R., "Effects of an image plane on the tiltrotor fountain flow," *Journal of the American Helicopter Society*, Vol. 45, 2000, pp. 90–96. doi: 10.4050/JAHS.45.90.

[84] Zanotti, A., Savino, A., Palazzi, M., Tugnoli, M., and Muscarello, V., "Assessment of a mid-fidelity numerical approach for the investigation of tiltrotor aerodynamics," *Applied Sciences*, Vol. 11, 2021, p. 3385. doi: 10.3390/app11083385.

[85] Potsdam, M. A., and Strawn, R. C., "CFD simulations of tiltrotor configurations in hover," *Journal of the American Helicopter Society*, Vol. 50, 2005, pp. 82–94. doi: 10.4050/1.3092845.

[86] Polak, D. R., and George, A. R., "Flowfield and acoustic measurements from a model tiltrotor in hover," *Journal of aircraft*, Vol. 35, 1998, pp. 921–929. doi: 10.2514/2.2387.

[87] Siclari, M. J., Migdal, D., Jr, T. W. L., Barche, J., and Palcza, J. L., "Development of theoretical models for jet-induced effects on V/STOL aircraft," *Journal of Aircraft*, Vol. 13, 1976, pp. 938–944. doi: 10.2514/3.58733.

[88] Huang, L., and El-Genk, M. S., "Heat transfer of an impinging jet on a flat surface," *International Journal of Heat and Mass Transfer*, Vol. 37, 1994, pp. 1915–1923. doi: 10.1016/0017-9310(94)90331-X.

[89] Cabrita, P. M., Saddington, A. J., and Knowles, K., "PIV measurements in a twin-jet STOVL fountain flow," *The Aeronautical Journal*, Vol. 109, 2005, pp. 439–449. doi: 10.1017/S0001924000000853.

[90] Saddington, A. J., Cabrita, P. M., and Knowles, K., "Large-scale instabilities in a STOVL upwash fountain," *Engineering Turbulence Modelling and Experiments 6*, 2005, pp. 667–676. doi: 10.1016/B978-008044544-1/50064-9.

[91] Stahl, S. L., Prasad, C., and Gaitonde, D. V., "Distinctions between single and twin impinging jet dynamics," *The Journal of the Acoustical Society of America*, Vol. 150, 2021, pp. 734–744. doi: 10.1121/10.0005727.

[92] Müller, L., Heinze, W., Kožulović, D., Hepperle, M., and Radespiel, R., "Aerodynamic Installation Effects of an Over-the-Wing Propeller on a High-Lift Configuration," *Journal of Aircraft*, Vol. 51, 2014, pp. 249–258. doi: 10.2514/1.C032307.

[93] Marcus, E. A., de Vries, R., Kulkarni, A. R., and Veldhuis, L. L., "Aerodynamic Investigation of an Over-the-Wing Propeller for Distributed Propulsion," *2018 AIAA Aerospace Sciences Meeting*, American Institute of Aeronautics and Astronautics, 2018, p. 2053. doi: 10.2514/6.2018-2053.

[94] Johnson, J. L., and White, R. E., "Exploratory low-speed wind-tunnel investigation of advanced commuterconfigurations including an over-the-wing propeller design," *Aircraft Design, Systems and Technology Meeting*, American Institute of Aeronautics and Astronautics, 1983, p. 2531. doi: 10.2514/6.1983-2531.

[95] Cooper, R., McCann, W. J., and Chapleo, A. Q., "Over wing propeller aerodynamics," *ICAS PROCEEDINGS*, American Institute of Aeronautics and Astronautics, 1992, pp. 266–266.

[96] Perry, A. T., Bretl, T., and Ansell, P. J., "Aeropropulsive Coupling Effects on a General-Aviation Aircraft with Distributed Electric Propulsion," *Journal of Aircraft*, Vol. 58, 2021, pp. 1351–1363. doi: 10.2514/1.C036048.

[97] de Vries, R., van Arnhem, N., Avallone, F., Ragni, D., Vos, R., Eitelberg, G., and Veldhuis, L. L. M., "Experimental Investigation of Over-the-Wing Propeller–Boundary-Layer Interaction," *AIAA Journal*, Vol. 59, 2021, pp. 2169–2182. doi: 10.2514/1.J059770.

[98] de Vries, R., and Vos, R., "Aerodynamic Performance Benefits of Over-the-Wing Distributed Propulsion for Hybrid-Electric Transport Aircraft," *Journal of Aircraft*, Vol. 60, 2023, pp. 1201–1218. doi: 10.2514/1.C036909.

[99] Petricelli, F., Chaitanya, P., Palleja-Cabre, S., Meloni, S., Joseph, P. F., Karimian, A., Palani, S., and Camussi, R., "An experimental investigation on the effect of in-flow distortions of propeller noise," *Applied Acoustics*, Vol. 214, 2023, p. 109682. doi: 10.1016/j.apacoust.2023.109682.

[100] Zhong, S., Zhou, P., Chen, W., Jiang, H., Wu, H., and Zhang, X., "An investigation of rotor aeroacoustics with unsteady motions and uncertainty factors," *Journal of Fluid Mechanics*, Vol. 956, 2023, p. A16. doi: 10.1017/jfm.2022.1097.

[101] Jamaluddin, N. S., Celik, A., Baskaran, K., Rezgui, D., and Azarpeyvand, M., "Experimental analysis of a propeller noise in turbulent flow," *Physics of Fluids*, Vol. 35, 2023. doi: 10.1063/5.0153326.

[102] Murray, H. H., Devenport, W. J., Alexander, W. N., Glegg, S. A. L., and Wisda, D., "Aeroacoustics of a rotor ingesting a planar boundary layer at high thrust," *Journal of Fluid Mechanics*, Vol. 850, 2018, pp. 212–245. doi: 10.1017/jfm.2018.438.

[103] Yang, Y., Sciacchitano, A., Veldhuis, L. L. M., and Eitelberg, G., "Spatial-temporal and modal analysis of propeller induced ground vortices by particle image velocimetry," *Physics of Fluids*, Vol. 28, 2016. doi: 10.1063/1.4964685.

[104] Yang, Y., Sciacchitano, A., Veldhuis, L. L. M., and Eitelberg, G., "Analysis of propeller-induced ground vortices by particle image velocimetry," *Journal of Visualization*, Vol. 21, 2018, pp. 39–55. doi: 10.1007/s12650-017-0439-1.

[105] R Sato, R. T., and Nishiyama, S., "Observation of flow on a horizontal flat plate above a working propeller and physics of propeller-hull vortex cavitation," *Proceedings of*

the International Symposium on Propeller and Cavitation, China International Book Trading Corporation, 1986, pp. 118–125.

[106] Andersson, J., Gustafsson, R., Johansson, R., and Bensow, R. E., "Propeller–hull interaction beyond the propulsive factors—A case study on the performance of different propeller designs," *Ocean Engineering*, Vol. 256, 2022, p. 111424. doi: 10.1016/j.oceaneng.2022.111424.

[107] Beck, S. C., Müller, L., and Langer, S. C., "Numerical assessment of the vibration control effects of porous liners on an over-the-wing propeller configuration," *CEAS Aeronautical Journal*, Vol. 7, 2016, pp. 275–286. doi: 10.1007/s13272-016-0186-3.

[108] Cros, E., Roger, M., and Serre, G., "On the very low frequency scattering of propeller noise by a neighboring cylinder," *AIAA AVIATION 2021 FORUM*, American Institute of Aeronautics and Astronautics, 2021, p. 2251. doi: 10.2514/6.2021-2251.

[109] Giraldo, D. A., Roger, M., Jacob, M. C., and Beriot, H., "Analytical study of the aerodynamic noise emitted by distributed electric propulsion systems," *28th AIAA/CEAS Aeroacoustics 2022 Conference*, American Institute of Aeronautics and Astronautics, 2022, p. 2830. doi: 10.2514/6.2022-2830.

[110] Hubbard, H. H., *Aeroacoustics of flight vehicles: theory and practice*, Vol. 1, National Aeronautics and Space Administration, Office of Management . . . , 1991.

[111] Zagaglia, D., Giuni, M., and Green, R. B., "Rotor-obstacle aerodynamic interaction in hovering flight: An experimental survey," *Proceedings of the AHS International 72nd Annual Forum*, 2016, pp. 1–9.

[112] Radhakrishnan, A., "An experimental investigation of ground effect on a quad tilt rotor in hover and low speed forward flight," Ph.D. thesis, University of Maryland, 2006.

[113] Chirico, G., Szubert, D., Vigevano, L., and Barakos, G. N., "Numerical modelling of the aerodynamic interference between helicopter and ground obstacles," *CEAS Aeronautical Journal*, Vol. 8, 2017, pp. 589–611. doi: 10.1007/s13272-017-0259-y.

[114] Britcher, C., and Landman, D., *Wind Tunnel Test Techniques: Design and Use at Low and High Speeds with Statistical Engineering Applications*, Academic Press, 2023.

[115] Zhang, J. X., and Hoshino, K., "Mechanical transducers: Cantilevers, acoustic wave sensors, and thermal sensors," *Molecular Sensors and Nanodevices*, 2019, pp. 311–412. doi: 10.1016/B978-0-12-814862-4.00006-5.

[116] Gardner, A. D., Wolf, C. C., and Raffel, M., "Review of measurement techniques for unsteady helicopter rotor flows," *Progress in Aerospace Sciences*, Vol. 111, 2019, p. 100566. doi: 10.1016/j.paerosci.2019.100566.

[117] Raffel, M., Willert, C. E., Scarano, F., Kähler, C. J., Wereley, S. T., and Kompenhans, J., *Particle image velocimetry: a practical guide*, springer, 2018.

[118] Faleiros, D. E., Tuinstra, M., Sciacchitano, A., and Scarano, F., "Generation and control of helium-filled soap bubbles for PIV," *Experiments in Fluids*, Vol. 60, 2019, pp. 1–17. doi: 10.1007/s00348-019-2687-4.

[119] Scarano, F., Ghaemi, S., Caridi, G. C. A., Bosbach, J., Dierksheide, U., and Sciacchitano, A., "On the use of helium-filled soap bubbles for large-scale tomographic PIV in wind tunnel experiments," *Experiments in Fluids*, Vol. 56, 2015, pp. 1–12. doi: 10.1007/s00348-015-1909-7.

[120] Hysa, I., Tuinstra, M., Sciacchitano, A., Scarano, F., Schwartz, N., Harrison, C., and Gebbink, R., "Three-dimensional quantitative flow visualization around a thrust reverser," *AIAA Journal*, Vol. 61, No. 12, 2023, pp. 5404–5414. doi: 10.2514/1.J063124.

[121] Hysa, I., Tuinstra, M., Sciacchitano, A., Scarano, F., van der Meulen, M.-J., Rockstroh, T., and Roosenboom, E. W., "A multi-directional redundant 3D-LPT system for ship–flight–deck wind interactions," *Experiments in Fluids*, Vol. 65, No. 8, 2024, p. 126. doi: 10.1007/s00348-024-03867-0.

[122] Mendez, M. A., Raiola, M., Masullo, A., Discetti, S., Ianiro, A., Theunissen, R., and Buchlin, J.-M., "POD-based background removal for particle image velocimetry," *Experimental Thermal and Fluid Science*, Vol. 80, 2017, pp. 181–192. doi: 10.1016/j.expthermflusci.2016.08.021.

[123] Honkanen, M., and Nobach, H., "Background extraction from double-frame PIV images," *Experiments in Fluids*, Vol. 38, 2005, pp. 348–362. doi: 10.1007/s00348-004-0916-x.

[124] Mejia-Alvarez, R., and Christensen, K. T., "Robust suppression of background reflections in PIV images," *Measurement Science and Technology*, Vol. 24, 2013, p. 027003. doi: 10.1088/0957-0233/24/2/027003.

[125] Willert, C., "Stereoscopic digital particle image velocimetry for application in wind tunnel flows," *Measurement Science and Technology*, Vol. 8, 1997, pp. 1465–1479. doi: 10.1088/0957-0233/8/12/010.

[126] Sciacchitano, A., and Scarano, F., "Elimination of PIV light reflections via a temporal high pass filter," *Measurement Science and Technology*, Vol. 25, 2014, p. 84009. doi: 10.1088/0957-0233/25/8/084009.

[127] Gui, L., "Evaluation of low image density recordings with the MQD method and application to the flow in a liquid bridge," *Journal of Flow Visualization & Image Processing*, Vol. 4, 1997, pp. 333–343.

[128] Zhao, C. X., Steijn, V. V., Richardson, I. M., Saldi, Z., and Kleijn, C. R., "Experimental characterization of GTA weld pool surface flow using PIV," *ASM Proceedings of the International Conference: Trends in Welding Research*, 2009, pp. 201–210.

[129] Scarano, F., "Iterative image deformation methods in PIV," *Measurement Science and Technology*, Vol. 13, 2002, pp. R1–R19. doi: 10.1088/0957-0233/13/1/201.

[130] Scarano, F., and Riethmuller, M. L., "Iterative multigrid approach in PIV image processing with discrete window offset," *Experiments in Fluids*, Vol. 26, 1999, pp. 513–523. doi: 10.1007/s003480050318.

[131] Schanz, D., Gesemann, S., and Schröder, A., "Shake-The-Box: Lagrangian particle tracking at high particle image densities," *Experiments in Fluids*, Vol. 57, 2016, pp. 1–27. doi: 10.1007/s00348-016-2157-1.

[132] Wieneke, B., "Volume self-calibration for 3D particle image velocimetry," *Experiments in Fluids*, Vol. 45, 2008, pp. 549–556. doi: 10.1007/s00348-008-0521-5.

[133] Schanz, D., Gesemann, S., Schröder, A., Wieneke, B., and Novara, M., "Non-uniform optical transfer functions in particle imaging: calibration and application to tomographic reconstruction," *Measurement Science and Technology*, Vol. 24, 2013, p. 024009. doi: 10.1088/0957-0233/24/2/024009.

[134] Wieneke, B., "Iterative reconstruction of volumetric particle distribution," *Measurement Science and Technology*, Vol. 24, 2013, p. 024008. doi: 10.1088/0957-0233/24/2/024008.

[135] Schneiders, J. F. G., and Scarano, F., "Dense velocity reconstruction from tomographic PTV with material derivatives," *Experiments in Fluids*, Vol. 57, 2016, pp. 1–22. doi: 10.1007/s00348-016-2225-6.

[136] Caridi, G. C. A., Ragni, D., Sciacchitano, A., and Scarano, F., "HFSB-seeding for large-scale tomographic PIV in wind tunnels," *Experiments in Fluids*, Vol. 57, 2016, p. 190. doi: 10.1007/s00348-016-2277-7.

[137] Lynch, K. P., and Scarano, F., "An efficient and accurate approach to MTE-MART for time-resolved tomographic PIV," *Experiments in Fluids*, Vol. 56, 2015, p. 66. doi: 10.1007/s00348-015-1934-6.

[138] Elsinga, G. E., Scarano, F., Wieneke, B., and van Oudheusden, B. W., "Tomographic particle image velocimetry," *Experiments in Fluids*, Vol. 41, 2006, pp. 933–947. doi: 10.1007/s00348-006-0212-z.

[139] Gesemann, S., Huhn, F., Schanz, D., and Schröder, A., "From noisy particle tracks to velocity, acceleration and pressure fields using B-splines and penalties," *18th international symposium on applications of laser and imaging techniques to fluid mechanics, Lisbon, Portugal*, 2016.

[140] Sciacchitano, A., "Uncertainty quantification in particle image velocimetry," *Measurement Science and Technology*, Vol. 30, 2019, p. 092001. doi: 10.1088/1361-6501/ab1db8.

[141] Christensen, K., "The influence of peak-locking errors on turbulence statistics computed from PIV ensembles," *Experiments in fluids*, Vol. 36, 2004, pp. 484–497. doi: 10.1007/s00348-003-0754-2.

[142] Sciacchitano, A., and Wieneke, B., "PIV uncertainty propagation," *Measurement Science and Technology*, Vol. 27, 2016, p. 084006. doi: 10.1088/0957-0233/27/8/084006.

[143] Adrian, R. J., "Dynamic ranges of velocity and spatial resolution of particle image velocimetry," *Measurement Science and Technology*, Vol. 8, 1997, pp. 1393–1398. doi: 10.1088/0957-0233/8/12/003.

[144] Ragni, D., Avallone, F., and Casalino, D., "Measurement techniques for aeroacoustics: from aerodynamic comparisons to aeroacoustic assimilations," *Measurement Science and Technology*, Vol. 33, 2022, p. 062001. doi: 10.1088/1361-6501/ac547d.

[145] Mueller, T. J., *Aeroacoustic measurements*, Springer Science & Business Media, 2002.

[146] VanDercreek, C., Merino-Martínez, R., Sijtsma, P., and Snellen, M., "Evaluation of the effect of microphone cavity geometries on acoustic imaging in wind tunnels," *Applied Acoustics*, Vol. 181, 2021, p. 108154. doi: 10.1016/j.apacoust.2021.108154.

[147] Bento, H. F. M., Vandercreek, C. P., Avallone, F., Ragni, D., Sijtsma, P., and Snellen, M., "Wall treatments for aeroacoustic measurements in closed wind tunnel test sections," *AIAA AVIATION 2023 Forum*, American Institute of Aeronautics and Astronautics, 2023, p. 4162. doi: 10.2514/6.2023-4162.

[148] Piezotronics, P., "Microphone Handbook," https://www.pcb.com/contentstore/mktgcontent/linkeddocuments/Acoustics/TM-AC-MicHandbook_lowres.pdf, 2009.

[149] Welch, P., "The use of fast Fourier transform for the estimation of power spectra: a method based on time averaging over short, modified periodograms," *IEEE Transactions on audio and electroacoustics*, Vol. 15, 1967, pp. 70–73.

[150] Jr, O. M. S., "PSD computations using Welch's method," *NASA STI/Recon Technical Report N*, Vol. 92, 1991, p. 23584.

[151] Sijtsma, P., "Elements of acoustic array data processing," Tech. Rep. NLR-TR-2014-003, NLR, 2014.

[152] Rademaker, E., Sijtsma, P., and Tester, B., "Mode detection with an optimised array in a model turbofan engine intake at varying shaft speeds," *7th AIAA/CEAS Aeroacoustics Conference and Exhibit*, American Institute of Aeronautics and Astronautics, 2001, p. 2181. doi: 10.2514/6.2001-2181.

[153] Sijtsma, P., and Brouwer, H., "Deconvolution of azimuthal mode detection measurements," *Journal of Sound and Vibration*, Vol. 422, 2018, pp. 1–14. doi: 10.1016/j.jsv.2018.02.029.

[154] Chiariotti, P., Martarelli, M., and Castellini, P., "Acoustic beamforming for noise source localization – Reviews, methodology and applications," *Mechanical Systems and Signal Processing*, Vol. 120, 2019, pp. 422–448. doi: 10.1016/j.ymssp.2018.09.019.

[155] Merino-Martínez, R., Sijtsma, P., Snellen, M., Ahlefeldt, T., Antoni, J., Bahr, C. J., Blacodon, D., Ernst, D., Finez, A., Funke, S., Geyer, T. F., Haxter, S., Herold, G., Huang, X., Humphreys, W. M., Leclère, Q., Malgoezar, A., Michel, U., Padois, T., Pereira, A., Picard, C., Sarradj, E., Siller, H., Simons, D. G., and Spehr, C., "A review of acoustic imaging methods using phased microphone arrays," *CEAS Aeronautical Journal*, Vol. 10, 2019, pp. 197–230. doi: 10.1007/s13272-019-00383-4.

[156] Sijtsma, P., "CLEAN Based on Spatial Source Coherence," *International Journal of Aeroacoustics*, Vol. 6, 2007, pp. 357–374. doi: 10.1260/147547207783359459.

[157] Brooks, T. F., and Humphreys, W. M., "A deconvolution approach for the mapping of acoustic sources (DAMAS) determined from phased microphone arrays," *Journal of Sound and Vibration*, Vol. 294, 2006, pp. 856–879. doi: 10.1016/j.jsv.2005.12.046.

[158] Sijtsma, P., Merino-Martinez, R., Malgoezar, A. M., and Snellen, M., "High-resolution CLEAN-SC: Theory and experimental validation," *International Journal of Aeroacoustics*, Vol. 16, 2017, pp. 274–298. doi: 10.1177/1475472X17713034.

[159] Dekker, H. N. J., Baars, W. J., Scarano, F., Tuinstra, M., and Ragni, D., "Unsteady flow behaviour of multi-rotors in ground proximity," *Flow*, Vol. 3, 2023. doi: 10.1017/flo.2023.21.

[160] Dekker, H. N. J., Tuinstra, M., Baars, W. J., Scarano, F., and Ragni, D., "Aero-propulsive Performance Modelling of Over-The-Wing Propulsion at Incidence," *AIAA Journal*, Vol. 63, 2025, pp. 3906–3922. doi: 10.2514/1.J064985.

[161] Dekker, H. N. J., Tuinstra, M., and Ragni, D., "Aeroacoustic Prediction of Over-wing Propulsion at Incidence," *AIAA Journal*, Vol. 63, 2025, pp. 3923–3938. doi: 10.2514/1.J064986.

[162] Dekker, H. N. J., Tuinstra, M., Baars, W. J., Scarano, F., and Ragni, D., "Experimental study of Tilt-Wing eVTOL Take-Off Aerodynamics," *DICUAM 2024*, 2024.

[163] Wolf, C. C., Schwarz, C., Kaufmann, K., Gardner, A. D., Michaelis, D., Bosbach, J., Schanz, D., and Schröder, A., "Experimental study of secondary vortex structures in a rotor wake," *Experiments in Fluids*, Vol. 60, 2019, pp. 1–16. doi: 10.1007/s00348-019-2807-1.

[164] Jeon, Y. J., Müller, M., Michaelis, D., and Wieneke, B., "Efficient reconstruction of flow field with pressure from particle tracks: VIC," *Bulletin of the American Physical Society*, Vol. 63, 2018.

[165] Weitsman, D., Stephenson, J. H., and Zawodny, N. S., "Effects of flow recirculation on acoustic and dynamic measurements of rotary-wing systems operating in closed anechoic chambers," *The Journal of the Acoustical Society of America*, Vol. 148, 2020, pp. 1325–1336. doi: 10.1121/10.0001901.

[166] Wieneke, B., "PIV uncertainty quantification from correlation statistics," *Measurement Science and Technology*, Vol. 26, 2015, p. 74002. doi: 10.1088/0957-0233/26/7/074002.

[167] Grande, E., Romani, G., Ragni, D., Avallone, F., and Casalino, D., "Aeroacoustic Investigation of a Propeller Operating at Low Reynolds Numbers," *AIAA Journal*, Vol. 60, 2022, pp. 860–871. doi: 10.2514/1.J060611.

[168] Yoon, S., Lee, H. C., and Pulliam, T. H., "Computational analysis of multi-rotor flows," *54th AIAA aerospace sciences meeting*, 2016, p. 812. doi: 10.2514/6.2016-0812.

[169] Alvarez, E. J., and Ning, A., "High-fidelity modeling of multirotor aerodynamic interactions for aircraft design," *AIAA Journal*, Vol. 58, 2020, pp. 4385–4400. doi: 10.2514/1.J059178.

[170] Carolus, T., Schneider, M., and Reese, H., "Axial flow fan broad-band noise and prediction," *Journal of sound and vibration*, Vol. 300, 2007, pp. 50–70. doi: 10.1016/j.jsv.2006.07.025.

[171] Abbott, W. A., and White, D. R., "The effect of nozzle pressure ratio on the fountain formed between two impinging jets," Tech. Rep. No. P1166, Royal Aircraft Establishment, 1989.

[172] Lumley, J. L., "The structure of inhomogeneous turbulent flows," *Atmospheric turbulence and radio wave propagation*, 1967, pp. 166–178.

[173] Berkooz, G., Holmes, P., and Lumley, J. L., "The proper orthogonal decomposition in the analysis of turbulent flows," *Annual review of fluid mechanics*, Vol. 25, 1993, pp. 539–575. doi: 10.1146/annurev.fl.25.010193.002543.

[174] George, W. K., "Insight into the dynamics of coherent structures from a proper orthogonal decomposition," *International seminar on wall turbulence*, 1988.

[175] Tinney, C. E., Shipman, J., and Panickar, P., "Proper-Orthogonal-Decomposition-Based Reduced-Order Models for Characterizing Ship Airwake Interactions," *AIAA Journal*, Vol. 58, 2020, pp. 633–646. doi: 10.2514/1.J058499.

[176] Cho, J., and Cho, J., "Quasi-steady aerodynamic analysis of propeller–wing interaction," *International journal for numerical methods in fluids*, Vol. 30, No. 8, 1999, pp. 1027–1042.

[177] Marretta, R. A., Davi, G., Lombardi, G., and Milazzo, A., "Hybrid numerical technique for evaluating wing aerodynamic loading with propeller interference," *Computers & fluids*, Vol. 28, No. 8, 1999, pp. 923–950.

[178] Li, Z., Maltsev, V., Modarres, A. H., and Da Ronch, A., "Rapid Aerodynamic Methods for the Analysis of Propeller Wing Interaction," *AIAA AVIATION FORUM AND ASCEND 2024*, 2024, p. 3521. doi: 10.2514/6.2024-3521.

[179] Cerny, M., and Breitsamter, C., "Investigation of small-scale propellers under non-axial inflow conditions," *Aerospace Science and Technology*, Vol. 106, 2020, p. 106048. doi: 10.1016/j.ast.2020.106048.

[180] Sinnige, T., "Aerodynamic and Aeroacoustic Interaction Effects for Tip-Mounted Propellers: An Experimental Study," Ph.D. thesis, Delft University of Technology, 2018. doi: 10.4233/uuid:214e1e9a-c53e-47c7-a12c-b1eb3ec8293b.

[181] Okulov, V. L., Sørensen, J. N., and Wood, D. H., "The rotor theories by Professor Joukowsky: Vortex theories," *Progress in Aerospace Sciences*, Vol. 73, 2015, pp. 19–46. doi: 10.1016/j.paerosci.2014.10.002.

[182] Tuck, E. O., "A criterion for leading-edge separation," *Journal of Fluid Mechanics*, Vol. 222, 1991, p. 33. doi: 10.1017/S0022112091000988.

[183] Viterna, L. A., and Corrigan, R. D., "Fixed pitch rotor performance of large horizontal axis wind turbines," *Large Horizontal-Axis Wind Turbines (NASA-CP-2230)*, NASA Conference Publication, 1982, pp. 69–86.

[184] Görtler, H., "Berechnung von Aufgaben der freien Turbulenz auf Grund eines neuen Näherungsansatzes ." *ZAMM - Journal of Applied Mathematics and Mechanics / Zeitschrift für Angewandte Mathematik und Mechanik*, Vol. 22, 1942, pp. 244–254. doi: 10.1002/zamm.19420220503.

[185] Sijtsma, P., Oerlemans, S., Tibbe, T. G., Berkefeld, T., and Spehr, C., "Spectral Broadening by Shear Layers of Open Jet Wind Tunnels," *20th AIAA/CEAS Aeroacoustics Conference*, American Institute of Aeronautics and Astronautics, 2014, p. 3178. doi: 10.2514/6.2014-3178.

[186] Champagne, F. H., Pao, Y. H., and Wygnanski, I. J., "On the two-dimensional mixing region," *Journal of Fluid Mechanics*, Vol. 74, 1976, pp. 209–250. doi: 10.1017/S0022112076001778.

[187] Liepmann, H. W., and Laufer, J., "Investigations of free turbulent mixing," Tech. Rep. NACA-TN-1257, National Advisory Committee for Aeronautics (NACA), 1947.

[188] Allen, J. B., and Berkley, D. A., "Image method for efficiently simulating small-room acoustics," *The Journal of the Acoustical Society of America*, Vol. 65, 1979, pp. 943–950. doi: 10.1121/1.382599.

[189] Acevedo Giraldo, D., Roger, M., Jacob, M. C., and Beriot, H., "Analytical study of the aerodynamic noise emitted by distributed electric propulsion systems," *28th AIAA/CEAS Aeroacoustics 2022 Conference*, 2022, p. 2830. doi: 10.2514/6.2022-2830.

[190] Beck, A. B., Cordioli, J. A., Bonomo, L. A., Fonseca, J. V. N., Simões, L. G., Tourinho, A. M., Casalino, D., Ragni, D., and Avallone, F., "Comparative Assessment of Isolated Propeller Noise Test Rigs," *30th AIAA/CEAS Aeroacoustics Conference (2024)*, 2024, p. 3323.

Acknowledgments

This thesis would not have been possible without the support and guidance of a number of people.

I would like start by thanking my promotor, Dani, and copromotor, Woutijn, who have been deeply engaged in my research from start to finish. Your generosity in acknowledging my contributions has been a real motivator for me throughout this project. I really enjoyed our regular progress meetings, which were both informal and helpful. A particular highlight for me was our time in San Diego, both during and after the AIAA conference. Dani, thank you for introducing me to the field of experimental rotor aerodynamics. Your willingness to invest time in helping me with experiments and analyses, regardless of the time, has been invaluable. Your blend of Dutch directness and Italian expressiveness promoted the fun and informal nature of our meetings. Woutijn, your expertise in statistical data analyses and turbulence has been a valuable resource for me. Furthermore, your thorough article reviews, and showing me the importance of a well-crafted schematic, have helped me to greatly improve my writing style. I appreciate your calm and patient approach, which complemented Dani's more expressive communication style perfectly.

Marthijn, as my supervisor from NLR, you deserve equal recognition. I appreciate the substantial time you invested for our in-depth discussions on my research project. Your vision from a research institute point of view complemented with the more academic view of the rest of the supervision-team. Furthermore, thank you for the support and guidance during the preparation and execution of the NLR-experiments, and showing me that there are alternative measurement techniques to PIV, although they are less superior of course.

I would also like to express my appreciation to Fulvio, who, despite not being part of the internal committee, took on an intense supervisory role throughout my PhD journey. Thank you, Fulvio, for asking the difficult, and sometimes annoying, questions that have helped me grow; I appreciate the value you placed on my personal development. Your in-depth knowledge of PIV has been an invaluable asset throughout my research.

Moreover, I am really grateful for the opportunity to have met and collaborated with PhD peers at TU Delft's Wind Energy and Aerodynamic sections, NLR, and within the Enodise project. Though there are too many to list here, I would like to specifically acknowledge a few who have made a notable impact. Ilda, with whom I shared a parallel PhD experience at NLR and TUD, allowing us to mutually support each other through common challenges. Fernanda, with whom I collaborate in the Enodise project, who made the meetings and joint-efforts much more enjoyable. I also wish to recognize my colleagues at NLR-AVVA department for providing regular feedback on my work and Sylvia for her administrative support and introducing me to TU Delft.

As my research relied heavily on experimental data, I would like to express my gratitude to the technical staff who supported me throughout my project. In particular, from NLR-AVVA, I wish to acknowledge the technical assistance from Tim and Laurens and software support from Paul during the preparation and execution of the experiments. Ad-

ditionally, I am thankful for the technical expertise provided by the staff at TUD-HSL: Dennis, Peter, Nico, Frits and Henk-Jan. On a personal note, I would also like to acknowledge my father Niels, who generously helped me with the design and manufacturing of the rotor mount for my first experiment.

Finally, I wish to acknowledge my close family. Meike, you are perhaps the only person that enjoys me finishing this PhD more than myself. Thank you for supporting me during all the difficult times. Your regular visits to Delft in the first year, during the time of Covid-restrictions, brought joy and pulled me through. Thank you for listening to all my complaints and worries, and helping with all the practical stuff; your talent in graphical design saved me countless times when designing sketches, covers and posters. Thank you Iris, Niels and Zoë for your endless support and regular check-ups on how I am doing, it really helped a lot.

Hasse
Arnhem, September 2025

Curriculum Vitæ

Hasse Nicolaas Jan Dekker

23/06/1995   Date of birth in Zutphen, The Netherlands

Education

2020-2025   PhD in Aerospace Engineering
                     Delft University of Technology
                     Delft - The Netherlands
                     Thesis: Interactions of Multi-Rotors with Surfaces:
                          Aerodynamic Characterization and
                          Performance Modelling

2017-2020   MSc in Mechanical Engineering
                     University of Twente
                     Enschede - The Netherlands
                     Thesis: Discontinuous Galerkin Method applied to
                          Incompressible Flow Equations

2014-2017   BSc in Mechanical Engineering
                     University of Twente
                     Enschede - The Netherlands
                     Thesis: Angled LED Schlieren photography for the analysis of
                          3D flow structures in supersonic cross-flows

List of Publications

Journal Publications

4. Dekker, H. N. J., Tuinstra, M., and Ragni, D., "Aeroacoustic Prediction of Overwing Propulsion at Incidence", *AIAA Journal*, Vol. 63, 2025, pp. 3923-3938, doi: 10.2514/1.J064986.

3. Dekker, H. N. J., Tuinstra, M., Baars, W. J., Scarano, F., and Ragni, D., "Aeropropulsive Performance Modelling of Over-The-Wing Propulsion at Incidence", *AIAA Journal*, Vol. 63, 2025, pp. 3906–3922, doi: 10.2514/1.J064985.

2. Dekker, H. N. J., Baars, W. J., Scarano, F., Tuinstra, M., and Ragni, D., "Unsteady flow behaviour of multi-rotors in ground proximity", *Flow*, Vol.3, 2023, doi: 10.1017/flo.2023.21.

1. Dekker, H. N. J., Ragni, D., Baars, W. J., Scarano, F., and Tuinstra, M., "Aerodynamic Interactions of Side-by-Side Rotors in Ground Proximity", *AIAA Journal*, Vol. 60, 2022, pp. 4267–4277, doi: 10.2514/1.J061105.

Conference Publications

6. Dekker, H. N. J., Tuinstra, M., Baars, W. J., Scarano, F., and Ragni, D., "Experimental study of Tilt-Wing eVTOL Take-Off Aerodynamics", *DICUAM 2024*, 2024.

5. Dekker, H. N. J., Baars, W. J., Scarano, F., Ragni, D., and Tuinstra, M., "Flow Field Measurements around an Over-The-Wing Propeller at Incidence", *20th International Symposium on Flow Visualization*, 2023.

4. Dekker, H. N. J., Tuinstra, M., Scarano, F., Baars, W. J., and Ragni, D., "Aeropropulsive Performance Modelling of Over-The-Wing Propulsion at Incidence", *AIAA AVIATION 2023 Forum*, 2023, doi: 10.2514/6.2023-3355.

3. Dekker, H. N. J., Brouwer, H., Kok, J. C., Laban, M., and Tuinstra, M., "Tonal Noise Measurements and Simulations of an Over-The-Wing Propeller", *AIAA AVIATION 2023 Forum*, 2023, doi: 10.2514/6.2023-3358.

2. Caputo, P., Dekker, H. N. J., Pavel, M. D., and Scarano, F., "Understanding the Vortex-Ring State for VTOL Aircraft in Vertical and Steep Descending Flight", *DICUAM 2022*, 2022.

1. Dekker, H. N. J., Ragni, D., Baars, W. J., Scarano, F., and Tuinstra, M., " Three-dimensional flow topology of a multi-rotor in ground effect", *DICUAM 2021*, 2021.

Datasets

1. Dekker, H. N. J., Tuinstra, M., and Ragni, D., H2020 Enodise: TUD/NLR Experimental database configuration B3 (2.0) [Data set]. *Zenodo*, 2023. doi: 10.5281/zenodo.8283630